STRUCTURE AND PROPERTIES OF SOME TRIANGULAR LATTICE MATERIALS

Lewis James Downie

A Thesis Submitted for the Degree of PhD
at the
University of St Andrews

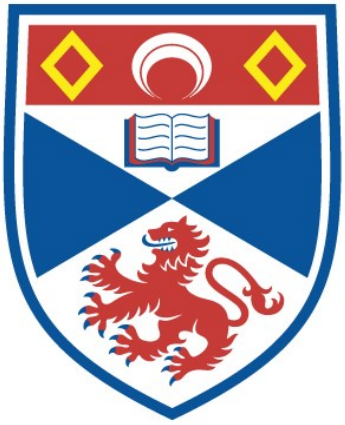

2014

Structure and Properties of Some Triangular Lattice Materials

Lewis James Downie

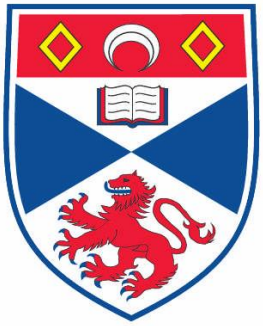

This thesis is submitted in partial fulfilment for the degree of
PhD
at the
University of St Andrews

1. Candidate's declarations:

I, Lewis James Downie, hereby certify that this thesis, which is approximately 38,000 words in length, has been written by me, that it is the record of work carried out by me and that it has not been submitted in any previous application for a higher degree.

I was admitted as a research student in March, 2010 and as a candidate for the degree of PhD in January, 2011; the higher study for which this is a record was carried out in the University of St Andrews between 2010 and 2013.

Date …… signature of candidate ……

2. Supervisor's declaration:

I hereby certify that the candidate has fulfilled the conditions of the Resolution and Regulations appropriate for the degree of PhD in the University of St Andrews and that the candidate is qualified to submit this thesis in application for that degree.

Date …… signature of supervisor ……

3. Permission for electronic publication: (*to be signed by both candidate and supervisor*)

In submitting this thesis to the University of St Andrews I understand that I am giving permission for it to be made available for use in accordance with the regulations of the University Library for the time being in force, subject to any copyright vested in the work not being affected thereby. I also understand that the title and the abstract will be published, and that a copy of the work may be made and supplied to any bona fide library or research worker, that my thesis will be electronically accessible for personal or research use unless exempt by award of an embargo as requested below, and that the library has the right to migrate my thesis into new electronic forms as required to ensure continued access to the thesis. I have obtained any third-party copyright permissions that may be required in order to allow such access and migration, or have requested the appropriate embargo below.

The following is an agreed request by candidate and supervisor regarding the electronic publication of this thesis:

Embargo on both [all or part] of printed copy and electronic copy for the same fixed period of 2 years (*maximum five*) on the following ground(s):

publication would preclude future publication;

Date …… signature of candidate …… signature of supervisor ……

A supporting statement for a request for an embargo must be included with the submission of the draft copy of the thesis. Where part of a thesis is to be embargoed, please specify the part and the reasons.

Abstract

This thesis is concerned with the study of two families of materials which contain magnetically frustrated triangular lattices. Each material is concerned with a different use; the first, analogues of $YMnO_3$, is from a family of materials called multiferroics, the second, $A_2MCu_3F_{12}$ (where A = Rb^{1+}, Cs^{1+}, M = Zr^{4+}, Sn^{4+}, Ti^{4+}, Hf^{4+}), are materials which are of interest due to their potentially unusual magnetic properties deriving from a highly frustrated Cu^{2+}-based kagome lattice.

$YFeO_3$, $YbFeO_3$ and $InFeO_3$ have been synthesised as their hexagonal polymorphs. $YFeO_3$ and $YbFeO_3$ have been studied in depth by neutron powder diffraction, A.C. impedance spectroscopy, Mössbauer spectroscopy and magnetometry. It was found that $YFeO_3$ and $YbFeO_3$ are structurally similar to hexagonal $YMnO_3$ but there is evidence for a subtle phase separation in each case. Low temperature magnetic properties are also reported, and subtle correlations between the structural, electrical and magnetic properties of these materials have been found. $InFeO_3$ was found to adopt a higher symmetry and is structurally similar to the high temperature phase of $YMnO_3$. $TbInO_3$ and $DyInO_3$ have also been synthesised and studied at various temperatures. The phase behaviour of $TbInO_3$ was analysed in detail using neutron powder diffraction and internal structural changes versus temperature were mapped out – there is also evidence for a subtle isosymmetric phase transition. Neither $DyInO_3$ nor $TbInO_3$ show long-range magnetic order between 2 and 300 K, or any signs of ferroelectricity at room temperature.

The new compounds $Cs_2TiCu_3F_{12}$ and $Rb_2TiCu_3F_{12}$ have both been synthesised and shown to be novel kagome lattice based materials. The former shows a transition from rhombohedral to monoclinic symmetry in the powder form and from rhombohedral to a larger rhombohedral unit cell in the single crystal – a particle size based transition pathway is suggested. For $Rb_2TiCu_3F_{12}$ a complex triclinic unit cell is found, which distorts with lowering temperature. Both materials show magnetic transitions with lowering temperature. The solid solution $Cs_{2-x}Rb_xSnCu_3F_{12}$ (x = 0, 0.5, 1.0, 1.5, 2.0) was synthesised and investigated crystallographically, demonstrating a range of behaviours. $Rb_2SnCu_3F_{12}$ displays a rare re-entrant structural phase transition. In contrast, $Cs_{0.5}Rb_{1.5}SnCu_3F_{12}$ shows only the first transition found in the Rb^+ end member. $CsRbSnCu_3F_{12}$ adopts a lower symmetry at both room temperature and below. $Cs_{1.5}Rb_{0.5}SnCu_3F_{12}$ and $Cs_2SnCu_3F_{12}$ show a rhombohedral → monoclinic transition, which is similar to that found in $Cs_2TiCu_3F_{12}$.

Acknowledgements

On completing this PhD thesis I would like to thank **Prof. Phil Lightfoot** for his generous supervision throughout the past three and a half years. The opportunity, and since then the calm and considered mentoring, has been invaluable in my development as a chemist.

Lesser, but still important, is my thanks to all the other academics and researchers that have helped me through my work with their specialist skills and understanding. Even though some results have not made it into this thesis they have still been essential in developing understanding and identifying future pathways for research. In the School of Chemistry: **Dr F. D. Morrison**, **Prof. A. M. Z. Slawin**, **Prof. W. Zhou** and **Mrs S. Williamson** have all helped in the acquisition of results and their analysis. Other specialists from further afield have also contributed their knowledge or helped me with new techniques or equipment. These include **Drs W. Kockelmann**, **A. Daoud-Aladine** and **D.A. Keen** of ISIS pulsed neutron and muon source, **Prof. C. C. Tang** and **Drs Stephen Thompson** and **J. E. Parker** of Diamond Light Source. Outside of central facilities support was found from **Dr S. D. Forder**, who ran a number of critical Mössbauer spectra, **Dr M. A. de Vries,** who has been a key collaborator in the collection and analysis of magnetic data, **Dr A. F. Kusmartseva** who helped with early magnetic measurements and **Dr A. L. Goodwin** who introduced me to pair distribution function analysis. **Prof. S. Parsons** was more than helpful with the collection of some particularly complex data and I am particularly indebted for his time and efforts.

I am very grateful for the warm hospitality and specialist instruction I received at the department of chemistry, Moscow State University from **Prof. V. A. Dolgikh**, **Drs E. I. Ardashnikova**, **P. S. Berdonosov** and **D. O. Charkin**. I am also appreciative of the further help I received from **Prof. A. N. Vasiliev** and **Mr A. Golovanov** of the low temperature physics department.

Outside of research I have received a great deal of support, patience and understanding from my partner, **Laura Mitchell**. I have also made many new friends within the chemistry department – and outside of it – who have been more than supportive both in terms of work and diversionary activities. Old friends have also supplied welcome encouragement. I would also like to thank my parents, **James Downie** and **Margaret Downie,** brother, **Jonathan Downie**, grandmother and other family members for their continued support throughout my research.

Contents

Selected Appendices

1 Introduction

This thesis is concerned with observing the – mostly structural – effects of substituting ions in two functional materials of current academic interest. Both materials contain magnetic lattices that are based upon a triangular motif, which is synonymous with magnetic frustration. However, the materials have very different characteristics – one looks to avoid magnetic order and thus enter into an exotic magnetic state called a "quantum spin liquid" whereas the other looks to magnetically order despite the frustration. The former, the $A_2MCu_3F_{12}$ family, is based upon a highly frustrated Cu^{2+} kagome lattice which has previously been shown to encourage novel and exotic magnetic behaviours. The latter, $YMnO_3$, is based upon a triangular Mn^{3+} lattice but has been shown to undergo long-range magnetic order; coupled with the ferroelectric properties of this material this yields a material called a "multiferroic" in which two or more forms of order are present within the material simultaneously. In this discussion it is advantageous to discuss the types of order possible in the two materials first.

1.1 Multiferroics

A multiferroic is a material that combines two types of ordering from the classes ferroelectric, magnetic and ferroelastic[1]. The term is principally associated with materials that combine both magnetic and ferroelectric ordering (even in cases of antiferromagnetic ordering) and so these form the focus of this introduction.[2] Ferroelastic materials are those which show a spontaneous deformation. Magnetoelectric multiferroics are of particular interest as there is the possibility of a linkage between the magnetic and ferroelectric ordering (the magnetoelectric effect). This linkage is usually found in materials where the source of magnetism and ferroelectricity are the same and are called type-II multiferroics. The preceding type-I multiferroics generally have different sources of magnetism and ferroelectricity and thus have only a weak, if observable, linkage.[2] Such cross interference is useful in areas such as data storage as one could write electrically and read magnetically, for example.[3]

It is important to have a basic understanding of ferroelectric and magnetic ordering in order to compare and contrast their requirements and to understand their measurement.

1.1.1 Magnetism

Many materials behave differently in magnetic environments and allow themselves, at high temperatures at least, to be broadly divided into two main classes; diamagnetic and paramagnetic. Diamagnetism is characteristic of a material in which the ions have paired electrons and thus there is only a minor, repulsive interaction with an applied magnetic field. Paramagnetic materials are those in which there are unpaired electrons; transition metals and lanthanides may have unpaired electrons in their *d* and *f* electron shells, respectively. The lack of an electron with opposing spin leads to no cancelling out of the magnetic moment on that atom. This has a physical manifestation in a Guoy balance – a diamagnetic material will show a decrease in force applied to the balance due to repulsion, whereas a paramagnetic material will show an increase due to attraction[4]. Quantitatively, if we consider both of these materials in a magnetic field, *H*, they both show different types of magnetic induction, *M*. In the diamagnetic sample the magnetic flux lines are expelled from the sample (and so *M* is negative) and in the paramagnetic sample the magnetic flux is increased (and so *M* is positive).

If both *M* and *H* are known then it is possible to calculate the magnetic susceptibility of the material (Equation 1.1)

$$\boldsymbol{\chi = \frac{M}{H}} \qquad 1.1$$

From this the molar susceptibility, χ_m, can be acquired leading to a comparative value for a number of different materials. However, this is comparative only if measured in the same conditions as this value is found to change with temperature. Such changes also betray the existence of more than the two behaviours previously alluded to.

1.1.1.1 Variations of magnetism with temperature

For diamagnetic materials there is no variation of χ with temperature as its origin is not subject to thermal disorder. Paramagnetism is subject to variation with temperature as its positive interaction is due to alignment of the unpaired electron spins with *H*. As the temperature is increased the tendency to align with *H* is reduced due to increasing thermal disorder. Most paramagnetic materials approximately follow the Curie law with varying temperature:

$$\boldsymbol{\chi = \frac{C}{T}} \qquad 1.2$$

(where C = Curie constant and T = Temperature)

A modification of the Curie law which often provides for a better fit is the Curie-Weiss law which takes into account the Weiss constant, T_{CW}, of the material[5].

$$\boldsymbol{\chi = \frac{C}{T - T_{CW}}} \qquad 1.3$$

The above formulae suggest the type of behaviour shown in Figure 1.1.

C is related to the magnetic moment, μ (in Bohr magnetons), by equation 1.4.

$$\boldsymbol{\mu_{eff} = \sqrt{8C}} \qquad 1.4$$

The magnetic moment can be compared to that expected for individual ions for transition metals (Equation 1.5) and lanthanides (Equation 1.6).

$$\boldsymbol{\mu = 2\sqrt{S(S+1)}} \qquad 1.5$$

(where S = spin state of the ion)

$$\boldsymbol{\mu = g_J\sqrt{J(J+1)}} \qquad \left(\boldsymbol{g_J = \frac{3}{2} + \frac{S(S+1) - L(L+1)}{2J(J+1)}}\right) \qquad 1.6$$

(where L and J are as defined by the microstate of the ion).

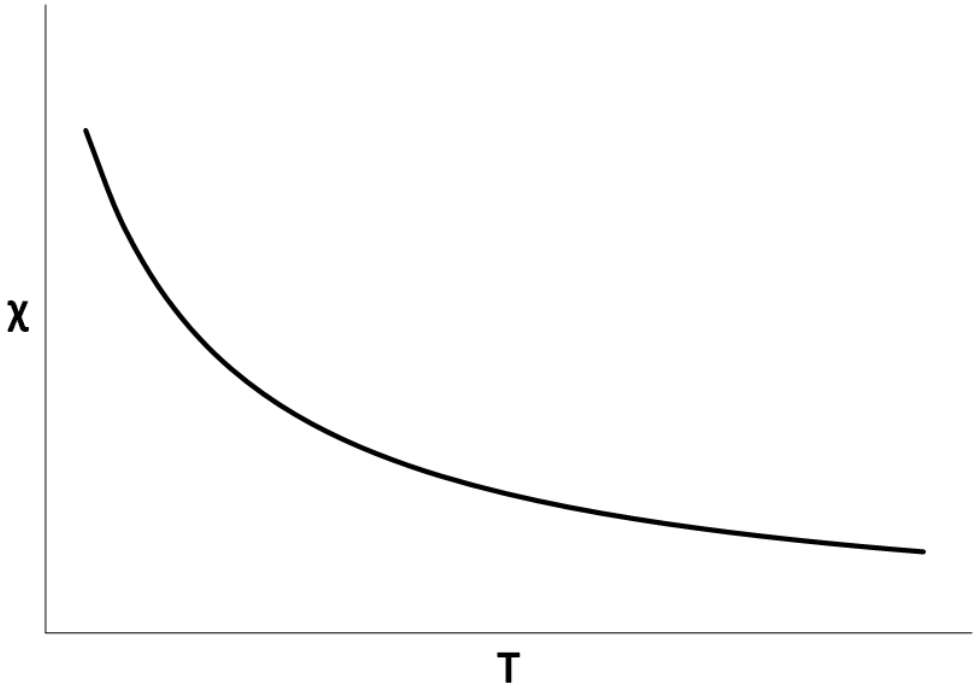

Figure 1.1: Qualitative behaviour for χ of a paramagnet as a function of temperature.

As suggested there are variations to paramagnetic behaviour[6]. On cooling, ferromagnetic materials shows a paramagnetic behaviour until a certain temperature (the Curie temperature, T_C) at which point χ increases markedly (Figure 1.2).

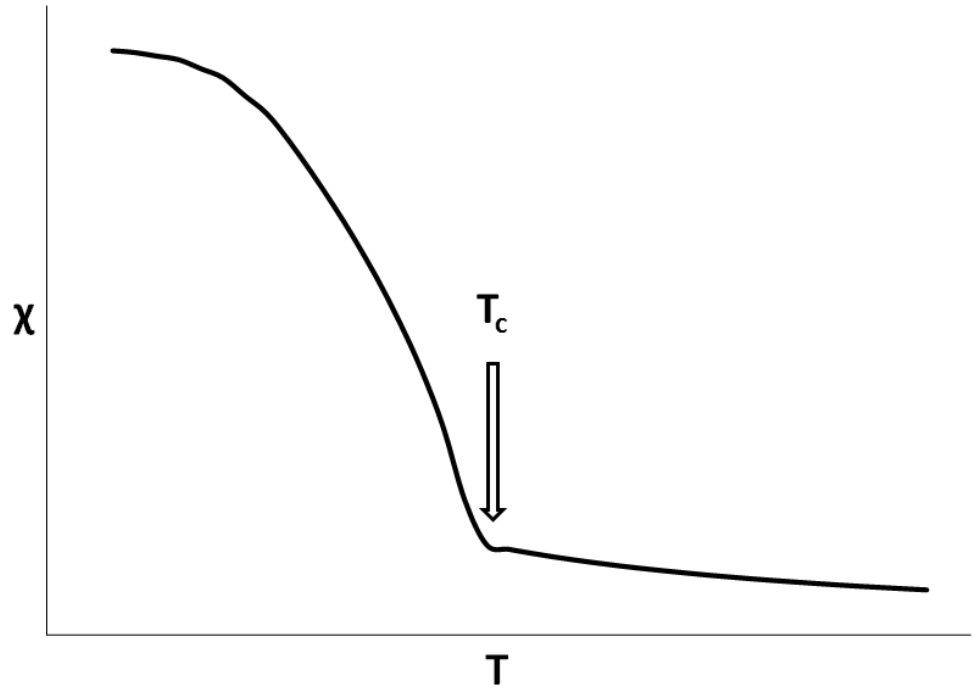

Figure 1.2: Qualitative behaviour of χ vs. T for a ferromagnetic sample.

The rapid increase in χ at T_C is due to the spins within the sample aligning with each other *and* the external field, *H*. For a paramagnetic sample the spins do not align with each other but align with the magnetic field independently; a process which leads to less overall alignment. Such a clear distinction exists between the two possible behaviours as at T_C the thermal energy is enough to overcome the spin ordering energy.

Ferromagnetic materials can show a hysteresis loop in their spontaneous magnetisation; they can retain a magnetic polarisation that has been previously applied to them. It is this retention of a residual magnetic field which is exploited for data storage. Different ferromagnetic materials have different hysteretic behaviours and so lend themselves to different applications.

Another exception to the two main regimes is antiferromagnetism. In this case the material appears as paramagnetic at elevated temperature but below a critical temperature it is found that χ begins to decrease (Figure 1.3). The transition temperature (the Néel point, T_N) signals the point at which spins begin to order internally but instead of aligning in the same direction, as for ferromagnetism, they align in opposite directions. This ordering leads to the magnetic moments cancelling out.

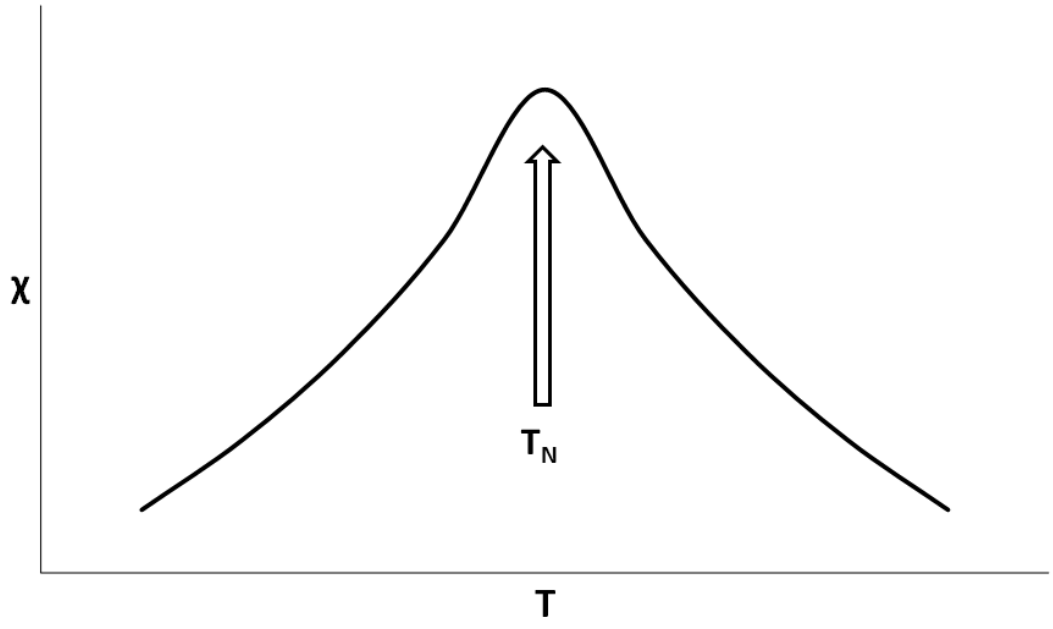

Figure 1.3: Qualitative behaviour of χ vs. T for an antiferromagnetic sample.

As well as these two ordering regimes there are also possible combinations. Ferrimagnetism, for example, occurs when there is partial cancellation of the magnetic moment; two spins could be pointing in one direction and one spin opposing this or the spins could be of equal number but differing magnitude. One can also consider the spins to be able to point in any direction and not just aligned parallel or anti-parallel. Such an arrangement allows for the presence of canted antiferromagnetism where spins do not completely cancel out (Figure 1.4).

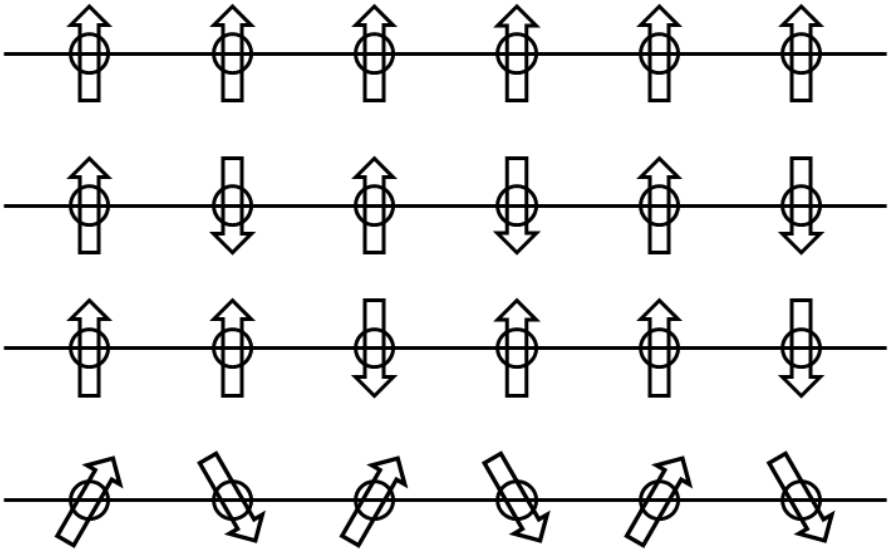

Figure 1.4: Different magnetic orders on a one dimensional line of spins; from top: ferromagnetism, antiferromagnetism, ferrimagnetism, canted ferromagnetism.

1.1.1.2 Variations of magnetism with size

In the bulk, the above effects are usually found but on reducing particle size unusual effects can occur. One of these effects is superparamagnetism. In this effect the particle size is so small that its entirety exists as one ferromagnetic or ferrimagnetic magnetic domain. The net magnetic moment is constantly changing and thus gives the appearance of zero moment. On the application of a magnetic field, however, there is the appearance of a larger magnetic field than would be given for a purely paramagnetic system. This is because there is a slight ferro/ferrimagnetic character to the system. On cooling, the time required for the domain to change direction increases and below a certain temperature, the blocking temperature, the systems appears as a ferro/ferrimagnetic system.[7]

1.1.2 Ferroelectricity

Ferroelectricity has many parallels with magnetism. Most inorganic insulators are found to be from a class of materials called dielectrics. This class is characterised by an electrical polarisation across the material when a potential difference is applied, but application of that potential difference does not lead to long-range movement of electrons or ions. The polarisation also disappears when the potential difference is removed; this is in analogy to a paramagnetic substance. This analogy is continued by the occurrence of a type of dielectric, a ferroelectric, which has a spontaneous electrical polarisation, *P*, and can align with and retain the direction of an electric field, *E*. *P* and *E* are the electrical equivalents of *M* and *H* in magnetism.[1] With a ferroelectric it is also possible to generate a hysteresis loop in *P* vs. *E*.[8]

1.1.2.1 Origins of ferroelectricity

There are three main origins of ferroelectricity, which all lead to the same effect – the presence of a dipole and as such an anisotropic electric field. This anisotropic field can be around a particular unit cell or smaller unit and these can form a crystal with no apparent polarisation – this is because individual domains can form and act to cancel each other out.

The first origin of ferroelectricity is that found in systems like $BaTiO_3$, for example. This perovskite-like structure has the B-site cation (Ti^{4+}) displaced off-centre, which leads to a polarisation (Figure 1.5). This is also manifested in the symmetry of the crystal, which is no longer cubic like the aristotype perovskite but tetragonal. This off-centre character is thought to be related to hybridization of the B-site 3*d* orbitals and oxygen 2*p* orbitals.[9]

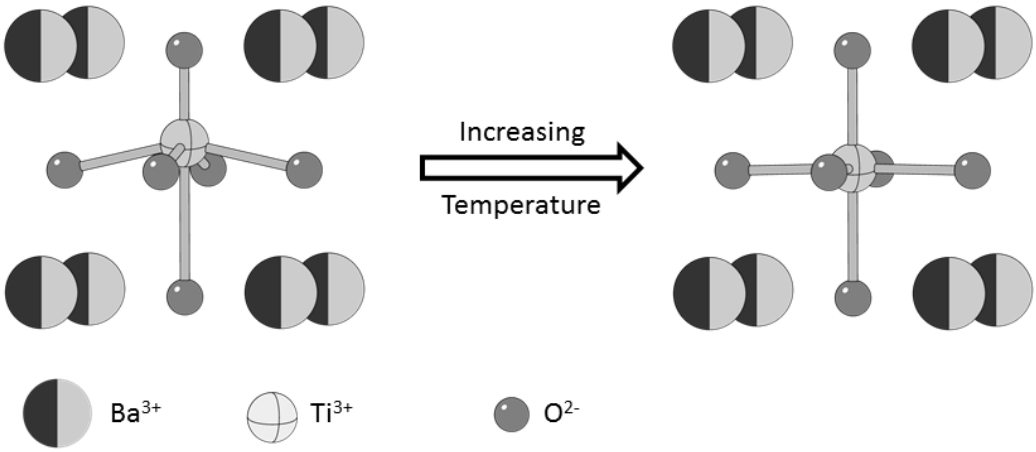

Figure 1.5: Ferroelectric state (left) and paraelectric state (right) for $BaTiO_3$ (off-centre Ti^{4+} position exaggerated for clarity).

Another origin of ferroelectricity depends on the presence of cations with an ns^2 lone pair; for example Pb^{2+}, Bi^{3+}. In these cases the orientation of the *s*-orbital lone pair leads to the creation of a distortion which causes a polarisation (Figure 1.6). This is the main source of polarisation in the multiferroic $BiFeO_3$.[10]

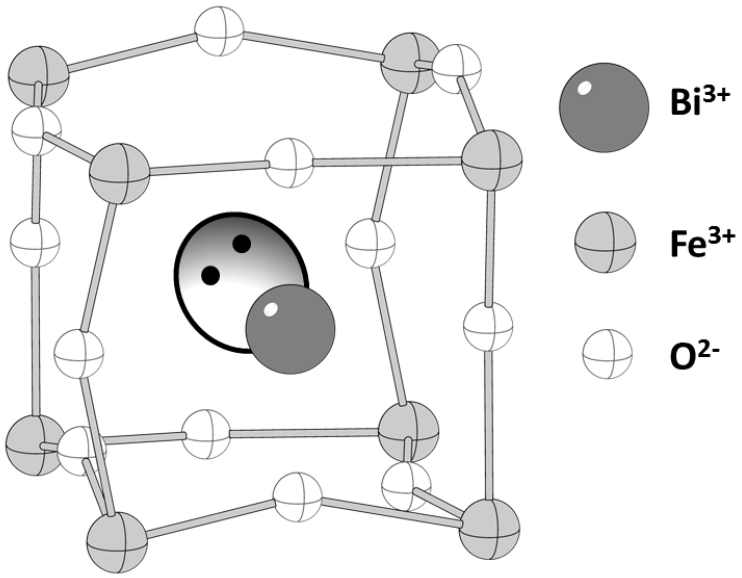

Figure 1.6: Model of $BiFeO_3$ in polarised room temperature state. Bi^{3+} has a particularly anisotropic quality due to the stereochemically active *s*-orbital lone pair (indicated).

The third origin of ferroelectricity – and most relevant to our consideration of the analogues of $YMnO_3$ – is "geometric" ferroelectricity. This ferroelectricity is characterised by the change from a ferroelectric phase to a paraelectric phase driven by a geometric size mis-match, but no direct "electronic" involvement. For $YMnO_3$ this is characterised as a high temperature paraelectric phase and a low temperature distorted phase which shows ferrielectric properties (with electrical dipoles analogous to ferrimagnetism in this case). The ferrielectric origin is due to the presence of a corrugation in the MnO_5 layer and corresponding uncompensated dipoles created by the bonding of Y^{3+} to O^{2-}(Figure 1.7).[11]

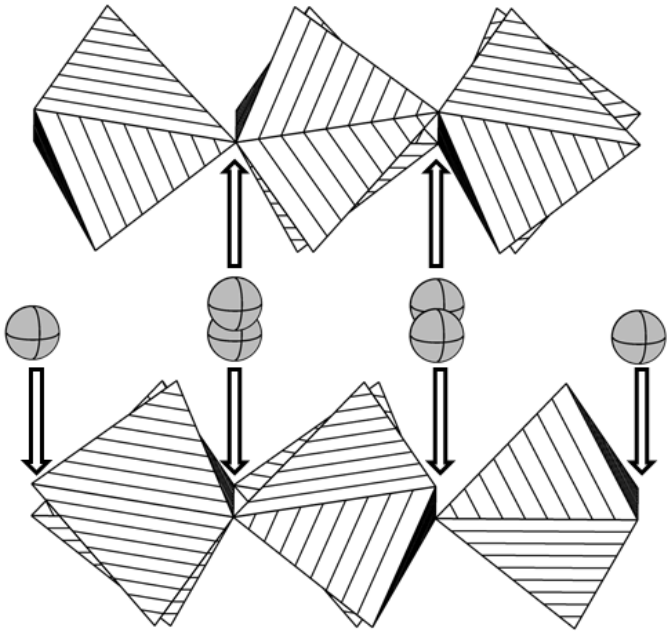

Figure 1.7: Section of the crystal structure of $YMnO_3$ showing the corrugation of the MnO_5 layer (striped polyhedra) and the resulting unbalanced displacement of the Y^{3+} (grey ellipses). Arrows indicated dipole directions.

All of the above origins of ferroelectricity require the unit cell to have no inversion symmetry.[1] The result of an inversion centre would cancel out any electrical anisotropy. In particular the crystallographic space group should be polar, rather than merely non-centrosymmetric.

1.1.3 Multiferroic materials

There are of course materials that combine both magnetic and electrical qualities; the first one to be discovered was nickel-iodine boracite, $Ni_3B_7O_{13}I$.[12] This is a complex material, however, and so does not lend itself well to structural analysis – especially in a time before high resolution synchrotron and neutron sources. A number of mixed perovskite examples sought to partially replace the B-site d^0 cation in a ferroelectric perovskite with a magnetic d^n cation. Examples of this include $Pb_2(FeTa)O_6$ [13] and $Pb_2(CoW)O_6$.[14] The issues with this can include a degree of magnetic dilution leading to lower ordering temperatures.

Since these early experiments a large amount of research has gone into the type-I ferroelectrics $BiFeO_3$ [15] and $BiMnO_3$.[16] In these examples the source of the magnetism (the

transition metal) and the source of the ferroelectricity (the Bi^{3+} cation) are different and so the individual orderings are unlikely to be strongly coupled.

In situations where there is a strong coupling it is called the magnetoelectric effect (ME). This is characterised by the ability to control the magnetisation with an electric field, or vice-versa, and is of great interest due to the potential technical uses.[3] This effect was first seen in the first multiferroics (e.g. boracite [17]) but it is a fundamentally electronic structure based phenomenon. If the magnetic and electronic structures are incommensurate (like type-I multiferroic) then the orders can be difficult to directly observe.[17] The origin of this effect is due to magnetism being driven by orbital overlaps which are dependent on bond distance and angle. Application of an electric field can alter these variables, thus affecting overlap.[18]

1.1.4 Hexagonal rare-earth manganites

The hexagonal rare earth manganites have the same stoichiometry as a perovskite, $MMnO_3$ (where M is a rare-earth), but a very different structure. The structure is formed from layers of corner-sharing MnO_5 trigonal bipyramids separated by M^{3+} cations which are found above and below the shared corners (Figure 1.8).

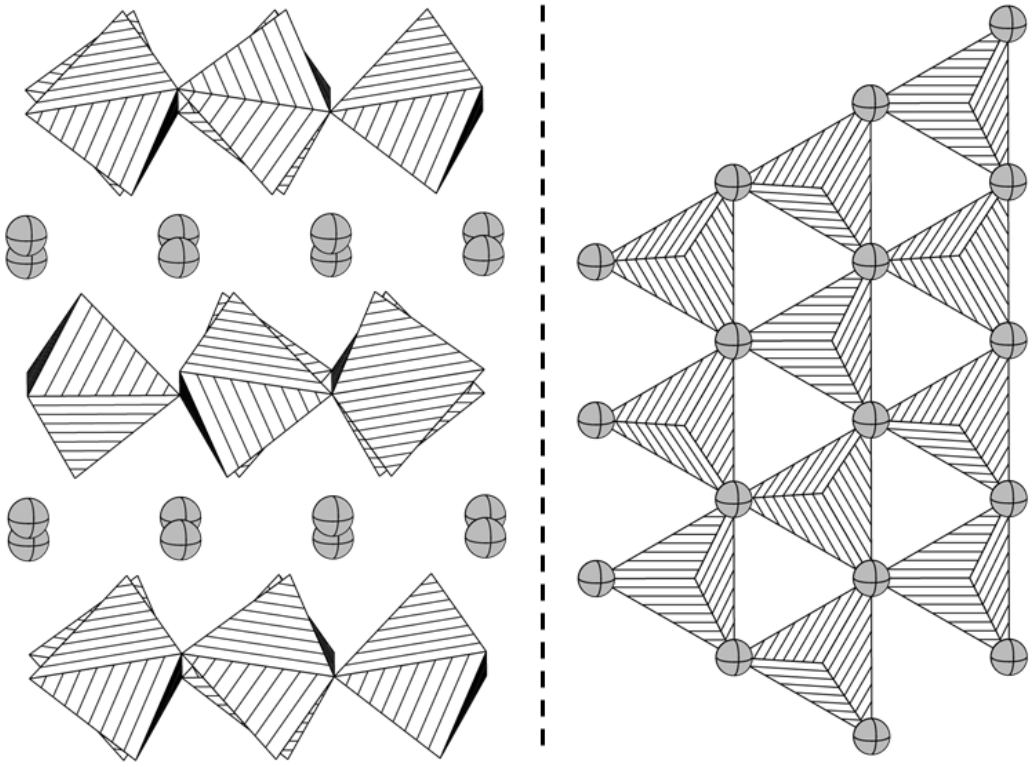

Figure 1.8: Crystal structure of $YMnO_3$ along the *ab*-plane (left) and down the *c*-axis (right).

The majority of these compounds were first discovered in 1960s, at which point both their hexagonal symmetry and ferroelectricity was confirmed.[19] The space group of $MMnO_3$ under ambient conditions is polar, $P6_3cm$, and so also non-centrosymmetric. This is because

the MnO_5 trigonal bipyramid layers are corrugated and the M^{3+} ions are unevenly displaced from each other along the *c*-axis in a 1:2 ratio. The Mn^{3+} lattice is the source of the magnetism and this occurs by super-exchange through the coordinating O^{2-}.

1.1.4.1 Magnetism in $MMnO_3$

At room temperature $MMnO_3$ is paramagnetic in nature. Further magnetic investigation in this area leads to a suggested Curie-Weiss behaviour with a Weiss constant of ~ -400 to -1000 K, suggesting that the magnetic interactions are primarily antiferromagnetic and strong.[20] On cooling, T_N is found to be between 70 and 130 K dependent on the identity of M^{3+}. A general trend is that with decreasing size of M^{3+} the MnO_5 layer present in the *ab*-plane can contract further thus maximising overlap.[21] It is found that the Weiss temperature also decreases with overlap; this is due to the antiferromagnetic interaction increasing.

The magnetic structure also has a 3 – dimensional property; there are further super-exchange interactions along the *c*-axis via $Mn^{3+} – O^{2-} – O^{2-} – Mn^{3+}$. This ensures inter-layer order. The triangular lattice leads to a degree of magnetic frustration within the structure and the frustration index (T_{CW}/T_N) is found to be ~ 10 for $YMnO_3$ (> 10 is indicative of a magnetically frustrated system).[21] This frustration can lead the spins to arrange in a non-collinear way and so frustrate antiferromagnetic ordering. For the $P6_3cm$ space group there are 6 possible (commensurate) magnetic unit cells (Figure 1.9).[22] The magnetic unit cell can vary not only with M^{3+} but also temperature.[23] This ordering only takes into account the transition metal however; when a rare-earth with a f^n electronic configuration is present there may be further ordering of those moments. This second ordering event is usually seen at lower temperature.[22]

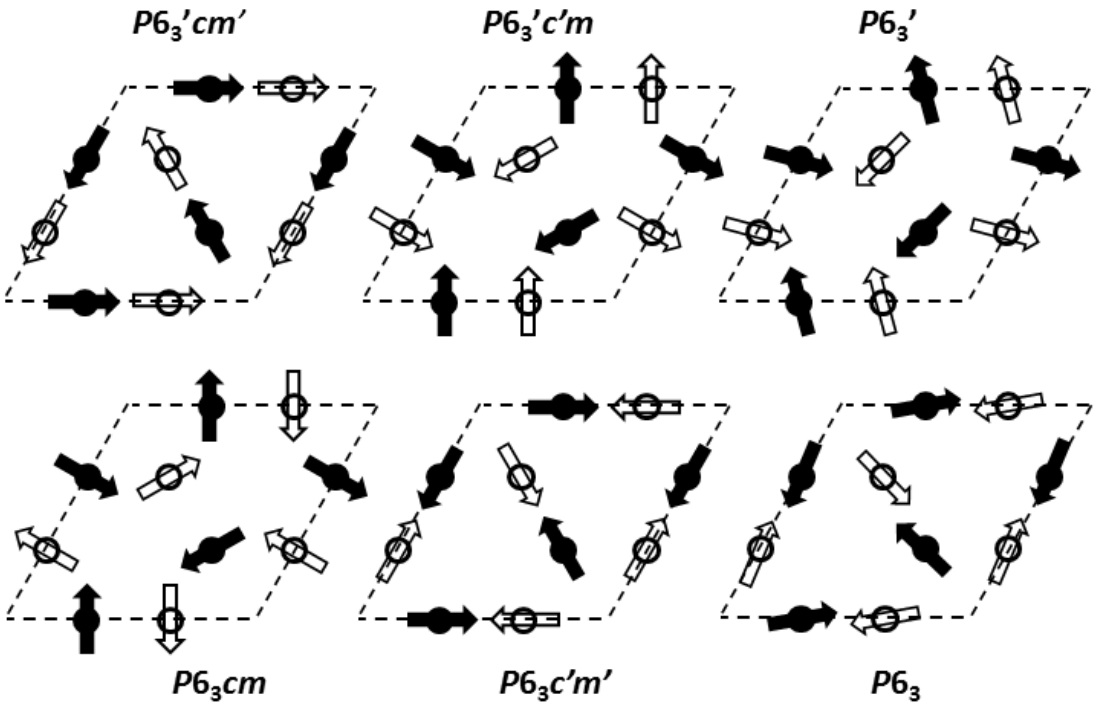

Figure 1.9: The six possible commensurate magnetic unit cells for $MMnO_3$ in a $P6_3cm$ crystallographic unit cell. Open circles/spins represent top layer of Mn^{3+} in unit cell, filled circles/spins represent bottom layer of Mn^{3+}.

1.1.4.2 Ferroelectricity in $MMnO_3$

$MMnO_3$ is found to be ferroelectric at room temperature, with the polarisation along the *c*-axis. This is primarily related to the M^{3+} ions being displaced asymmetrically along the *c*-axis. This varies the $M^{3+} – O^{2-}$ distance creating dipoles. For two of the M^{3+} the cation moves 'up' the *c*-axis, for the other four of the M^{3+} present in the unit cell the movement is 'down' the *c*-axis. Thus, $MMnO_3$ shows ferrielectric ordering.[2]

Heating $MMnO_3$ leads to the disappearance of ferroelectricity at 800 – 1400 K depending on M^{3+} (and in some cases the study).[24] This is part of a structural transition from $P6_3cm$ symmetry to $P6_3/mmc$; a non-polar space group (Figure 1.10). This transition leads the M^{3+} ions to align in a single plane and the trigonal bipyramidal MnO_5 plane to lose its corrugation.

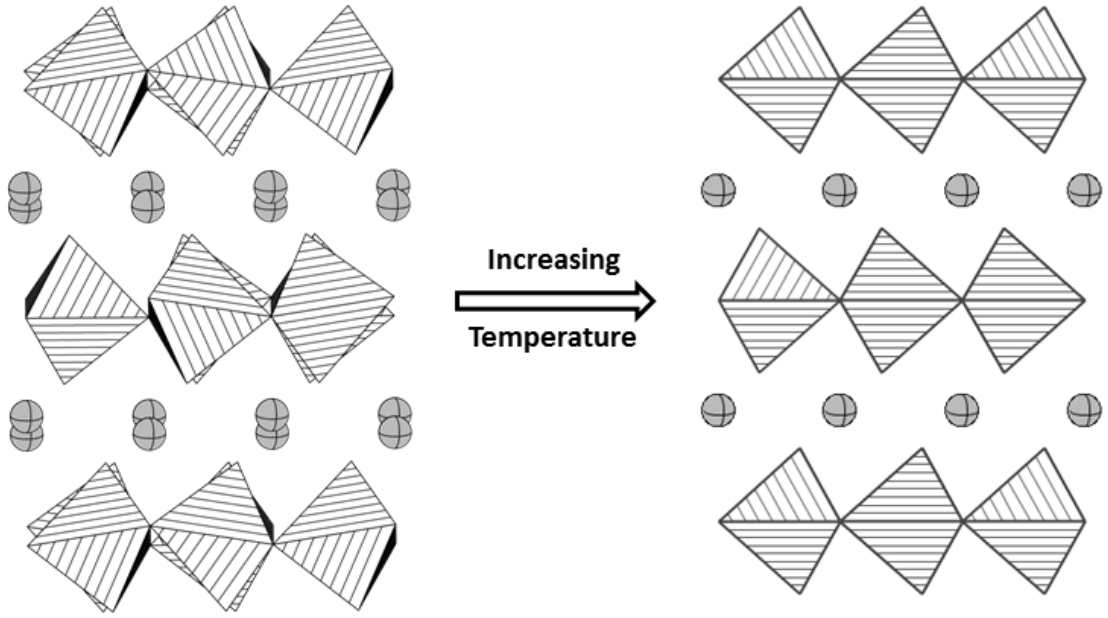

Figure 1.10: Crystal structures of $MMnO_3$ in the low temperature ferroelectric phase (left) and the paraelectric, high temperature phase (right).

The $P6_3cm$ phase is found to have a unit cell of three times the volume of the high symmetry $P6_3/mmc$ phase, as the *a* and *b* parameters are $\sqrt{3}$ times the size.[25] It has been suggested that the transition temperature is related to the size of the M^{3+} ion but there are also suggestions of hybridisation between the Mn^{3+} 3*d* – O^{2-} 2*p* orbitals and the M^{3+} 4*d* – O^{2-} 2*p* orbitals. The latter hybridisation is thought to be crucial for the stabilisation of the ferroelectric state.[26]

The exact nature of the ferroelectric – paraelectric transition is also a controversial topic. There is a body of evidence that suggests the transition between the ferroelectric and paraelectric phases occurs via an intermediate phase. Dilatometry and differential thermal analysis experiments have shown a second transition and this could explain the disagreements in the literature.[27] Recent crystallographic investigations have found evidence for an

isosymmetric intermediate phase which retains ferroelectricity, which agrees with some previous suggestions.[28]

1.1.4.3 The magnetoelectric effect in $MMnO_3$

Strong magnetoelectric coupling in $MMnO_3$ is unexpected as, much like for $BiFeO_3$ and $BiMnO_3$ previously discussed, the sources of the magnetism and the ferroelectricity differ. There are also symmetry restrictions, as the magnetism is isolated to the *ab*-plane whereas the ferroelectricity is present along the *c*-axis. However, there are changes in the dielectric constant at the magnetic transition temperature in $YMnO_3$ [29] which suggests that there may be some link. In cases where M^{3+} is a f^n lanthanide it has been found that the application of an electrical field can control the magnetism of the M^{3+} lattice.[30]

1.2 Quantum spin liquids

Magnetic frustration was indicated for $MMnO_3$ and it is found to be an area of major study, encompassing a range of compounds.[31-33] The simplest realisation of frustration is a triangle with spins on each corner capable of up or down spin only. Ordering the spins in an antiferromagnetic manner in this system proves impossible as the spin on one corner is always pointing in the same direction as another (Figure 1.11). It is found that there are a number of architectures that share this geometric frustration and it is due to the existence of triangular motifs; kagome, tetrahedra; (Figure 1.12) and hyperkagome [34] frameworks.

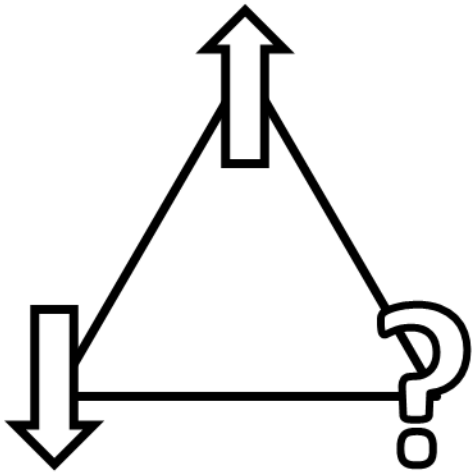

Figure 1.11: Triangle with two spins arranged antiferromagnetically – note it is not possible to assign the spin on the third corner.

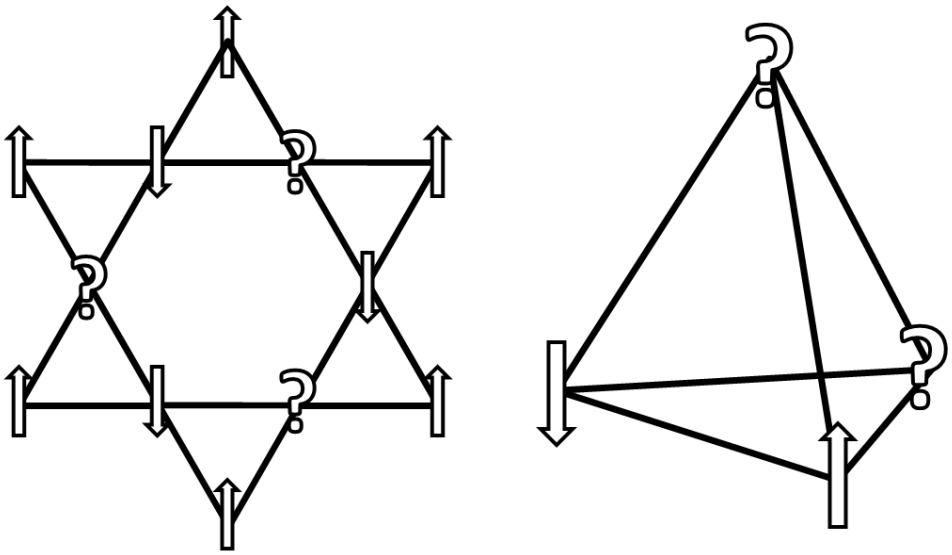

Figure 1.12: Kagome lattice (left) and tetrahedron (right) – note it is not possible to assign mutually antiferromagnetic spins on every adjacent corner.

Although the triangular motif shows great difficulty in satisfying antiferromagnetism when presented as a perfect triangle it is found that there are a number of distortions and ordered states which can occur. There is the possibility of a structural distortion that alleviates the degeneracy, and the synthesis of materials that continue to show perfect triangle motifs down to low temperatures is a key challenge in crystal engineering.[35] Another possibility is the canting of spins, which can allow for an ordered state to form, but it is often found that there are a number of degenerate, almost energy-equivalent microstates; this is the case in $MMnO_3$ were there are a number of potential ordered states which can vary with M^{3+} and temperature (Figure 1.9).[23] A further possibility is the formation of a spin glass in which the spins have a random (but close to equal) distribution of ferromagnetic and antiferromagnetic interactions. If, however, the ions concerned in the frustration have a spin $S = ½$ then quantum fluctuations can take place which do not require thermal energy to occur; quantum mechanical uncertainty leads to the continued fluctuation of the spins.[36] This state is called a quantum spin liquid (QSL) and is of great interest as there is the possibility of understanding and generating some very exotic magnetic states.[37]

The QSL state is complex and is characterised by long range entanglements of spins. These spins are constantly changing and re-entangling (Figure 1.13). This QSL state (also called a resonating valence bond (RVB)) was first suggested by Anderson in the '70s.[38] The longer-range these entanglements, the easier they are to break and create non-spin paired excited states. A related state is the valence bond solid (VBS) which shows no fluctuations; instead short range spin pairing occurs with its own symmetry (Figure 1.14).[36] This has been recently experimentally found in a Cu^{2+} containing kagome lattice compound, $Rb_2SnCu_3F_{12}$.[39] The QSL state has proven elusive and a great challenge to not only realise but also characterise.[36]

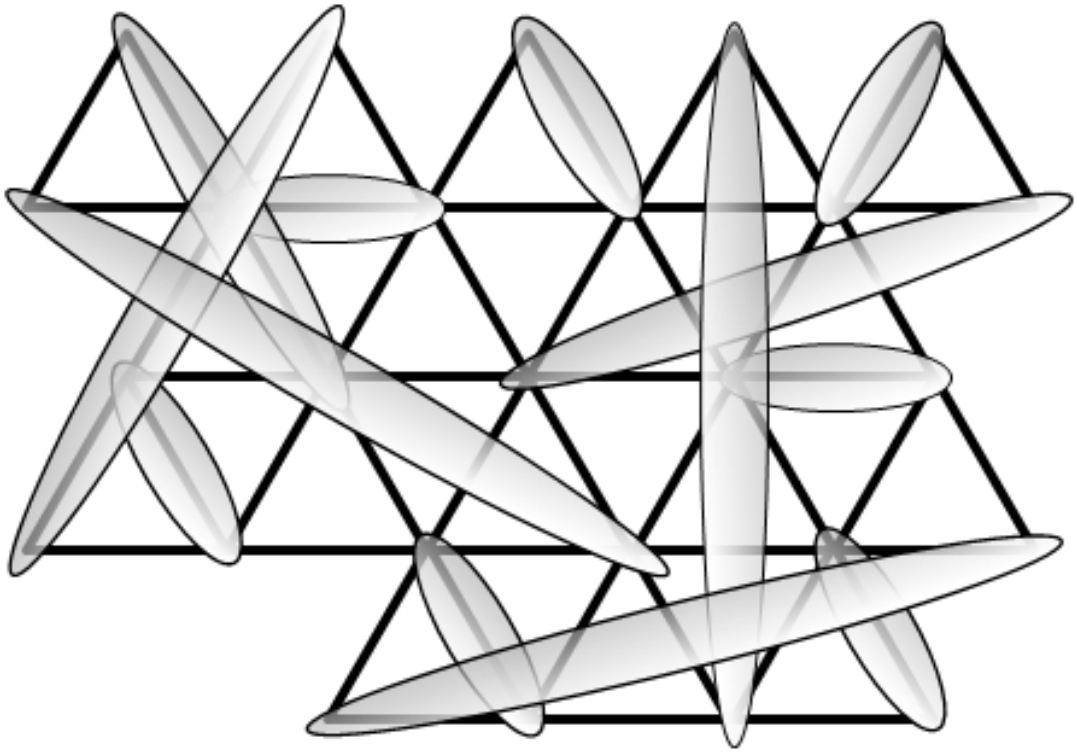

Figure 1.13: Triangular lattice showing spin entanglements (represented by ovals). Note there is no clear pattern or uniform distance and the pairings are constantly changing.

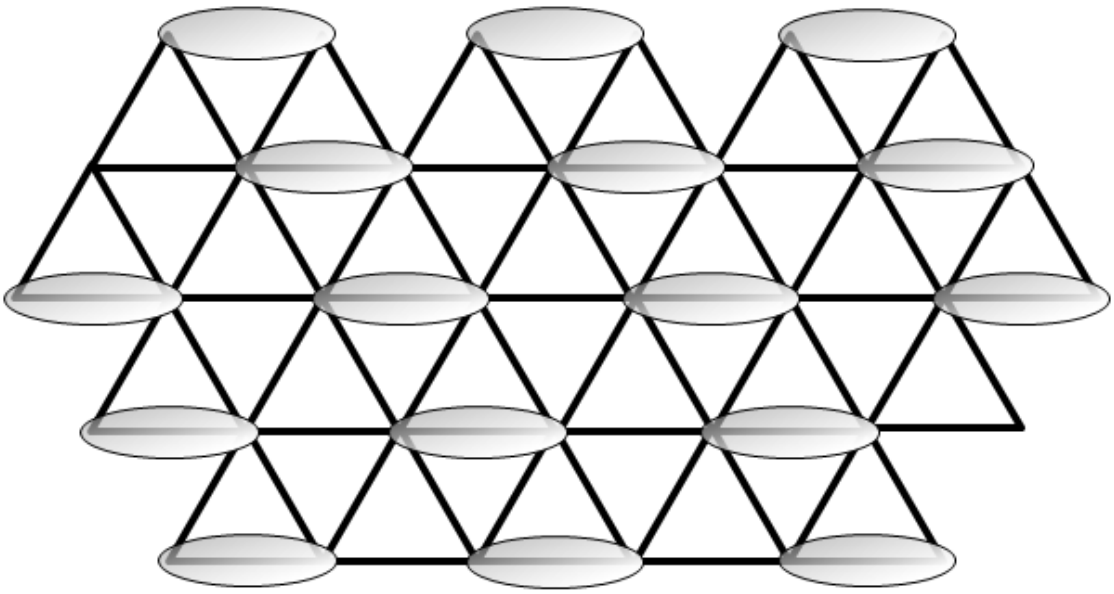

Figure 1.14: Triangular lattice showing valence bond solid (VBS) state. The ovals represent paired spins. Note the clear repeating pattern, but without long-range spin correlation.

1.2.1 Possible quantum spin liquids

As mentioned above, the characterisation of a QSL is challenging; this is in part due to there being no one experiment or experimental feature that can assign a material as a QSL. The

starting points are standard magnetic measurements and then the determination of the frustration parameter, with large numbers (> 100) being indicative of a level of frustration sufficient to seriously impede magnetic order. Other options involve searching for spin freezing using nuclear magnetic resonance (NMR) or muon spin rotation (μSR) experiments.[36, 40, 41]

The majority of inorganic candidate QSL materials contain a kagome lattice, S = ½, consisting of either Cu^{2+} (d^9) or V^{4+} (d^1) ions. Some key examples are Herbertsmithite ($ZnCu_3(OH)_6Cl_2$),[42] Kapellasite (a Herbertsmithite polymorph)[43] and DQVOF ($[NH_4]_2[C_7H_{14}N][V_7O_6F_{18}]$).[44]

1.2.1.1 Herbertsmithite

Herbertsmithite, ($ZnCu_3(OH)_6Cl_2$), is a naturally occurring mineral with a Cu^{2+} containing kagome lattice (in CuO_4Cl_2 octahedra) separated by ZnO_6 octahedra (Figure 1.15).[42] It has been synthesised in the laboratory[45] and found to show no magnetic ordering down to 50 mK.[46] This makes it a promising QSL candidate and as such has been the subject of many studies in order to determine its magnetic behaviour.[41, 47, 48] One remaining issue, however, is mixing of Cu^{2+} and Zn^{2+} sites. These metals are of approximately the same size (Cu^{2+} r = 0.73 Å, Zn^{2+} r = 0.74 Å for 6-coordinate[49]) and of the same charge. This intersite mixing leads to defects in the kagome lattice and interlayer magnetic interactions, however the Cu^{2+} cation prefers the cation site so is dominant in this position.[50] Despite this non-perfect kagome there has been little to suggest that it is not a QSL.

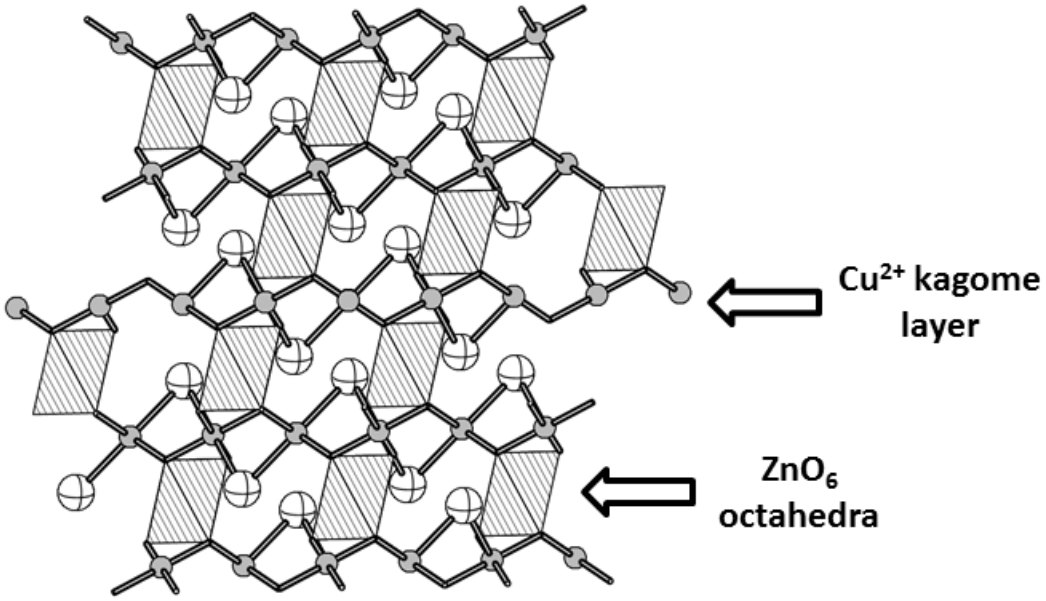

Figure 1.15: Herbertsmithite viewed perpendicular to the kagome lattice. Note kagome layers separated by ZnO_6 octahedra. The O ligand is actually OH, bridging to Cl^-, but H has been omitted for clarity.

1.2.1.2 Kapellasite

Kapellasite, ($ZnCu_3(OH)_6Cl_2$), is a polymorph of Herbertsmithite which is again naturally occurring.[51] In this case there are no interlayer ZnO_6 octahedra and instead the Zn^{2+} occupies

the pores in the kagome lattice (Figure 1.16). This neatly avoids the possibility of interplanar magnetic coupling but cannot create the perfect kagome lattice as intersite mixing still exists. Although at low temperature there are competing short range interactions a spin liquid phase is still retained.[43]

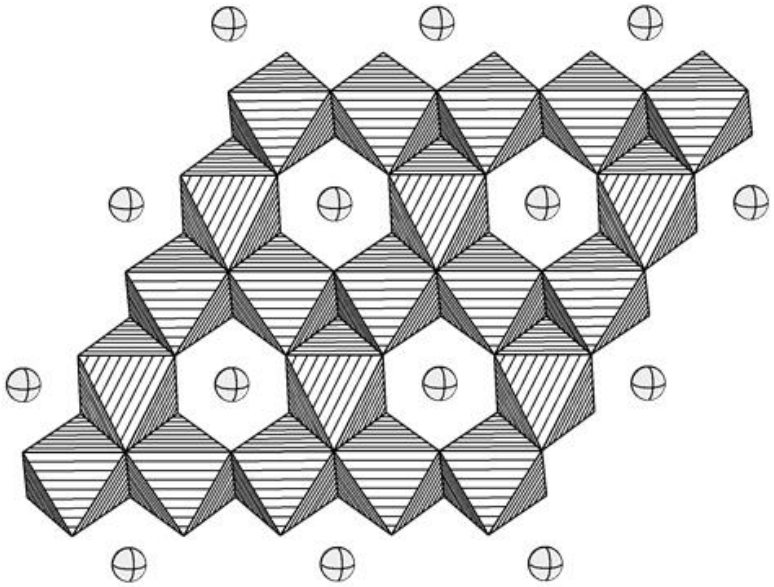

Figure 1.16: Kapellasite looking down the *c*-axis. The striped polyhedra represent CuO_4F_2 octahedra and the ellipsoids Zn^{2+}, which are in the same plane. This layer repeats.

1.2.1.3 DQVOF

DQVOF, diammonium quinuclidinium vanadium (III,VI) oxyfluoride, ($[NH_4]_2[C_7H_{14}N][V_7O_6F_{18}]$), is different from the first two examples in a more fundamental way; the S = ½ cation in this case is V^{4+}. This compound is characterised by a kagome double layer composed of corner-sharing $V^{4+}OF_5$ octahedra with $V^{3+}F_6$ octahedra. This building unit section is then separated from other layers by quinuclidinium cations (Figure 1.17).[44] Although there is a direct linkage between the kagome V^{3+} layers and the intralayer V^{4+} via a shared F^- it is found that the interaction between the two kagome layers is minimal. It is found that there is no magnetic ordering down to 40 mK and the spins are found to still be fluctuating.[40]

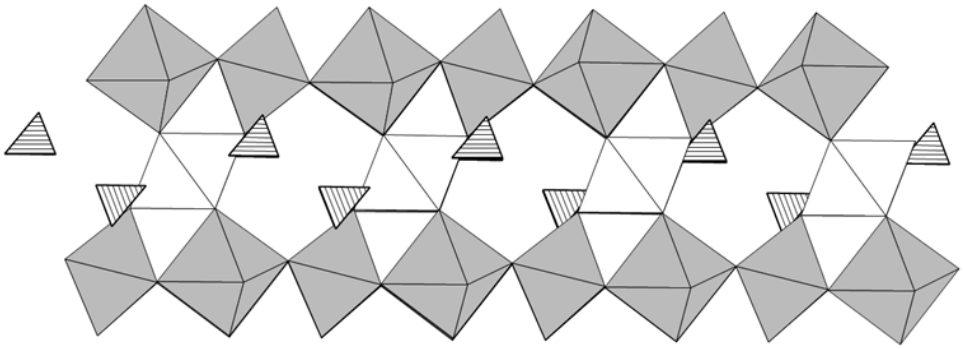

Figure 1.17: Kagome bi-layer of DQVOF; separating this unit from the next is a layer of quinuclidinium cations (not shown). Grey polyhedra = $V(IV)OF_5$ octahedra, white polyhedra = $V(III)F_6$ octahedra, striped polyhedra = NH_4.

1.2.2 The $A_2MCu_3F_{12}$ family

As can be seen above the majority of candidate quantum spin liquids have taken the form of kagome lattices with Cu^{2+} ions as the source of the $S = ½$ ion. One group of materials that may be a clear avenue of research is the family $A_2MCu_3F_{12}$. This family of compounds is chemically very flexible and able to accommodate a range of A^{1+} and M^{4+} cations. The inspiration for the series is from the non-magnetic compound, $Cs_2NaAl_3F_{12}$ which adopts a $R\bar{3}m$ unit cell and, importantly, consists of a perfect kagome lattice.[52] This kagome lattice is based upon corner sharing AlF_6 octahedra and the layers are linked by NaF_6 octahedra. The Cs^{1+} ions occupy the spaces above or below the pores (Figure 1.18).

The first copper bearing members of the family were $Cs_2ZrCu_3F_{12}$ and $Cs_2HfCu_3F_{12}$ reported in 1995, both showing perfect kagome lattices at room temperature isotypic with $Cs_2NaAl_3F_{12}$. At the time these were only briefly studied magnetically.[53] Further magnetic study leads to the agreement of previous results but different origins are suggested. Rather than high temperature transitions being Néel temperatures, as originally suggested, it appears they are actually first order structural transitions (~ 210 K for $Cs_2ZrCu_3F_{12}$ and ~ 175 K for $Cs_2HfCu_3F_{12}$). Magnetic ordering is found at 23.5 and 24.5 K for M = Zr^{4+} and Hf^{4+}, respectively. The magnetic ordering is found to be of antiferromagnetic character but due to spin canting presents itself as weakly ferromagnetic.[54] Further structural investigations of $Cs_2ZrCu_3F_{12}$ have found that there is a structural transition at ~ 225 K. This transition is characterised by a buckling of the kagome lattice – a F^- ion in the planar section of the kagome lattice moves in order to increase the coordination number of Zr^{4+} to seven.[55]

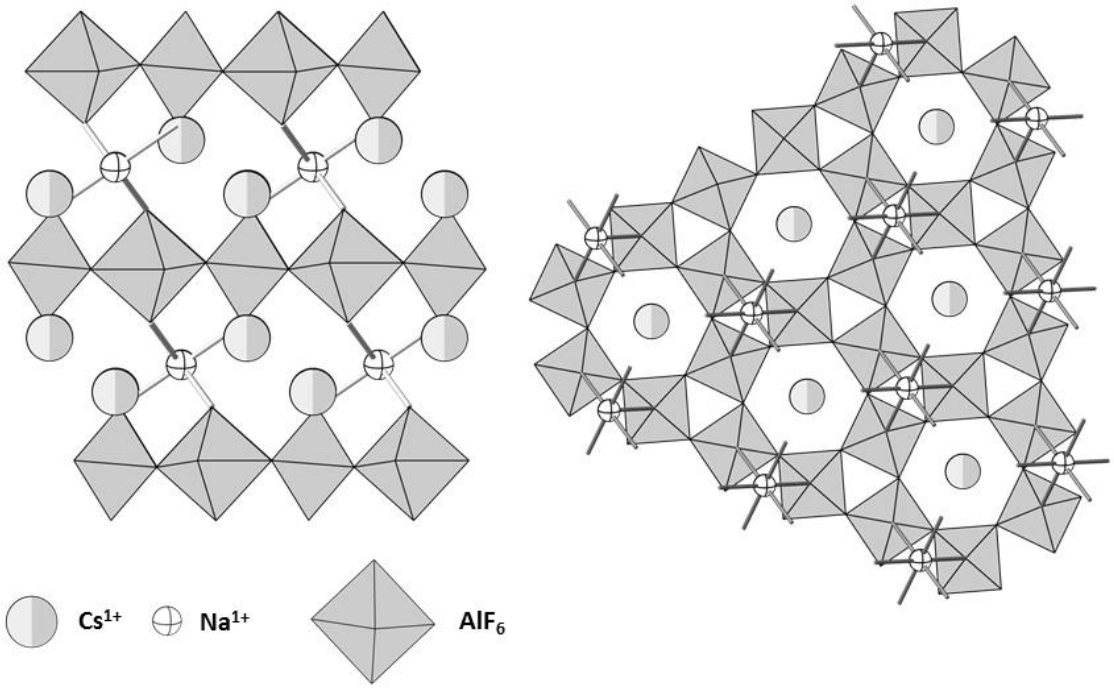

Figure 1.18: Structure of $Cs_2NaAl_3F_{12}$ looking along *ab*-plane (left) and down the *c*-axis (right).

Further substitutions led to the synthesis of $Cs_2SnCu_3F_{12}$[56] and $Rb_2SnCu_3F_{12}$.[57] The former proves to again be very similar structurally to $Cs_2NaAl_3F_{12}$. Magnetic data suggests

there is a low temperature transition at ~ 185 K followed by long-range magnetic ordering at ~20 K. The structural change seen in magnetic susceptibility data appears to be different from that found for $Cs_2HfCu_3F_{12}$ and $Cs_2ZrCu_3F_{12}$ as it is much more subtle. The magnetic ordering is found to lead to no net magnetic moment parallel to the *c*-axis and a small moment perpendicular, indicating that again Néel ordering occurs but with some weak ferromagnetism, likely due to spin canting.[56] $Rb_2SnCu_3F_{12}$ is found to deviate from the crystal structures found for $Cs_2MCu_3F_{12}$ (M = Zr^{4+}, Hf^{4+}, Sn^{4+}); there is a doubling of the *a* and *b* parameters of the unit cell (in hexagonal axes) and the symmetry is reduced to $R\bar{3}$.[57] This is found to result from four different Cu^{2+} – Cu^{2+} bond distances, possibly related to the reduced size of Rb^{1+} compared to Cs^{1+} (1.61 Å vs. 1.74 Å for 8 coordinate, respectively[49]). There is also a disorder of the F^- in the SnF_6 octahedra. Magnetically, $Rb_2SnCu_3F_{12}$ proves to be particularly interesting; it is found to be an example of a valence bond solid (VBS). This VBS state creates a pinwheel arrangement (Figure 1.19).[39] Such an exotic state is promising as it suggests that these phases may be worth investigating as the substitutional flexibility may lead to the ability to tune and probe certain magnetic behaviours.

Another member of the family that shows a very different structural has also been synthesised; $Cs_2CeCu_3F_{12}$. This sample has a highly corrugated kagome lattice due to the large Ce^{4+} becoming 7 coordinate (Figure 1.20); this leads to very different exchange interactions. The magnetic ordering is composed of one dimensional chains linking through CuF_6 octahedra.[58] Magnetically this leads to a complex system with the chains ordering antiferromagnetically but the Cu^{2+} between the chains is classed as "dangling". It is found that these dangling spins have a complex ordering with half ordering ferromagnetically and half remaining paramagnetic.[59]

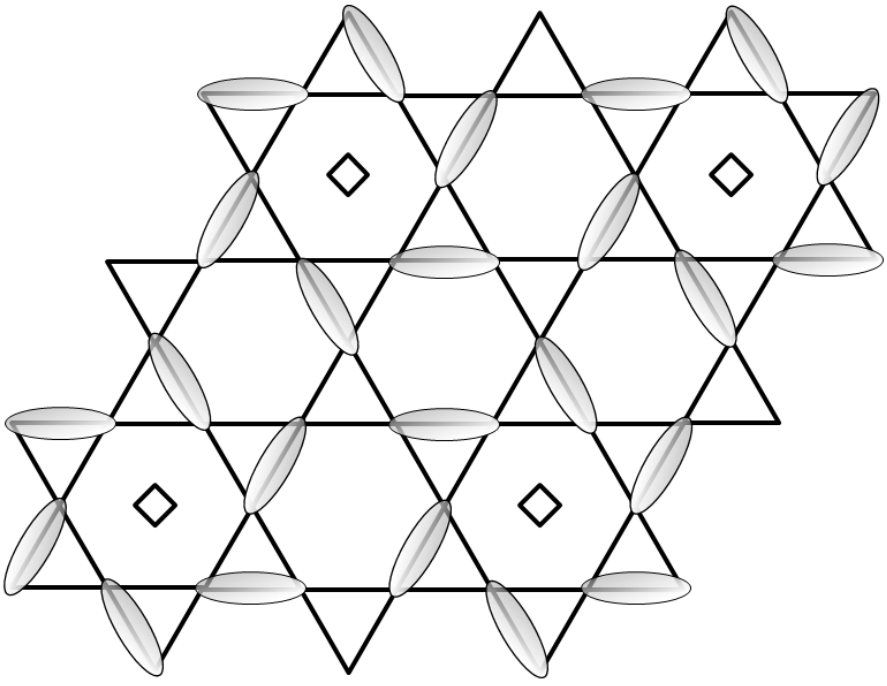

Figure 1.19: Kagome lattice in $Rb_2SnCu_3F_{12}$ viewed down the *c*-axis, with ovals representing paired spins. Diamonds are a guide to the eye showing the centres of "pinwheels".

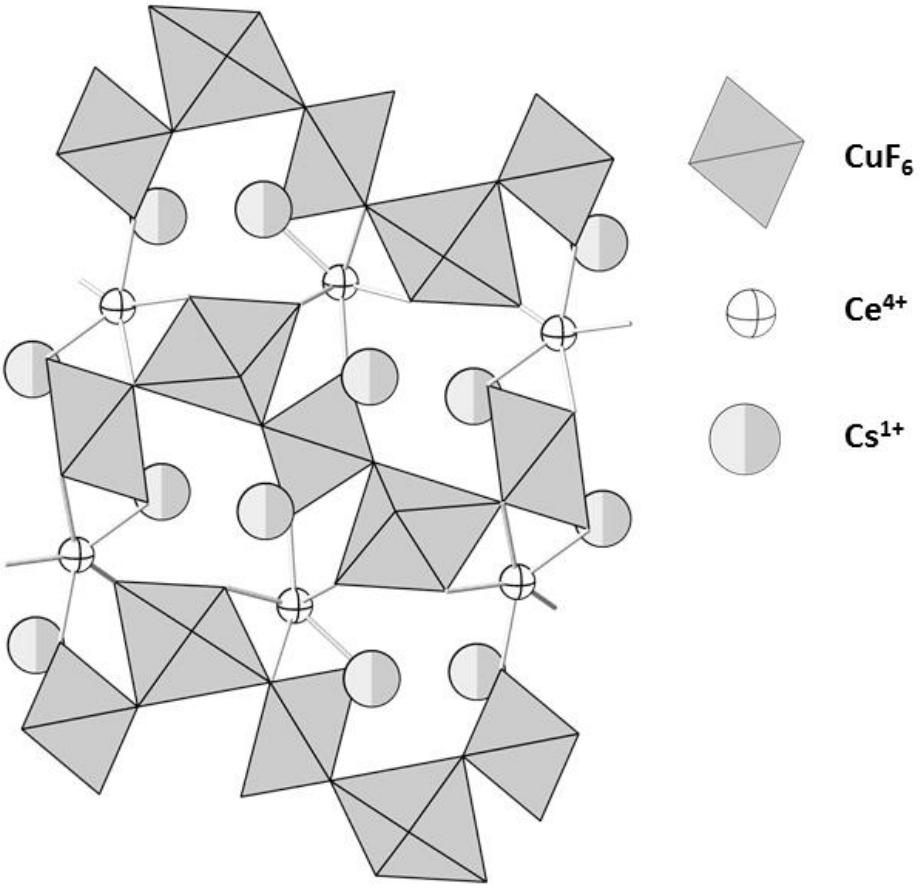

Figure 1.20: $Cs_2CeCu_3F_{12}$ viewed along the *ab*-plane. Note the twisting of the kagome lattice compared to Figure 1.17 and the extra coordination of Ce^{4+}.

The desired behaviour would be for a high-symmetry system like that found for $Cs_2SnCu_3F_{12}$ to retain a perfect kagome lattice down to low temperatures, as opposed to the structural transition and magnetic ordering found. It can be seen that the identity of A and M plays a part in this by observing the structural transition temperatures of $Cs_2MCu_3F_{12}$ (where M = Zr^{4+}, Hf^{4+}, Sn^{4+}). It is also noted that there appear to be different behaviours even within this small series. It is suggested that by manipulating the ion size and identity it may be possible to avoid any structural phase transitions while also avoiding the imperfect kagome lattices found for $Rb_2SnCu_3F_{12}$ and $Cs_2CeCu_3F_{12}$.

1.3 Aims

The aims of this project are two-fold. In the first instance there is the aim of furthering the understanding of the $A_2MCu_3F_{12}$ family in order to better appreciate the reasons behind the deviation from the perfect kagome lattice with reducing temperature. In principle, one would wish to use these findings to support the synthesis of a sample which maintains the perfect kagome lattice down to low temperatures and thus maximise frustration. This aim proves challenging as there are clear distortional effects over a number of different compositions however all is not lost; the distorted members show frustrated magnetic behaviours which can be of interest and the transition itself is crystallographically interesting.

The second aim of this work concerns the investigation of the effects of substitution on $YMnO_3$. The substitution of Mn^{3+} by Fe^{3+} is of interested as they are isostructural but not isoelectronic. This could have interesting effects on the magnetic behaviour and also the ferroelectric behaviour and as yet has not been investigated in any detail. It is also of interest to observe the effect of a magnetic ion only being present on the Y^{3+} site. This can be achieved using trivalent lanthanides as substitutes for Y^{3+} and In^{3+} as a substitute for Mn^{3+}.

1. N. A. Hill, *J. Phys. Chem. B*, 2000, **104**, 6694-6709.
2. D. Khomskii, *Physics*, 2009, **2**, 20.
3. M. Fiebig, *J. Phys. D: Appl. Phys.*, 2005, **38**, R123-R152.
4. A. Saunderson, *Phys. Educ.*, 1968, **3**, 272.
5. A. R. West, *Basic Solid State Chemistry*, Wiley, 1997.
6. M. J. Geselbracht, A. M. Cappellari, A. B. Ellis, M. A. Rzeznik and B. J. Johnson, *J. Chem. Educ.*, 1994, **71**, 696-703.
7. S. Sun, *Adv. Mater.*, 2006, **18**, 393-403.
8. D. Damjanovic, *Rep. Prog. Phys.*, 1998, **61**, 1267-1324.
9. R. E. Cohen, *Nature*, 1992, **358**, 136-138.
10. G. Catalan and J. F. Scott, *Adv. Mater.*, 2009, **21**, 2463-2485.
11. B. B. Van Aken, T. T. M. Palstra, A. Filippetti and N. A. Spaldin, *Nat. Mater.*, 2004, **3**, 164-170.
12. E. Ascher, H. Rieder, H. Schmid and H. Stossel, *J. Appl. Phys.*, 1966, **37**, 1404-1405.
13. D. N. Astrov, R. V. Al'shin, R. V. Zorin and L. A. Drobyshev, *Sov. Phys. JETP*, 1969, **28**, 1123-1125.
14. W. Brixel, J.-P. Rivera, A. Steiner and H. Schmid, *Ferroelectrics*, 1988, **79**, 201-204.
15. J. Wang, J. B. Neaton, H. Zheng, V. Nagarajan, S. B. Ogale, B. Liu, D. Viehland, V. Vaithyanathan, D. G. Schlom, U. V. Waghmare, N. A. Spaldin, K. M. Rabe, M. Wuttig and R. Ramesh, *Science*, 2003, **299**, 1719-1722.
16. M. Grizalez, E. Martinez, J. Caicedo, J. Heiras and P. Prieto, *Microelectron. J.*, 2008, **39**, 1308-1310.
17. W. Eerenstein, N. D. Mathur and J. F. Scott, *Nature*, 2006, **442**, 759-765.
18. H. Lueken, *Angew. Chem. Int. Ed.*, 2008, **47**, 8562-8564.
19. H. L. Yakel, W. C. Koehler, E. F. Bertaut and E. F. Forrat, *Acta Crystallogr.*, 1963, **16**.
20. J. E. Greedan, M. Bieringer, J. F. Britten, D. M. Giaquinta and H. C. Zurloye, *J. Solid State Chem.*, 1995, **116**, 118-130.
21. T. Katsufuji, S. Mori, M. Masaki, Y. Moritomo, N. Yamamoto and H. Takagi, *Phys. Rev. B*, 2001, **64**, 104419.
22. M. Fiebig, D. Frohlich, K. Kohn, S. Leute, T. Lottermoser, V. V. Pavlov and R. V. Pisarev, *Phys. Rev. Lett.*, 2000, **84**, 5620-5623.
23. P. J. Brown and T. Chatterji, *J. Phys. Condens. Matter*, 2006, **18**, 10085-10096.
24. T. Lonkai, D. G. Tomuta, U. Amann, J. Ihringer, R. W. A. Hendrikx, D. M. Tobbens and J. A. Mydosh, *Phys. Rev. B*, 2004, **69**, 134108.
25. S. C. Abrahams, *Acta Crystallogr., Sect. B: Struct. Sci.*, 2001, **57**, 485-490.
26. D. Y. Cho, J. Y. Kim, B. G. Park, K. J. Rho, J. H. Park, H. J. Noh, B. J. Kim, S. J. Oh, H. M. Park, J. S. Ahn, H. Ishibashi, S. W. Cheong, J. H. Lee, P. Murugavel, T. W. Noh, A. Tanaka and T. Jo, *Phys. Rev. Lett.*, 2007, **98**, 217601.
27. G. Nenert, M. Pollet, S. Marinel, G. R. Blake, A. Meetsma and T. T. M. Palstra, *J. Phys. Condens. Matter*, 2007, **19**, 466212.

28. A. S. Gibbs, K. S. Knight and P. Lightfoot, *Phys. Rev. B*, 2011, **83**, 094111.
29. Z. J. Huang, Y. Cao, Y. Y. Sun, Y. Y. Xue and C. W. Chu, *Phys. Rev. B*, 1997, **56**, 2623-2626.
30. T. Lottermoser, T. Lonkai, U. Amann, D. Hohlwein, J. Ihringer and M. Fiebig, *Nature*, 2004, **430**, 541-544.
31. A. Harrison, *J. Phys. Condens. Matter*, 2004, **16**, S553-S572.
32. A. P. Ramirez, *Annu. Rev. Mater. Sci.*, 1994, **24**, 453-480.
33. I. Mirebeau and S. Petit, *Eur. Phys. J. Spec. Top.*, 2012, **213**, 37-51.
34. Y. Okamoto, M. Nohara, H. Aruga-Katori and H. Takagi, *Phys. Rev. Lett.*, 2007, **99**, 137207.
35. K. R. Poeppelmeier and M. Azuma, *Nat. Chem.*, 2011, **3**, 758-759.
36. L. Balents, *Nature*, 2010, **464**, 199-208.
37. P. A. Lee, *Science*, 2008, **321**, 1306-1307.
38. P. W. Anderson, *Mater. Res. Bull.*, 1973, **8**, 153-160.
39. K. Matan, T. Ono, Y. Fukumoto, T. J. Sato, J. Yamaura, M. Yano, K. Morita and H. Tanaka, *Nat. Phys.*, 2010, **6**, 865-869.
40. L. Clark, J. C. Orain, F. Bert, M. A. De Vries, F. H. Aidoudi, R. E. Morris, P. Lightfoot, J. S. Lord, M. T. F. Telling, P. Bonville, J. P. Attfield, P. Mendels and A. Harrison, *Phys. Rev. Lett.*, 2013, **110**, 207208.
41. A. Olariu, P. Mendels, F. Bert, F. Duc, J. C. Trombe, M. A. de Vries and A. Harrison, *Phys. Rev. Lett.*, 2008, **100**, 087202.
42. R. S. W. Braithwaite, K. Mereiter, W. H. Paar and A. M. Clark, *Mineral. Mag.*, 2004, **68**, 527-539.
43. B. Fak, E. Kermarrec, L. Messio, B. Bernu, C. Lhuillier, F. Bert, P. Mendels, B. Koteswararao, F. Bouquet, J. Ollivier, A. D. Hillier, A. Amato, R. H. Colman and A. S. Wills, *Phys. Rev. Lett.*, 2012, **109**, 037208.
44. F. H. Aidoudi, D. W. Aldous, R. J. Goff, A. M. Z. Slawin, J. P. Attfield, R. E. Morris and P. Lightfoot, *Nat. Chem.*, 2011, **3**, 801-806.
45. M. P. Shores, E. A. Nytko, B. M. Bartlett and D. G. Nocera, *J. Am. Chem. Soc.*, 2005, **127**, 13462-13463.
46. P. Mendels, F. Bert, M. A. de Vries, A. Olariu, A. Harrison, F. Duc, J. C. Trombe, J. S. Lord, A. Amato and C. Baines, *Phys. Rev. Lett.*, 2007, **98**, 077204.
47. M. A. de Vries, J. R. Stewart, P. P. Deen, J. O. Piatek, G. J. Nilsen, H. M. Ronnow and A. Harrison, *Phys. Rev. Lett.*, 2009, **103**, 237201.
48. G. J. Nilsen, M. A. de Vries, J. R. Stewart, A. Harrison and H. M. Ronnow, *J. Phys. Condens. Matter*, 2013, **25**, 106001.
49. R. D. Shannon, *Acta Crystallogr., Sect. A: Found Crystallogr.*, 1976, **32**, 751-767.
50. S. H. Lee, H. Kikuchi, Y. Qiu, B. Lake, Q. Huang, K. Habicht and K. Kiefer, *Nat. Mater.*, 2007, **6**, 853-857.
51. W. Krause, H. J. Bernhardt, R. S. W. Braithwaite, U. Kolitsch and R. Pritchard, *Mineral. Mag.*, 2006, **70**, 329-340.
52. G. Courbion, C. Jacoboni and R. Depape, *Acta Crystallogr., Sect. B: Struct. Sci.*, 1976, **32**, 3190-3193.
53. M. Muller and B. G. Muller, *Z. Anorg. Allg. Chem.*, 1995, **621**, 993-1000.
54. Y. Yamabe, T. Ono, T. Suto and H. Tanaka, *J. Phys. Condens. Matter*, 2007, **19**, 145253.
55. S. A. Reisinger, C. C. Tang, S. P. Thompson, F. D. Morrison and P. Lightfoot, *Chem. Mater.*, 2011, **23**, 4234-4240.
56. T. Ono, K. Morita, M. Yano, H. Tanaka, K. Fujii, H. Uekusa, Y. Narumi and K. Kindo, *Phys. Rev. B*, 2009, **79**, 174407.

57. K. Morita, M. Yano, T. Ono, H. Tanaka, K. Fujii, H. Uekusa, Y. Narumi and K. Kindo, *J. Phys. Soc. Jpn.*, 2008, **77**, 043707.
58. T. Amemiya, M. Yano, K. Morita, I. Umegaki, T. Ono, H. Tanaka, K. Fujii and H. Uekusa, *Phys. Rev. B*, 2009, **80**, 100406.
59. T. Amemiya, I. Umegaki, H. Tanaka, T. Ono, A. Matsuo and K. Kindo, *Phys. Rev. B*, 2012, **85**, 144409.

2 Experimental techniques

The work presented in this thesis has made use of a variety of techniques. Prime among them is diffraction (Section 2.1) which has been used to probe, in detail, the structure of the materials synthesised. A number of other techniques have been used to acquire important further details of the materials synthesised; these include magnetometry (Section 2.2), A.C. impedance spectroscopy (Section 2.3) and Mössbauer spectroscopy (Section 2.4).

2.1 Diffraction

The majority of ionic solids present themselves in a crystalline ordered state. This means that they have long range order such that they can be represented as an infinite structure built up from the stacking of one, identical building block. These building blocks (or unit cells) can be divided into seven different crystal systems which describe their fundamental symmetry (Table 2.1).[1]

Table 2.1: The seven crystal systems.[1]

System	Bravais lattices	Axial lengths	Axial angles	Defining symmetry
Cubic	*P*, *I*, *F*	$a = b = c$	$\alpha = \beta = \gamma = 90°$	4 triads equally inclined at 109.47 °
Tetragonal	*P*, *I*	$a = b \neq c$	$\alpha = \beta = \gamma = 90°$	1 rotation tetrad or inversion tetrad
Orthorhombic	*P*, *I*, C, F	$a \neq b \neq c$	$\alpha = \beta = \gamma = 90°$	3 diads equally inclined at 90 °
Trigonal	*P*, *R*	$a = b = c$	$\alpha = \beta = \gamma \neq 90°$	1 rotation triad or inversion triad
Hexagonal	*P*	$a = b \neq c$	$\alpha = \beta = 90°, \gamma = 120°$	1 rotation hexad or inversion hexad
Monoclinic	*P*, *C*	$a \neq b \neq c$	$\alpha = \gamma = 90° \neq \beta$	1 rotation diad or inversion diad
Triclinic	*P*	$a \neq b \neq c$	$\alpha \neq \beta \neq \gamma$	None

The "Bravais lattices" referred to in Table 2.1 indicate the position of the nodes (or lattice points) of the unit cell, i.e. parts of space that can be considered as identical and therefore mark the ending of one cell and the beginning of the next. *P* stands for primitive and indicates that there are only nodes at the corners of the unit cell. *I* means body-centred and indicates that there are nodes at the corners of the unit cell and the body-centre. *C* is similar to body centred except, along with nodes at the corners, there is no node in the centre of the cell but the centre of two opposite faces. *F* indicates face-centred and means that there are nodes on the corner of the unit cell and the centre of each face (i.e. simultaneous *A*, *B* and *C*-centring).

Within these unit cells the arrangement of atoms can have further symmetry. This can take the form of glide planes, mirror planes, rotations axes and screw axes, the specifics of which will not be discussed here. It is both the internal and external unit cell symmetry – the crystallinity – that provides us with a method for determining the locations of the atoms inside the unit cell. On application of monochromatic X-rays to a crystalline material it is found that there are some unusual interference effects – there are X-rays given off at particular angles with respect to the sample. This is the result of X-rays being scattered by the atoms and the

regular spacings between them leads to these useful interference effects. The reason X-rays, in particular, cause this effect is due to the similarity in their wavelength and these spacings; ~ 10^{-10} m. The same effect is not found for other energies in the electromagnetic spectrum. A good, artificial construct which models the interaction of X-rays with a crystalline sample is to observe the arrangement of atoms as simplified flat planes (Figure 2.1).

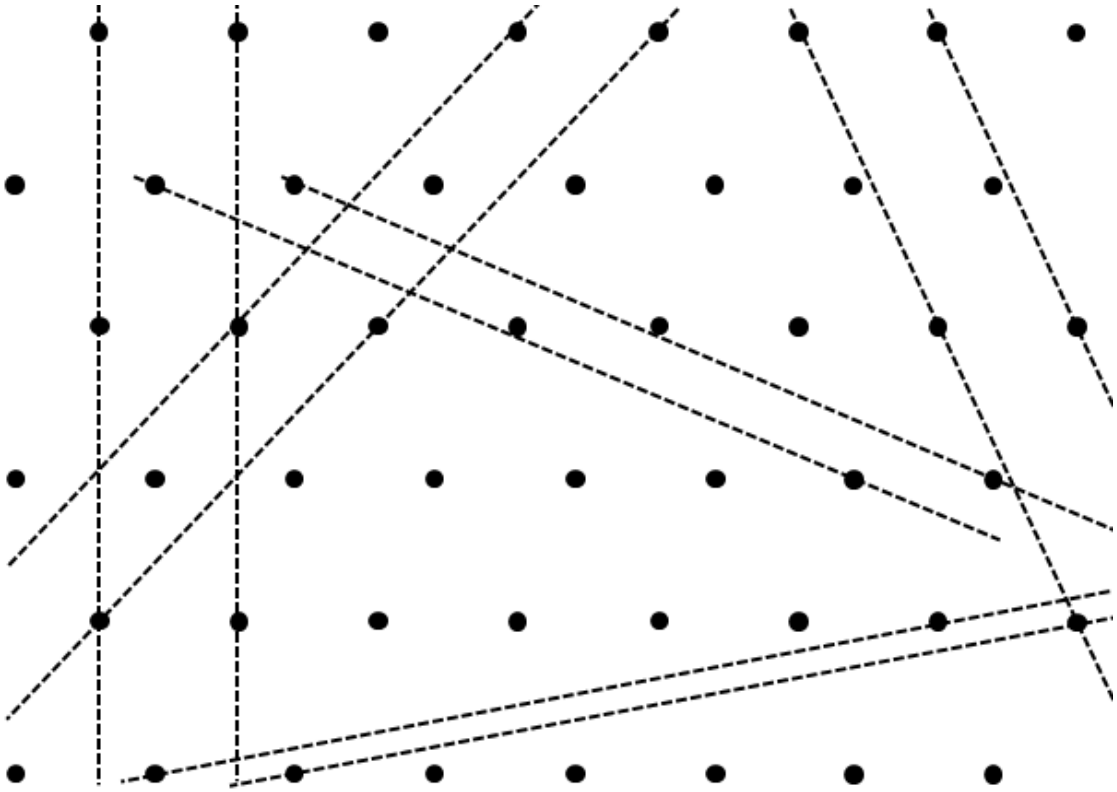

Figure 2.1: A 2-dimensional lattice (black dots) showing some of the possible planes (dashed lines).

The interaction of the waves we are interested in is called diffraction and it is described by Bragg's law. In Bragg's law the artificial planes are considered as infinite and semi-transparent such that they only reflect back some of the incident X-rays (Figure 2.2). It also assumes that due to symmetry the planes are all an identical distance apart, d.

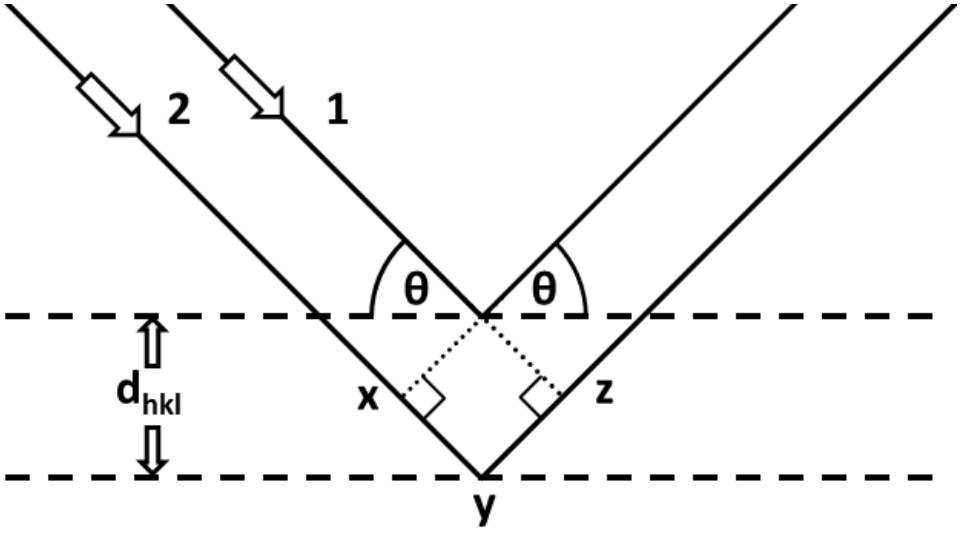

Figure 2.2: Two planes (dashed lines) and two waves diffracting (solid lines). The distance between the planes is indicated as "d_{hkl}".

Figure 2.2 shows a Bragg model with two planes and two waves, one reflecting off the first plane and one off the second. Diffraction makes use of constructive and destructive interference; if the waves are in phase when entering the material this means they must emerge in phase in order to give constructive interference. In terms of Figure 2.2 this means that wave 2 must travel the same distance as wave 1 plus an integer number of wavelengths; i.e. equation 2.1 must be satisfied.

$$xyz = n\lambda \tag{2.1}$$

(where xyz is the distance from x to y to z, n is an integer and λ is the wavelength)

From Figure 2.2 we can also find the key geometric relationships, equations 2.2 and 2.3.

$$xy = yz = d_{hkl}sin\theta \tag{2.2}$$

$$xyz = 2d_{hkl}sin\theta \tag{2.3}$$

If equations 2.1 and 2.3 are combined then we reach Bragg's law,[2] equation 2.4.

$$2d_{hkl}sin\theta = n\lambda \tag{2.4}$$

When Bragg's law is satisfied then diffraction can occur.

d_{hkl}-spacing defines the angle of diffraction, θ, but the intensity has a different origin. For X-rays this is related to the number of electrons present on the atoms which are diffracting; the interaction is related to the square of the atomic number. One way of quantifying the position and type of atoms and their relationship to the intensity of the diffracted X-rays is the structure factor, F_{hkl} (Equation 2.5).

$$F_{hkl} = \sum_{n=0}^{n=N} f_n exp2\pi i(hx_n + ky_n + lz_n) \qquad 2.5$$

The terms in equation 2.5 are defined as follows:[1]

- f_n is the atomic scattering factor of atom *n* which varies with each ion,
- $hx_n + ky_n + lz_n$ are the fractional coordinates of atom *n* in the unit cell with repeat units *x*, *y* and *z*,
- 2π is the phase difference between two waves,
- and *i* is present as the equation contains both real and imaginary parts which relate the phase difference to a wave relationship.

The atomic scattering factors vary between atoms and can vary even for atoms with the same number of electrons (Figure 2.3) – this is related to the size of the electron cloud which surrounds the atom in question.

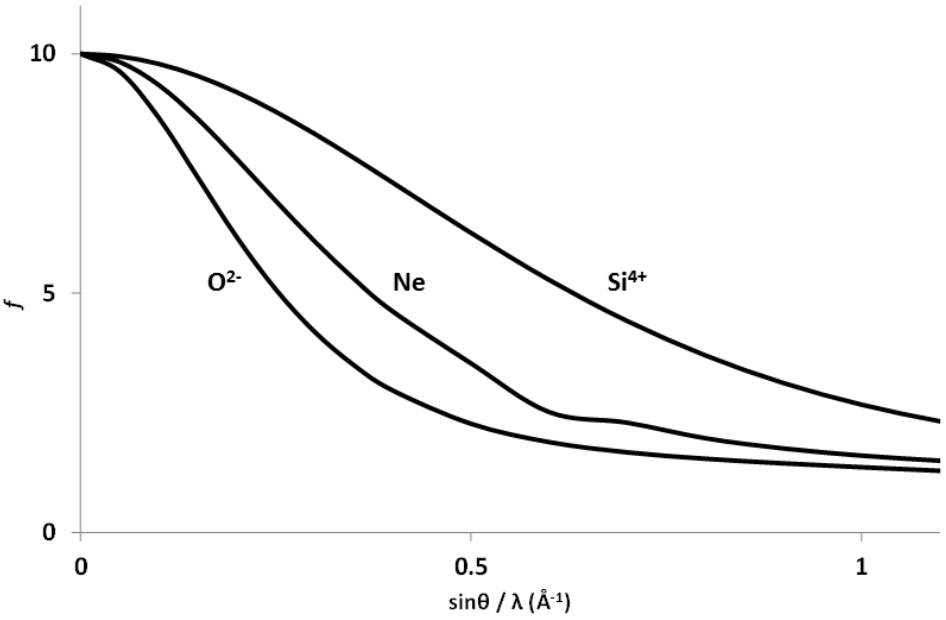

Figure 2.3: Scattering factors for 3 different 10 electron atoms/ions (O^{2-},[3] Ne and Si^{4+})[4].

2.1.1 Diffraction in practice

To carry out a basic X-ray diffraction experiment, very little apparatus is required: an X-ray source, a sample and an X-ray detector. From the Bragg equation there are two possible variables; θ, the angle of the detector relative to the source and the sample, or λ, the wavelength of the X-ray. Usually, θ is varied rather than λ. If a sample was ideally powdered (as in powder X-ray diffraction, PXRD) it would be possible to see "cones" of diffraction (Debye-Scherrer cones). This is powder X-ray diffraction. If the sample is a single crystal (SCXRD) then the diffraction condition has to be satisfied in 3 dimensions and will only give a spot (Laue spots) (Figure 2.4).

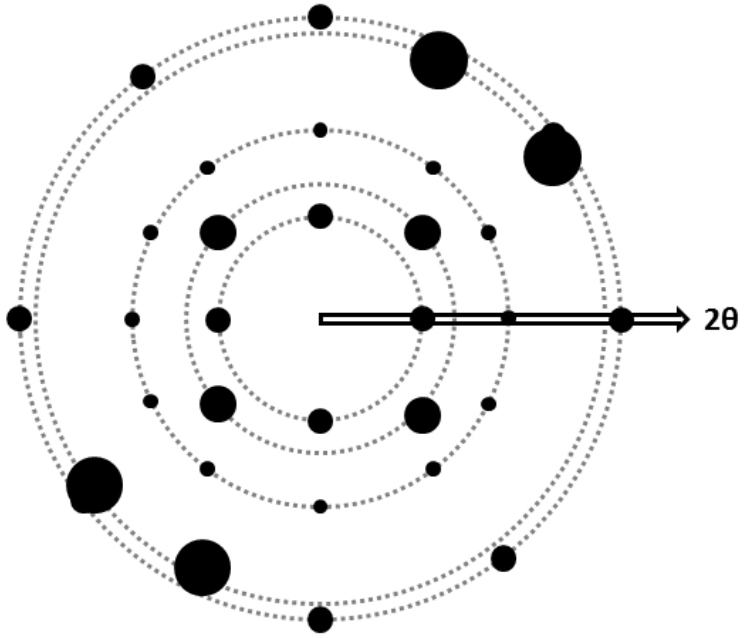

Figure 2.4: Laue spots (black spots) and Debye-Scherrer cones (dashed lines) shown on the same image. In practice only one of these dominates. The centre of the circles is adjacent to the X-ray source.

The cones or spots can be picked up as areas of higher X-ray intensity. If we consider the powder case and a detector composed of a photographic film the length of the whole of 2θ then the Debye-Scherrer cones would cause parts of the film to become exposed, leaving lines (Figure 2.5).

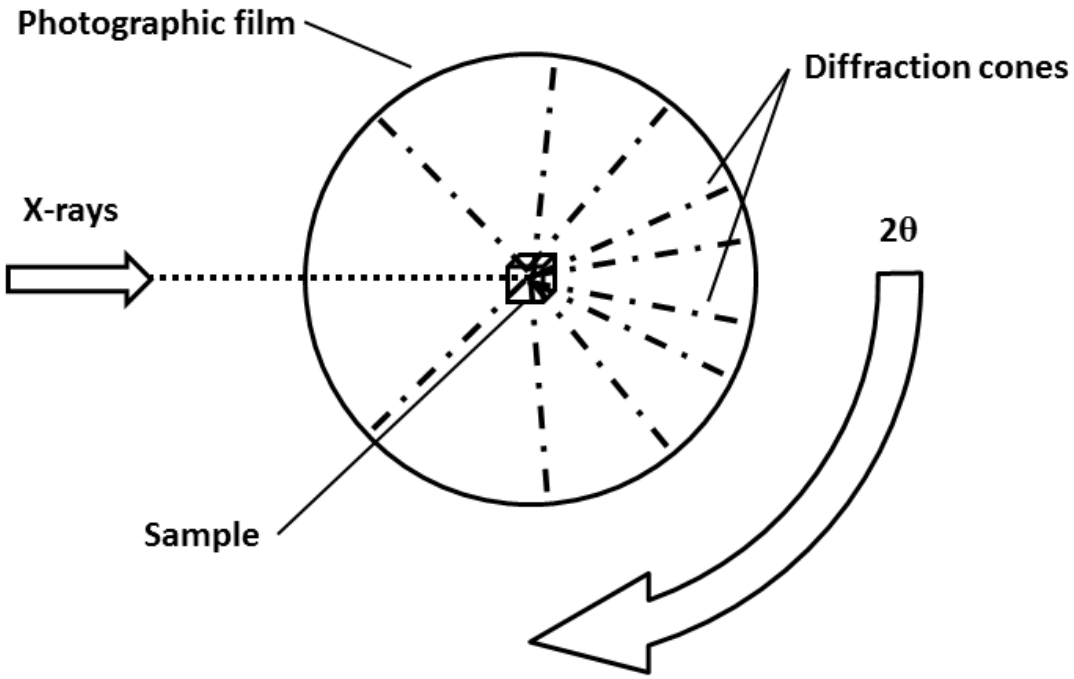

Figure 2.5: A basic PXRD set-up. See annotations on diagram.

Although photographic film can measure the presence of X-ray radiation modern techniques make use of electronic detectors such as charge coupled devices (CCDs). Modern systems can also make use of a number of X-ray sources including molybdenum, copper and silver; the basis of most laboratory systems being the acceleration of an electron across a potential difference into the metal of interest. This acceleration across a potential difference and into the metal leads to an ejection of a core electron which is swiftly followed by the dropping of an electron from a higher orbital into the vacant core orbital. As this second electron is now in a lower energy state it emits energy in the form of an X-ray. In general it is necessary to monochromate the X-ray source in order to achieve only one X-ray wavelength.

2.1.1.1 Structural model refinement

In most cases, diffraction data is used against a model structure that is then refined in order to best match the data. The derivation of this data is either by prior knowledge and comparison to analogous systems or by "solving" the data. The latter is commonplace for single crystal diffraction and is usually achieved by complex mathematical algorithms. Refinement of single crystal models can also be a complex process but generally involves the refinement of lattice parameters, atomic coordinates, thermal parameter, absorption and a number of further minor variables which can affect the resulting models pattern. In the case of powder diffraction we also have a key interest and modelling the peak shape. This is considerably important in Rietveld refinements as it can help to take overlapping peaks into account – something which occurs in powder diffraction due to the loss of dimensionality.

Divergence from a perfectly diffracted, infinite line to a peak with a width and possible asymmetry is due to a number of reasons and often needs to be taken into account before an accurate model can be established. From the sample there are two primary features that affect line width; crystallite size and microstrain. Both of these broaden the peak profile and it is also possible to retrieve information from them. Other key line width contributions are usually from the diffractometer itself. These can include axial divergence (asymmetry on low angle peaks), flat specimen effects (in Bragg-Brentano geometry this can cause asymmetry) and imperfections in the X-ray source image. A large number of these can be accounted for using pre-described mathematical functions. Key components of these functions are the Lorentzian and Gaussian line shapes as well as asymmetric components.[5]

Another key component of both single crystal and powder diffraction model refinements is the inclusion of thermal parameters. Atoms and ions in crystals are rarely fixed solidly on one spot – there are small movements related to the presence of thermal energy. These need to be modelled as they can have effects on the intensity of peaks due to a dilution of electronic density over a volume larger than that of the atom/ion. This can be taken account of either anisotropically or isotropically. The former is common place in powder diffraction as there is a loss of data due to reflection overlap. The latter, isotropic thermal parameters are common in single crystal diffraction where there is commonly more data available. Isotropic thermal parameters can show the thermal movements of atoms in 3-dimensions and can act as good indicators of structural disorder; particularly large displacements in one direction can be a tell-tale sign.

Other frequently refined variables are the zero-point of the diffraction equipment and other geometric parameters which can change from set-up to set-up. Site occupancies in some samples can be less than one and this can be measured as it is directly related to the electron density. The background signal also needs to be taken into account in most cases – this is particularly important in powder diffraction refinements as it can be of similar magnitude to the Bragg peaks.

After all these variables have been refined it is often necessary to quantify to the proximity of the resultant model to the experimental data. This can be achieved by a number of statistical measures. Commonly in powder diffraction, and referred to in this thesis are R_p (equation 2.6) and wR_p (equation 2.7).[5]

$$R_p = \frac{\sum|y_i(obs) - y_i(calc)|}{\sum y_i(obs)} \quad 2.6$$

$$wR_p = \left\{\frac{\sum w_i(y_i(obs) - y_i(calc))^2}{\sum w_i(y_i(obs))^2}\right\}^{1/2} \quad 2.7$$

Similar measures exist for single crystal diffraction. The use of these measures allows different models to be compared to each other and the effect of refining different variable to be noted. They are also critical in the validation of models especially from single crystal diffraction data.

2.1.2 Synchrotron X-ray diffraction

In order to increase the intensity of the available X-rays, for more in depth structural analysis for example, it is necessary to substitute the X-ray generation techniques commonly found in the laboratory and to increase their complexity significantly. This is generally achieved using a synchrotron. A synchrotron is a form of particle accelerator that consists of a circular vacuum tube containing packets of electrons travelling at approximately the speed of light. Large magnets provide energy to increase the speed of the electrons but due to relativistic effects they cannot increase and so the extra energy applied is released as electromagnetic energy. This takes the form of a broad spectrum but it is possible to tune the spectrum using special magnets which cause the electrons to move in waves. Further tuning can be performed ante-sample using specialist mirrors in order to provide monochromatic X-rays.

As these facilities tend to be at a national scale, and as such are expensive to build and maintain, the quality of detector is accordingly increased. The combination of the enhanced X-ray intensity and high performance detectors often leads to superior signal to noise ratios. However, there are occasional disadvantages to this technique despite its power; the interaction of X-rays with atoms is related to the square of the number of electrons. Due to this relationship, seeing lighter atoms such as hydrogen and lithium in crystals with heavier atoms can be challenging and discerning between similar atoms like copper and zinc can also be problematic.

2.1.3 Neutron diffraction

The primary criterion for a wave to interact with a crystal lattice is a wavelength of a similar magnitude to the gaps between the lattice planes. Particles can also behave as waves due to quantum effects and this can be quantified by the de Broglie wavelength (equation 2.8).

$$\lambda = \frac{h}{mv} \qquad 2.8$$

(where m is the mass of the particle, v is the velocity and h is Planck's constant)

It is found that – at the correct velocity – neutrons have an appropriate de Broglie wavelength and so can be used in diffraction experiments. Neutrons of the correct wavelength can be realised experimentally in two ways:

1. A fission reactor can be adapted to channel out some neutrons and the neutron flux subsequently monochromated. These neutrons are then directed towards the sample. In this case the scattering angle, θ, is the variable (so-called "angle-dispersive" mode).
2. A "spallation source" can be used. This involves firing protons at a heavy metal target (usually tungsten) which causes the release of a wide spectrum of neutrons. In general, the protons are held in a synchrotron and ejected towards the target at known times. As the time of proton impact is known the time of neutron release is also known. The sample is then a known distance from the target and so the speed of the neutrons can be calculated and from that the wavelength. In this type of diffractometer the variable is wavelength, λ (so-called "energy-dispersive" mode).

Both systems are in widespread use and have their own advantages. In general, neutron diffraction has a number of advantages and disadvantages when compared to X-ray diffraction. Sample size is an issue however, the flux from either neutron source is substantially lower than from a synchrotron; this leads to large samples being required or long exposure times. Absorption effects can also be problematic and access to particular tables of data or isotopes may be required. One key advantage though is that the interaction of neutrons is not related to atomic number; thus neutrons can act as a stand-alone technique or as a complementary technique to X-ray diffraction.

2.1.3.1 Neutrons and the determination of magnetic structure

Neutron diffraction can also give us information about the magnetic state in the correct circumstances. In a magnetically ordered sample it is the electron spins that are ordered. The incident neutron also possesses a non-zero spin and so also has a magnetic moment. This allows for an interaction between the electron and the neutron which leads to extra information about the magnetic unit cell. For example in an artificial 2-dimensional cubic cell if the lattice points are antiferromagnetically ordered then the structural unit cell will remain the same but the magnetic cell will be doubled (Figure 25).

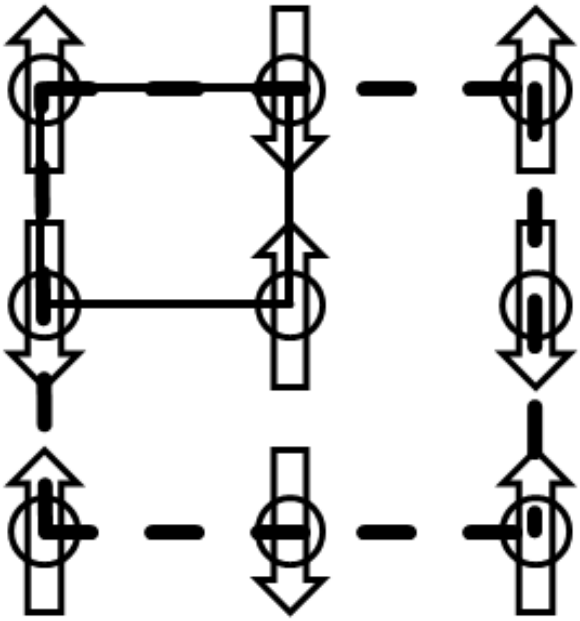

Figure 2.6: An arrangement of nuclei with antiferromagnetic ordering. The "nuclear" (or structural) unit cell is indicated by the solid line; the magnetic unit cell is indicated by the dashed line.

The symmetries of these magnetic unit cells can be different from the 230 space groups found when only crystal structures are considered, and have been compiled into their own class called Shubnikov groups. The Shubnikov groups take into account the extra inversions ("time-reversal symmetry") that must be taken into account when dealing with spins and their symmetry relationships.

2.2 Magnetometry

The measurement of magnetic phenomena is a complex process and there are a number of ways by which it can be performed. The work in this thesis has made use of two different experimental methods; namely the SQUID (superconducting quantum interference device) magnetometer and the VSM (vibrating sample magnetometer).

Both these measurement systems are capable of determining the magnetic moment from the sample, which then requires further correction for the number of moles of either the sample or the magnetic ions within the sample, depending on further intentions for the data. Both systems are theoretically (and in most cases practically) capable of measuring both magnetisation as a function of temperature and as a function of applied magnetic field. In either case, the typical measurement consists of cooling the sample outside of a magnetic field before heating within one and measuring the magnetic moment. A second, usually directly commenced, measurement cools the sample in a field and heats the sample in the same field while also measuring the magnetic moment. Such measurements can also indicate the nature of the magnetic moment interactions.

2.2.1 SQUID magnetometer measurements

The operation of the SQUID magnetometer depends on a small loop of superconducting material that contains a gap called a Josephson junction. This junction acts as a highly

sensitive switch which allows magnetic measurements as low as 10^{-15} Tesla to be recorded. A measurement is performed in a magnetic field with the superconducting coil at its centre. The sample is drawn through this coil which, due to the magnetic moment of the sample, leads to a change in electric current. This change in current is proportional to the magnetic field and, as the superconducting coil is connected in a closed loop to the SQUID input coil, the current also changes by an equal amount in the SQUID. The SQUID itself acts as a linear current to voltage converter, which leads to an output voltage that is proportional to the magnetic field.[6]

2.2.2 VSM measurements

The operation of the VSM instrument is dependent upon the vibration of the sample through a conducting coil (the "pick-up coil") in a magnetic field. The magnetised sample causes a change in voltage in the "pick-up" coil. It is this voltage that can be used to find the dipole moment of the sample (equation 2.9).

$$V_{RMS} = \delta\omega PQ \qquad 2.9$$

(where V_{RMS} = root mean squared of the voltage induced in the coil, δ = vibration amplitude, ω = $2\pi \times$ frequency, P = dipole moment and Q = geometry dependent constant).[7]

The VSM instrument is found to be inferior to the SQUID in terms of sensitivity.

2.3 Electrical measurements

Impedance spectroscopy is a technique used to measure the electrical properties of a material. It measures the impedance, Z, of a material; this is the material's ability to restrict the flow of electrons, and it has two parts; a real component, Z', which is related to the resistance of the material and an imaginary part, Z", which is related to the capacitance of the material.

$$Z = Z' + jZ" \qquad 2.10$$

(where Z" also = $1/\omega C$; $\omega = 2\pi \times$ frequency, C = capacitance)

If considered in this way a material can be simplified to a circuit with a capacitor and a resistor in parallel. A more thorough description of impedance is given by equation 2.11.

$$Z(\omega) = \frac{V(t)}{I(t)} = \frac{V_0 \sin(\omega t)}{I_0 \sin(\omega t + \theta)} = |Z| \frac{\sin(\omega t)}{\sin(\omega t + \theta)} = Z' + jZ" \qquad 2.11$$

(where V = voltage, I = current, t = time, θ = phase angle)[8]

Phase angle, θ, differs for resistance and capacitance. Resistance follows ohms law (I= V/R) and so the current magnitude is directly related to the voltage; thus, θ = 0 (Figure 2.7). For a capacitor there is a key difference; as the voltage reaches a maximum the current stored reaches a maximum and so the current present in the circuit drops to zero. Then, when the voltage direction is inverted the current begins to reach a maximum as the stored charge is released. For a pure capacitor θ = 90 ° (Figure 2.8).

In general data is collected at a range if frequencies and temperature in order to observe a material fully. Z can also be converted to a range of other measurements:[8]

- M, electrical modulus
- Y, admittance (comprising Y' = conductance, σ, and Y" = susceptance, which is related to 1/C)
- ε, dielectric permittivity (comprising ε' = dielectric constant and ε" = dielectric loss)

In this work the main interest is the dielectric constant (or relative permittivity) and the dielectric loss. The former is the capacitive ability of the material and the latter is the dissipation of energy from the material as a side-product. Both these values can depend on the structure of the material and so lend themselves to locating phase transitions.

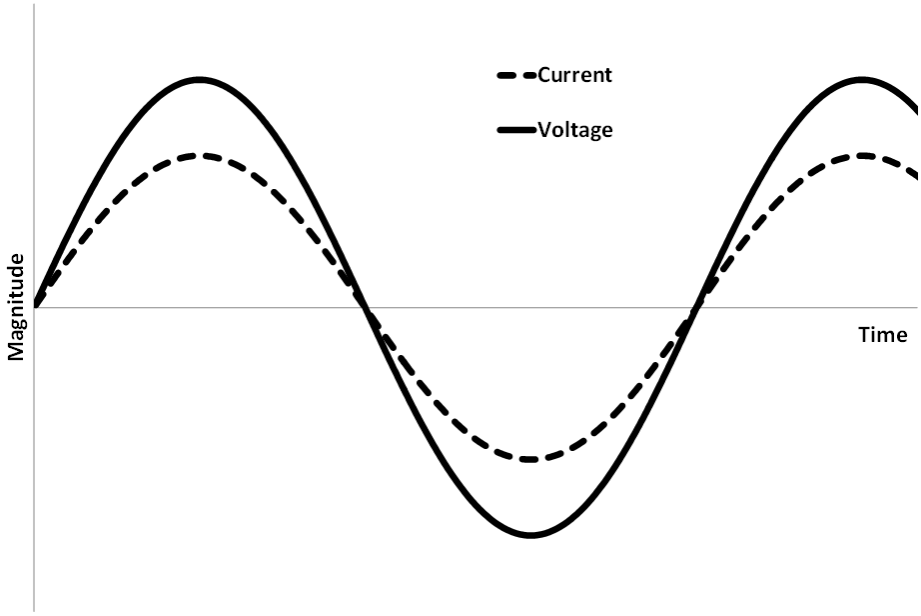

Figure 2.7: Current changing as a function of voltage through a resistor.

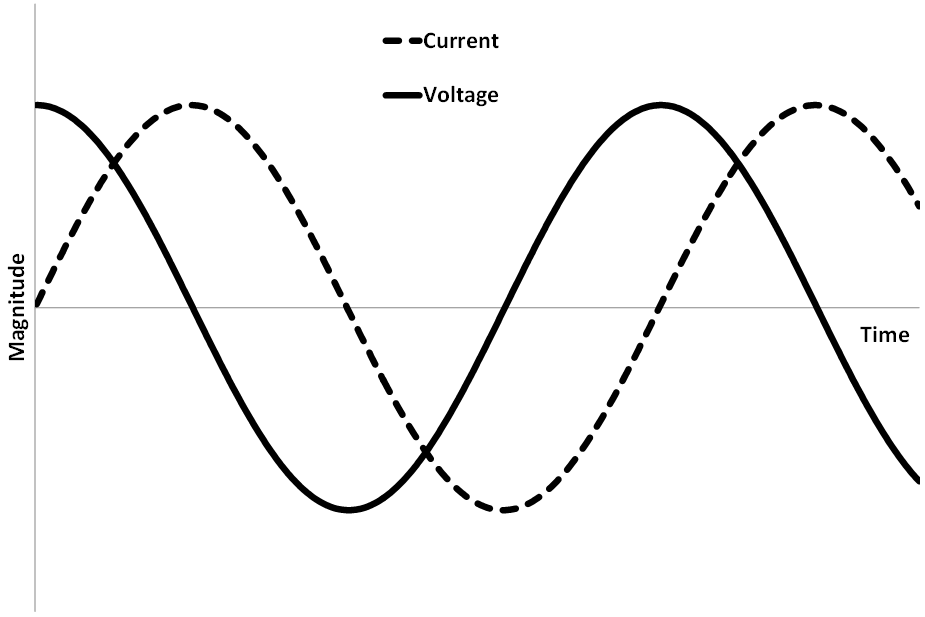

Figure 2.8: Current changing as a function of voltage for a capacitor.

2.4 Mössbauer spectroscopy

Mössbauer spectroscopy makes use of the resonant absorption of radiation by nuclei; emission of a photon by one nucleus and direct absorbance by another. Due to quantum mechanics, this can only occur if the energy if the photon is the same as one of the nuclear energy levels. Resonant absorption is found in the gas state for X-rays however higher energy γ-rays do not show this. This is due to the high energy of the γ-ray and conservation of momentum – when a γ-ray is released there is a large recoil on the emitting nucleus, the energy for which is taken from the emitted photon such that equation 2.12 holds.

$$E_{total} = E_{photon} + E_{recoil} \qquad 2.12$$

(where E = energy (arbitrary units)

As the energy has been partially removed the emitted photon is no longer of the appropriate energy to be absorbed and so resonant absorption can no longer take place. In the case of a solid emitter and absorber however there are other considerations. The emission (and absorption) of a photon by a solid leads to a different form of recoil – the entire solid is unable to recoil and so internal lattice vibrations occur which act to dissipate the recoil energy. These lattice vibrations are quantum mechanical in nature, however, and so can only occur at specific energies, including zero. It is found that it is indeed possible to have a zero energy vibration and in effect a "recoil free event". This is the Mössbauer effect.[9]

It is the Mössbauer effect that is manipulated in order to conduct highly sensitive spectroscopy. If suitable γ-rays are generated and emitted at a sample that can resonantly absorb these γ-rays then a few of the γ-rays will be absorbed. If there is a range of γ-rays around the required energy then a decrease in γ-ray transmittance is observed (Figure 2.9).

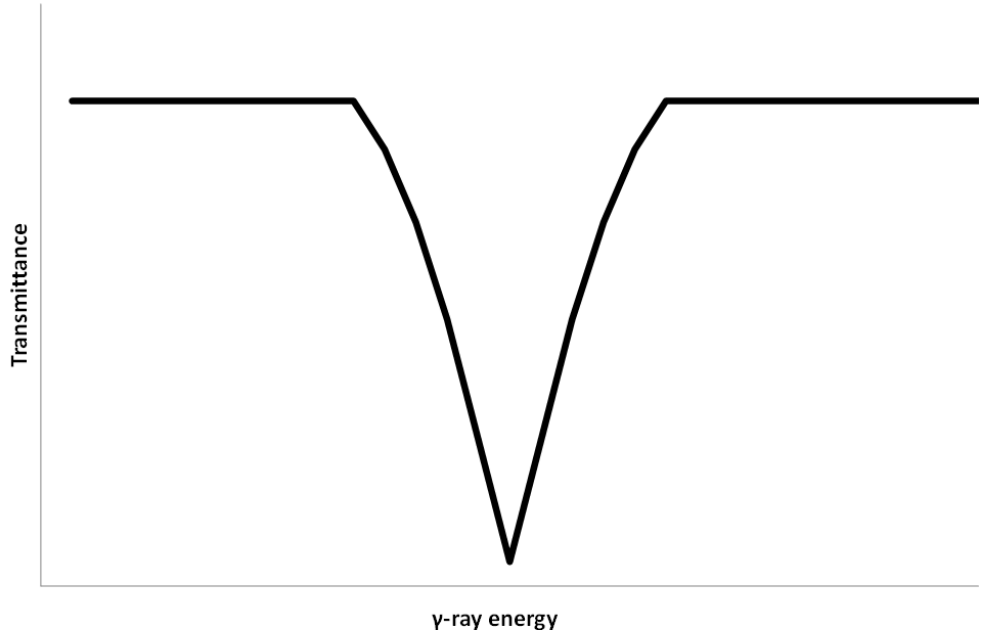

Figure 2.9: Plot of transmittance vs. γ-ray energy for a single absorption site.

This requires two issues to be solved: the generation of a suitable γ-ray and the micro-manipulation of its energy in order to probe the absorbance sites in the sample. In the case of γ-ray production, radioactive decay is employed; in general a suitable γ-ray can be generated by a decay which has a daughter isomer identical to the nucleus that one wishes to observe; e.g. Co^{57} decays to an excited state of Fe^{57}, which emits a γ-ray on transition to its ground state. Thus, Co^{57} can be used as a γ-ray source for examining Fe^{57}. Tuning the energy is necessary as the nuclei will have slightly different energies depending on their local environment and if the energy is not exact then absorption will not occur. Micro-manipulation of the energy can be done by the Doppler effect – the source is accelerated through a range of velocities which gives a range of γ-ray energies. Although crude, this method allows an extremely high resolution – up to 1 in 10^{12}.

Spectra appear like that in Figure 2.9; the positions of the peaks are different depending on their energy (isomer shift), splitting of the peaks can also occur due to the angular momentum quantum number, I, being > ½ (quadrupolar splitting, much in analogy to NMR) and further splitting can occur due to magnetism (Zeeman energy levels are very close in energy and so absorbance is found for these as well). The presence of splitting and isomer shift adds to the information that can be extracted from Mössbauer spectra.[10]

1. C. Hammond, *The Basics of Crystallography and Diffraction*, Oxford University Press, 2010.
2. W. L. Bragg, *Proc. Cambridge Philos. Soc.*, 1913, **17**, 43-57.
3. E. Hovestreydt, *Acta Cryst.*, 1983, **A39**, 268-269.
4. P. J. Brown, A. G. Fox, E. N. Maslen, M. A. O'Keefe and B. T. M. Willis, in *International Tables for Crystallography*, 2006, vol. C, ch. 6.1, pp. 554-595.
5. R. A. Young, *The Rietveld Method*, Oxford, 1996.
6. M. McElfresh, *Fundamentals of Magnetism and Magnetic Measurements Featuring Quantum Design's Magnetic Property Measurement System*, Quantum Design, 1994.
7. N. V. Frederick, *IRE Trans. Instrum.*, 1960, **I-9**, 194-196.
8. F. D. Morrison and D. C. Sinclair, presented in part at the ISIF 2011, Cambridge, 2011.
9. L. Eyges, *Am. J. Phys.*, 1965, **33**, 790.
10. RSC, http://www.rsc.org/membership/networking/interestgroups/mossbauerspect/intropart1.asp, Accessed 13/10/11.

3 Crystallographic and magnetic studies of the novel kagome compounds $A_2TiCu_3F_{12}$ (where A = Rb, Cs)

In order to gain a proper understanding of a structure-activity relationship it is important to have a number of structures from which observations can be made. To date the smallest ion used in the M^{4+} site of the $A_2MCu_3F_{12}$ family is Sn^{4+} (ionic radius 0.690 Å [1]) but it was sought to decrease the size of this site even further. Ti^{4+} (ionic radius 0.605 Å [1]) was identified as a suitable ion, as it also has the benefit of being a d^0 species which means that it will not directly give rise to any magnetic interactions. The coordination number of the Ti^{4+} ion is also unlikely to increase beyond 6 making the transition found for $Cs_2ZrCu_3F_{12}$ [2] improbable.

3.1 Experimental

The synthesis of this compound was not performed by the solid-state combination of binary fluorides due to the low boiling temperature of TiF_4 (557 K). Due to this, the precursor compounds A_2TiF_6 (A = Rb, Cs) were synthesised by hydrothermal means which have been previously reported in the case of Cs_2TiF_6.[3] It was then possible to synthesise the desired materials from A_2TiF_6 and CuF_2 by solid-state reaction. The heating times and rates have also been adapted in order to maximise the sample purity at the expense of crystallinity – as the aim was to make significant use of powder diffraction this presented no major issues. Longer heating times and slower cooling rates appeared to favour larger crystallites but the purity of the entire sample appeared to decrease. Crystallographic analysis was performed on both single crystal and powder samples in the case of A = Cs and on a powder sample only for A = Rb, making use of both laboratory based single crystal diffractometers and synchrotron powder diffraction (Diamond Light Source Ltd.). Magnetic analysis was performed on both powders and "single-crystals" (a number of single crystals combined) for both A = Rb and Cs.

3.1.1 Synthesis of A_2TiF_6

The synthesis of Cs_2TiF_6 single crystals by hydrothermal means has previously been described [3] and this was modified in order to obtain pure samples of A_2TiF_6. CsCl (0.3367 g, 2 mM, Sigma Aldrich, 99 %) OR RbCl (0.2418 g, 2mM, Sigma Aldrich, 99.8 %) and TiO_2 (0.0799 g, 1 mM, ~ 99 %) were dissolved in water (4 ml) in a 40 ml, Teflon lined autoclave. Ethylene glycol (5ml, Fischer Scientific, > 99 %) and $HF_{(aq)}$ (1 ml, 48-51 %, Alfa Aesar) were then added and the autoclave was then sealed and heated under autogenous pressure at 433 K for 18 hours. The resulting crystalline powders were filtered – washing with a 1:1 mixture of water:ethylene glycol – then dried overnight at ~ 330 K. The resulting A_2TiF_6 powders were then dried further at 390 K and ~ 10^{-4} mbar for 24 hours.

3.1.2 Synthesis of $A_2TiCu_3F_{12}$

For powders for crystallographic analysis, A_2TiF_6 (as prepared above) and CuF_2 (Sigma Aldrich, 98 %) were mixed and ground – in a 1:3 stoichiometric ratio – in an argon filled glovebox. The resulting mixture was then sealed in a gold tube before transferring to a tube furnace and heating under argon in the following manner: 20 K min^{-1} 373 – 873 K, 12 hours at 873 K, 20 K min^{-1} 873 – 373 K. The resulting grey powder was the target compound of approximately 94 % purity for A = Cs and 88 % for A = Rb. Notable impurities (all < 5 %) were found to be A_2TiF_6, CuO and for A = Rb in particular $RbCuF_3$ and Cu_2O. For clarity these compounds shall be named X_{Cs} and X_{Rb}, respectively.

For single crystals the above method was followed with the exception of adjusting the stoichiometric ratio to 1:2 and the heating rates as follows: 20 K min^{-1} 373 – 1073 K, 12 hours at 1073 K, ~ 3 K min^{-1} 1073 – 823 K, 20 K min^{-1} 823 – 373 K. This method yielded colourless, transparent crystals with a platy morphology. Diffraction quality crystals were only found for $Cs_2TiCu_3F_{12}$ – in the case of $Rb_2TiCu_3F_{12}$ a large degree of non-merohedral twinning aggravated any single crystal diffraction analysis. These samples will be named Y_{Cs} and Y_{Rb} for $Cs_2TiCu_3F_{12}$ and $Rb_2TiCu_3F_{12}$, respectively.

In order to synthesise magnetically pure samples an alternative synthesis technique was required.[a] CsF (or RbF), TiF_4 and CuF_2 were ground in stoichiometric amounts (2:1:3 molar ratio) and pelletised inside an argon filled glove box. The pellet was then placed in a copper tube (pre-annealed under hydrogen gas) which already had one end sealed. A small crystal (approx. 1 x 2 x 2 mm) of XeF_2 was also added to the copper tube in order to supply a fluorine rich atmosphere on decomposition. The tube was then removed from the glove box with a rubber bung in the empty end. About an inch from this open end the tube was sealed firstly with a press using 8 tons of pressure and then further sealed using a hammer. The now crudely sealed tube was then placed with its pre-sealed end in a water bath with the crudely sealed end protruding from the water. A blow-torch utilising oxygen and natural gas was then used to weld the tube completely shut. Heating regimes were then different for each composition:

- $Cs_2TiCu_3F_{12}$: the sealed tube was first heated to 423 K for 1 day before heating at 873 K for 3 days. The tube was then breached and the pellet inside reground and re-pelletised in a glove box. The new pellet was placed in a new tube with more XeF_2 and resealed as above before heating to 873 K for 2 days. This yielded a sample which, on analysis of the powder pattern, suggested the presence of only $Cs_2TiCu_3F_{12}$ and Cs_2TiF_6.
- $Rb_2TiCu_3F_{12}$: the sealed tube was first heated to 423 K for 1 day before heating at 873 K for 2 days. The tube was then breached and the pellet inside reground and re-pelletised in a glove box. The new pellet was placed in a new tube with more XeF_2 and resealed as above before heating to 873 K for 3 days. This yielded a sample which, on analysis of the powder pattern, suggested the presence of only $Rb_2TiCu_3F_{12}$, Rb_2TiF_6 and a small amount (< 1 %) $RbCuF_3$.

The magnetically pure samples will be named Z_{Cs} and Z_{Rb} for A = Cs and Rb, respectively.

3.1.3 Analysis techniques

Laboratory based X-ray powder diffraction (XRPD) for the purpose of phase identification was performed on a PANalytical Empyrean X-ray diffractometer using Cu $K_{\alpha 1}$ radiation and operating in either Bragg-Brentano geometry or transmission mode at the University of St Andrews and a Stoe Stadi-P diffractometer using Cu $K_{\alpha 1}$ radiation and operating in transmission mode at Moscow State University.

[a] Performed on a collaborative visit to Profs V. A. Dolgikh and E. I. Ardashnikova, Moscow State University, Moscow, Russia.

Synchrotron X-ray powder diffraction (SXPD) was performed at beamline I11, Diamond Light Source Ltd., Oxfordshire.[4] This utilised glass capillaries and operated in Debye-Scherrer mode typically with radiation of $\lambda \approx 0.82$ Å (precisely predetermined using a known standard). For analysis of $A_2TiCu_3F_{12}$ a multi-analysing crystal based detector was used in order to collect the highest resolution data possible. Samples were either ran for 15 or 30 minutes at a range of temperatures; for A = Rb the temperatures were cooling from 300 – 100 K in 20 K steps followed by further cooling to 85 K before heating from 100 – 300 K in 20 K steps. For A = Cs, patterns were collected from 300 – 100 K in 20 K steps. On reaching the required temperature a brief period (5 – 10 minutes) was employed in order ensure that the sample was equilibrated appropriately.

Neutron powder diffraction (NPD) was performed at beamline HRPD (High resolution powder diffraction), ISIS pulsed neutron and muon source, Oxfordshire. Samples of ~ 2 g were mounted in 8mm vanadium cans before loading into the diffractometer in the standard manner. Patterns were collected at room temperature.

Rietveld refinement was performed using GSAS [5] and the EXPGUI interface.[6] This analysis sought to fit lattice parameters, phase fractions, peak profile shape (both Gaussian and Lorentzian and, in the case of A = Cs, anisotropic peak broadening), thermal parameters (grouped by atom type) and, in the case of A = Cs, atomic coordinates.

Single crystal X-ray diffraction (SCXD) was performed on a Rigaku SCXmini diffractometer using Mo $K_{\alpha 1}$ radiation. Indexing and data processing was performed with Rigaku CrystalClear 2.0 and the model was solved using Shelxs-97 [7] and the WinGX [8] add-on. Single crystal data collection was performed both at room temperature and 125 K.

At Edinburgh University, magnetometry used a Quantum Designs MPMS-XL SQUID. Powder samples were mounted in gelatine capsules before being secured in plastic straws. The straws were then mounted on the end of a standard rod. Single crystal samples made use of capton tape to adhere a number of small single crystals which were then covered in another layer of capton tape. The resulting sample was then suspended securely in a plastic straw. In both cases multiple readings were taken at different temperatures (1.9 K – 390 K) and different fields (± 70000 Oe). At Moscow State University [b] the magnetic measurements were taken using a Quantum Designs PPMS using a VSM add-on unit. Samples were mounted in plastic holders which were provided by the manufacturer for use. The specifics of measurements and analysis will be referred to in the following text.

3.2 Crystallography of $Cs_2TiCu_3F_{12}$

$Cs_2TiCu_3F_{12}$ was synthesised in both powder and single crystal form allowing thorough assessment of the structural changes at both room temperature and sub-ambient conditions. In this section the analysis of both powder (X_{Cs}) and single crystal forms (Y_{Cs}) of $Cs_2TiCu_3F_{12}$ is

[b] Under the direction of Prof. A. N. Vasiliev and Mr A. Golovanov, Faculty of Physics, Moscow State University, Moscow, Russia.

performed showing a phase transition in both samples but, curiously, a different low temperature phase depending on crystallite size.

3.2.1 Variable temperature studies of $Cs_2TiCu_3F_{12}$ by powder diffraction

The SXPD data for $Cs_2TiCu_3F_{12}$ reveals that the sample at 300 K has many similarities with its sister phase, $Cs_2SnCu_3F_{12}$. The pattern is fitted well with a rhombohedral unit cell of dimensions a = 7.090321(18) Å and c = 19.91021(9) Å (vs. a = 7.142(4) Å and c = 20.381(14) Å for M^{4+} = Sn^{4+} [9]) and the best fit – taking into account the extra degrees of freedom available to space groups of lower symmetry – was found to be in space group $R\bar{3}m$ (Table 3.1).

Table 3.1: Comparison of rhombohedral space group fits to $Cs_2TiCu_3F_{12}$ SXPD data at 300 K.

		Fitted		-Background	
Space Group	χ^2	wR_p (%)	R_p (%)	wR_p (%)	R_p (%)
R3	5.89	8.33	6.40	6.13	5.36
$R\bar{3}$	5.97	8.39	6.42	6.28	5.43
R3m	5.99	8.40	6.46	6.29	5.46
$R\bar{3}m$	6.06	8.45	6.48	6.45	5.54

The above fits are inclusive of the refinement of atomic coordinates and examination shows further similarities between the M^{4+} = Ti^{4+} and M^{4+} = Sn^{4+} systems. This is corroborated by the neutron diffraction data which agree well with the synchrotron data and a good fit is found over two high-resolution detector banks (back scattering and 90 ° w.r.t. the sample; χ^2 = 2.74, wR_p = 5.9 %, R_p = 6.04 % (fitted), wR_p = 8.22 %, R_p = 7.5 % (-background); Table 3.2, Figure 3.1).

Table 3.2: Comparison of reported $Cs_2SnCu_3F_{12}$ atomic coordinates with refined coordinates for $Cs_2TiCu_3F_{12}$ at 300K.

Atom	x	y	z	U_{ISO} ($Å^2$) x 100
$Cs_2SnCu_3F_{12}$ [9]				
Cs	0	0	0.1060(1)	3.2(1)
Ti	0	0	½	1.3(1)
Cu	½	0	0	1.1(1)
F	0.2042(2)	-0.2042(2)	0.9845(1)	2.2(1)
F	0.1312(2)	-0.1312(2)	0.4465(1)	3.6(1)
$Cs_2TiCu_3F_{12}$ (SXPD)				
Cs	0	0	0.11125(3)	2.895(17)
Ti	0	0	½	0.62(4)
Cu	½	0	0	0.684(16)
F	0.20373(15)	-0.20373(15)	0.98092(10)	2.87(5)
F	0.12311(15)	-0.12311(15)	0.44766(9)	2.87(5)
$Cs_2TiCu_3F_{12}$ (NPD)				
Cs	0	0	0.10982(13)	2.16(7)
Ti	0	0	½	1.06(11)
Cu	½	0	0	1.043(35)
F	0.20277(9)	-0.20277(9)	0.98077(7)	2.52(3)
F	0.12279(10)	-0.12279(10)	0.44776(7)	2.52(3)

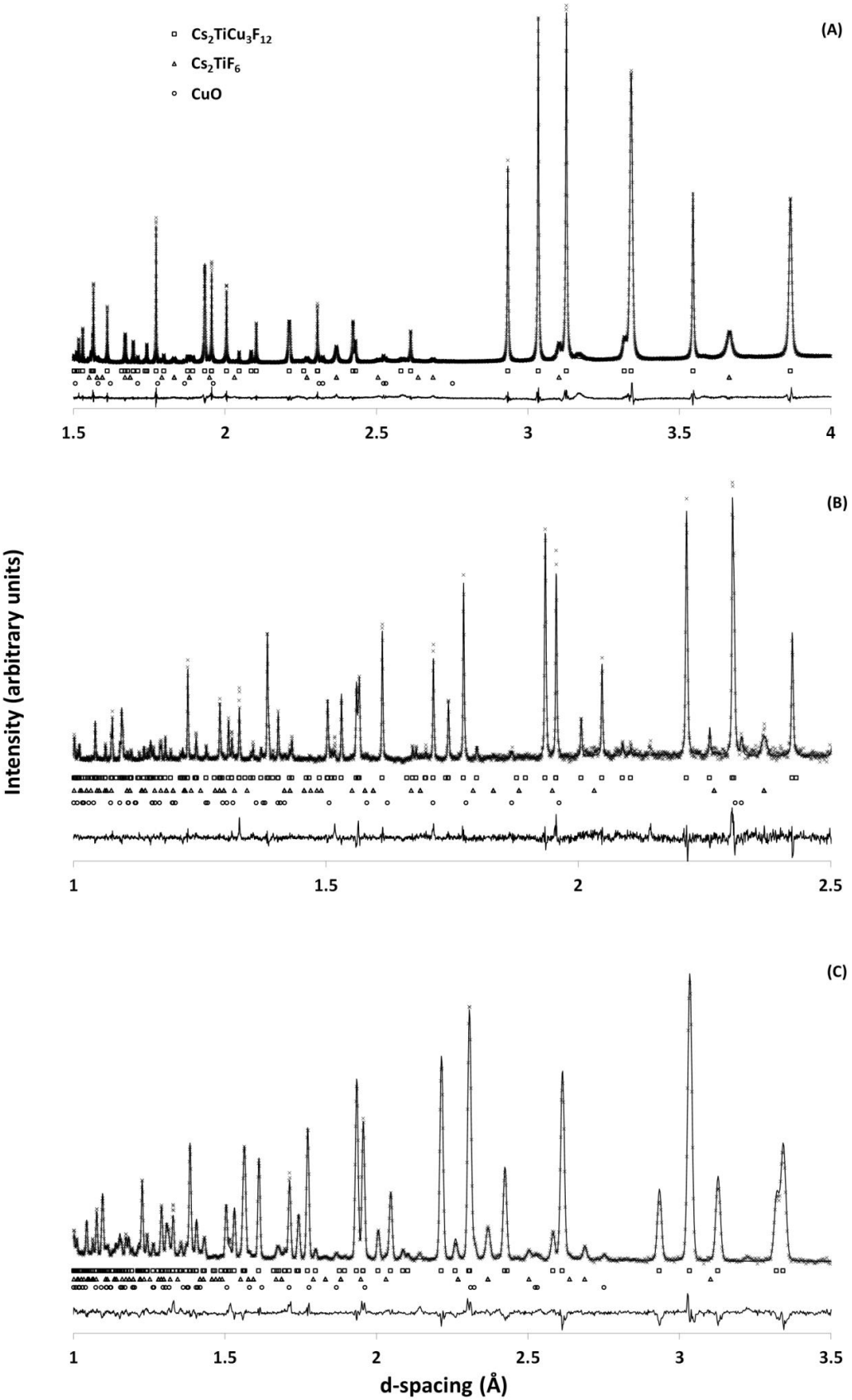

Figure 3.1: Powder patterns for $Cs_2TiCu_3F_{12}$ at 300 K; (A) SXPD, (B) NPD backscattering bank, (C) NPD 90 ° bank. SXPD performed at I11, Diamond Light Source, ltd., NPD performed at HRPD, ISIS neutron and muon source.

Most atoms are still located in very similar positions (< 0.06 Å of movement) with the exception of the Cs^{+} ions which have changed position along the z-axis by ~ 0.1 Å. This is indicative of a move out of the kagome lattice hexagonal "pore". It is suggested that this move is due to the decreasing size of the MF_6 octahedra compared to the relatively fixed size of the CuF_6 octahedra which creates further space for the Cs^{1+}. This can be quantified in terms of the Cs – Cs distance through the hexagonal "pore"; it is found that for $M^{4+} = Sn^{4+}$ the Cs – Cs distance is 4.321(4) Å and for $M^{4+} = Ti^{4+}$ 4.4311(10) Å. This agrees with the decreasing M^{4+} – F2 bond length on substitution of Sn^{4+} for Ti^{4+} (Figure 3.2 and Table 3.3).

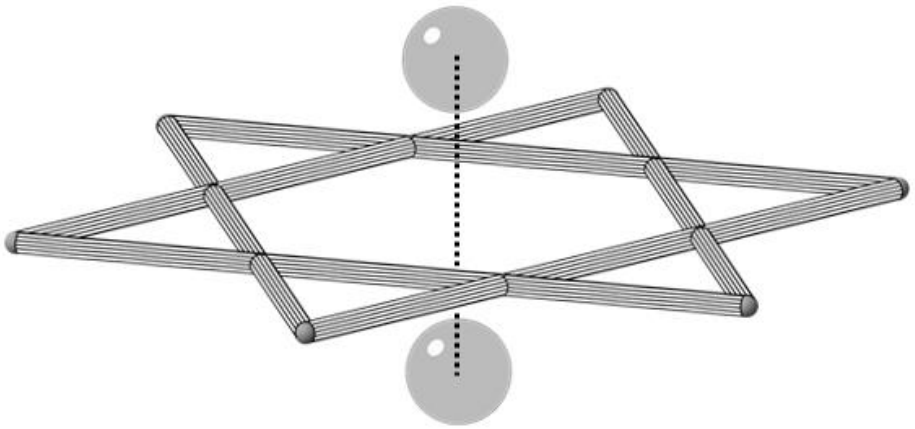

Figure 3.2: Hexagonal pore through kagome lattice; the dashed line links the two opposing Cs^{1+} ions.

Table 3.3: Comparison of metal – fluoride bond lengths for $Cs_2TiCu_3F_{12}$ and $Cs_2SnCu_3F_{12}$ at room temperature.

Metal – fluoride bond	$M^{4+} = Ti^{4+}$ (Å)	$M^{4+} = Sn^{4+}$ (Å) [9]
Cs – F1	3.1029(19)	3.1278(21)
Cs – F2	3.3567(19)	3.4156(26)
Cu – F1	1.8998(7)	1.8997(14)
Cu – F2	2.3383(18)	2.3478(25)
M^{4+} – F2	1.8363(18)	1.9553(16)

The superior resolution of the SXPD data allows another important feature of the data to be identified; anisotropic peak broadening. This has successfully been taken into account by using a technique developed by P. W. Stephens [10] and implemented using the GSAS program [c] (Figure 3.3). This broadening is particularly accentuated on the (0,0,3), (0,0,6) and (0,0,9) peaks which is indicative of a platy morphology. It is not clear whether the crystallites show this as-synthesised or if it is due to post-process grinding. The latter would indicate a

[c] This is available as profile function 4 (constant wavelength) in GSAS.

particular weakness along the c-axis. Use of the Scherrer formula [d] allows the calculation of the particle size; for the (003) peak it is found that the particle size is ~ 1187 Å and for (110) peak the particle size is found to be ~ 1953 Å. From the peak broadening calculations we can see that the particles are approximately double the size in the *ab*-plane than it is in the *c*-axis.

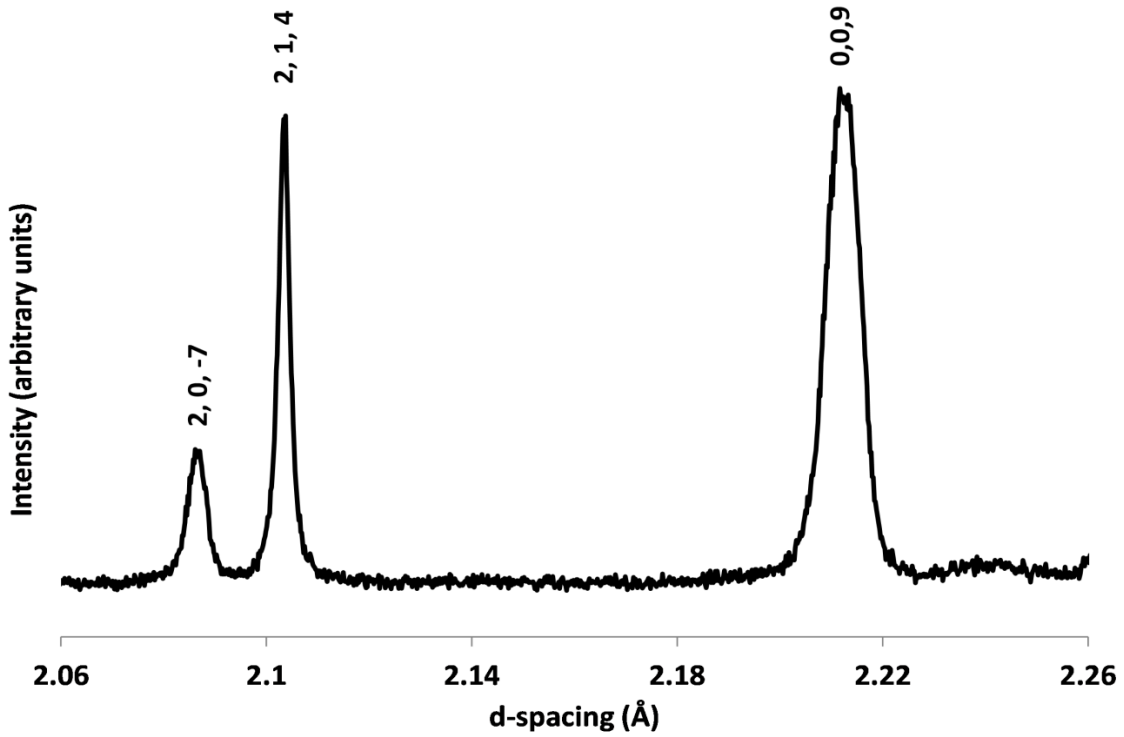

Figure 3.3: A selection of SXPD reflections from $Cs_2TiCu_3F_{12}$ at 300 K. Note the broadening of the (0,0,9) reflection compared to (2,1,4). Such broadening is indicative of an anisotropy in crystallite shape.

At 100 K, the lowest temperature recorded for this sample, there is clear splitting of peaks indicating a lowering of unit cell symmetry (Figure 3.4). Indexing using the DICVOL91 program [11] suggests a monoclinic cell with the metrics $a \approx 10.44$ Å, $b \approx 7.04$ Å, $c \approx 7.76$ Å, $\beta \approx 96.9$ °. There are a number of possible distortions from the rhombohedral unit cell which have these metrics. The ISODISTORT program [12] suggests 5 key possibilities, in space groups *I2/m*, *P2/m*, *P2/n*, *$P2_1/m$* and *$P2_1/n$*. The correct option can be selected on a trial and error basis. Reflections indexable as (1,2,0), (0,2,3) and (0,3,2) occur which breaks the $h + k + l = 2n$ reflection condition for a body-centred cell. However, the data are consistent with the presence of an *n*-glide plane, as all *h*0*l* satisfy the condition $h + l = 2n$. *$P2_1/n$* can be uniquely identified as the correct symmetry after a comparative refinement against *P2/n* (Table 3.4). The corresponding Rietveld refinement is shown in Figure 3.4. The atomic coordinates and selected metal fluoride distances are presented in Table 3.5 and Table 3.6, respectively.

[d] $\tau = \frac{k\lambda}{\beta cos\theta}$ where k is a the Scherrer constant, 0.9, λ is the wavelength used for diffraction (Å), β is the FWHM (radians, 2θ), θ is the peak position (radians, θ).

Table 3.4: Comparison of primitive space group fits ($P2_1/n$ and $P2/n$) to $Cs_2TiCu_3F_{12}$ SXPD data at 100 K.

		Fitted		-Background	
Space Group	χ^2	wR_p (%)	R_p (%)	wR_p (%)	R_p (%)
$P2_1/n$	5.15	8.03	6.24	6.54	5.54
$P2/n$	5.85	8.56	6.68	7.02	5.98

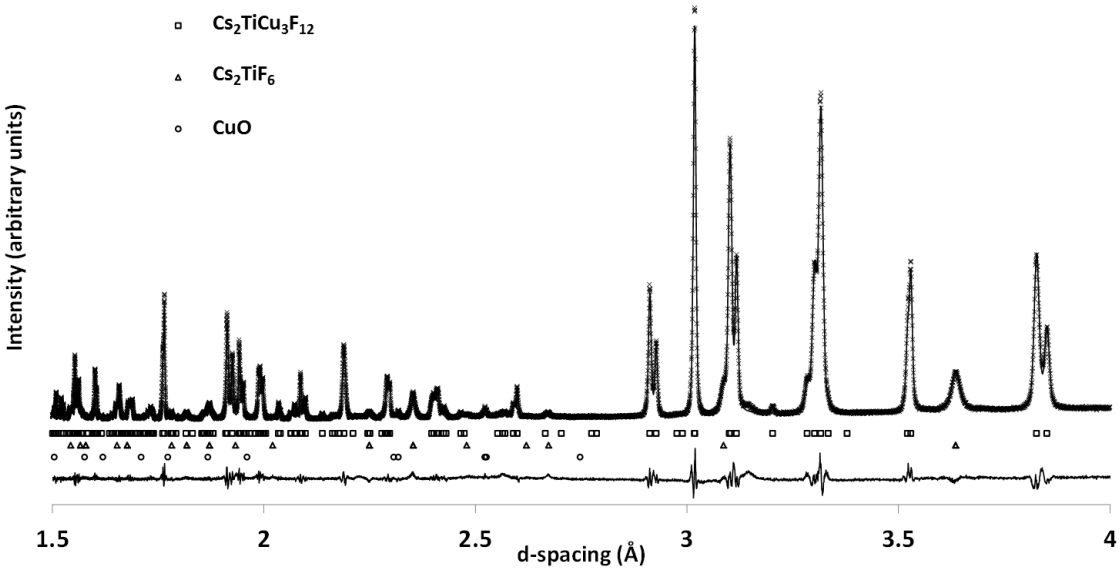

Figure 3.4: $Cs_2TiCu_3F_{12}$ SXPD Rietveld fit ($P2_1/n$ model) at 100 K.

Table 3.5: Atomic coordinates ($P2_1/n$ model) for $Cs_2TiCu_3F_{12}$ derived from SXPD data at 100 K.

Atom	x	y	z	U_{ISO} (Å^2) x 100
Cs	0.77484(7)	-0.00380(15)	0.11443(5)	0.502(11)
Cu1	½	0	½	-0.11(2)
Cu2	0.2538(3)	0.2305(2)	0.24322(17)	-0.11(2)
Ti	0	0	½	-0.39(3)
F1	0.4573(7)	0.1705(7)	0.3565(5)	0.01(4)
F2	0.9258(7)	0.7140(7)	0.8949(5)	0.01(4)
F3	0.2464(5)	-0.0298(7)	0.1786(4)	0.01(4)
F4	0.5264(6)	0.3541(7)	0.8570(5)	0.01(4)
F5	0.0575(6)	0.7787(7)	0.4108(5)	0.01(4)
F6	0.2273(5)	0.0473(7)	0.5621(4)	0.01(4)

Table 3.6: Selected metal – fluoride distances for $Cs_2TiCu_3F_{12}$ at 100 K as derived from SXPD data.

Metal – fluoride bond	Bond length (Å)
Cs – F3	3.051(4)
Cs – F1	3.086(5)
Cs – F2	3.102(5)
Cs – F4	3.185(5)
Cs – F5	3.201(5)
Cs – F5	3.242(5)
Cs – F6	3.275(5)
Cu1 – F2 (x2)	1.912(6)
Cu1 – F1 (x2)	1.917(6)
Cu1 – F6 (x2)	2.310(6)
Cu2 – F3	1.875(5)
Cu2 – F1	1.903(6)
Cu2 – F2	1.921(6)
Cu2 – F3	1.952(5)
Cu2 – F4	2.319(6)
Cu2 – F5	2.325(6)
Ti – F6 (x2)	1.835(4)
Ti – F4 (x2)	1.843(5)
Ti – F5 (x2)	1.896(5)

On analysis of the full temperature range studied it is found that the transition occurs between 240 and 260 K and can be tracked by comparing powder patterns at different temperatures (Figure 3.5). There is also a clear variation in the change of unit cell volume as a function of temperature in this region (Figure 3.6).[e]

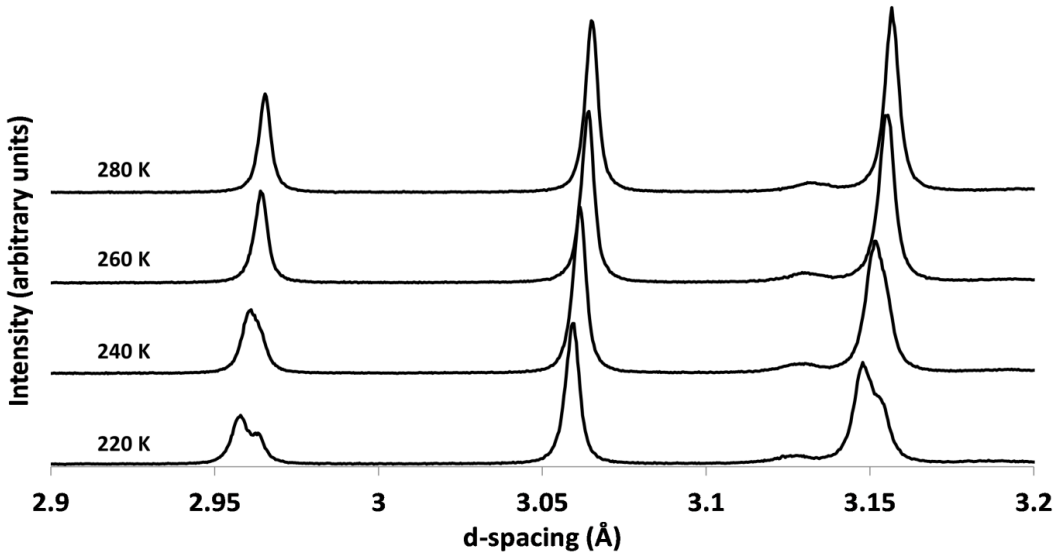

Figure 3.5: SXPD patterns for $Cs_2TiCu_3F_{12}$ at a range of temperatures; note peak splittings appearing < 260 K. Patterns off-set on y-axis for clarity.

[e] Full lattice parameters, unit cell volumes and fit statistics available in Appendix A.3.2.1.

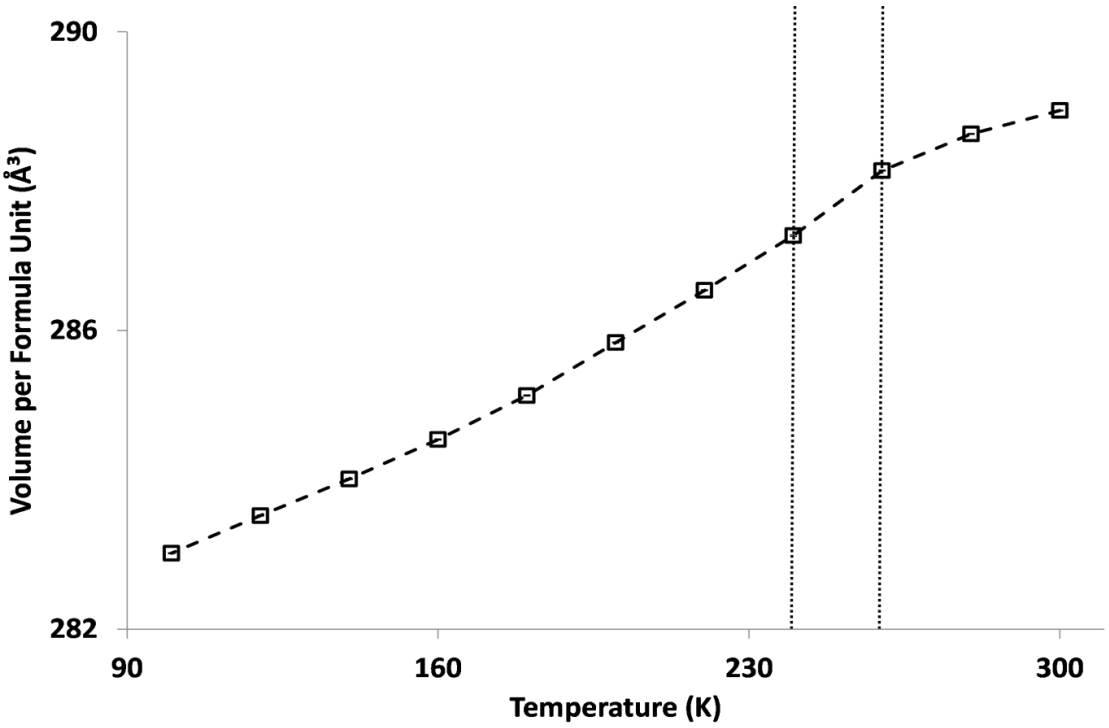

Figure 3.6: Unit cell volume per formula unit vs. temperature for $Cs_2TiCu_3F_{12}$ powder as derived from SXPD data. Note the change in gradient indicated by the vertical dashed lines.

This transition is characterised in the high temperature symmetry by a straight forward reduction in cell parameters. On reaching 240 K the best model was found to be the primitive cell found at 100 K, indicating a more comprehensive transition was beginning to occur. Examination of this lower symmetry phase shows a "twisting" of the kagome lattice away from the perfect hexagonal structure (Figure 3.7). There is also a twisting of the TiF_6 octahedra leading to rows pointing in different directions in an A-B-A-B fashion (Figure 3.8).

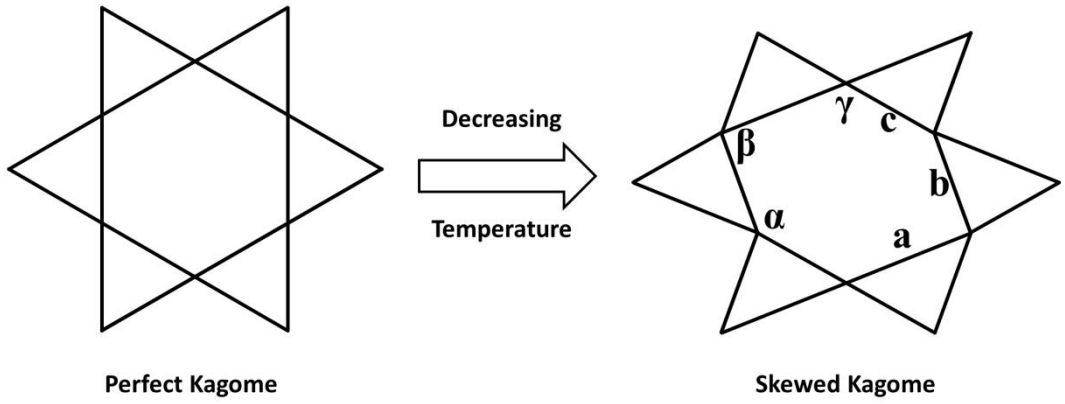

Figure 3.7: Exaggerated skewing of the kagome lattice with decreasing temperature. The perfect kagome has all angles inside the hexagon equal and all bond lengths equal. In the skewed case at 100 K (for the powder sample), the angles vary by ~ 3-4 ° (α ≈ 123 °, β ≈ 116 °, γ ≈ 120 °) and the bind lengths vary by ~ 0.03-0.04 nm (a ≈ 3.50 nm, b ≈ 3.53 nm, c ≈ 3.57 nm).

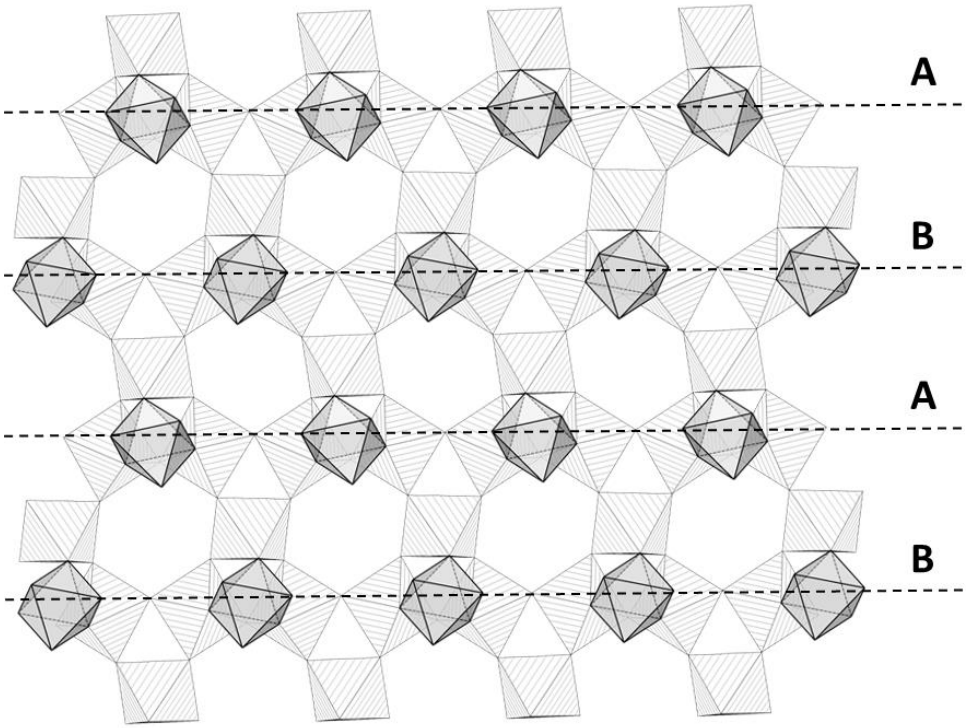

Figure 3.8: Twisting of TiF_6 octahedra (foreground) in an A-B-A-B fashion against a CuF kagome background as found in $Cs_2TiCu_3F_{12}$ below the rhombohedral → monoclinic transition temperature.

A closer analysis of the structural details gives a possible motivation for this; at room temperature the Cu-F and Ti-F bond valence sums (BVS) are not ideal. Titanium fluoride containing compounds appear to have a large variation in their BVS (e.g.: Cs_2TiF_6 4.52 [3], TiF_4 4.638 [13], $BaTiOF_4$ 4.344 [14]) which suggests that the value at room temperature, although high, is acceptable. On cooling, the high temperature symmetry approximately retains the same value for the Ti^{4+} BVS. At 240 K and below, however, it changes (Table 3.7).

Table 3.7: Bond valence sums for the cations in $Cs_2TiCu_3F_{12}$ as a function of temperature calculated using VaList[15]. Note the changes in Ti^{4+} and Cs^+

	BVS			
Temperature (K)	Ti^{4+}	$Cu1^{2+}$	$Cu2^{2+}$	$Cs1^+$
300 (NPD)	4.938	1.996		0.885
300 (SXPD)	4.884	2.016		0.858
280	4.884	2.012		0.867
260	4.884	2.014		0.870
240	4.934	1.990	2.037	0.919
220	4.714	1.950	2.009	0.946
200	4.676	1.954	2.002	0.961
180	4.678	1.988	1.985	0.970
160	4.676	1.960	1.994	0.983
140	4.652	1.986	1.987	0.991
120	4.672	1.990	1.977	0.998
100	4.616	1.970	1.975	1.019

The above table (Table 3.7) shows that while the Cu-F BVS remains fairly constant, the Ti-F BVS decreases sharply below 240 K in order to closer match the ideal 4+ value. This suggests that the transition in this case is largely motivated by the requirement of Ti-F to attain the ideal bond length and the higher temperature case is somehow stabilised. Also notable is the simultaneous increase in the Cs^{1+} BVS to the preferred value, 1. This differs significantly from the only other sample of this family which has been characterised over this temperature range with powder diffraction, $Cs_2ZrCu_3F_{12}$.[2] In that case the transition is motivated by the desire of the larger Zr^{4+} to have a coordination sphere of > 6; something which is unlikely for Ti^{4+}.

3.2.2 Single crystal X-ray diffraction studies of $Cs_2TiCu_3F_{12}$

At room temperature, the macroscopic crystalline form of $Cs_2TiCu_3F_{12}$ shows many of the structural features that are found for the micro-crystalline (powder) form (Table 3.8).

Table 3.8: Atomic coordinates of $Cs_2TiCu_3F_{12}$ derived from SXPD and SCXD ($R\bar{3}m$, SXPD a = 7.090321(18), c = 19.91021(9), SCXD a = 7.1014(14), c = 19.955(2)) at room temperature.

Atom	x	y	z	U_{ISO} (Å^2) x 100
$Cs_2TiCu_3F_{12}$ (SXPD)				
Cs	0	0	0.11128(3)	2.895(17)
Ti	0	0	½	0.62(4)
Cu	½	0	0	0.684(16)
F1	0.20380(15)	-0.20380(15)	0.98084(10)	2.87(5)
F2	0.12308(15)	-0.12308(15)	0.44758(9)	2.87(5)
$Cs_2TiCu_3F_{12}$ (SCXD)				
Cs	0	0	0.11080(4)	3.40(7)
Ti	0	0	½	1.39(7)
Cu	½	0	0	1.49(11)
F1	0.2037(3)	-0.2037(3)	0.9808(2)	2.56(15)
F2	0.1252(3)	-0.1252(3)	0.4474(2)	4.22(18)

These similarities also extend to the high Ti-F BVS, 4.53, which although smaller than the powder case appears to be due to the movement of F2 along the x and y axes. There is also likely to be a smaller impact from the larger unit cell parameters reported compared to the powder (a + 0.0111 Å, c + 0.0448 Å).

On cooling to 125 K there is a divergence from the expected behaviour and we find the cell a/b parameter doubles instead of becoming the primitive monoclinic cell described for the powder.

This low temperature unit cell is similar to that previously reported for room temperature $Rb_2SnCu_3F_{12}$ [16] however there is no evidence of the type of F atom disorder reported for that compound. This is neatly shown by investigation of the anisotropic thermal parameters of the asymmetric unit (Figure 3.9).

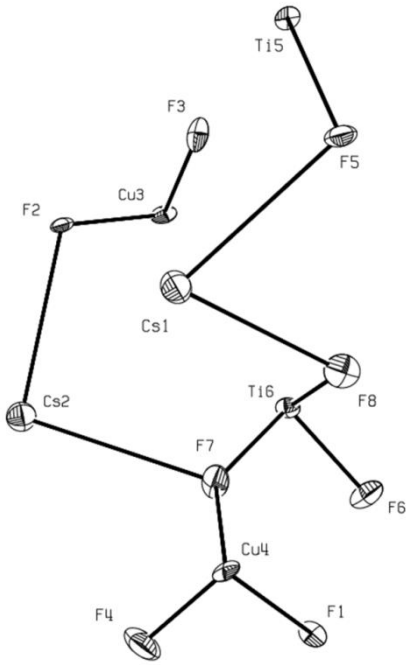

Figure 3.9: Asymmetric unit of $Cs_2TiCu_3F_{12}$ at 125 K, space group $R\bar{3}$, derived from single crystal data using SHELX. Note the small anisotropic thermal ellipsoids indicating a lack of disorder.

Table 3.9: Single crystal data and refinement details for $Cs_2TiCu_3F_{12}$ at room temperature and 125 K using the SHELX program.[f]

	Room Temperature	125 K
formula	$Cs_2TiCu_3F_{12}$	
crystal system	Rhombohedral	
space group	$R\bar{3}m$	$R\bar{3}$
a	7.1014(14)	14.163(3)
c	19.955(2)	19.865(6)
volume (Å^3)	871.5(2)	3450.88(15)
Z	3	12
wavelength (Å)	0.71073	
ρ (calc.) (g cm^{-3})	4.186	4.229
absorption coefficient (mm^{-1})	12.385	12.511
crystal size (mm)	0.18 x 0.15 x 0.03	0.31 x 0.26 x 0.10
θ range for data collection (°)	3.1 – 27.5	2.0 – 27.5
reflections collected	3063	10280
independent reflections	280	1410
max. & min. transmission	1, 0.425	1, 0.416
data/restraints/parameters	280/0/24	1410/0/113
goodness-of-fit on F^2	0.808	0.718
R indices [$I > 2\sigma(I)$], *R*1, *wR*2	0.033, 0.094	0.045, 0.139
R indices (all data), *R*1, *wR*2	0.039, 0.102	0.062, 0.151
largest diff. peak & hole (e Å^{-3})	1.01, -2.259	1.533, -1.175

[f] .cif and structure factor files for both temperatures can be found in appendix A.3.2.2.

Once again there is a decrease in the Ti-F bond valence sum with reducing temperature (Table 3.10). The low temperature single crystal structure also appears to be motivated by the decrease in Ti-F bond valence sum but achieves this in a different way. In this case only a third of TiF_6 octahedra are rotated and the kagome layer shows a different form of twist (Figure 3.10, Figure 3.11).

Table 3.10: Bond valence sums for cations present in $Cs_2TiCu_3F_{12}$ single crystals at both room temperature and 125 K.

	BVS					
Temp.	Ti1	Ti2	Cu1	Cu2	Cs1	Cs2
RT	4.530		2.004		0.759	
125 K	4.422	4.422	2.127	1.812	0.956	0.741

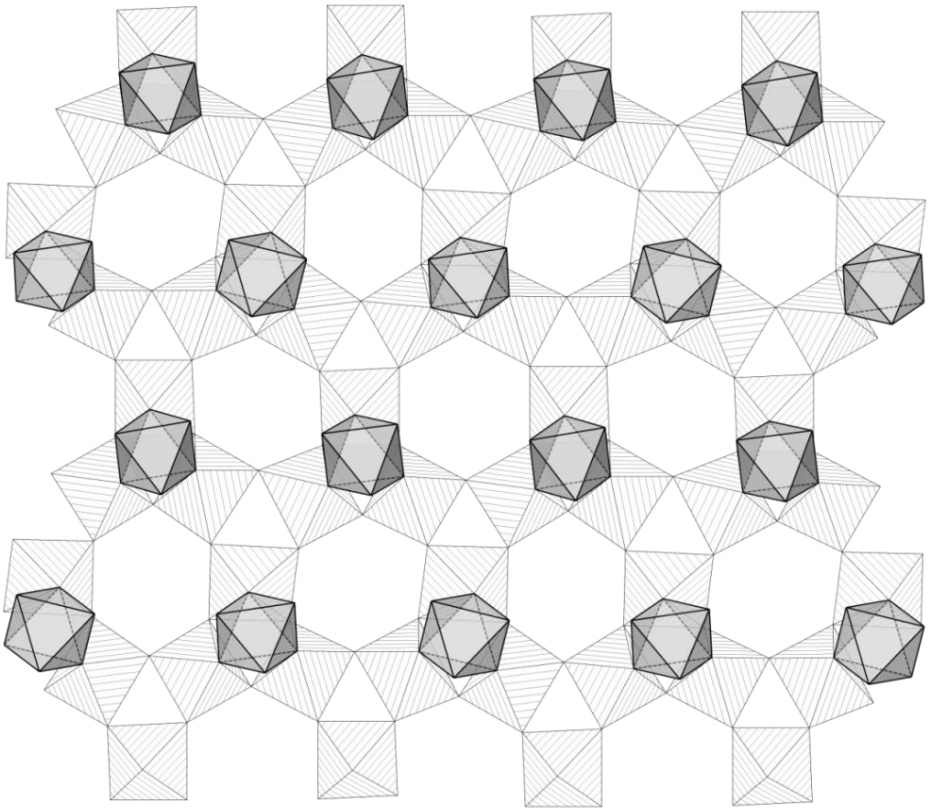

Figure 3.10: Twisting of TiF_6 octahedra (foreground) against a CuF kagome background found at 125 K (below the $R\bar{3}m \rightarrow R\bar{3}$ transition); note only a third are rotated.

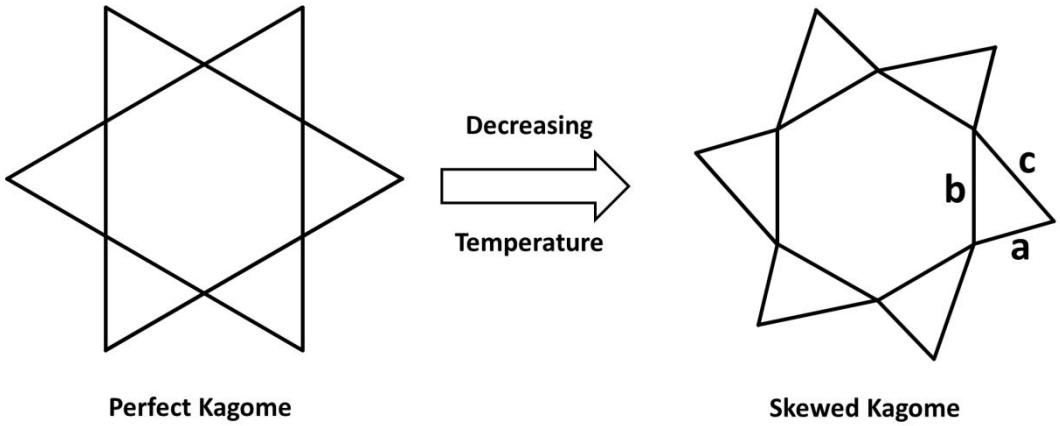

Figure 3.11: Exaggerated skewing of the kagome lattice with decreasing temperature ($R\bar{3}m$ on right, $R\bar{3}$ on left). In the perfect case all bond lengths and angles in the kagome triangles are equal. At 125 K (in the skewed model) the difference in angles is found to be ~ 1 ° and the bond lengths differ by ~ 0.03 Å (a ≈ 3.514 Å, a ≈ 3.539 Å, c ≈ 3.569 Å).

3.2.3 $Cs_2TiCu_3F_{12}$: a material with crystallite size dependent phase transitions

From sections 3.2.1 and 3.2.2 it is clear that the phase change that occurs in $Cs_2TiCu_3F_{12}$ with reducing temperatures shows some crystallite size dependence. It is important to confirm that the phase changes seen are indeed correct. For the powder we can compare the expected reflections for the doubled rhombohedral cell and the monoclinic ($P2_1/n$) cell and we find that the rhombohedral cell is inadequate for modelling the pattern (Figure 3.12).

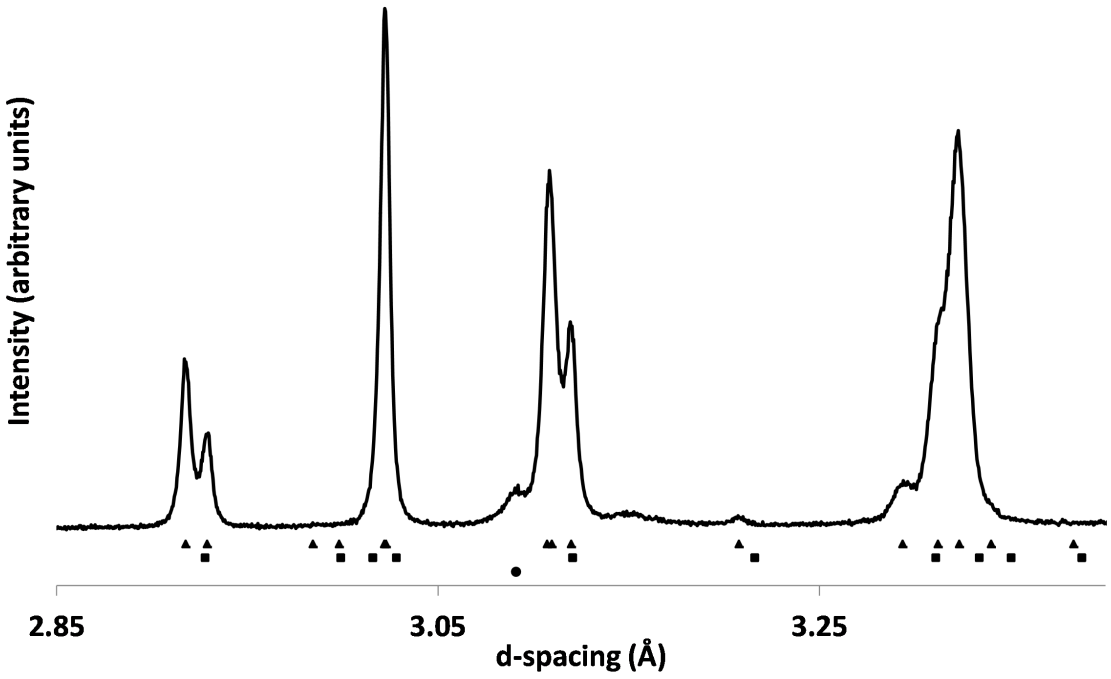

Figure 3.12: SXPD pattern for $Cs_2TiCu_3F_{12}$ at 300 K; triangles are reflections permitted for the monoclinic ($P2_1/n$) unit cell, squares for the doubled rhombohedral cell and circles for the impurity Cs_2TiF_6.

Indexing of the single crystal images also shows the inadequacy of a primitive monoclinic model to fit the data. The data are, however, well fitted by the doubled rhombohedral cell (Figure 3.13).

The reasons for this particular morphology dependent polymorphism are unknown although the general theme has come under study in the past. There have been a number of studies which have correlated surface energy to phase transition temperatures/pressures and polymorphism and these have tended to compare bulk and nanoparticulate phases. It is suggested that surface energy is a dominant factor and it is imagined that this would also be seen in the case of $Cs_2TiCu_3F_{12}$.[17-19] The platy nature of even the powdered crystallites – evidenced by the broadenings in the powder diffraction – may also give an extra degree of freedom with regard to phase transitions, which allows the adoption of a lower energy polymorph that the surface structure of the single crystal will not allow.

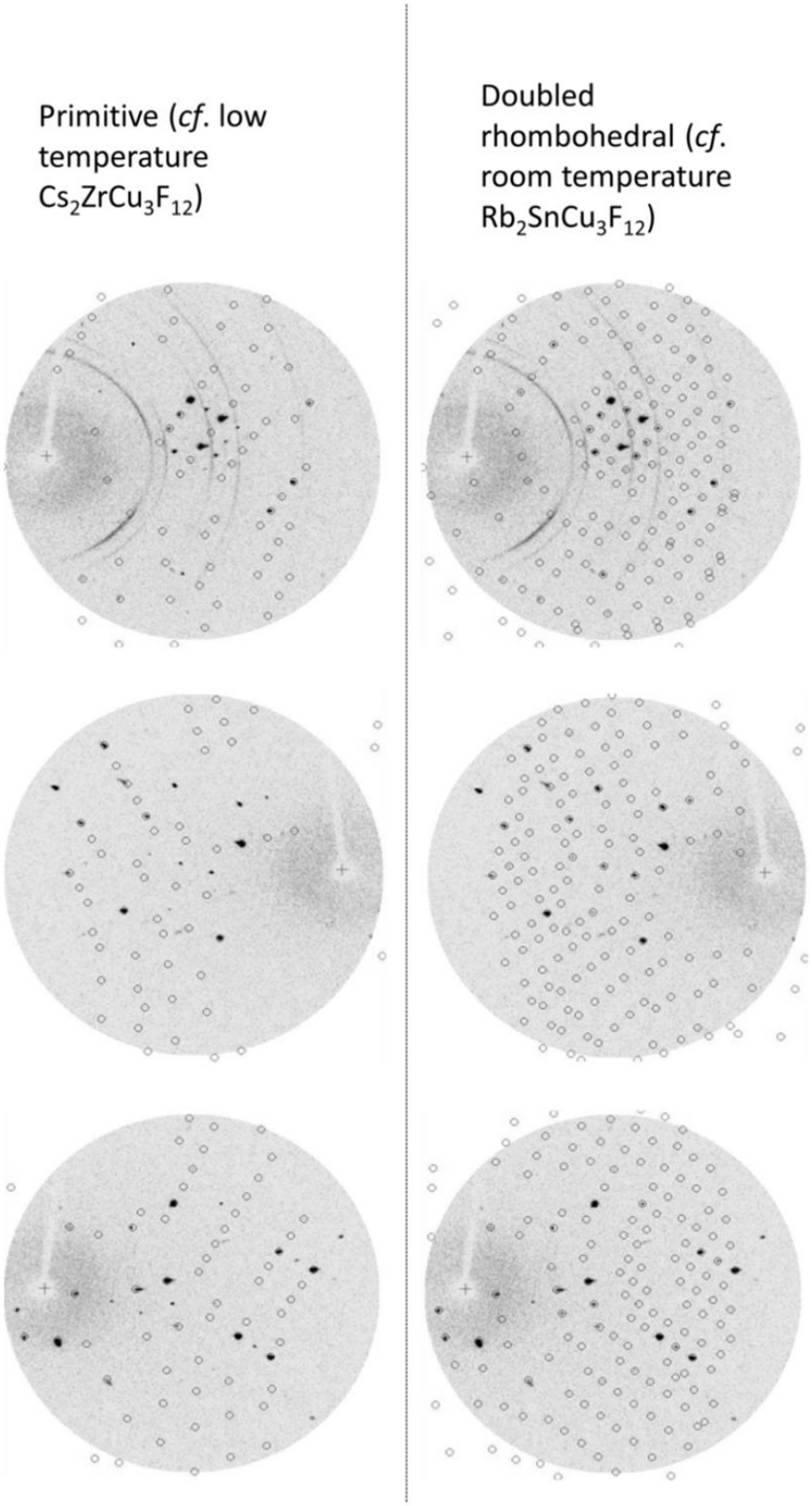

Figure 3.13: Single crystal diffraction images (from Rigaku CrystalClear 2.0), with indexed peaks circled. The primitive unit cell is indicated on the left and the doubled rhombohedral cell on the right. Note the inadequacy of the primitive cells allowed reflection positions.

3.3 Crystallography of $Rb_2TiCu_3F_{12}$

It proved very challenging to synthesise a diffraction quality single crystal of $Rb_2TiCu_3F_{12}$ and so this study has depended upon powder diffraction in order to determine the structural properties of the material.

At room temperature, $Rb_2TiCu_3F_{12}$ (X_{Rb}) is found to present itself as a triclinic unit cell, space group $P\bar{1}$, which is related to the doubled rhombohedral cell by the matrix:

$$\begin{bmatrix} 2/3 & 1/3 & 1/3 \\ -1/3 & 1/3 & 1/3 \\ -1/3 & -2/3 & 1/3 \end{bmatrix}$$

when $a = b = c$ and $\alpha = \beta = \gamma$. The triclinic symmetry was confirmed by neutron diffraction experiments which gave a similar, but not coincident cell (Table 3.11).

Table 3.11: Comparison of room temperature lattice parameters of $Rb_2TiCu_3F_{12}$ from SXPD and NPD data.

Unit Cell Parameter	SXPD	NPD
a (Å)	10.3592(8)	10.3703(15)
b (Å)	10.3506(9)	10.3521(19)
c (Å)	10.3440(3)	10.3369(14)
α (°)	83.838(8)	83.717(17)
β (°)	83.832(8)	83.635(14)
γ (°)	83.9111(15)	83.921(8)

The reasons for the differences in cell parameters are unknown but it is interesting to note that the parameters for the impurities also differ. For this reason the explanation that some in-beam heating may occur for the synchrotron data or another source of temperature difference is suggested. The sample is also not perfect as a number of impurities are present (a typical overall sample composition is: 85.4 % $Rb_2TiCu_3F_{12}$, 8.4 % Rb_2TiF_6, 4.9 % CuO, 1.2 % Cu_2O plus other unidentified peaks). Due to the difference in lattice parameters there is the important caveat that temperature errors and diffractometer offsets may play some part in the final data analysis.[g]

Due to the complex triclinic model used (38 unique atoms, Table 3.12) it was not possible to refine the atomic coordinates reliably in order to generate a more accurate model. However, even without this there are still some interesting features in the data. On cooling we see that the unit cell further diverges from the case where $a = b = c$ and $\alpha = \beta = \gamma$ indicating that the sample is becoming less like the rhombohedral model. This allows us to extrapolate upwards in temperature to suggest an approximate temperature where the sample would have rhombohedral symmetry like $Rb_2SnCu_3F_{12}$ (Figure 3.15). In this case it is feasible to suggest that a transition to a high symmetry state would occur somewhere between 320 and 350 K. Another feature of note is a hysteresis between ~ 150 and 300 K; the lattice parameters

[g] A more extensive comparison including impurity phases is presented in appendix A.3.3.

are notably not superimposable like at lower temperatures. This indicates that the phase transition may be first order and as the hysteresis occurs below the assumed temperature of "transition" it may indicate a phase change which occurs in two parts. It should be noted, however, that there is no clear hysteresis in the cell volume parameter.

Compared to $Cs_2TiCu_3F_{12}$ it can be seen that the temperature of transition has increased once again and it would seem appropriate to suggest that the temperature of transition has some dependence on the size of both the A^+ and M^{4+} cations.

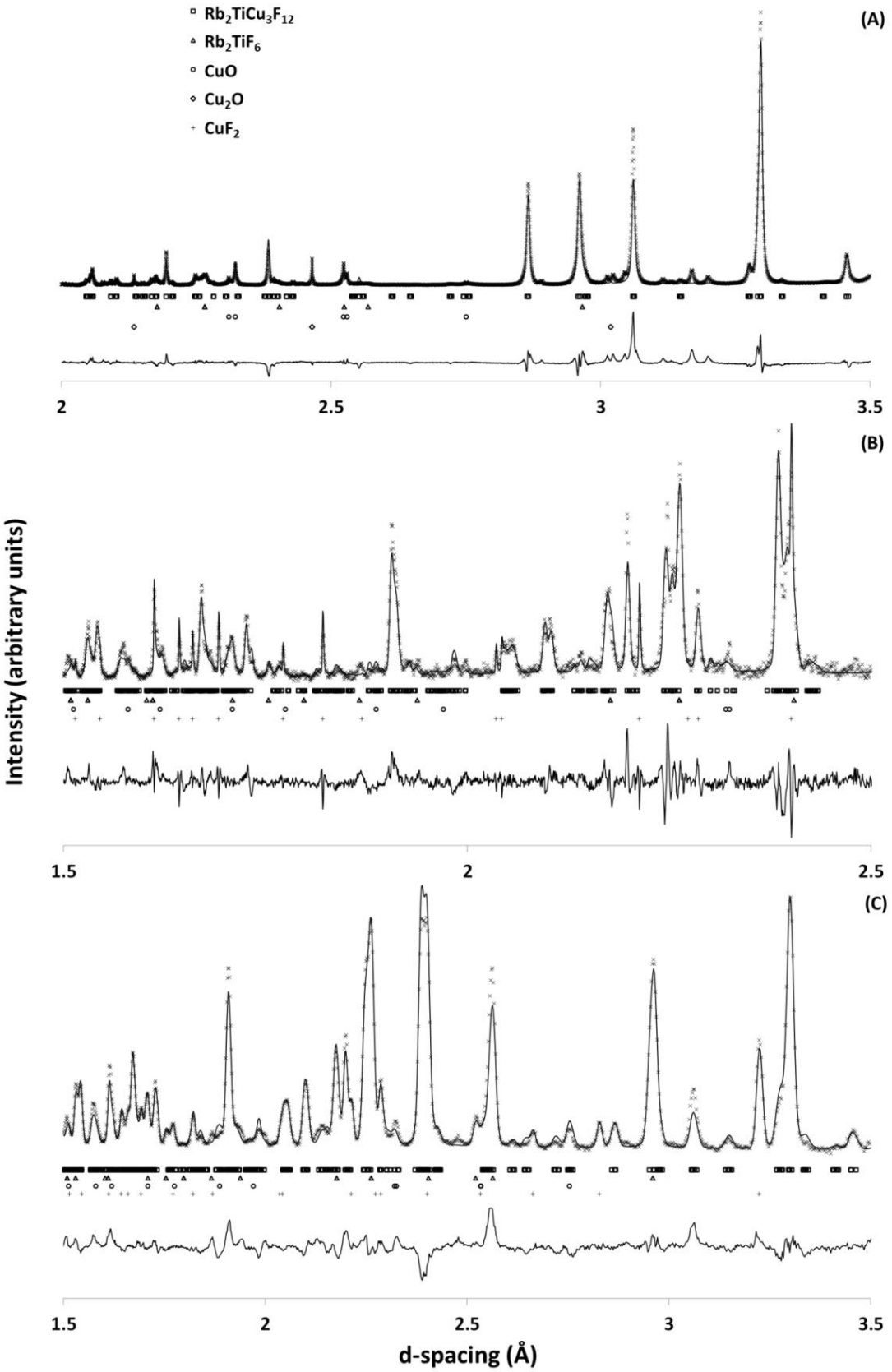

Figure 3.14: Rietveld fits for $Rb_2TiCu_3F_{12}$ at 300 K; (A) SXPD, (B) NPD backscattering bank, (C) NPD 90 ° bank (atomic coordinates not refined). SXPD data from Diamond Light Source. Ltd, NPD data from HRPD, ISIS neutron and muon source.

Table 3.12: Triclinic model used for $Rb_2TiCu_3F_{12}$ powder data refinement; the model is derived from the $Rb_2SnCu_3F_{12}$ model [16] using the ISODISTORT program [12] with the removal of disorder and no further structural refinement.

Atom	x	y	z
Rb	0.3999	0.8933	0.8991
Rb	0.8991	0.3999	0.8933
Rb	0.8933	0.8991	0.3999
Rb	0.6020	0.6020	0.6020
Cu	0.7628	0.7401	0.0017
Cu	0.0017	0.7628	0.7401
Cu	0.7401	0.0017	0.7628
Cu	0.5285	0.7530	0.2492
Cu	0.2492	0.5285	0.7530
Cu	0.7530	0.2492	0.5285
Ti	½	½	0
Ti	0	½	½
Ti	½	0	½
Ti	0	0	0
F	0.8195	0.5856	0.1049
F	0.1049	0.8195	0.5856
F	0.5856	0.1049	0.8195
F	0.8848	0.6803	0.8666
F	0.8666	0.8848	0.6803
F	0.6803	0.8666	0.8848
F	0.6686	0.8217	0.1412
F	0.1412	0.6686	0.8217
F	0.8217	0.1412	0.6686
F	0.0633	0.9370	0.8337
F	0.8337	0.0633	0.9370
F	0.9370	0.8337	0.0633
F	0.4004	0.5948	0.8668
F	0.8668	0.4004	0.5948
F	0.5948	0.8668	0.4004
F	0.5336	0.6644	0.0525
F	0.0525	0.5336	0.6644
F	0.6644	0.0525	0.5336
F	0.6484	0.5084	0.8717
F	0.8717	0.6484	0.5084
F	0.5084	0.8717	0.6484
F	0.3928	0.6842	0.3619
F	0.3619	0.3928	0.6842
F	0.6842	0.3619	0.3928

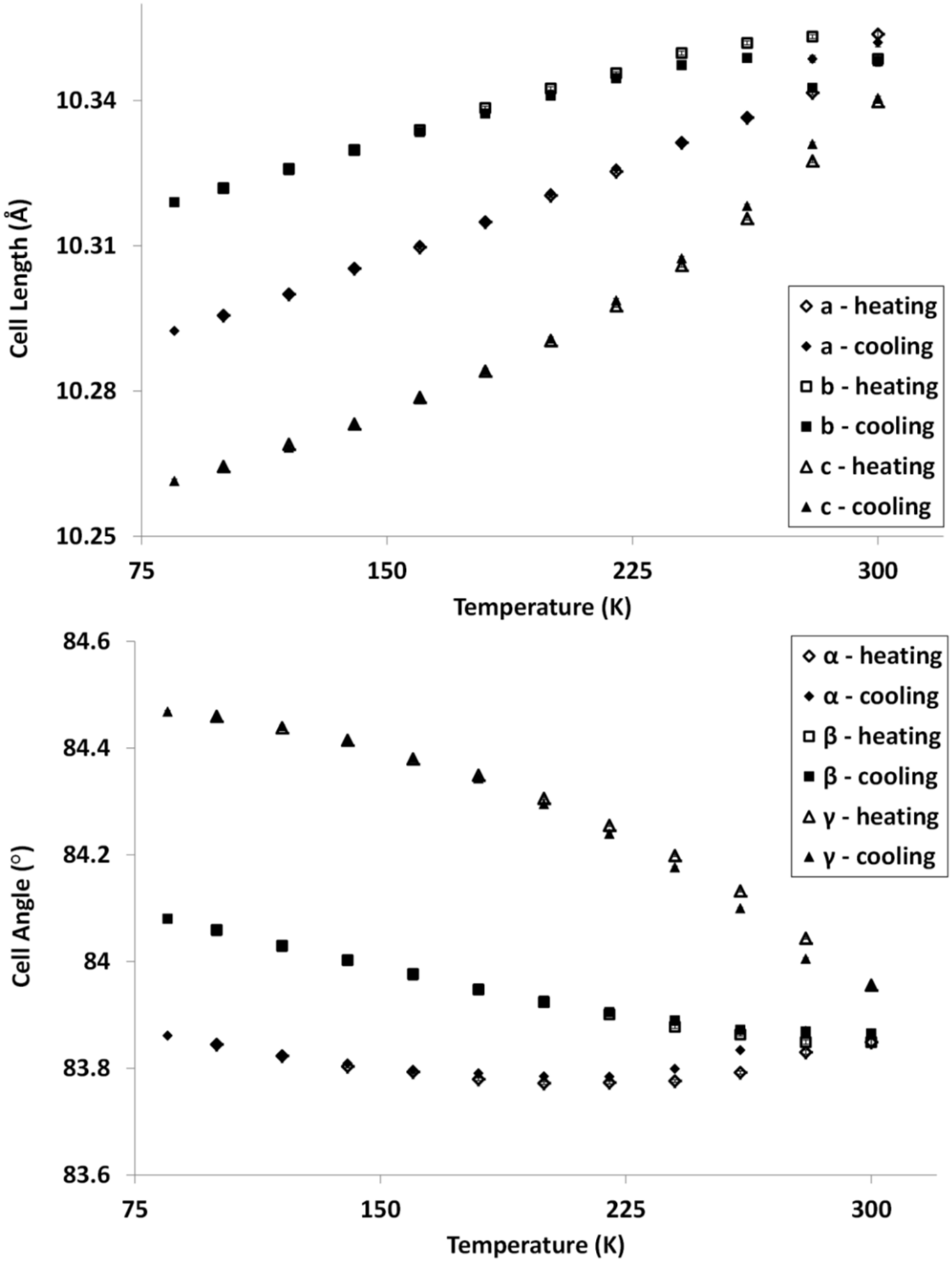

Figure 3.15: Lattice parameters derived from SXPD data for $Rb_2TiCu_3F_{12}$ powder as a function of temperature (error bars included).[h] Data acquired at I11, Diamond Light Source.

[h] Refinements and tables of cell parameters for both heating and cooling can be found in appendix A.3.3.

3.4 Magnetic properties of $Cs_2TiCu_3F_{12}$

0.01774g of $Cs_2TiCu_3F_{12}$ powder (Z_{Cs}) of approximately 80 % purity (0.0581 mM Cu^{2+}) was used in these measurements [i] which took place at Moscow State University. The sample was initially cooled to 2 K and a field of 2000 Oe applied. The sample was then heated while measuring magnetism to 190 K (zero field cooled or ZFC) before cooling (in field) to 2 K again. The sample was then reheated while measuring to 300 K (field cooled or FC). Both ZFC and FC data show a large anomaly beginning at ~21 K and peaking at ~ 16 K. The ZFC and FC data are superimposable only beyond approximately 145 K. The data were plotted as a function of $1/\chi_m$ vs. T (Figure 3.16) and a linear region was found between 150 and 300 K in the FC data which corresponds to Curie-Weiss magnetism; from this some quantitative data can be extracted (Table 3.13).

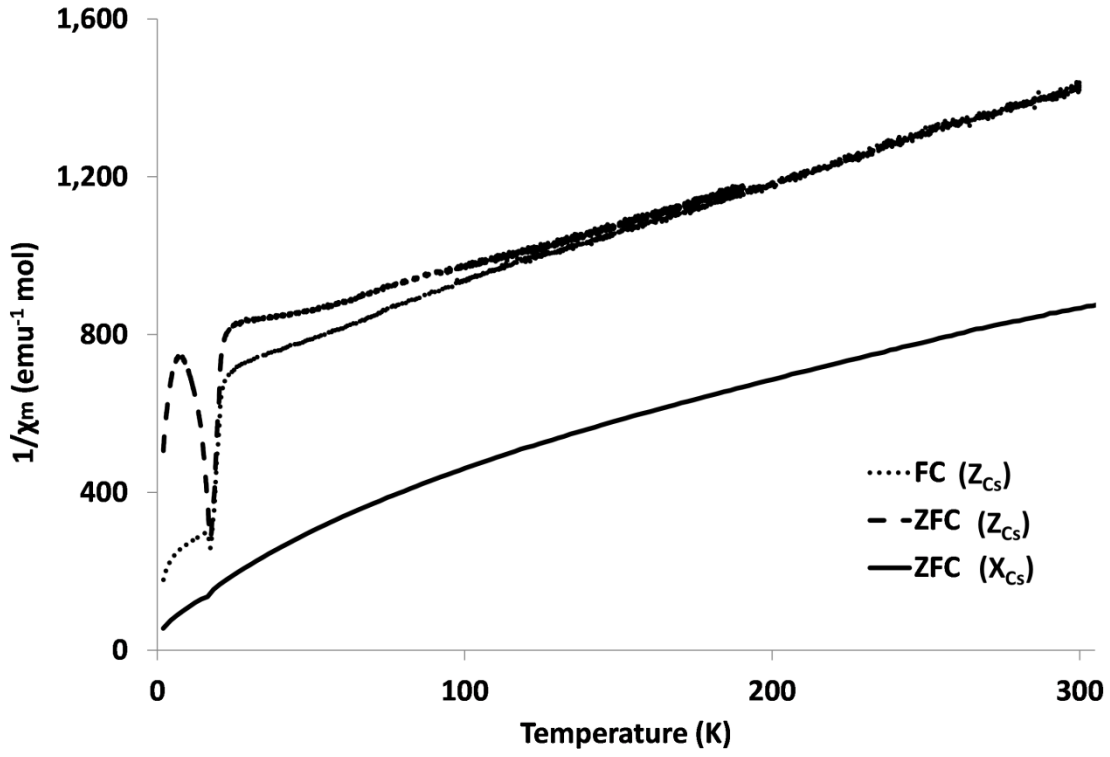

Figure 3.16: $1/\chi_m$ vs T for magnetically pure $Cs_2TiCu_3F_{12}$ powder (Z_{Cs}) at 2000 Oe (both ZFC and FC) and $1/\chi_m$ vs T for magnetically impure $Cs_2TiCu_3F_{12}$ powder (X_{Cs}) at 2000 Oe (ZFC only). Note that the magnetically impure data (X_{Cs}) obscures the magnetic detail visible in the pure data (Z_{Cs}).

Table 3.13: Quantitative magnetic data for $Cs_2TiCu_3F_{12}$ powder (Z_{Cs}) from FC measurements at 2000 Oe.

Curie constant, C, (emu K mol_{Cu}^{-1})	0.380
Effective moment, μ_{eff}, (μ_{BM})	1.74
Curie-Weiss temperature, T_{CW}, (K)	-276.9

[i] The magnetic data can be found in appendix A.3.4 in .csv format.

From the quantitative data it can be seen that the system is strongly antiferromagnetically coupled (large negative Curie-Weiss temperature, T_{CW}). The experimental magnetics moment, μ_{eff}, also compares well with the theoretical value for Cu^{2+}, 1.73 – 1.90 μ_{BM} for the octahedral state.[20]

In order to probe the sample further a ZFC measurement was performed at low field (20 Oe) (Figure 3.17). This, curiously, showed a negative magnetic moment beginning at the transition point found at high field (21 K); this is usually synonymous with materials that show superconductivity. It would be unlikely that $Cs_2TiCu_3F_{12}$ is a superconductor as it is white in colour – superconductors are usually darker indicating a small band-gap and therefore a low barrier to conductivity. One other possible explanation is a remnant field in the coils of the PPMS system but this would only lead to a very small moment.

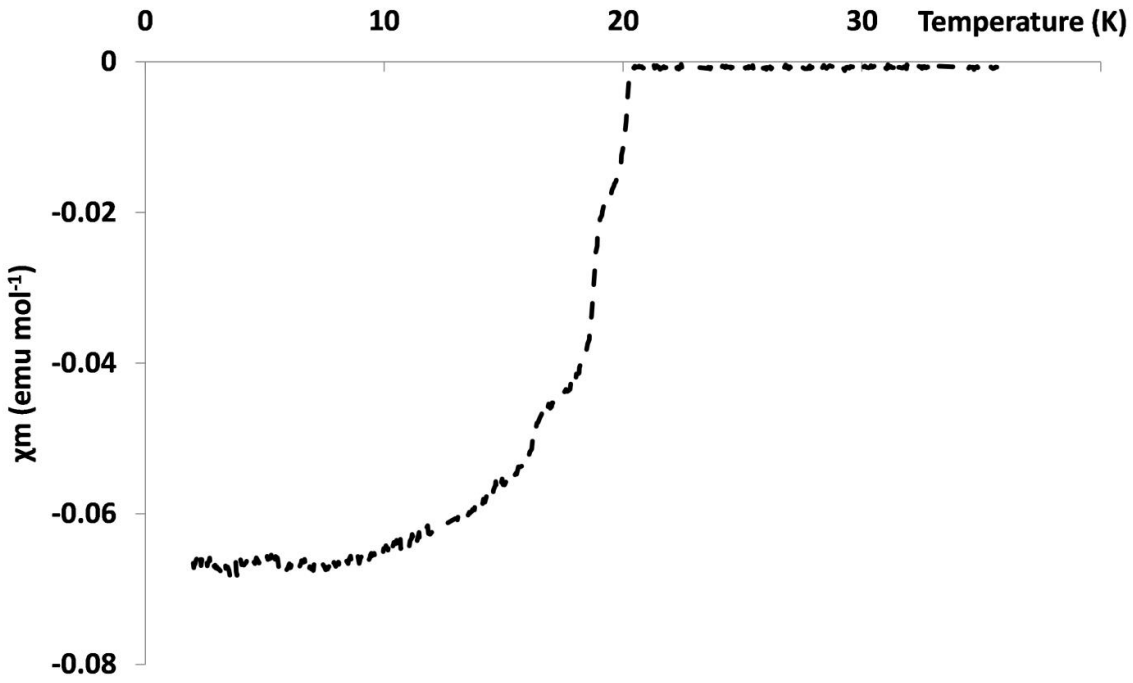

Figure 3.17: Low field (20 Oe) ZFC measurement for $Cs_2TiCu_3F_{12}$ powder (Z_{Cs}) performed at Moscow State University.

In order to probe the sample further, magnetism vs. field measurements were performed[j] in the range ± 70000 Oe on a sample that was made in St Andrews (X_{Cs}) so therefore less magnetically pure. At the lowest temperature surveyed, 1.9 K, a small hysteresis was observed between ± 2000 Oe with the beginnings of saturation appearing beyond ± 30000 Oe (Figure 3.18).

[j] With Dr. M. De Vries, School of Chemistry, University of Edinburgh

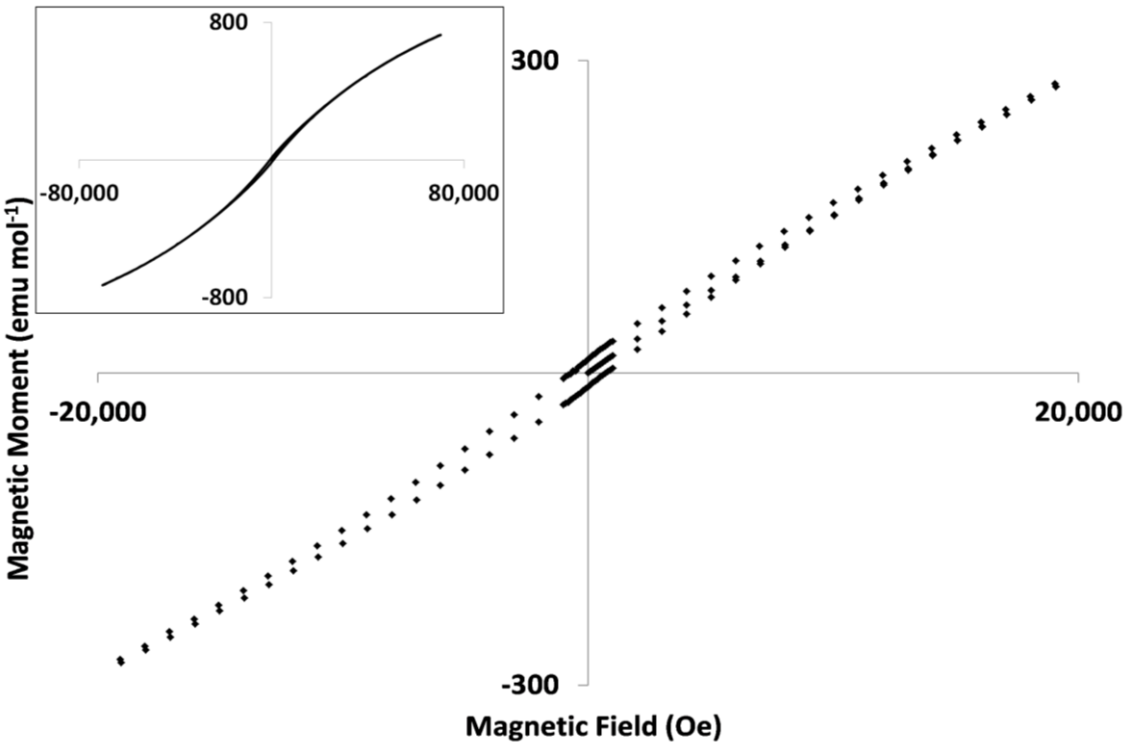

Figure 3.18: Magnetisation as a function of field for $Cs_2TiCu_3F_{12}$ powder (X_{Cs}) at 1.9 K (inset shows full range surveyed).

In order to see if the 20 K anomaly peak is significant or related to some ordering event, magnetism vs. field measurements were also taken at 20 K on this sample. In this case there was no observable hysteresis which suggests that there is some event occurring between 20 and 1.9 K. One possibility is that there is a degree of spin freezing occurring – an antiferromagnetically ordered system (which a negative T_{CW} would indicate) would not show a hysteresis. Also under consideration is the possibility of impurities. In the case of samples made in St Andrews (X_{Cs}, X_{Rb}) the two most common impurities are CuO and Cs_2TiF_6 and their magnetic behaviours – as well as some other possible impurities – are presented in Table 3.14. Analysis of these suggests that there are no impurities which have an ordering transition between 1.9 and 20 K. For this reason it is proposed that $Cs_2TiCu_3F_{12}$ undergoes some spin freezing with reducing temperature.

Table 3.14: Magnetic behaviours of some known and possible impurities in $Cs_2TiCu_3F_{12}$ powder.

Compound	Magnetic behaviour
CuO	Antiferromagnetic, $T_N \approx 230$ K [21]
CuF_2	Antiferromagnetic, $T_N \approx 70$ K [22]
Cu_2O	Non-magnetic in bulk (d^{10}) [k]
Cs_2TiF_6	Non-magnetic in bulk (all electrons paired)

[k] Cu_2O phase can be slightly more complicated due to particle size/shape effects and non-stoichiometry.

In order to see if the magnetic properties varied with morphology, the magnetic properties of a collection of single crystals (Y_{Cs}) (0.003g, 0.0123 mM Cu^{2+}) were measured. FC and ZFC measurements were performed between 1.8 and 390 K under a field of 2000 Oe. This yielded results which appeared to be very different from the powder (Figure 3.19).

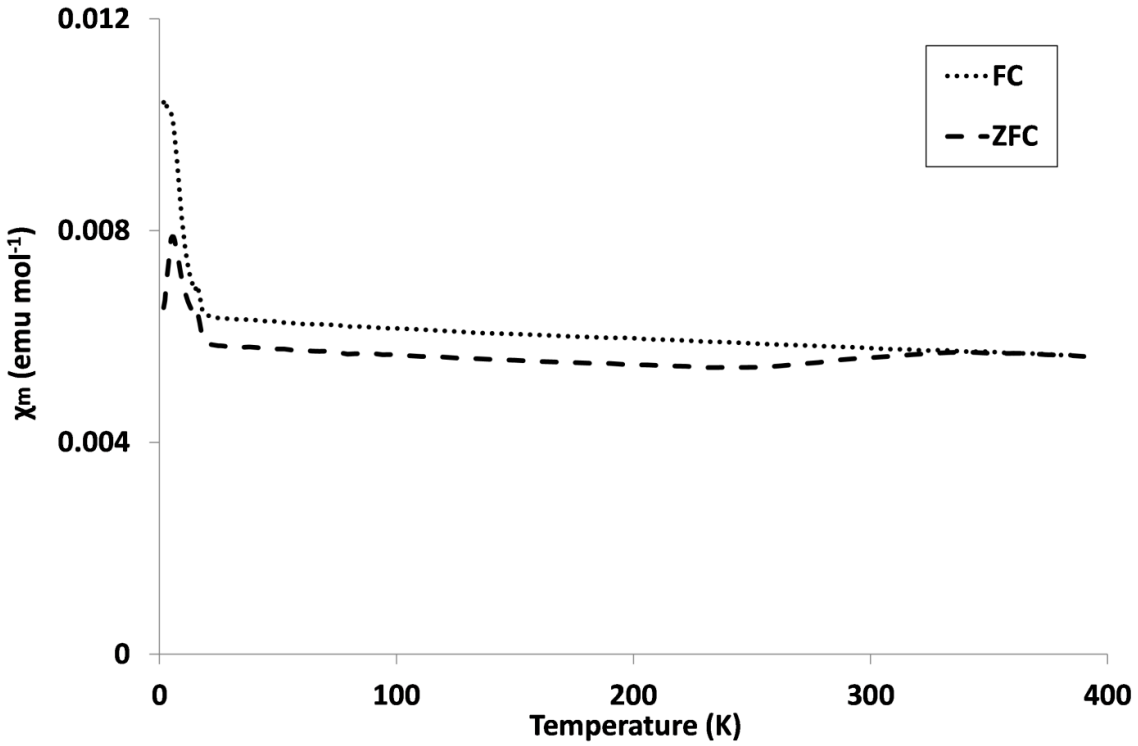

Figure 3.19: χ_m vs T for $Cs_2TiCu_3F_{12}$ single crystals (Y_{Cs}) for FC and ZFC measurements minus the contribution from Kapton for an applied field of 2000 Oe. Measurements performed at the University of Edinburgh.

A divergence between FC and ZFC data was found to begin at ~340 K and there is also a large temperature independent paramagnetism (TIP) at all temperatures. An anomaly is present at ~16 K (4 K lower than the powder) which is also where the data begins to converge (on cooling). The next anomaly is a divergence that begins at ~4.8 K. The contribution of the Kapton films has been removed.[I] This, however, makes little difference and can only be assumed as a minor component of the TIP. Fitting of the FC data can usually be achieved using the equation:

$$\chi_m = \chi_0 + {}^{C}/_{(T - T_{cw})}$$

where χ_0 is a constant describing the TIP and all other variables have their standard meaning. Fitting the FC data between 110 and 270 K like for the powder data fails to give any reasonable values, however. Using the values found for the powder and varying χ_0 fails to yield an

[I] The details of this can be found in appendix A.3.4 as well as the raw data for the Kapton in .csv format.

acceptable fit. This indicates that the single crystals may be behaving differently but the over-complication of the TIP makes deconvolution and a reliable conclusion difficult to come to.

Further analysis was performed on the sample (Y_{Cs}) in the form of magnetic moment vs. field measurements at 1.8 K. A hysteresis is found indicating the presence of spin freezing (Figure 3.20). The low temperature divergence in the ZFC and FC data agrees with this.

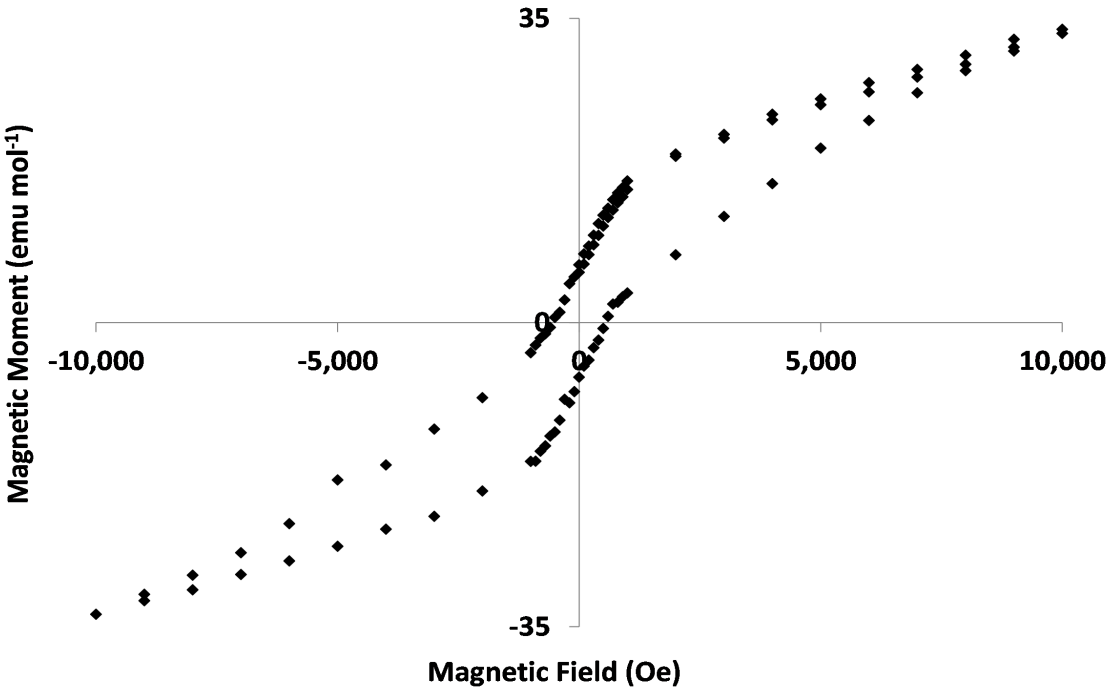

Figure 3.20: Magnetisation as a function of field for $Cs_2TiCu_3F_{12}$ single crystals (Y_{Cs}) at 1.8 K. Measurements performed at the University of Edinburgh.

The reasons for the difference between the powder and the single crystal samples may be related to the difference in sample morphology. It is noted that there are no obvious anomalies coincident with the structural transitions suggesting the high temperature transitions are not motivated by magnetic interactions.

3.5 Magnetic properties of $Rb_2TiCu_3F_{12}$

$Rb_2TiCu_3F_{12}$ was subject to the same magnetic analysis as $Cs_2TiCu_3F_{12}$. In this case 0.03299 g (0.124 mM Cu^{2+}) of sample of approximately 80 % purity (Z_{Rb}) was used and the ZFC and FC measurements completed with 2000 Oe.[m] This sample was synthesised at MSU and so assumed to be almost magnetically pure (< 1 % $RbCuF_3$). In this case there is a large anomaly beginning at 50 K and only above this temperature are the ZFC and FC lines superimposable. A

[m] The magnetic data can be found in appendix A.3.5 in .csv format.

plot of $1/\chi_m$ vs. T shows Curie-Weiss behaviour between 200 and 300 K (Figure 3.21) from which we can once again extract some quantitative values (Table 3.15).

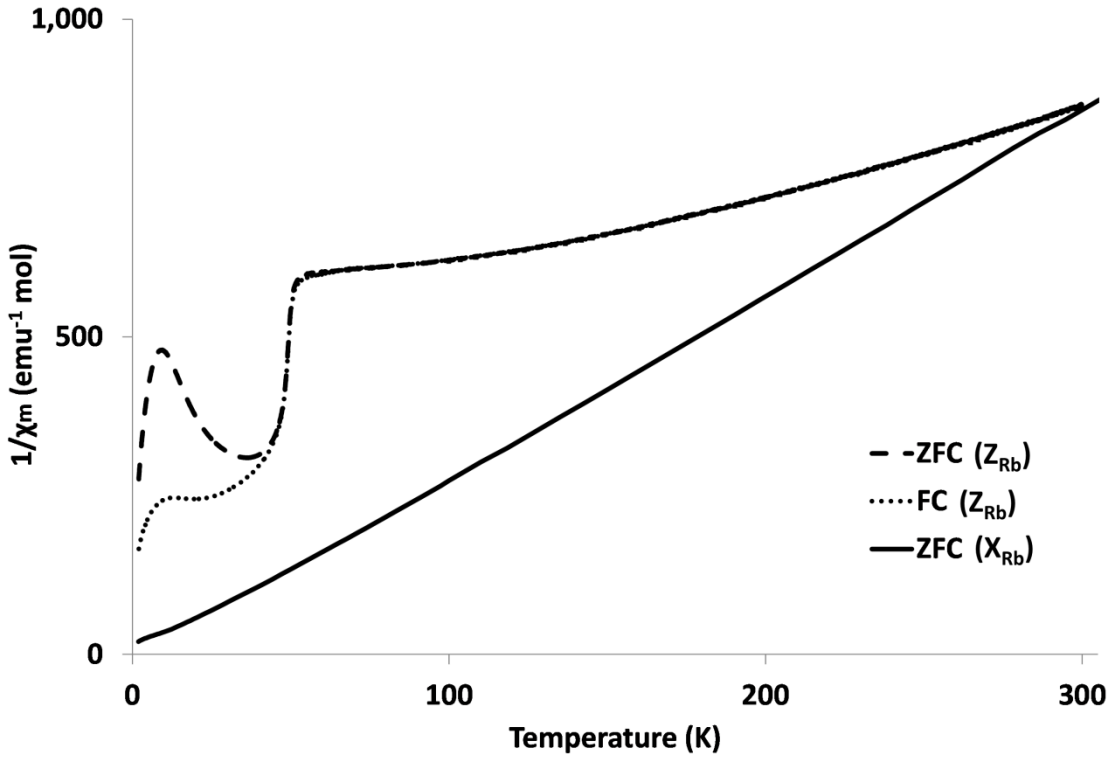

Figure 3.21: $1/\chi_m$ vs T for magnetically pure $Rb_2TiCu_3F_{12}$ powder (Z_{Rb}) at 2000 Oe (both ZFC and FC) and $1/\chi_m$ vs T for magnetically impure $Rb_2TiCu_3F_{12}$ powder (X_{Rb}) at 2000 Oe (ZFC only). Note that the magnetically impure data (X_{Rb}) obscures the magnetic detail visible in the pure data (Z_{Rb}).

Table 3.15: Quantitative magnetic data for $Rb_2TiCu_3F_{12}$ powder (Y_{Rb}) from measurements at 2000 Oe.

Curie constant, C, (emu K mol_{Cu}^{-1})	0.680
Effective moment, μ_{eff}, (μ_{BM})	2.33
Curie-Weiss temperature, T_{CW}, (K)	-286.9

Once again, it is found that the μ_{eff} values are close to that expected for Cu^{2+}, indicating that the sample consists of the anticipated stoichiometry. T_{CW} is large and negative indicating antiferromagnetic interactions dominate. This is also observed in the sister phase, $Cs_2TiCu_3F_{12}$.

Further analysis was performed in the form of magnetic moment vs. field measurements between ± 10000 Oe at 1.9 K (Figure 3.22) on a slightly less pure sample synthesised at the University of St Andrews (X_{Rb}, see section 3.3 for an example of impurities). This showed no clear hysteresis indicating that the impurity level is too high for useful measurements; the splitting of ZFC/FC at low temperature insists that there should be a hysteresis present.

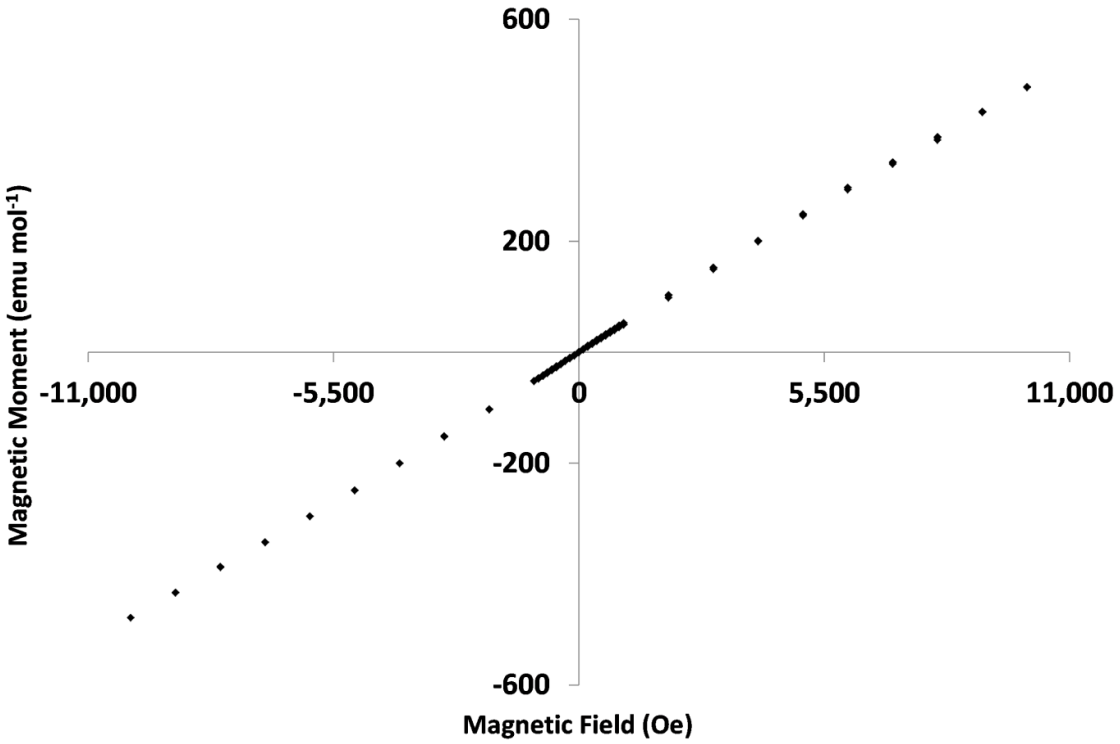

Figure 3.22: Magnetic moment vs. field measurement for $Rb_2TiCu_3F_{12}$ powder (X_{Rb}) at 1.9K. Measurements performed at the University of Edinburgh.

$Rb_2TiCu_3F_{12}$ was also subject to ZFC and FC measurements on a number of single crystals (Y_{Rb}) (Figure 3.23). In this case 0.0021 g (0.0116 mM Cu^{2+}) of crystals were used in a field of 2000 Oe between 1.8 and 390 K. Once again this showed TIP but not as far reaching as found for the $Cs_2TiCu_3F_{12}$ data. There is also an anomaly at 16 K but the divergence below this was not to the same degree as $Cs_2TiCu_3F_{12}$. The same non-superimposability at high temperature is also visible. Corrections were again made for the presence of Kapton tape however it is noted that this may not be perfect.

In this case it is possible to extract some values from a fit of the data with equation:

$$\chi_m = \chi_0 + {}^{C}/_{(T - T_{cw})}$$

Allowing the mathematical fitting program SciDAVis [23] to iterate freely we get the values (and errors) given in Table 3.16 using the data between 100 and 300 K. The Curie constant from this is not the expected value and this leads to a different μ_{eff} value which corresponds to ~ 51 % of the total spins expected. There is a problem however in that one can also fit the line well by fixing the Curie constant and varying the χ_0 and T_{CW} values (also Table 3.16). For this reason it is difficult to draw any solid conclusions from the ZFC and FC measurements.

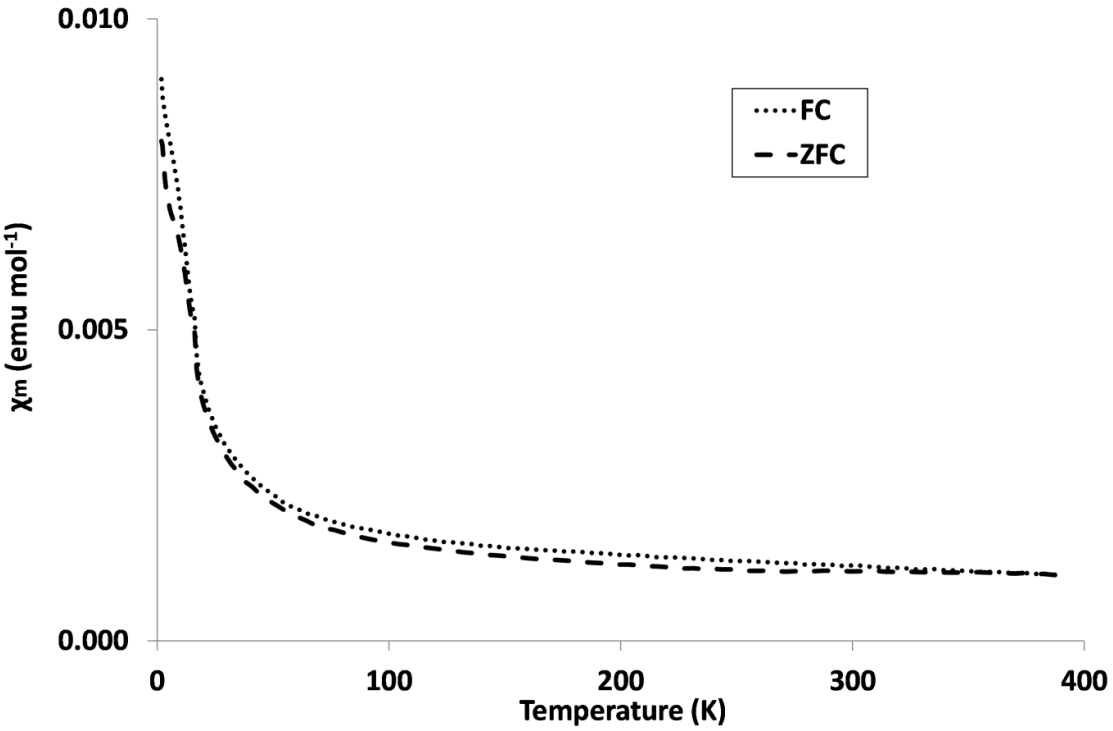

Figure 3.23: χ_m vs T for $Rb_2TiCu_3F_{12}$ single crystals (Z_{Rb}) for FC and ZFC measurements minus the contribution from Kapton. Measurements performed at the University of Edinburgh.

Table 3.16: Quantitative values derived from the ZFC and FC single crystal data for $Rb_2TiCu_3F_{12}$ (Y_{Rb}) for C refined and C fixed at the expected value in the SciDAVis program[23].

	C as a variable	C fixed
Curie constant, C, (emu K mol_{Cu}^{-1})	0.210(19)	0.414
Effective moment, μ_{eff}, (μ_{BM})	1.30(6)	1.819
Curie-Weiss temperature, T_{CW}, (K)	-109(13)	-224.4(2.1)
TIP, χ_0, (emu mol^{-1})	0.00069(3)	0.000413(5)
R^2	0.9971	0.9948

Once again the sample (Y_{Rb}) was subject to magnetic moment vs. field measurements between ± 10000 Oe at 1.8 K. These show a hysteresis which was not observed in the powder case (Figure 3.24). This, along with the antiferromagnetic interactions, suggests that there is some low temperature spin freezing. The difference in the ZFC and FC data at low temperature (< 10 K) supports this.

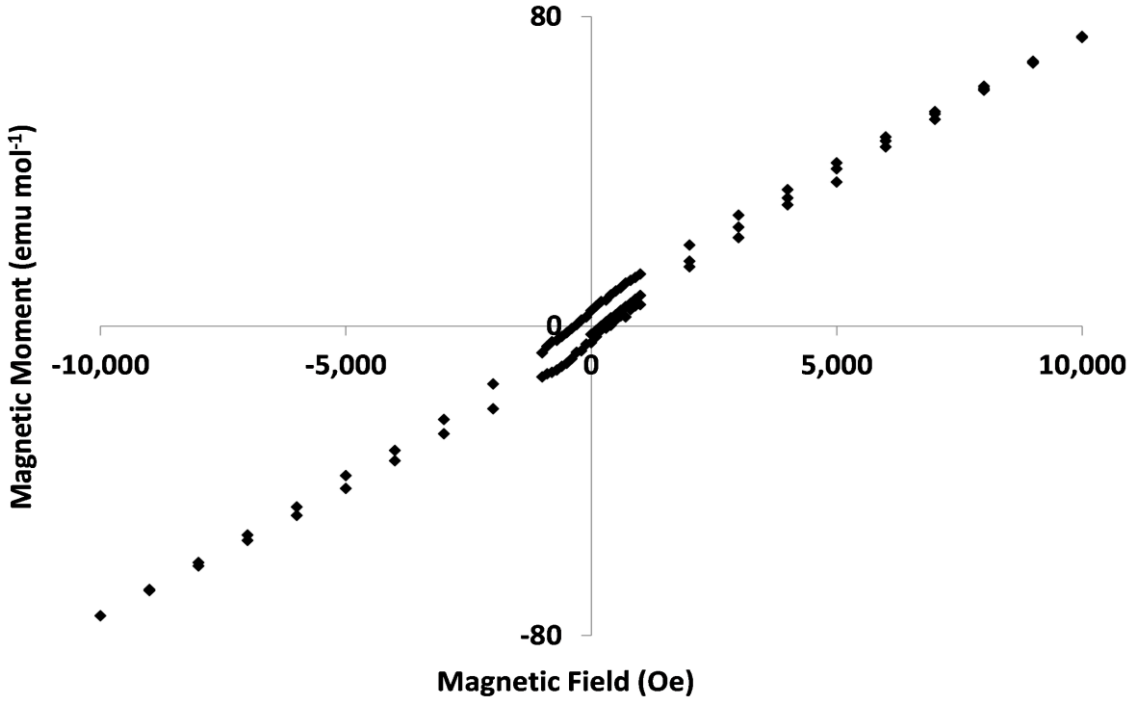

Figure 3.24: Magnetic moment vs. field measurements for $Rb_2TiCu_3F_{12}$ single crystals (Y_{Rb}) at 1.8 K. Measurements performed at the University of Edinburgh.

3.6 Conclusions

$Cs_2TiCu_3F_{12}$ crystallises in a rhombohedral space group ($R\bar{3}m$) at room temperature as expected by comparison to its sister phases $Cs_2SnCu_3F_{12}$ and $Cs_2ZrCu_3F_{12}$. On reducing temperature it is found that the powder undergoes a phase transition into a primitive space group ($P2_1/n$) which is possibly motivated by the Ti^{4+} and Cs^+ cations' need to adopt a BVS which is closer to the 4 and 1 expected. This phase transition is not observed in the single crystal however; in this case it is found that the unit cell doubles in the *a* and *b* parameter and has a closer resemblance to the cell found for $Rb_2SnCu_3F_{12}$. $Cs_2TiCu_3F_{12}$ does not show the disorder that has been previously reported for $Rb_2SnCu_3F_{12}$, however. It is suggested that the difference in phase transitions is related to the crystallite size under study. $Rb_2TiCu_3F_{12}$ appears as a much more complex unit cell at room temperature – the triclinic cell has $P\bar{1}$ symmetry and 38 unique atoms. This hampers the refinement of atomic coordinates and the detailed structural description of the system but it is possible that $Rb_2TiCu_3F_{12}$ adopts a higher symmetry structure between 320 and 350 K. Unfortunately, the synthesis of diffraction quality single crystals was not possible and so not part of this study. Magnetically both systems appear to be quite complex. $Cs_2TiCu_3F_{12}$ is found to have strong antiferromagnetic interactions in the powder form and possibly spin freezing at lower temperatures but the single crystal is harder to analyse; a large TIP prevents any quantitative data being extracted but low temperature divergences suggest – more definitely than in the powder case – that some spin freezing occurs. $Rb_2TiCu_3F_{12}$ powder magnetic measurements suggest that there are antiferromagnetic interactions in the sample much like $Cs_2TiCu_3F_{12}$. There is also no evidence of a hysteresis in magnetic moment vs. field measurements at low temperature suggesting that no positive ordering or spin freezing occurs. The single crystal case also shows TIP but to a

far lower degree than $Cs_2TiCu_3F_{12}$. Due to this it is possible to extract some quantitative values but their reliability is questionable. At low temperature there is also a hysteresis in magnetic moment vs. field measurements which suggests the presence of spin ordering which is not seen at the same temperature in the powder.

Further work on these compounds should take the form of further magnetic study of magnetically pure samples and also possibly heat capacity measurements. In case of $Rb_2TiCu_3F_{12}$ obtaining a diffraction quality single crystal would be advantageous. These steps would allow the magnetic properties to be established more exactly and a greater comparison made between powder and single crystal properties.

1. R. D. Shannon, *Acta Crystallogr., Sect. A: Found Crystallogr.*, 1976, **32**, 751-767.
2. S. A. Reisinger, C. C. Tang, S. P. Thompson, F. D. Morrison and P. Lightfoot, *Chem. Mater.*, 2011, **23**, 4234-4240.
3. D. W. Aldous, University of St Andrews, 2008.
4. S. P. Thompson, J. E. Parker, J. Potter, T. P. Hill, A. Birt, T. M. Cobb, F. Yuan and C. C. Tang, *Rev. Sci. Instrum.*, 2009, **80**, 075107.
5. A. C. Larson and R. L. Von Dreele, 2000.
6. B. H. Toby, *J. Appl. Cryst.*, 2001, **34**, 210-213.
7. G. M. Sheldrick, *Acta Crystallogr., Sect. A: Found. Crystallogr.*, 2008, **64**, 112-122.
8. L. J. Farrugia, *J. Appl. Crystallogr.*, 2012, **45**, 849-854.
9. T. Ono, K. Morita, M. Yano, H. Tanaka, K. Fujii, H. Uekusa, Y. Narumi and K. Kindo, *Phys. Rev. B*, 2009, **79**, 174407.
10. P. W. Stephens, *J. Appl. Crystallogr.*, 1999, **32**, 281-289.
11. A. Boultif and D. Louer, *J. Appl. Crystallogr.*, 1991, **24**, 987-993.
12. B. J. Campbell, H. T. Stokes, D. E. Tanner and D. M. Hatch, *J. Appl. Crystallogr.*, 2006, **39**, 607-614.
13. H. Bialowons, M. Muller and B. G. Muller, *Z. Anorg. Allg. Chem.*, 1995, **621**, 1227-1231.
14. M. P. Crosnier and J. L. Fourquet, *Eur. J. Solid State Inorg. Chem.*, 1992, **29**, 199-206.
15. A. S. Wills, Program available from www.ccp14.ac.uk edn.
16. K. Morita, M. Yano, T. Ono, H. Tanaka, K. Fujii, H. Uekusa, Y. Narumi and K. Kindo, *J. Phys. Soc. Jpn.*, 2008, **77**, 043707.
17. H. Z. Zhang and J. F. Banfield, *J. Mater. Chem.*, 1998, **8**, 2073-2076.
18. S. H. Tolbert and A. P. Alivisatos, *Science*, 1994, **265**, 373-376.
19. J. M. McHale, A. Auroux, A. J. Perrotta and A. Navrotsky, *Science*, 1997, **277**, 788-791.
20. I. Ardelean, M. Peteanu, E. Burzo, F. Ciorcas and S. Filip, *Solid State Commun.*, 1996, **98**, 351-355.
21. O. Kondo, M. Ono, E. Sugiura, K. Sugiyama and M. Date, *J. Phys. Soc. Jpn.*, 1988, **57**, 3293-3296.
22. T. Chatterji and T. C. Hansen, *J. Phys. Condens. Matter*, 2011, **23**, 276007.
23. T. Benkert and K. Franke, 0.2.4 edn., 2010.

4 Studies of $Rb_2SnCu_3F_{12}$ – a kagome compound with a re-entrant structural phase transition

$Rb_2SnCu_3F_{12}$ has been previously synthesised [1] and reported to undergo only one phase transition between 1.8 and 300 K, at ~ 215 K, for which no structure or mechanism has been reported.[2] It is reported to be related to the $Cs_2MCu_3F_{12}$ family (M = Sn, Zr, Hf) but with a unit cell which is doubled in the *a* and *b* directions (Figure 4.1) and so not a perfect kagome lattice at room temperature.[3] It has also been shown to undergo no magnetic ordering down to 1.8 K and instead adopts a "pinwheel" valence bond solid (VBS) ground state. The adoption of this state is related to the structure being a non-perfect kagome lattice [2] (Figure 4.2).

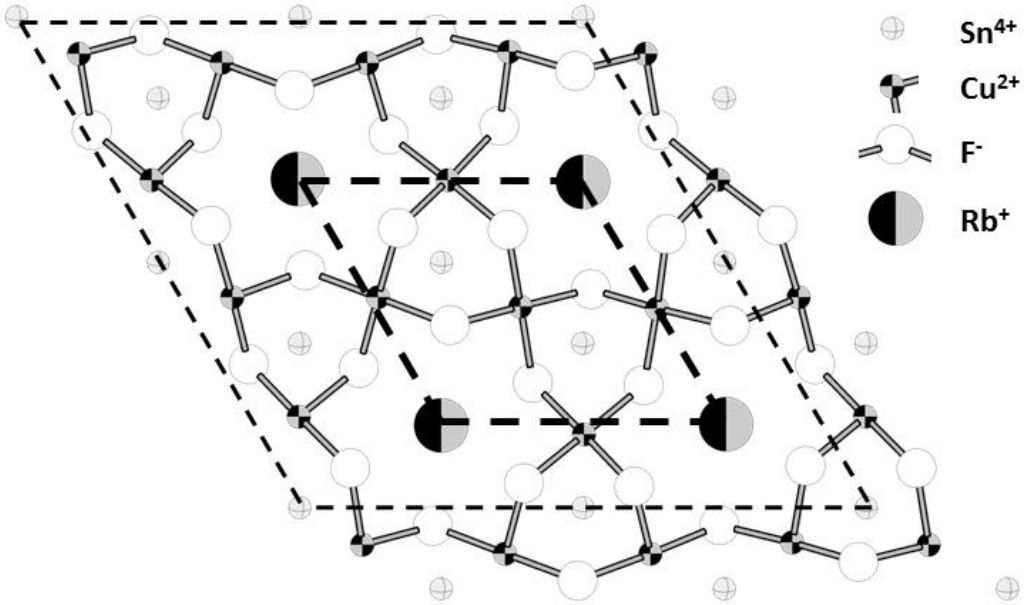

Figure 4.1: Unit cell of $A_2MCu_2F_{12}$ looking down the *c*-axis. Thick dashed line (smaller cell) is that found for $Cs_2SnCu_3F_{12}$ and $Cs_2ZrCu_3F_{12}$; thinner dashed line (larger cell) is that found for $Rb_2SnCu_3F_{12}$ at room temperature.

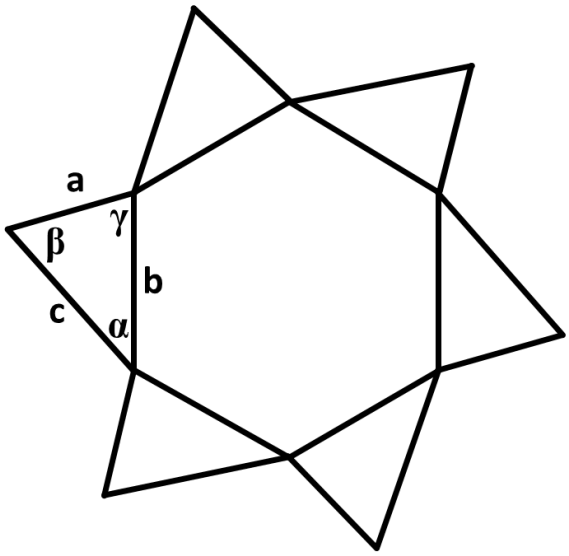

Figure 4.2: "Pinwheel" kagome structure (exaggerated for clarity) reported for $Rb_2SnCu_3F_{12}$. At room temperature the angle within the triangle can vary by ~ 4 ° (α ≈ 56.3 °, β ≈ 61.2 °, γ ≈ 62.6 °) and the Cu – Cu bond distances can vary by ~ 0.2 Å (a ≈ 3.35 Å, b ≈ 3.53 Å, c ≈ 3.58 Å)

The adoption and explanation of this VBS state therefore assumes no major structural deformations of the kagome lattice occur down to 1.8 K. This would be surprising given the other members of this family, all of which show phase transitions that largely affect the symmetry of the kagome lattice in the range 100 – 300 K.[3] For this reason it was decided to investigate $Rb_2SnCu_3F_{12}$ further in order to check for unreported phase transitions.

4.1 Experimental

The synthesis of $Rb_2SnCu_3F_{12}$ has been previously reported [1] and small changes were made in order to make the best use of available equipment and to synthesise a powder sample.

4.1.1 Synthesis of $Rb_2SnCu_3F_{12}$

RbF (Sigma Aldrich 99.8 %) and SnF_4 (Sigma Aldrich) were dried by heating at 390 K under a vacuum of ~ 10^{-4} mbar for 24 hours. They were then mixed and ground with CuF_2 (Sigma Aldrich, 98 %) under argon in the molar ratio 2:1:3 ($RbF:SnF_4:CuF_2$) for powders and 3:2:3 for single crystals. The resulting mixtures were then sealed in a gold tube before heating under flowing argon. The heating conditions also differed depending on the desired morphology; for powders the furnace was heated to 873 K at 10 K min^{-1} and held at that temperature for twelve hours before cooling at the same rate. For single crystals the furnace was heated at a rate of 10 K min^{-1} to 1073 K before cooling at ~ 3 K hr^{-1} to 823 K and then further cooling at 10 K min^{-1}. In both cases pure samples were never realised with notable impurities being Rb_2SnF_6 (~ 15 – 20 %), CuO and $RbCuF_4$ (< 5 %). Single crystals of the size previously reported (5 × 5 × 0.5 mm) were also not realised; a better description would be 0.2 × 0.2 × 0.05 mm colourless plates. It is suggested that small amounts of retained water in the starting materials may be the cause of the impurities and also the small size of the crystals.

4.1.2 Analysis techniques

Laboratory based X-ray powder diffraction (XRPD) for the purpose of phase identification was performed on a PANalytical Empyrean X-ray diffractometer using Cu $K_{\alpha 1}$ radiation and operating in either Bragg-Brentano or transmission geometry.

Synchrotron X-ray powder diffraction (SXPD) was performed at beamline I11, Diamond Light Source Ltd., Oxfordshire.[4] This utilised glass capillaries and operated in Debye-Scherrer mode typically with radiation of $\lambda \approx 0.82$ Å (predetermined using a known standard). A multi-analysing crystal (MAC) based detector was used in order to collect the highest resolution data possible. In the first SXPD experiment the sample was measured at 300 K before being cooled to 100 K and patterns taken at 30 K steps to 490 K before a final pattern was recorded at 500K. In the second SXPD experiment the sample was cooled from 300 – 165 K and patterns recorded every 15 K. The sample was then heated from 165 – 300 K and patterns recorded at the same increments. On reaching the required temperature a brief period (5 – 10 minutes) was employed in order ensure that the sample was equilibrated appropriately.

Neutron powder diffraction (NPD) was performed at beamline HRPD (High resolution powder diffraction), ISIS pulsed neutron and muon source, Oxfordshire. Samples of ~ 5 g were mounted in 5mm vanadium flat-plate cans before loading into the diffractometer, which was

fitted with a cryostat. Patterns were collected at 300, 220, 150 and 25 K. The determination of structural parameters proved challenging due to the number of impurities and significant background scattering from the sample environment, which could be described by austenite.

Rietveld refinement was performed using GSAS [5] and the EXPGUI interface.[6] This analysis sought to fit lattice parameters, phase fractions, peak profile shape (both Gaussian and Lorentzian) and thermal parameters (grouped by atom type). The analysis included impurities but grouped the thermal parameters for each atom in the phase together.

Single crystal X-ray diffraction (SCXD) was performed with a Bruker Apex-II diffractometer and an Agilent SuperNova diffractometer using Mo $K_{\alpha 1}$ radiation.[a] The model was solved using Shelxs-97 [7] and the WinGX [8] add-on. Single crystal data collection was performed at 300, 245, 230, 220 and 140 K using an Oxford Cryosystems cooler.

4.2 SXPD studies of $Rb_2SnCu_3F_{12}$

At 300 K, $Rb_2SnCu_3F_{12}$ appears in the doubled *a* and *b* rhombohedral unit cell, $R\bar{3}$, which has been previously described [1] (in this case *a* = 13.90210(4) Å, *c* = 20.34514(10) Å). This is evidenced by clear superstructure peaks which are not found in the standard unit cell for $Cs_2MCu_3F_{12}$ (M = Sn, Zr, Hf) ($R\bar{3}m$) shown in Figure 4.3. The crystallite size can be derived from peak widths as approximately 2132 Å.[b]

Previous structural reports have suggested a fluorine disorder around the TiF_6 octahedra [1]; from the SXPD data it was difficult to confirm or deny this as the difference between model patterns is minor. This was exacerbated due to no attempt being made to refine the structural parameters; for the $R\bar{3}$ case there are a significant number of refinable structural parameters (34 omitting any disorder). Refinement may not reliably be achieved taking into account the purity of the samples (60 – 75 %). For clarity, all models used for the powder data utilised the previously reported model, containing the disorder.[1]

On heating ("run 1" [c]), $Rb_2SnCu_3F_{12}$ retains $R\bar{3}$ symmetry up to the highest temperature measured, 500 K. To a degree, there is a linear increase in unit cell volume between 300 and 500 K which supports the assertion that there are no phase changes or transitions in this region. Deviations from a linear trend are at a maximum of 0.5 $Å^3$ (with the trend suggesting an increase of 0.2771 $Å^3\ K^{-1}$) which could be accounted for by errors in temperature setting or lagging thermal equilibrium. Disagreeing with this, however, is the trend of the *a* and *c* lattice parameters. In these there is a change at ~ 370 K where the gradient of change starts to increase for *a* and decrease for *c* (Figure 4.4). Also of note is the large relative change of *c* compared to the *ab*-plane. This is expected as there is less freedom in the *ab*-plane due to the linking of the copper fluoride kagome lattice.

[a] Performed at the University of Edinburgh in collaboration with Prof. S. Parsons.
[b] Derived from an average of the peaks (003), (20-1) and (202) using the Scherrer formula.
[c] All SXPD Rietveld refinements are available in appendix A.4.2

On cooling we first see a deviation from the $R\bar{3}$ symmetry at ~ 250 K. Initially, attempts were made to model this pattern using a monoclinic model, like that derived for $Cs_2ZrCu_3F_{12}$ [9] but this failed to index some key peaks and splittings and is not a direct distortion of the doubled rhombohedral $R\bar{3}$ unit cell. Further investigation using the ISODISTORT program [10] allowed the suggestion of a unit cell with triclinic symmetry (specifically $P\bar{1}$) which is related to the $R\bar{3}$ unit cell by the matrix:

$$\begin{bmatrix} 2/3 & 1/3 & 1/3 \\ -1/3 & 1/3 & 1/3 \\ -1/3 & -2/3 & 1/3 \end{bmatrix}$$

At 250 K *a* = 10.49567(13) Å, *b* = 10.47100(10) Å, *c* = 10.50961(12) Å, α = 82.7888(10) °, β = 83.1582(7) °, γ = 82.7769(10) ° (using the primitive setting of the rhombohedral cell, *a* =*b* =*c* and α = β = γ). The triclinic model derived is reported in Table 4.1.

In the triclinic case it also proved unfeasible to refine the atomic coordinates reliably and for this reason no attempt has been made to define an accurate structural model using the SXPD data alone. It is also found that above 250 K (up to approximately 310 K) there is evidence for both the triclinic and rhombohedral phases being present simultaneously. This suggests that the phase transition is first order.

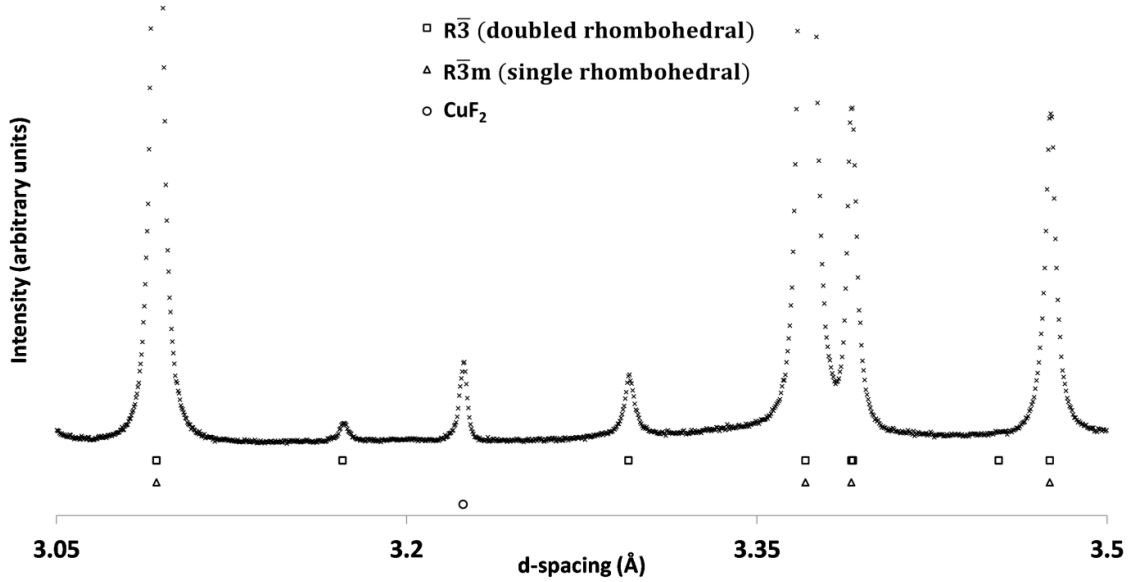

Figure 4.3: SXPD pattern of $Rb_2SnCu_3F_{12}$ at 300 K showing allowed reflections for both the $R\bar{3}$ (doubled rhombohedral) and $R\bar{3}m$ ($Cs_2MCu_3F_{12}$-type) unit cells.

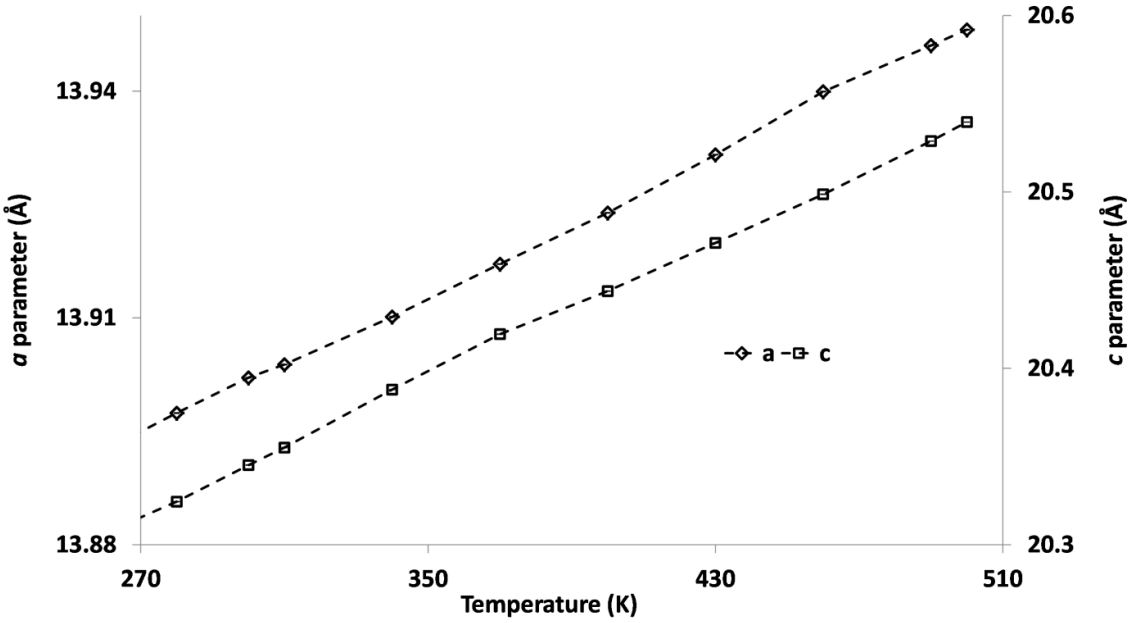

Figure 4.4: *a* and *c* lattice parameters in $Rb_2SnCu_3F_{12}$ between 270 and 500 K derived from SXPD data. Note the scales are not relative.

Table 4.1: Triclinic model used for $Rb_2SnCu_3F_{12}$ powder data refinement; The model is derived from the room temperature $R\bar{3}$ model for $Rb_2SnCu_3F_{12}$ using the ISODISTORT program [10]. The previously reported disorder is retained and no further structural refinement is performed.

Atom	*x*	*y*	*z*	Occupancy
Rb 1	0.3999	0.8933	0.8991	1
Rb 2	0.8991	0.3999	0.8933	1
Rb 3	0.8933	0.8991	0.3999	1
Rb 4	0.6020	0.6020	0.6020	1
Cu 1	0.7628	0.7401	0.0017	1
Cu 2	0.0017	0.7628	0.7401	1
Cu 3	0.7401	0.0017	0.7928	1
Cu 4	0.5285	0.7530	0.2492	1
Cu 5	0.2492	0.5285	0.7530	1
Cu 6	0.7530	0.2492	0.5285	1
Sn 1	½	½	0	1
Sn 2	0	½	½	1
Sn 3	½	0	½	1
Sn 4	0	0	0	1
F 1	0.8195	0.5856	0.1049	1
F 2	0.1049	0.8195	0.5856	1
F 3	0.5856	0.1049	0.8195	1
F 4	0.8848	0.6803	0.8666	1
F 5	0.8666	0.8848	0.6803	1
F 6	0.6803	0.8666	0.8848	1
F 7	0.6686	0.8217	0.1412	1
F 8	0.1412	0.6686	0.8217	1
F 9	0.8217	0.1412	0.6686	1
F 10	0.0633	0.9370	0.8337	1
F 11	0.8337	0.0633	0.9370	1
F 12	0.9370	0.8337	0.0633	1
F 13	0.4004	0.5948	0.8668	1
F 14	0.8668	0.4004	0.5948	1
F 15	0.5948	0.8668	0.4004	1
F 16A	0.5336	0.6644	0.0525	0.773
F 17A	0.0525	0.5336	0.6644	0.773
F 18A	0.6644	0.0525	0.5336	0.773
F 19A	0.6484	0.5084	0.8717	0.773
F 20A	0.8717	0.6484	0.5084	0.773
F 21A	0.5084	0.8717	0.6484	0.773
F 16B	0.4490	0.6518	0.0879	0.227
F 17B	0.0879	0.4490	0.6518	0.227
F 18B	0.6518	0.0879	0.4490	0.227
F 19B	0.6536	0.5724	0.9150	0.227
F 20B	0.9150	0.6536	0.5724	0.227
F 21B	0.5724	0.9150	0.6536	0.227
F 22	0.3928	0.6842	0.3619	1
F 23	0.3619	0.3928	0.6842	1
F 24	0.6842	0.3619	0.3928	1

Further cooling leads to a second phase transition, which begins to become visually apparent at 190 K (Figure 4.5). This phase transition leads to a simplification of the powder pattern; i.e. a large number of splittings have disappeared. This third phase can be well fitted by the $R\bar{3}$ symmetry cell that is found at room temperature (and for clarity will be referred to as the $R\bar{3}$-LT phase).

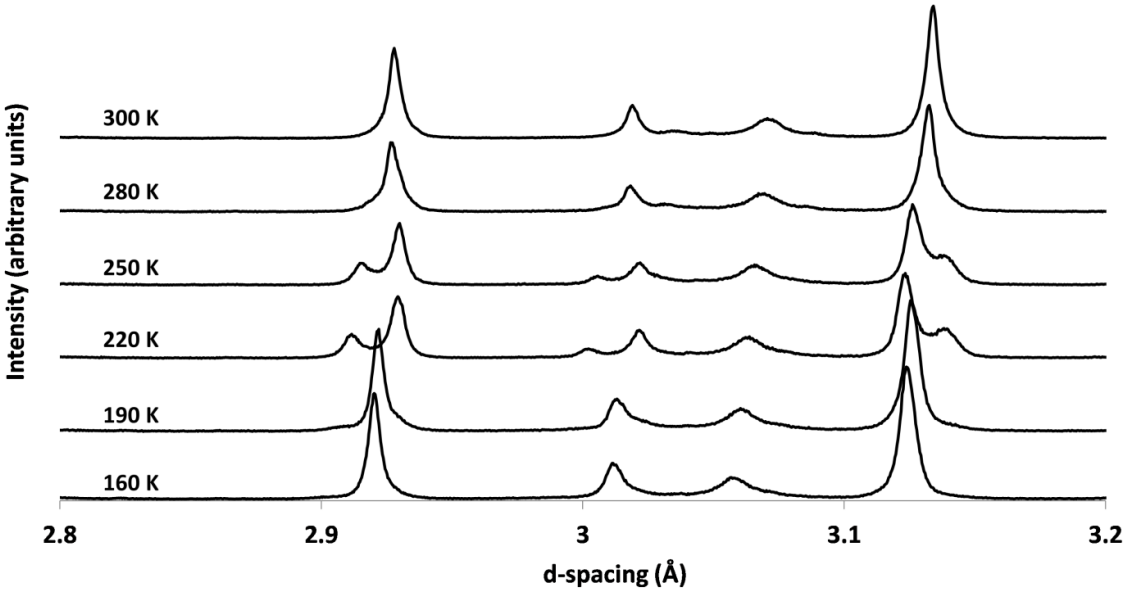

Figure 4.5: SXPD patterns for $Rb_2SnCu_3F_{12}$ at a range of temperatures. Patterns off-set on y-axis for clarity.

This structural re-entrant behaviour is very rare and there are few examples of such phenomena.[11, 12] For this reason the experiment was performed again ("run 2") in order to confirm the observed behaviour, except this time with both heating and cooling cycles. The previous example measured between 100 and 500 K involved a fast cool to 100 K before taking measurements while heating – if the transition to the triclinic phase is sluggish then observation of the rhombohedral phase could be an artefact of the experimental set up. Once again, the triclinic phase was observed without the rhombohedral phase on both heating and cooling between 240 – 255 K and 225 – 240 K, respectively, suggesting that neither the triclinic nor $R\bar{3}$-LT phase is a metastable state. Phase mixing is also observed either side of the triclinic phase in agreement with the previous experiment (Figure 4.6).

This phase mixing shows a small hysteresis for run 2 which reinforces the suggestion of a first order phase transition.[d] Although there is not perfect agreement between run 1 and run 2 (both heating) they do both agree on the temperature region where the sample is uniquely triclinic. The areas of mixed phase may disagree due to the particulars of the heating/cooling rates of each experiment.

[d] Full tables of the relative quantities and the fit quality are available in appendix A.4.2 – these include lattice parameters and cell volumes

Taking account of the temperature range 100 – 300 K the volume change appears mostly linear with a small decrease in gradient with reducing temperature (in this case only run 2 is considered). No hysteresis is apparent but there are some outliers which generally arise from the minority phase. This may indicate that there is an excess stress on the phase or that the exact determination of lattice parameters proves challenging. The latter is supported by the large error bars on these particular data points (Figure 4.7).

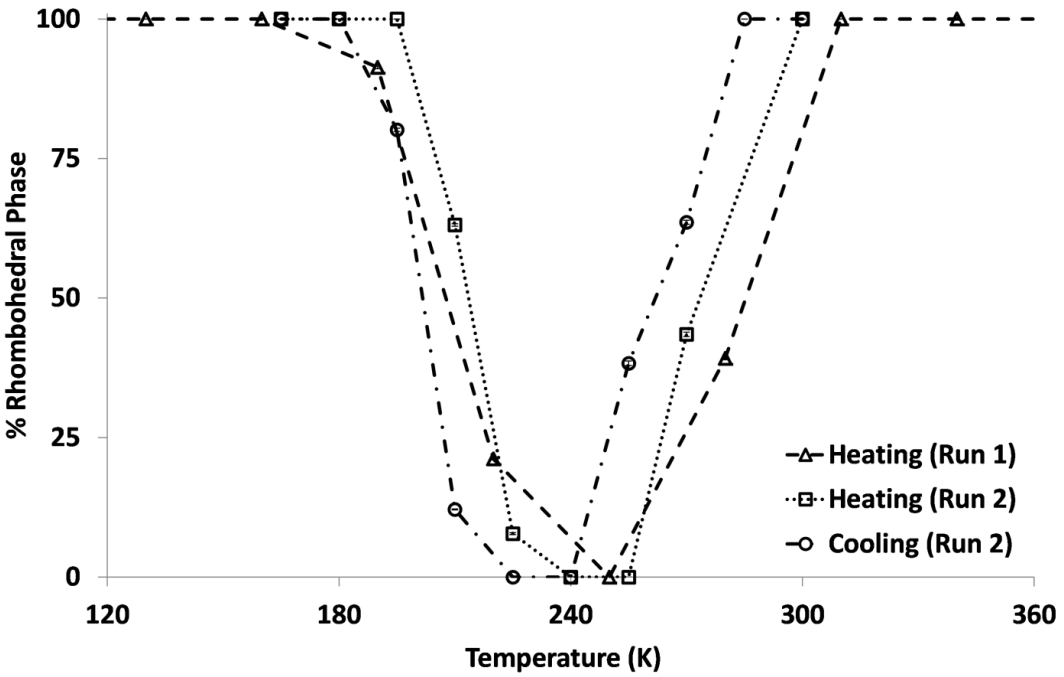

Figure 4.6: Phase weight fractions (x % rhombohedral phase, 100 – x % triclinic phase) for $Rb_2SnCu_3F_{12}$ as a function of temperature as derived from SXPD data. Note the small hysteresis for "run 2".

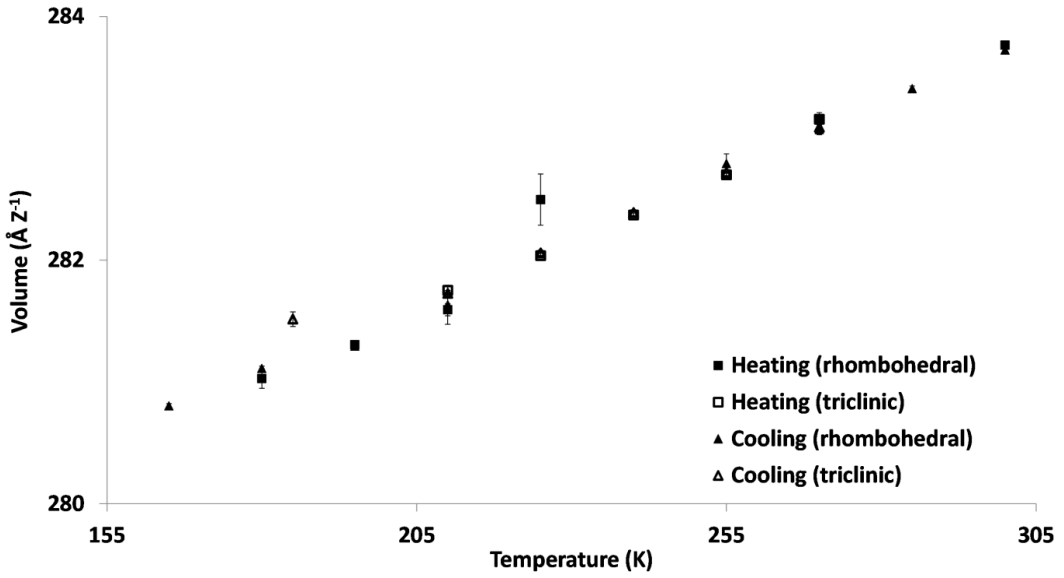

Figure 4.7: Volume per chemical formula unit of $Rb_2SnCu_3F_{12}$ between 165 and 300 K on both heating and cooling as derived from SXPD data.

Qualitatively, as for unit cell volume, the lattice parameters on heating and cooling appear to be similar. Both the triclinic cell lengths and angles diverge quickly with reducing temperature until the sample becomes fully rhombohedral again. Observing the triclinic lattice parameters on cooling there is no indication that the rhombohedral cell will be re-attained, indicating a very sudden (i.e. first order) low temperature transition (Figure 4.8). There is no evidence of the previously reported transition at ~ 215 K.

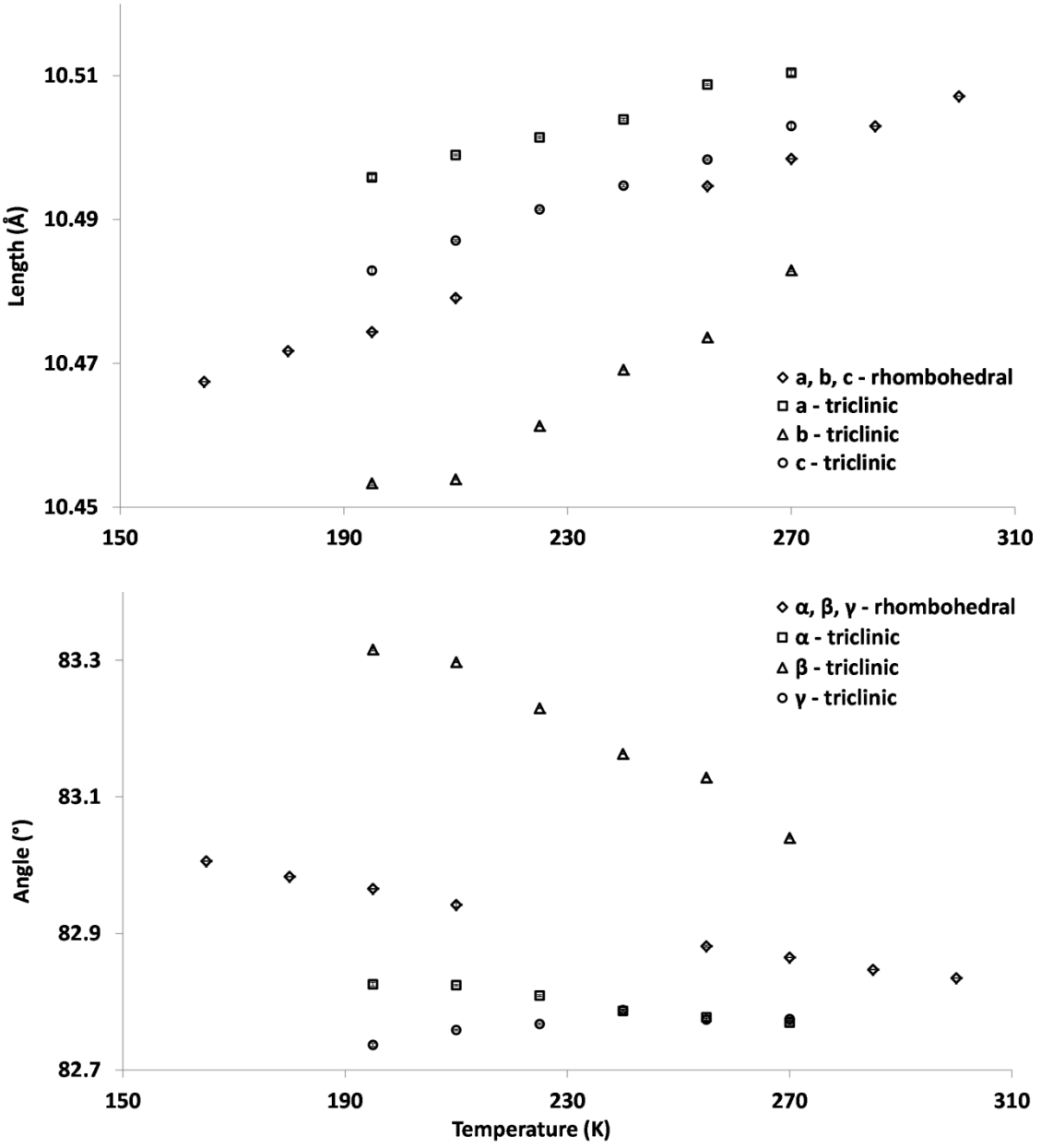

Figure 4.8: Unit cell lengths (top) and angles (bottom) for $Rb_2SnCu_3F_{12}$ on cooling from 300 to 165 K as derived from SXPD data. Note that for a number of temperatures both phases are present and in those cases the data for both phases are reported.

4.3 NPD Studies of $Rb_2SnCu_3F_{12}$

NPD studies of $Rb_2SnCu_3F_{12}$ were undertaken in order to gain further insight into the changing structural parameters. Unfortunately, this proved to be of limited use due to a large number of impurities present within the sample (Table 4.2) and a prominent sample environment background which could be modelled as austenite (as a Le Bail fit, since the exact austenite composition is unknown, Figure 4.9).[e, f]

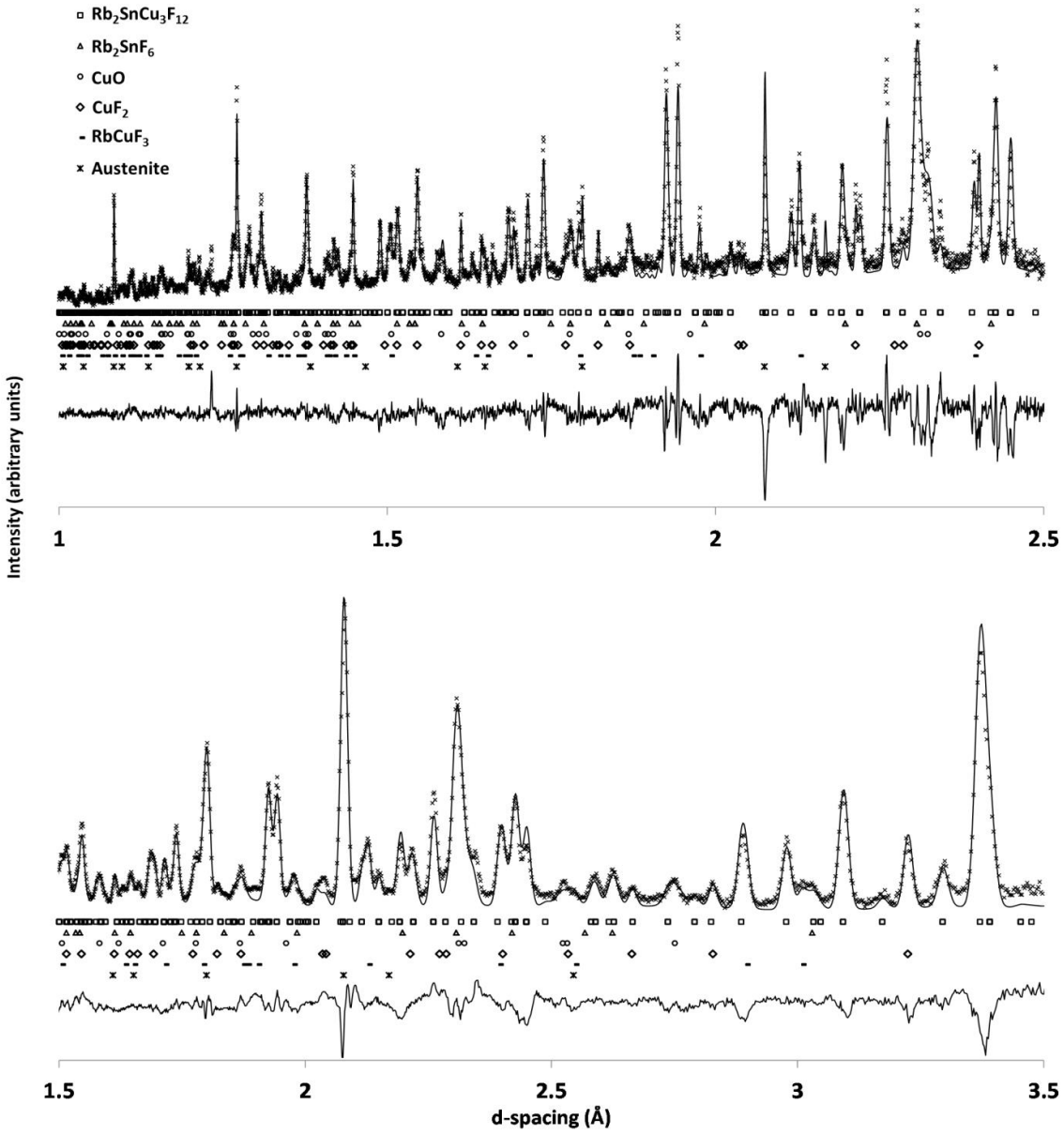

Figure 4.9: NPD Rietveld refinements for $Rb_2SnCu_3F_{12}$ in the $R\bar{3}$ model at 300 K; backscattering detector bank (top) and 90 ° detector bank (bottom). Note the large number of materials present.

[e] Rietveld refinements can be found in appendix A.4.3.
[f] Tables of lattice parameters and fit qualities are included in appendix A.4.3.

Table 4.2: Phases and their weight % present within the sample used for NPD diffraction. Data derived from NPD data using the GSAS program.[5]

Phase	% weight present
$Rb_2SnCu_3F_{12}$	58.7
Rb_2SnF_6	18.7
CuO	8.7
CuF_2	6.3
$RbCuF_3$	7.6

Some conclusions can be derived from the NPD data, however. There is an impurity-free area between a d-spacing of 1.9 and 1.95 Å, which has suitably high resolution to observe a peak splitting on the reduction of symmetry. From this we can see that at 300 and 150 K, $Rb_2SnCu_3F_{12}$ is found in the $R\bar{3}$ symmetry unit cell and at 220 K the peaks are split and well fitted by the $P\bar{1}$ model (Figure 4.10).

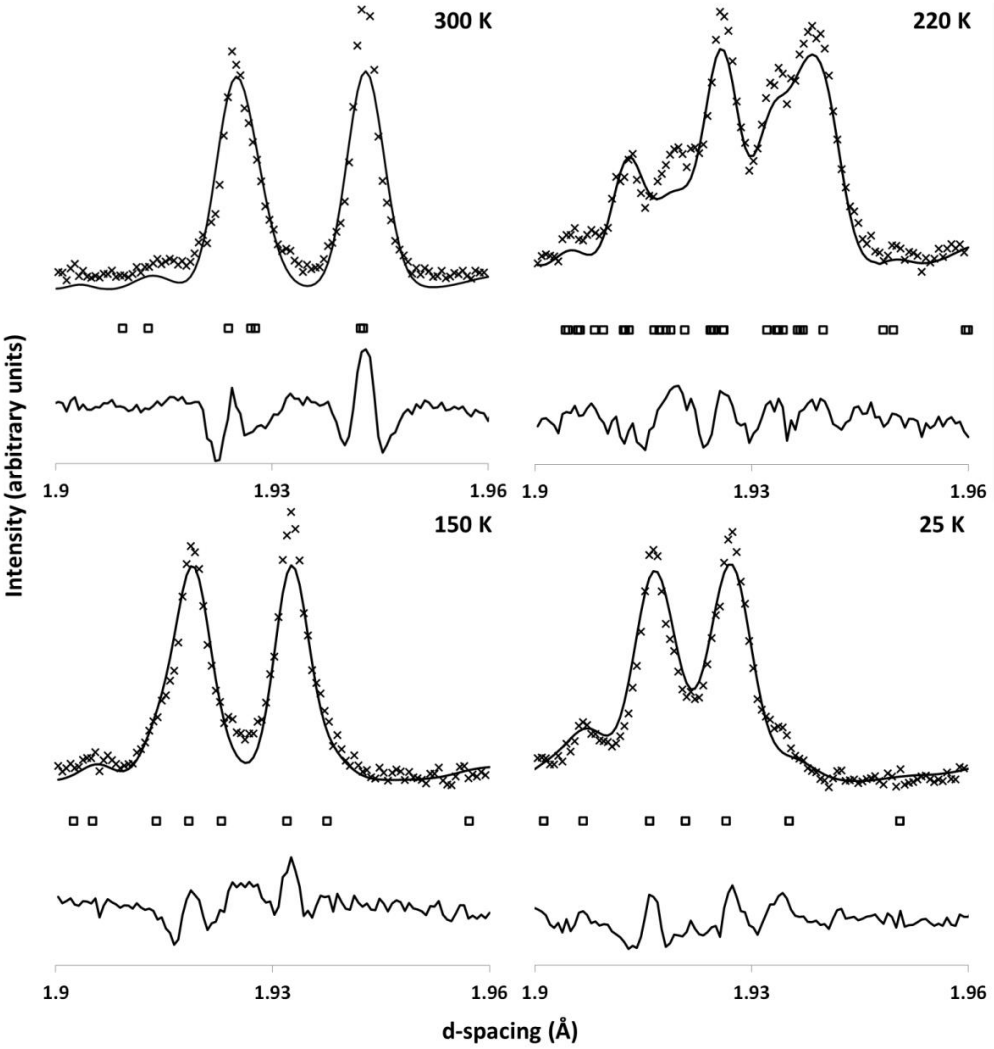

Figure 4.10: NPD Rietveld refinements for $Rb_2SnCu_3F_{12}$ at 300, 220, 150 and 25 K. Note that no atomic coordinates have been refined. For the 220 K data set the $P\bar{1}$ model has been used, for the others the $R\bar{3}$ model was chosen.

The lattice parameters derived from the NPD and SXPD data also agree well (Table 4.3). The lowest temperature attained for the sample during NPD data collection was 25 K. Analysis at this temperature suggests that $Rb_2SnCu_3F_{12}$ is still best described by the $R\bar{3}$ model (Figure 4.10). Due to the number of impurities it is hard to be drawn on the conclusion that there is a further transition at 215 K.[2] It is suggested that this transition is not apparent in the powder samples at this temperature.

Table 4.3: Lattice parameters for $Rb_2SnCu_3F_{12}$ derived from both SXPD and NPD data over a range of temperatures.

T (K)		a (Å)	b (Å)	c (Å)
300	NPD	13.9009(4)	= a	20.3415(9)
	SXPD	13.90210(4)	= a	20.34514(10)
220	NPD	10.4850(10)	10.4506(6)	10.5025(10)
	SXPD [g]	10.48901(11)	10.45747(10)	10.50346(11)
150	NPD	13.8664(3)	= a	20.1928(8)
160	SXPD	13.86966(5)	= a	20.21848(12)
		α (°)	β (°)	γ (°)
300	NPD	90	90	120
	SXPD	90	90	120
220	NPD	87.746(7)	83.319(4)	82.829(7)
	SXPD [f]	82.7510(9)	83.2737(8)	82.8137(9)
150	NPD	90	90	120
160	SXPD	90	90	120

[g] The SXPD data suggests the presence of both triclinic and rhombohedral phases at this temperature, whereas the NPD data suggests triclinic only.

4.4 Single crystal studies of $Rb_2SnCu_3F_{12}$

Single crystal studies were performed in order to derive a full structural model for the triclinic phase. A single crystal was first examined at 300 K in order to compare with the powder data and the previously reported structure. Similar lattice parameters were recorded as well as atomic coordinates (Table 4.4).

Table 4.4: Lattice parameters and fractional atomic coordinates at 300 K for $Rb_2SnCu_3F_{12}$ for both the synthesised single crystal and previously reported single crystal ($R\bar{3}$ model).

	$Rb_2SnCu_3F_{12}$ (SCXD)			$Rb_2SnCu_3F_{12}$ [1]		
a (Å)	13.9053(13)			13.917(2)		
c (Å)	20.333(3)			20.356(3)		
	x	y	z	x	y	z
Rb1	$^2/_3$	$^1/_3$	-0.06466(6)	$^2/_3$	$^1/_3$	-0.0647(1)
Rb2	0.33565(5)	0.16501(4)	0.06410(3)	0.3358(1)	0.1650(1)	0.0641(1)
Sn1	$^1/_2$	0	0	$^1/_2$	0	0
Sn2	$^2/_3$	$^1/_3$	$^1/_3$	$^2/_3$	$^1/_3$	$^1/_3$
Cu1	0.59463(5)	0.16666(6)	0.16812(3)	0.5946(1)	0.1665(1)	0.1682(1)
Cu2	0.35126(4)	-0.07249(5)	0.17680(2)	0.3516(1)	-0.0723(1)	0.1769(1)
F1	0.6494(2)	0.0649(3)	0.16987(12)	0.6495(02)	0.0651(2)	0.1700(1)
F2	0.7403(3)	0.2773(3)	0.14372(15)	0.7409(2)	0.2773(2)	0.1439(1)
F3	0.4576(3)	0.0691(3)	0.21000(15)	0.4581(2)	0.0693(2)	0.2105(1)
F4	0.7854(3)	0.4442(3)	0.27882(14)	0.7853(2)	0.4443(2)	0.2780(1)
F5	0.4457(3)	0.0856(3)	-0.04645(14)	0.4464(3)	0.0872(3)	-0.0460(1)
F6A	0.4519(4)	0.0319(4)	0.08386(19)	0.4501(4)	0.0310(4)	0.0835(2)
F7A	0.6415(4)	0.1376(4)	0.0071(3)	0.6389(3)	0.1378(3)	0.0095(3)
F6B	0.3889(10)	-0.0184(10)	0.0655(5)	0.3861(11)	-0.0250(11)	0.0629(6)
F7B	0.6132(10)	0.1333(10)	0.0444(6)	0.6066(10)	0.1320(10)	0.0470(6)
F8	0.2463(3)	-0.2158(3)	0.14646(15)	0.2465(2)	-0.2156(2)	0.1462(1)

In this case the disorder between the F6A/B and F7A/B is refined to be 0.688(8)/0.312(8) compared to the 0.773(8)/0.227(8) previously reported. There is also an element of twinning which is taken into account using the twin law (0, 1, 0),(1, 0, 0),(0, 0, -1). This leads to a high quality fit (R1 = 2.87 %, wR2 = 6.64 %) [h].

In order to observe the rhombohedral – triclinic transition the crystal was cooled to 245 K. No transition is observed and the crystal is fully indexed in the $R\bar{3}$ symmetry unit cell found at 300 K. The fit was found to be of high quality (R1 = 3.49 %, wR2 = 9.08 %) and to still be best described using the disordered model. The refined disorder is also found to match well with that found at room temperature (FXA/B 0.690(12)/0.310(12)), although the fitting statistics are better at room temperature suggesting that there is possibly an approach to a transition.

[h] All CIF are present in appendix A.4.4

The same crystal was then further cooled and examined at 140 K in order to compare to the room temperature phase. Previous reports [2] suggest that at this temperature the *a* and *b* parameters of the lattice should be further doubled (to $a \approx 27.7$, $c \approx 20.2$). When refining against the $R\bar{3}$ model the data appears to be well fitted (R1 = 5.64 %, wR2 = 11.33 %) but closer inspection shows that some ellipsoids are physically unreasonable. This may be indicative of the incorrect space group or cell being used. Integrating the data within the bigger unit cell allows us to assess the superstructure peaks which would be required for the $a \approx 27.7$, $c \approx 20.2$ unit cell. This shows that there are possibly peaks present but they are very weak, as previously suggested – the largest superstructure peak (-3, -2, 10) is found to be ~ 1 % of the intensity of the most intense *hk0* = 2n peak (-8, 16, 0). This suggests that any change in structure is small and indeed was deemed to be negligible in previous theoretical magnetic modelling calculations [2].

In order to confirm that the single crystal did not undergo the rhombohedral – triclinic transition a second crystal was picked and subject to a more rigorous investigation between 220 and 245 K. Firstly the crystal was cooled from RT to 220 K and measured. It was then reheated to 300 K before re-cooling to 230 K and then re-measuring. The crystal was then heated to 245 K before measuring for a third time. In all cases the diffraction pattern was found to be well indexed and modelled by the $R\bar{3}$ symmetry unit cell (Table 4.5). The F^- disorder was also apparent at all three temperatures. Although the fit statistics are comparatively high, this may be due to the morphology of the crystal. In no case was the crystal indexable in the triclinic cell indicating that the single crystal does not undergo the rhombohedral – triclinic transition.

Table 4.5: Lattice parameters and R values for $Rb_2SnCu_3F_{12}$ at various temperatures derived from single crystal refinements at a range of temperatures.

Temperature (K)	*a* (Å)	*c* (Å)	R1 (%)	wR2 (%)
220	13.8783(8)	20.2283(15)	4.79	8.73
230	13.8771(8)	20.2392(13)	4.70	9.64
245	13.8749(10)	20.2458(14)	5.15	11.01

Table 4.6: Single crystal data and refinement details for $Rb_2SnCu_3F_{12}$ at 300, 245 and 140 K (on cooling).

	300 K	245 K	140 K
Formula	$Rb_2SnCu_3F_{12}$		
crystal system	Rhombohedral		
space group	$R\bar{3}$		
a	13.9053(13)	13.8940(4)	13.8636(4)
c	20.333(3)	20.2723(7)	20.1758(4)
volume (Å^3)	3404.8(7)	3389.13(18)	3358.25(14)
Z	12		
wavelength (Å)	0.71073		
ρ (calc.) (g cm^{-3})	4.145	4.162	4.203
absorption coefficient (mm^{-1})	16.337	16.453	16.604
crystal size (mm)	0.19 x 0.10 x 0.04		
θ range for data collection (°)	1.97 – 29.96	1.97 – 28.63	1.97 – 29.99
reflections collected	19473	13075	17879
independent reflections	2191	1839	2156
max./min. transmission	1/0.387	1/0.433	1/0.473
data/restraints/parameters	2191/0/112	1839/0/112	2156/0/111
goodness-of-fit on F^2	1.030	1.080	1.200
R indices [$I > 2\sigma(I)$], *R*1, *wR*2	0.0287, 0.0644	0.0349, 0.0908	0.0580, 0.1170
R indices (all data), *R*1, *wR*2	0.0434, 0.0736	0.0443, 0.0948	0.0656, 0.1200
largest diff. peak/hole (e Å^{-3})	1.177/-1.001	1.049/-0.819	1.663/-2.525

Table 4.7: Single crystal data and refinement details for $Rb_2SnCu_3F_{12}$ at 220, 230 (after re-heating to 300 K) and 245 K (on heating).

	220 K	230 K	245 K
Formula	$Rb_2SnCu_3F_{12}$		
crystal system	Rhombohedral		
space group	$R\bar{3}$		
a	13.8783(8)	13.8771(8)	13.8749(10)
c	20.2283(15)	20.2392(13)	20.2458(14)
volume (Å^3)	3374.1(4)	3375.4(4)	3375.4(4)
Z	12		
wavelength (Å)	0.71073		
ρ (calc.) (g cm^{-3})	4.183	4.181	4.181
absorption coefficient (mm^{-1})	16.526	16.520	16.520
crystal size (mm)	0.543 x 0.292 x 0.056		
θ range for data collection (°)	3.02 – 28.57	3.02 – 28.50	3.02 – 28.86
reflections collected	5938	5893	5911
independent reflections	1707	1705	1679
max./min. transmission	0.343/0.023	0.309/0.028	0.397/0.026
data/restraints/parameters	1707/0/112	1705/0/112	1679/0/112
goodness-of-fit on F^2	1.030	1.168	1.124
R indices [$I > 2\sigma(I)$], *R*1, *wR*2	0.0479, 0.0873	0.0470, 0.0964	0.0515, 0.1101
R indices (all data), *R*1, *wR*2	0.0617, 0.0914	0.0592, 0.1014	0.0707, 0.1189
largest diff. peak/hole (e Å^{-3})	1.205/-1.193	1.017/-1.013	1.092/-1.503

4.5 Structurally re-entrant transitions

There are only four other reported structurally re-entrant transitions:

- Malononitrile, $CH_2(CN)_2$, is a molecular system which shows $P2_1/n \rightarrow P\bar{1} \rightarrow P2_1/n$ phase transitions at 141 and 295 K; a sequence which is suggested to originate from spontaneous strain and molecular rotations.[12]
- Rochelle salt, $NaKC_4H_4O_6 \cdot 4H_2O$, shows a $P2_12_12 \rightarrow P2_1 \rightarrow P2_12_12$ transitions with the intermediate phase being ferroelectric. It is suggested that this transition is a second order as well as an order-disorder transition.[13]
- Li_2TiO_3 which goes from $Fm\bar{3} \rightarrow$ C2/c $\rightarrow Fm\bar{3}$ at 573 K and 1428 K in a first-order cation order-disorder transition.[14]
- $BaFe_2(PO_4)_2$ is the transitions $R\bar{3} \rightarrow P\bar{1} \rightarrow R\bar{3}$ at 140 and 75 K, respectively. In this case it is suggested to be driven by competing forces between Jahn-Teller distortions and uniaxial magnetism.[11]

The above systems appear to have little in common with each other and also with the phase of interest, $Rb_2SnCu_3F_{12}$. The closest circumstance, $BaFe_2(PO_4)_2$, shows a very similar type of transition, going between the same group – subgroup relationships. In our case, however, there is a fairly linear change in volume and no negative thermal expansion as reported for $BaFe_2(PO_4)_2$. One other point of interest is that there are two possible conformations of $Rb_2SnCu_3F_{12}$ in the $R\bar{3}$ symmetry; the pinwheel can either be clockwise or anticlockwise. This may create a double-well potential for each conformation, something that is seen in Rochelle salt for hydrogen positioning. Each conformation could also be present within the same grain of a crystallite which would be present as separate structural domains. It may be speculated that the re-entrant phase transition is related to some domain reorganisation due to some asymmetry in the double well potential which is brought on as a function of temperature. This reorganisation may not be possible in the single crystal as it would require flexibility of the surface.

4.6 Conclusions

It has been confirmed that $Rb_2SnCu_3F_{12}$ adopts an $R\bar{3}$ symmetry unit cell with ($a \approx 13.9$, $c \approx 20.3$) at room temperature. Only slight evidence has been found for a further doubling of the a and b parameters of this unit cell below 215 K in a single crystal sample. For the powder sample a first order re-entrant phase transition is found of the form $R\bar{3} \rightarrow P\bar{1} \rightarrow R\bar{3}$ (the transitions beginning at approximately 280 and 220 K, respectively). Despite several attempts, data of high enough quality from which to suggest a full and precise model for the two low temperature phases was not acquired. The re-entrant phase transition has also been confirmed not to occur in the single crystal, further exacerbating attempts to determine the structure of the intermediate, triclinic phase. Nevertheless, the observations of differing behaviour in the powder and single crystal forms is an intriguing and reproducible one, and a phenomenon which must be taken into account in further understanding of the electronic behaviour of this complex system.

1. K. Morita, M. Yano, T. Ono, H. Tanaka, K. Fujii, H. Uekusa, Y. Narumi and K. Kindo, *J. Phys. Soc. Jpn.*, 2008, **77**, 043707.
2. K. Matan, T. Ono, Y. Fukumoto, T. J. Sato, J. Yamaura, M. Yano, K. Morita and H. Tanaka, *Nat. Phys.*, 2010, **6**, 865-869.
3. T. Ono, K. Morita, M. Yano, H. Tanaka, K. Fujii, H. Uekusa, Y. Narumi and K. Kindo, *Phys. Rev. B*, 2009, **79**, 174407.
4. S. P. Thompson, J. E. Parker, J. Potter, T. P. Hill, A. Birt, T. M. Cobb, F. Yuan and C. C. Tang, *Rev. Sci. Instrum.*, 2009, **80**, 075107.
5. A. C. Larson and R. L. Von Dreele, 2000.
6. B. H. Toby, *J. Appl. Cryst.*, 2001, **34**, 210-213.
7. G. M. Sheldrick, *Acta Crystallogr., Sect. A: Found. Crystallogr.*, 2008, **64**, 112-122.
8. L. J. Farrugia, *J. Appl. Crystallogr.*, 2012, **45**, 849-854.
9. S. A. Reisinger, C. C. Tang, S. P. Thompson, F. D. Morrison and P. Lightfoot, *Chem. Mater.*, 2011, **23**, 4234-4240.
10. B. J. Campbell, H. T. Stokes, D. E. Tanner and D. M. Hatch, *J. Appl. Crystallogr.*, 2006, **39**, 607-614.
11. H. Kabbour, R. David, A. Pautrat, H. J. Koo, M. H. Whangbo, G. Andre and O. Mentre, *Angew. Chem. Int. Ed.*, 2012, **51**, 11745-11749.
12. M. T. Dove, *J. Phys. Condens. Matter*, 2011, **23**, 225402.
13. R. R. Levitskii, A. Y. Andrusyk and I. R. Zachek, *Condens. Matter Phys.*, 2010, **13**, 13705.
14. A. Laumann, K. T. Fehr, H. Boysen, M. Hoelzel and M. Holzapfel, *Z. Kristallogr.*, 2011, **226**, 53-61.

5 Crystallographic studies of $Cs_{2-x}Rb_xSnCu_3F_{12}$ (where x = 0, 0.5, 1.0, 1.5)

As seen in Chapter 4 the compound $Rb_2SnCu_3F_{12}$ shows a rare and previously unreported re-entrant structural phase transition. This is only seen in the powder and not the previously studied single crystal.[1] It is of interest to study other members of this family to discover if they show similar behaviours. In particular, study of the solid solution $Cs_{2-x}Rb_xSnCu_3F_{12}$ will allow understanding of the effect of alkali cation size on the structural and electronic response.

$Cs_2SnCu_3F_{12}$ has previously been reported and suggested to undergo a phase transition from the aristotype $R\bar{3}m$ unit cell (with a = 7.142(4) Å and c = 20.381(14) Å) at 185 K to a cell with doubled a and b parameters[2] apparently like that found for $Rb_2SnCu_3F_{12}$.[1] However, no structural model has yet been presented. Our first aim is therefore to probe the nature of this phase transition in a powder sample of $Cs_2SnCu_3F_{12}$ and then extend this study to a number of intermediate family members between $Rb_2SnCu_3F_{12}$ and $Cs_2SnCu_3F_{12}$.

5.1 Experimental

The syntheses of both $Cs_2SnCu_3F_{12}$ and $Rb_2SnCu_3F_{12}$ have been previously reported[1, 2] and our main techniques were similar to these, with some small modifications.

5.1.1 Synthesis of $Cs_{2-x}Rb_xSnCu_3F_{12}$

RbF (Sigma Aldrich 99.8 %), CsF (Sigma Aldrich, 99.9 %) and SnF_4 (Sigma Aldrich) were dried by heating at 390 K under a vacuum of ~ 10^{-4} mbar for 24 hours. They were then mixed and ground with CuF_2 (Sigma Aldrich, 98 %) under argon in the appropriate molar ratio; so as to acquire a mixture of 2:1:3 $AF:SnF_4:CuF_2$ (where A = Rb or Cs). The resulting mixtures were then sealed in a gold tube before heating under flowing argon. The furnace was heated to 873 K at 10 K min^{-1} and held at that temperature for twelve hours before cooling at the same rate. Pure samples were never realised, with notable impurities being Rb_2SnF_6, Cs_2SnF_6, CuO and $RbCuF_3$. It is suggested that small amounts of retained water in the starting materials may be the cause of the impurities.

A magnetically pure sample (i.e. one containing no magnetic impurities like CuO) of $Cs_2SnCu_3F_{12}$ was synthesised by a different technique.[a] CsF, SnF_4 and CuF_2 were ground in stoichiometric amounts (2:1:3 molar ratio) and pelletised inside an Argon filled glove box. The pellet was then placed in a copper tube (pre-annealed under hydrogen gas) which already had one end sealed. A small crystal (approx. 1 x 2 x 2 mm) of XeF_2 was also added to the copper tube in order to supply a fluorine rich atmosphere on decomposition. The tube was then removed from the glove box with a rubber bung in the empty end. About an inch from this open end the tube was sealed firstly with a press using 8 tons of pressure and then further sealed using a hammer. The now crudely sealed tube was then placed with its pre-sealed end in a water bath with the crudely sealed end protruding from the water. A blow-torch utilising oxygen and natural gas was then used to weld the tube completely shut. The tube was then heated to 773 K for 3 days before cooling and then repeating the sealing/heating cycle in order to have a total heating time of 6 days. This sample was used exclusively for magnetic measurements.

[a] In partnership with Professors V. A. Dolgikh and E. I. Ardashnikova, Moscow State University.

5.1.2 Analysis techniques

Laboratory based X-ray powder diffraction (XRPD) for the purpose of phase identification was performed on either a PANalytical Empyrean X-ray diffractometer operating in either Bragg-Brentano or transmission geometry or a Stoe Stadi-P operating in transmission mode. Both systems utilised Cu $K_{\alpha 1}$ radiation.

Synchrotron X-ray powder diffraction (SXPD) was performed at beamline I11, Diamond Light Source Ltd., Oxfordshire.[3] This utilised glass capillaries and operated in Debye-Scherrer mode typically with radiation of $\lambda \approx 0.82$ Å (predetermined using a known standard). A multi-analysing crystal (MAC) based detector was used in the case of $Cs_2SnCu_3F_{12}$ in order to collect the highest resolution data possible. For $Cs_{2-x}Rb_xSnCu_3F_{12}$ (x = 0.5, 1.0, 1.5) a position sensitive detector was utilised in order to collect a large number of patterns while maintaining data quality. For $Cs_2SnCu_3F_{12}$ patterns were collected at 100, 120, 140, 150, 160, 170, 180, 190, 200, 210, 220, 240, 260, 280, 300 K on heating (and 220 – 160 K on cooling as well) – "Run 1". A second run was also employed – "Run 2" – taking measurements for a longer period of time at 300, 200, 190, 180, 170, 165, 160, 150, 140 K. For $Cs_{2-x}Rb_xSnCu_3F_{12}$ (x = 0.5, 1.0, 1.5) patterns were collected between 300 and 100 K in 10 K increments on cooling using a position sensitive detector (PSD). In all cases a minimum of ten minutes was allowed in order to equilibrate the temperature of the air stream and the sample.

Neutron powder diffraction (NPD) was performed on $Cs_2SnCu_3F_{12}$ at beamline HRPD (High resolution powder diffraction), ISIS pulsed neutron and muon source, Oxfordshire. Samples of ~ 5 g were mounted in 5mm vanadium flat-plate cans before loading into the diffractometer, which was fitted with a cryostat. Patterns were collected at 300, 165, 150 and 100 K.

Rietveld refinement was performed using GSAS [4] and the EXPGUI interface.[5] This analysis sought to fit lattice parameters, phase fractions, peak profile shape (both Gaussian and Lorentzian) and thermal parameters (grouped by atom type). The analysis included impurities but grouped the thermal parameters for each atom in the phase together.

Magnetic measurements were taken using a Quantum Designs PPMS using a VSM add-on unit[b]. Samples were mounted in plastic holders which were provided by the manufacturer. Samples were subject to cooling to ~ 2 K from 300 K in zero-field before applying a magnetic field and measuring while heating to 300 K (zero-field cooling or "ZFC"). The samples were then cooled to ~ 2 K while still in the magnetic field and then once again measuring while heating to 300 K (field cool or "FC"). The particular fields are noted in the text.

5.2 Crystallography of $Cs_2SnCu_3F_{12}$

As stated before, $Cs_2SnCu_3F_{12}$ has been suggested to undergo a structural phase transition at 185 K from a $R\bar{3}m$ unit cell to a cell with doubled *a* and *b* parameters like that found for $Rb_2SnCu_3F_{12}$.[2] As has been found in Chapters 3 and 4, however, the powder can behave

[b] Under the direction of Prof. A. N. Vasiliev and Mr A. Golovanov, Faculty of Physics, Moscow State University.

differently from the single crystal. Initial SXPD studies of $Cs_2SnCu_3F_{12}$ at room temperature suggest a unit cell that matches well with that derived from the previous single crystal.[2] Peak breadth analysis suggests an approximate particle size of 2225 Å.c NPD also suggests a very similar cell (Table 5.1, Table 5.2 and Figure 5.1). In both cases there is also a small degree of preferential orientation which suggests that the crystallites may be anisotropic.

Table 5.1: Comparison of unit cell parameters (at ambient temperature) from single crystal and powder diffraction (SXPD and NPD) for $Cs_2SnCu_3F_{12}$.

Source	*a* (Å)	*c* (Å)
Single crystal[2]	7.142(4)	20.381(14)
SXPD	7.131778(10)	20.36703(4)
NPD	7.13155(6)	20.3609(3)

Table 5.2: Comparison of previously reported atomic coordinates for single crystal and experimentally derived from powder for $Cs_2SnCu_3F_{12}$ in space group $R\bar{3}m$. All data recorded at ambient temperature.

	x	y	z	U_{ISO} (Å^2) x 100
Previously reported single crystal[2]				
Cs	0	0	0.1060(1)	3.2(1)
Cu	½	0	0	1.1(1)
Sn	0	0	½	1.3(1)
F1	0.2042(2)	-0.2042(2)	0.9845(1)	2.2(1)
F2	0.1312(2)	-0.1312(2)	0.4465(1)	3.6(1)
SXPD Rietveld refinement				
Cs	0	0	0.10627(3)	2.10(16)
Cu	½	0	0	-0.062(15)
Sn	0	0	½	0.404(16)
F1	0.20541(15)	-0.20541(15)	0.98475(10)	1.73(5)
F2	0.13211(15)	-0.13211(15)	0.44676(10)	1.73(5)
NPD Rietveld refinement				
Cs	0	0	0.1057(3)	2.28(13)
Cu	½	0	0	0.56(6)
Sn	0	0	½	1.04(12)
F1	0.20419(19)	-0.20419(19)	0.98422(12)	1.58(7)
F2	0.13008(19)	-0.13009(19)	0.44697(14)	3.44(10)

[c] Average of peaks (101), (10-2) and (104) derived from the Scherrer formula.

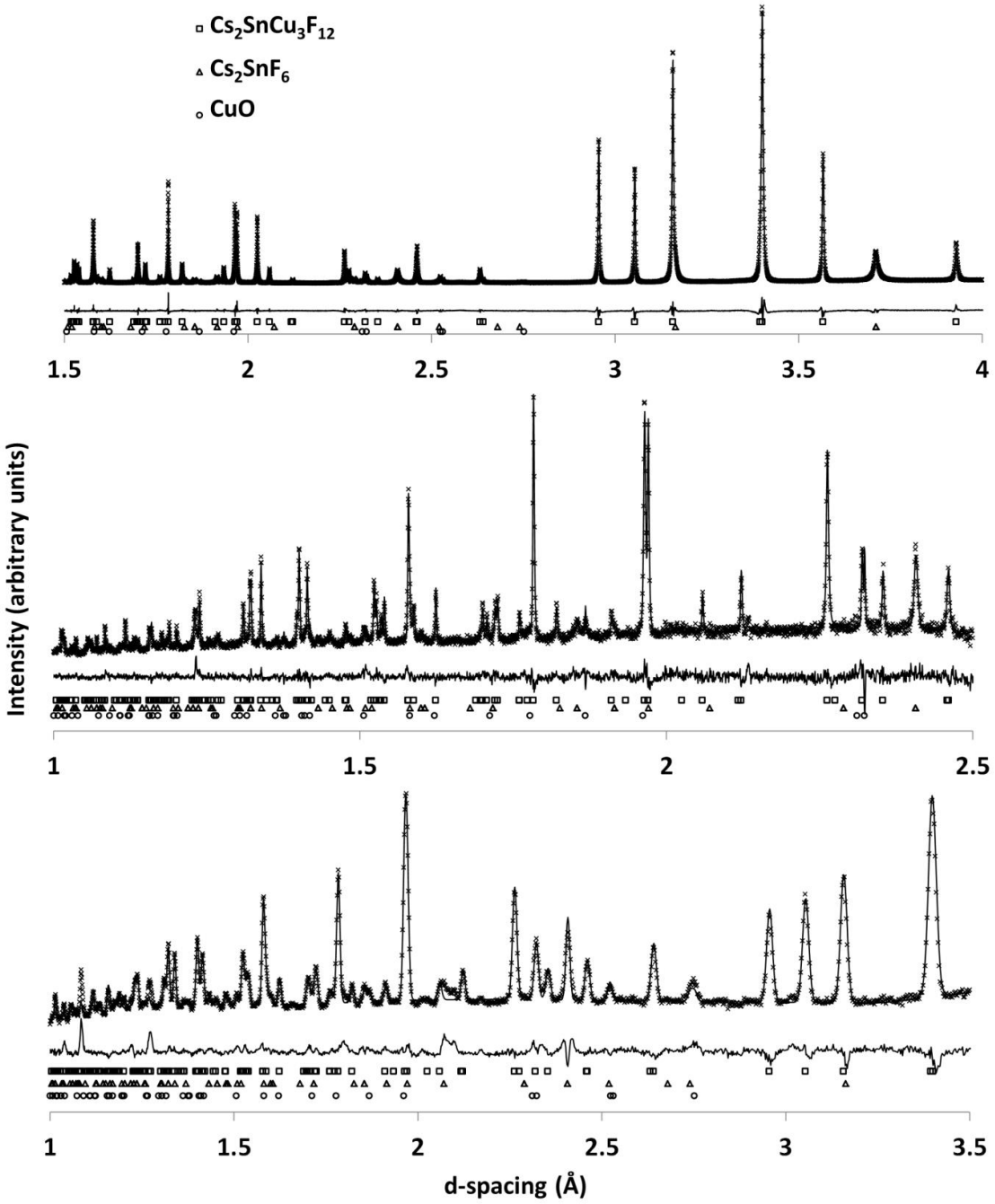

Figure 5.1: SXPD (top) and NPD (lower two; middle is backscattering detector bank, bottom is 90 ° detector bank.) data for $Cs_2SnCu_3F_{12}$ at room temperature with the models found in Table 5.2. Atomic coordinates and preferential orientation has also been refined in order to achieve the best fit.

On cooling we observe a change in the powder pattern consistent with a change in unit cell symmetry. This is seen to begin to occur at 170 K; 15 K below the temperature previously reported (Figure 5.2). This may indicate that the powder is undergoing a different transition from the single crystal. Indexing of SXPD data at 100 K suggests a monoclinic unit cell with parameters a = 10.5970 Å, b = 7.1003 Å, c = 7.9011 Å, β = 97.871 °. This leads to a number of possible models but it is found that this is restricted to the primitive cases as a peak indexable as (1 2 0) is clearly visible at 100 K in both the SXPD and NPD data and no related

peak at 300 K. This breaks the reflection conditions that would be required for either a body-centred or C-centred unit cell. Further investigation of the neutron data at 100 K suggests that the best model occurs in space group $P2_1/n$ [d] (Table 5.3). These models were derived from the rhombohedral cell using ISODISTORT software.[6]

Table 5.3: Fits of various primitive monoclinic unit cell models to the NPD data for $Cs_2SnCu_3F_{12}$ at 100 K (using 2 detector banks and including atomic coordinate refinement and preferential orientation refinement). All values in % and found using the GSAS program.[4]

	Fitted		-Bknd	
space group	wRp	Rp	wRp	Rp
$P2_1/n$	4.34	3.49	4.70	3.42
$P2_1/m$	5.18	4.09	5.45	4.25
$P2/n$	5.12	4.30	6.10	4.67
$P2/m$	5.47	4.32	5.94	4.71

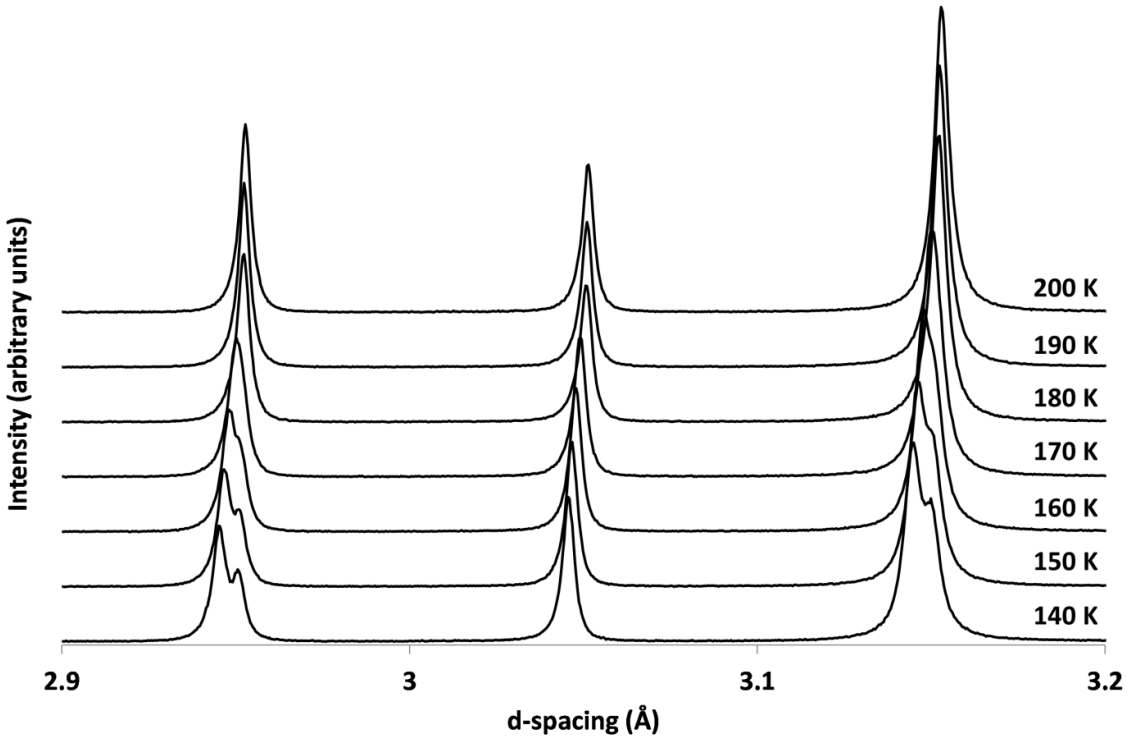

Figure 5.2: SXPD patterns for $Cs_2SnCu_3F_{12}$ as a function of temperature. Note the presence of peak splitting ≤ 170 K. Patterns off-set on y-axis for clarity.

The low temperature phase (as derived from NPD data) appears to be similar to the unit cell reported for $Cs_2TiCu_3F_{12}$ at low temperature with the clear difference of the larger M-F (where M= Ti^{4+}, Sn^{4+}) distance in the Sn case. This is also reflected in the larger lattice parameters of this system.

[d] Including refinement of atomic coordinates and preferential orientation.

The transition was then subject to further scrutiny. SXPD data suggests a transition directly between $R\bar{3}m$ and $P2_1/n$ with no indication of a centred intermediate phase. The presence of a small peak indexed as (1 2 0) indicates that the primitive cell is the correct choice (Figure 5.3). This is verified by NPD data at 165K – the very beginning of the transition – which also shows a peak indexable as (0 1 4).

Examining the molar unit cell volume changes as a function of temperature shows a clear increase in the gradient of unit cell shrinkage at the transition point.[e] Heating and cooling through the phase change shows no appreciable hysteresis in the transition temperature (Figure 5.4). This suggests a second-order phase transition is taking place.

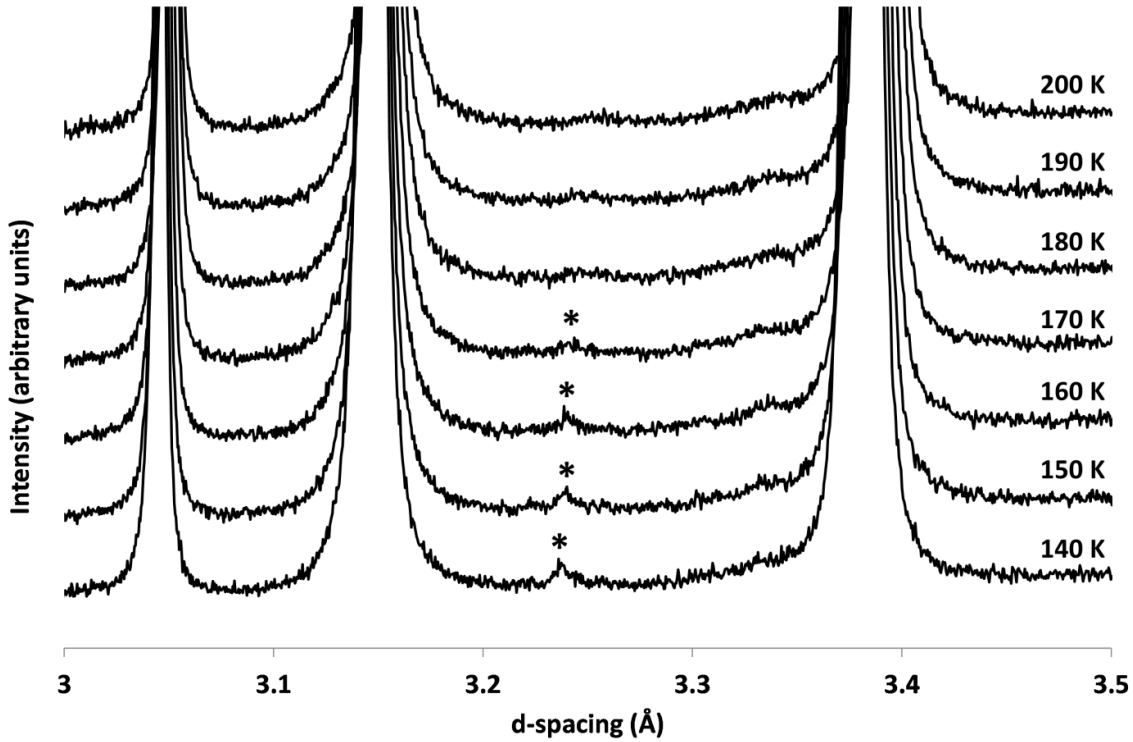

Figure 5.3: Close-up of $Cs_2SnCu_3F_{12}$ SXPD patterns at a range of temperatures. * indicates (1 2 0) peak. Patterns off-set on the y-axis for clarity.

[e] All refinements and a table of lattice parameters as a function of temperature available in Appendix A.5.2.

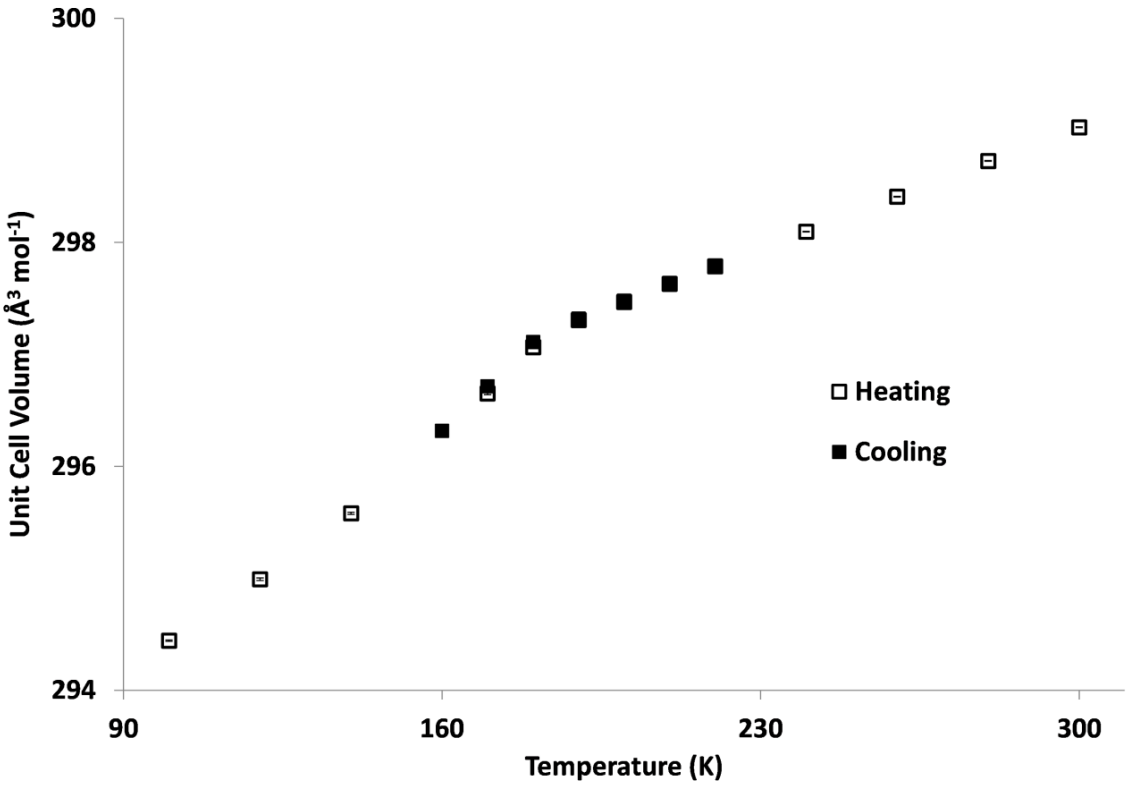

Figure 5.4: Unit cell volume (in units of Å mol^{-1}) vs. temperature for $Cs_2SnCu_3F_{12}$ as derived from SXPD data.

Closer examination of the models yielded from the NPD data shows the distortion which is occurring. It is found to be very similar to that found for $Cs_2TiCu_3F_{12}$ (Chapter 3) which – in terms of the kagome lattice – shows a skewing (Figure 5.5).

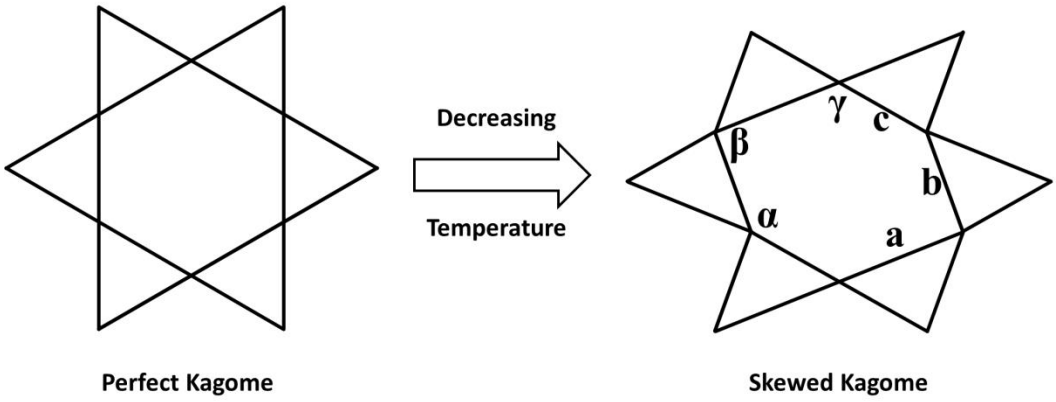

Figure 5.5: Exaggerated skewing of the kagome lattice in $Cs_2SnCu_3F_{12}$ with lowering temperature. At room temperature the angles within the kagome hexagonal pore are equal, likewise the Cu – Cu distances. The angles at reduced temperature vary by ~ 4 ° (α ≈ 116 °, β ≈ 123 °, γ ≈ 120) and the Cu – Cu distances by ~ 0.04 Å (a ≈ 3.58 Å, b ≈ 3.55 Å, a ≈ 3.54 Å).

In order to assess the motivations for the phase transition more thoroughly, the NPD derived models at various temperatures were then subject to bond valence sum (BVS) calculations [7] (Table 5.4).

Table 5.4: Bond Valence Sums for $Cs_2SnCu_3F_{12}$ at various temperatures (as derived from NPD data).

	BVS			
Temperature (K)	Sn^{4+}	$Cu1^{2+}$	$Cu2^{2+}$	$Cs1^{+}$
300	4.626	2.016		1.039
165	4.508	1.926	2.050	0.887
150	4.502	2.106	1.972	0.908
100	4.554	2.030	2.002	0.942

One possible motivation for the transition is that it may just provide the most efficient way of reducing the unit cell volume in line with shrinking bonds. The bond lengths are presented in Table 5.5. Sn^{4+} is also over-bonded (the BVS is suggested to be over 4.5 which is slightly larger than expected). With reducing temperature we find that this decreases slightly, along with the Sn – F bond length increasing. It may be that the structure is trying to adopt the most stable configuration with respect to the contained oxidation states.

Table 5.5: Selected metal – fluoride distances for $Cs_2SnCu_3F_{12}$ at 300 and 100 K as derived from NPD data (shaded cells are intentionally blank)

	Bond length (Å)	
Metal – fluoride bond	300 K	100 K
Cs – F3		3.058(11)
Cs – F1		3.161(10)
Cs – F1	3.115(4) (x3)	3.291(9)
Cs – F2	3.418(4) (x3)	3.042(10)
Cs – F4		3.265(11)
Cs – F5		3.303(11)
Cs – F5		3.388(10)
Cs – F6		3.367(11)
Cu1 – F2		1.934(8) (x2)
Cu1 – F1	1.8983(8) (x4)	1.874(8) (x2)
Cu1 – F6	2.3564(28) (x2)	2.304(7) (x2)
Cu2 – F3		1.976(11)
Cu2 – F1		1.925(9)
Cu2 – F2		1.878(10)
Cu2 – F3		1.839(11)
Cu2 – F4		2.351(8)
Cu2 – F5		2.355(9)
Sn – F6		1.940(7) (x2)
Sn – F4		1.945(7) (x2)
Sn – F5		1.950(6) (x2)
Sn – F2	1.9392(27) (x6)	

5.3 Crystallography of $Cs_{2-x}Rb_xSnCu_3F_{12}$

Comparing $Cs_2SnCu_3F_{12}$ and $Rb_2SnCu_3F_{12}$ there is clearly a difference in behaviour with lowering temperature between 300 and 100 K. $Cs_2SnCu_3F_{12}$ shows a transition from a rhombohedral

cell (with $a \approx 7.13$, $c \approx 20.36$) to a primitive monoclinic cell and $Rb_2SnCu_3F_{12}$ shows a re-entrant transition between a rhombohedral (with $a \approx 13.90$, $c \approx 20.35$) and a primitive, triclinic unit cell. It is of interest to observe the solid solution to see if there is a clear crossing point between these two behaviours.

5.3.1 $Cs_{1.5}Rb_{0.5}SnCu_3F_{12}$

$Cs_{1.5}Rb_{0.5}SnCu_3F_{12}$ is found to be similar to $Cs_2SnCu_3F_{12}$ and indexable in a unit cell with symmetry $R\bar{3}m$ and parameters a = 7.121128(22), c = 20.35953(10) at room temperature (Figure 5.6).

No attempt has been made to refine the atomic coordinates as there is the general assumption that the nearest end-member of the solid solution will be a guide as to the behaviour and the quality of the data may not allow a reasonable model to be found. Refinement of the relative ion occupation on the A-site (assuming full occupancy) suggests that the ratio of Cs:Rb is, as expected, 3:1.

On reducing the temperature we find a transition from the rhombohedral cell in the form of splitting of a few peaks (Figure 5.7). The SXPD pattern at 100 K is well fitted by a $P2_1/n$ symmetry unit cell (as used for the low temperature form of $Cs_2SnCu_3F_{12}$) and this is the case up to the visual transition point. In order to determine the exact transition point the quality of fit was examined for each temperature. This suggested the transition point to be around 250 K (Figure 5.8). At 250 K there is the beginning of a divergence between the fit quality of the primitive and rhombohedral unit cells.[f]

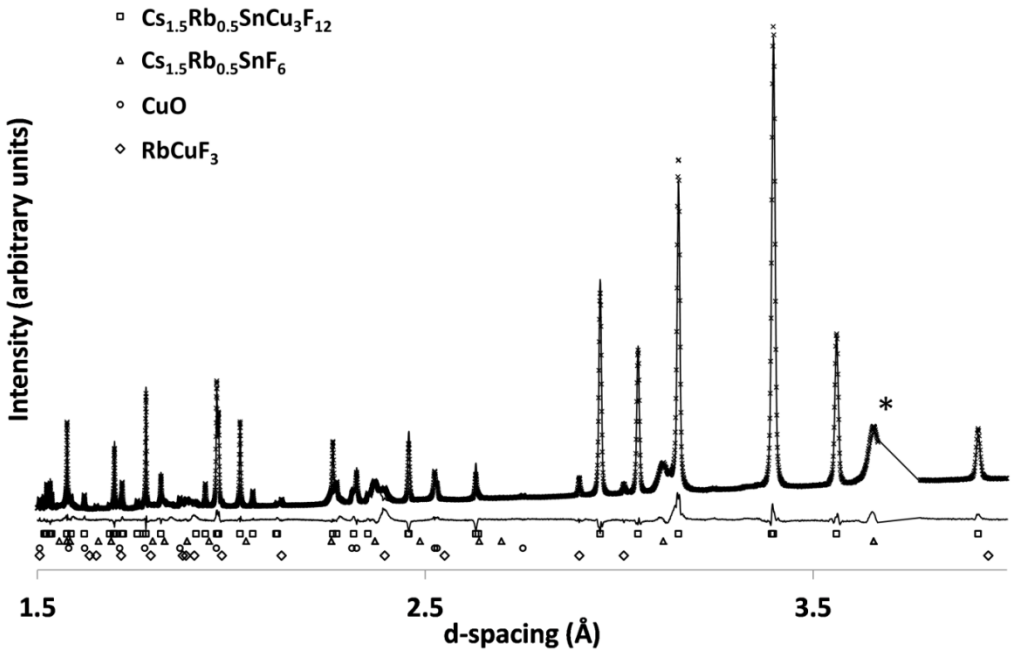

Figure 5.6: SXPD data and Rietveld refinement for $Cs_{1.5}Rb_{0.5}SnCu_3F_{12}$ at 300 K (* is a redacted area due to difficulty in fitting – most likely due to phase separation between the impurities Cs_2SnF_6 and Rb_2SnF_6).

[f] All refinements and a table of lattice parameters as a function of temperature available in Appendix A.5.3.1.

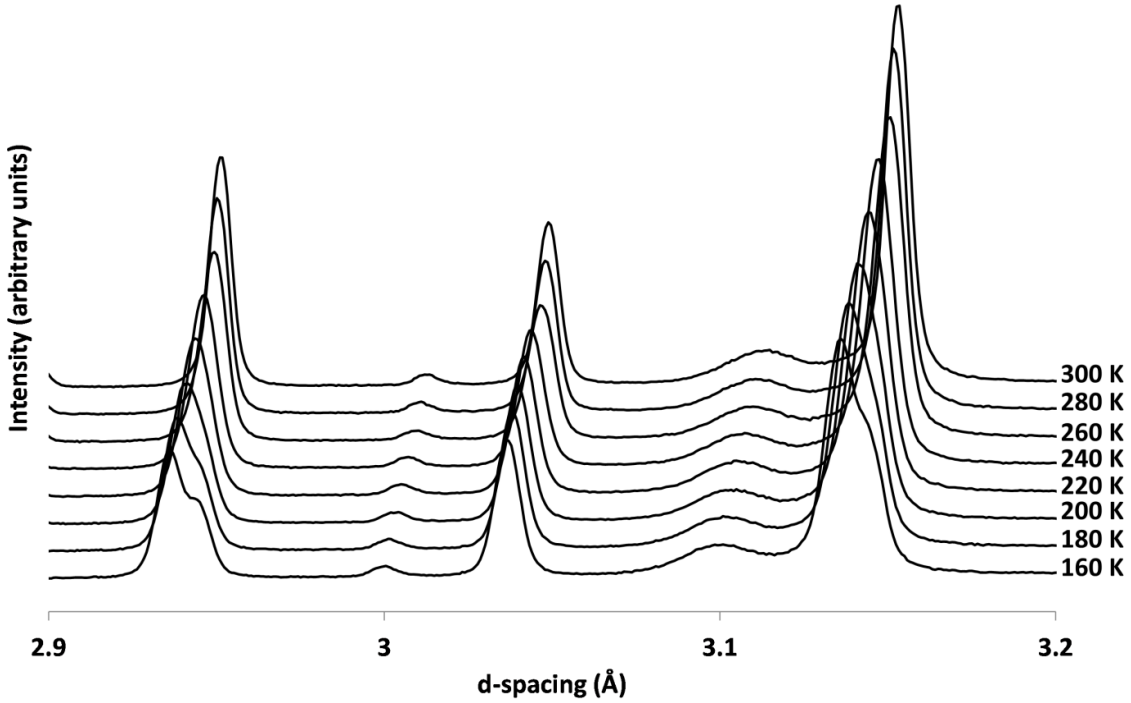

Figure 5.7: $Cs_{1.5}Rb_{0.5}SnCu_3F_{12}$ SXPD data at various temperatures. Patterns off-set on y-axis for clarity.

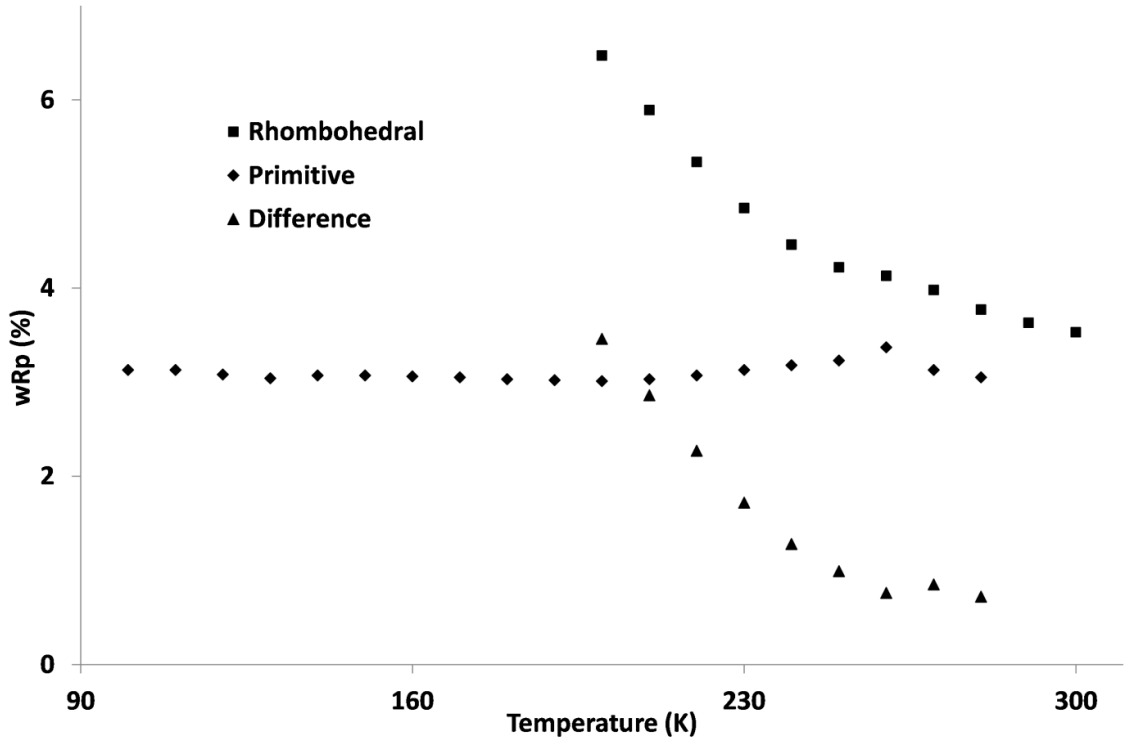

Figure 5.8: wRp (%) for rhombohedral ($R\bar{3}m$) and primitive ($P2_1/n$) model Rietveld refinements for $Cs_{1.5}Rb_{0.5}SnCu_3F_{12}$ at various temperatures showing the preference for the primitive model at ~ 250 K.

Refinement of lattice parameters at all temperatures shows an anomaly in the unit cell volume at the transition temperature (Figure 5.9). This shows an increase in the gradient of the unit cell shrinkage at the phase transition, which is consistent with that found for $Cs_2SnCu_3F_{12}$. This suggests that the behaviour of $Cs_{1.5}Rb_{0.5}SnCu_3F_{12}$ is similar to the closest end-member, with the exception of the slightly higher transition temperature (250 K vs. 170 K).

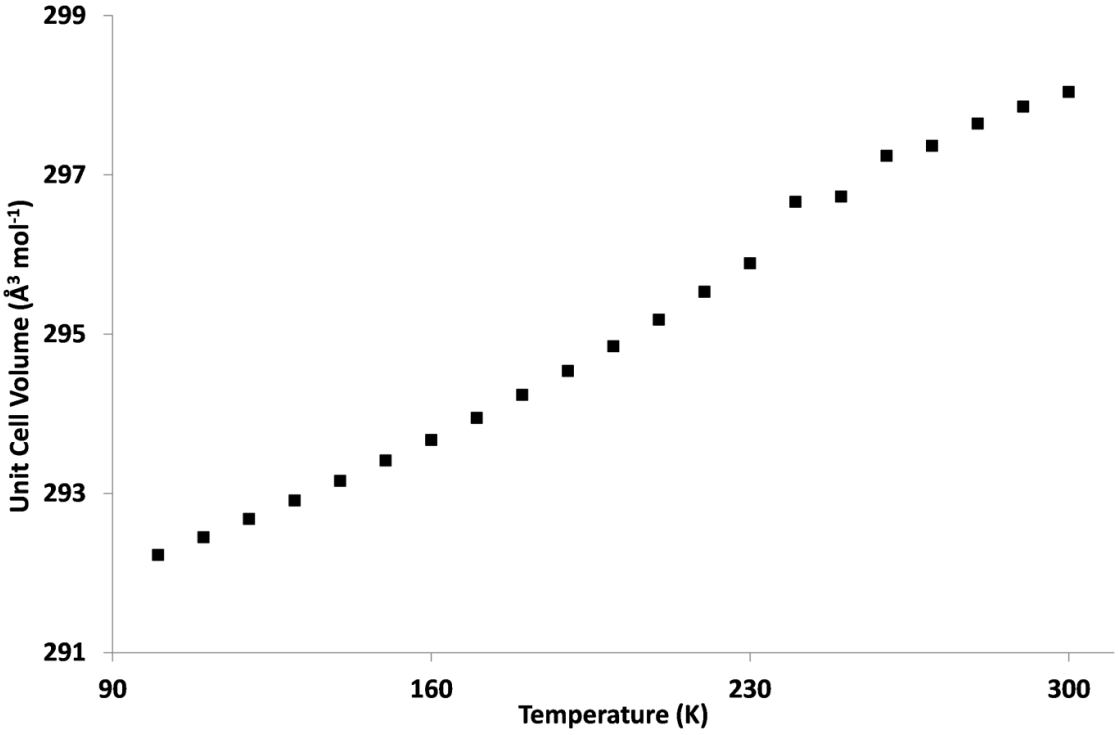

Figure 5.9: Unit cell volume (adjusted to per mole) for $Cs_{1.5}Rb_{0.5}SnCu_3F_{12}$ at a range of temperatures as derived from SXPD data.

5.3.2 $CsRbSnCu_3F_{12}$

$CsRbSnCu_3F_{12}$ is the middle member of the solid solution and so the natural assumption might be for it to behave like one end-member in particular despite its equal proximity to both. Surprisingly, the room temperature phase is poorly fitted by a rhombohedral cell (either of similar metrics to that found for $Cs_2SnCu_3F_{12}$ or the larger $Rb_2SnCu_3F_{12}$ unit cell) when compared to a primitive monoclinic cell (Table 5.6). This is principally on a statistical basis on that found from Rietveld refinement; splittings only start to become clear at reduced temperature and then they are particularly subtle.

Table 5.6: Comparison of model fit for rhombohedral ($R\bar{3}$ – derived from $Rb_2SnCu_3F_{12}$) and primitive monoclinic ($P2_1/n$) unit cells for $CsRbSnCu_3F_{12}$.

		Fitted		-Bknd	
	χ^2	wRp (%)	Rp(%)	wRp(%)	Rp(%)
$R\bar{3}$[g]	20.38	4.87	3.08	11.41	6.33
$P2_1/n$	14.93	3.85	2.51	7.96	4.67

[g] Of the type previously described for $Rb_2SnCu_3F_{12}$ with $a \approx 14.15$ Å and $c \approx 20.36$Å.

In order to elucidate further the features of this phase it was decided to focus on the data at the lowest temperature acquired (100 K) where any splittings might be anticipated to be maximised. This yielded few clues except that the primitive monoclinic phase was the best choice and $P2_1/n$ was found to be the best description (Figure 5.10); the possibility of a centred unit cell is quashed by the presence of a peak indexable as (1 2 0), there are no peaks which break n-glide condition: this limits us to two possible symmetries – $P2/n$ and $P2_1/n$ – of which the latter is found to give a superior fit. Interestingly the $P2_1/n$ model only allows for a single alkali metal site – an early consideration was the possibility of ordering of Cs^+ and Rb^+.

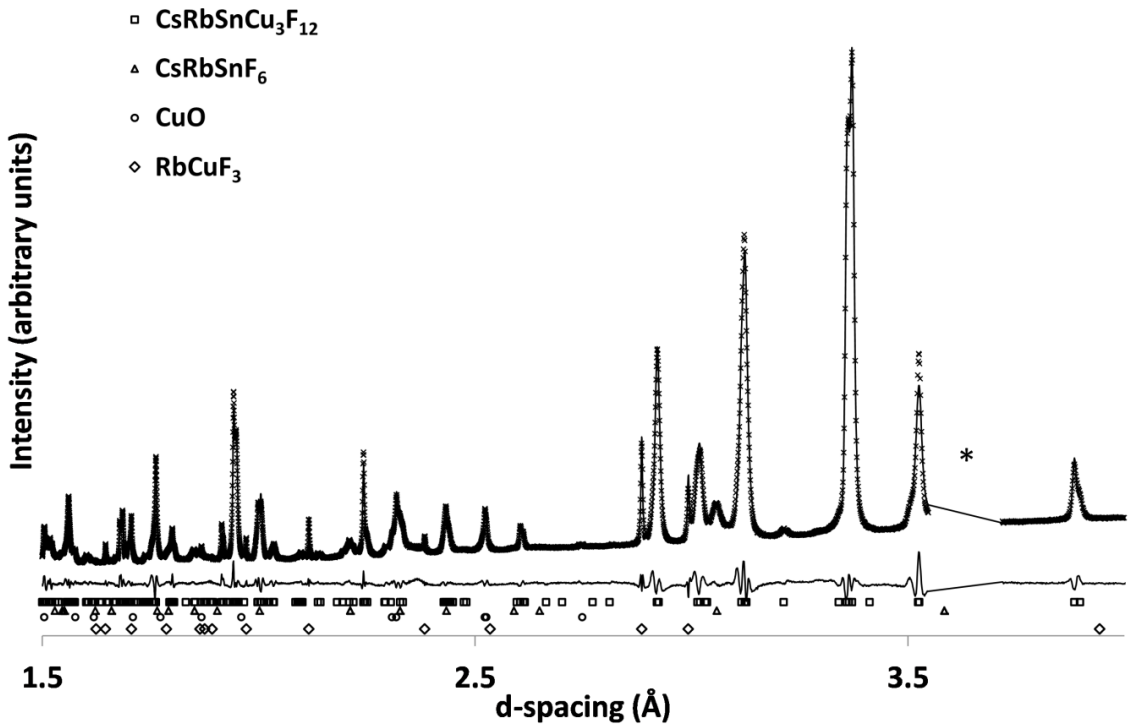

Figure 5.10: SXPD data and Rietveld refinement for $CsRbSnCu_3F_{12}$ at 100 K (* is a redacted area due to difficulty in proposing a high enough quality model for the impurity A_2SnF_6 phase – most likely due to phase separation between Cs_2SnF_6 and Rb_2SnF_6).

The 100 K data set was refined for both atomic coordinates and preferential orientation (which has been found for other members of the family). Unfortunately, BVS calculations suggest that the model refined is incorrect; the BVS for Sn^{4+} is 5.5, which is unrealistic. One key finding at this temperature, though, is the assignment of all the peaks. There is no indication that the unit cell is anything but primitive monoclinic (with $a \approx 7.88$ Å, $b \approx 7.05$ Å, $c \approx 10.53$ Å, $\beta \approx 10.53$ °) even when doubling the monoclinic axes is considered. If the cell was found to be $P2/m$ or $P2_1/m$ then it may be possible to have some form of alkali metal ordering as these unit cells have two A^{1+} sites. Refinement was attempted for these two space groups but in both cases the site occupancy refined to approximately 50:50 Rb^+:Cs^+.

If there is no ordering then it is difficult to suggest why $CsRbSnCu_3F_{12}$ is primitive at room temperature (and presumably has a particularly high transition temperature). The

volume of the unit cell (per molar unit) also shows no anomaly in this case – a clear indicator of a phase transition in the Cs^+ rich phases (Figure 5.11).[h]

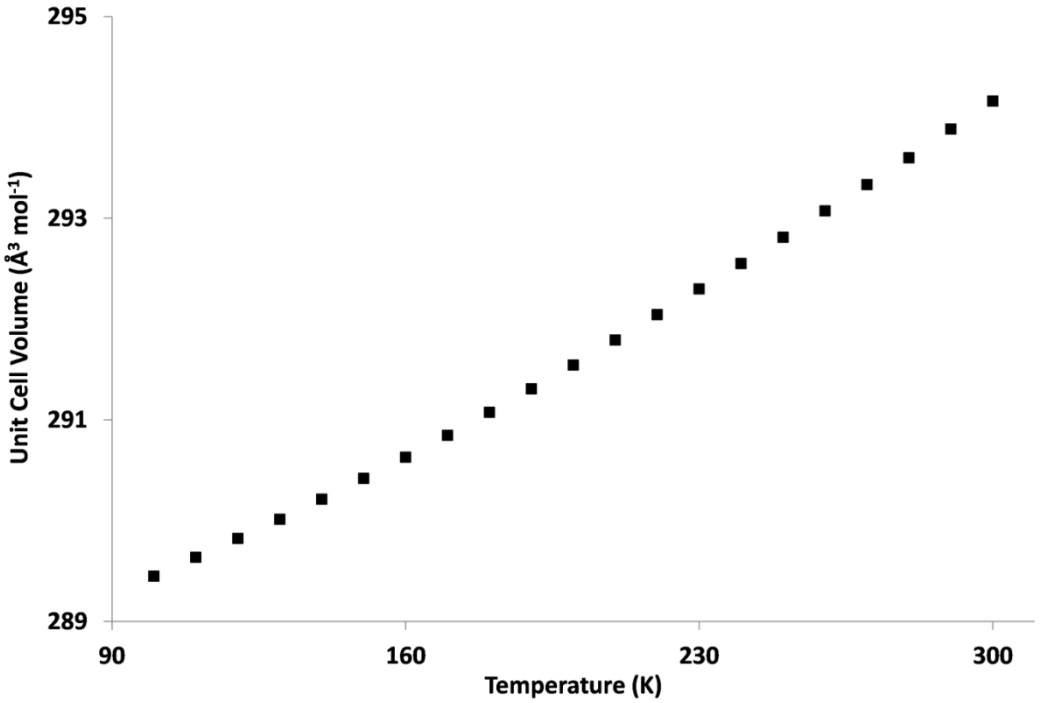

Figure 5.11: Molar volume as a function of temperature for $CsRbSnCu_3F_{12}$ as derived from SXPD data; note the lack of anomaly suggesting a lack of transition.

5.3.3 $Cs_{0.5}Rb_{1.5}SnCu_3F_{12}$

On increasing Rb^+ content to 75 % of the total alkali metal content the behaviour becomes more consistent with the rubidium-rich end-member. This is first seen at 300 K where a good fit is found with an $R\bar{3}$ unit cell of metrics ($a \approx 14.02$ Å, $c \approx 20.36$ Å). Further indication of the doubled, $Rb_2SnCu_3F_{12}$-like, unit cell is given by peaks indexable as (3 1 -1), (3 1 2) and (1 1 3) (Figure 5.12).

It is impossible to determine if there is the presence of the fluorine disorder which has been previously reported in this structure,[1] as the difference between the ordered and disordered pattern is minimal. In order to compare to $Rb_2SnCu_3F_{12}$ the sample was cooled. This resulted in a change in pattern mainly composed of peak broadening and changes in intensity (Figure 5.13).

This broadened phase is retained to the lowest temperature recorded (100 K). In the case of $Rb_2SnCu_3F_{12}$ there is a return to the rhombohedral phase at ~ 190 K. No further phase change is seen in this case down to the lowest temperature surveyed (100 K). The low temperature pattern is fitted well by the triclinic phase previously derived for $Rb_2TiCu_3F_{12}$ and $Rb_2SnCu_3F_{12}$ (see Chapters 3 and 4, respectively). Thus, $Cs_{0.5}Rb_{1.5}SnCu_3F_{12}$ appears to only behave like $Rb_2SnCu_3F_{12}$ in respect of the first transition. The low temperature cell can be

[h] All refinements and a table of lattice parameters as a function of temperature available in Appendix A.5.3.2.

assigned as a $P\bar{1}$ triclinic cell with metrics (at 100 K) $a \approx 10.48$ Å, $b \approx 10.54$ Å, $c \approx 10.50$ Å, $\alpha \approx 83.68$ °, $\beta \approx 83.19$ °, $\gamma \approx 83.34$ ° (Figure 5.14).

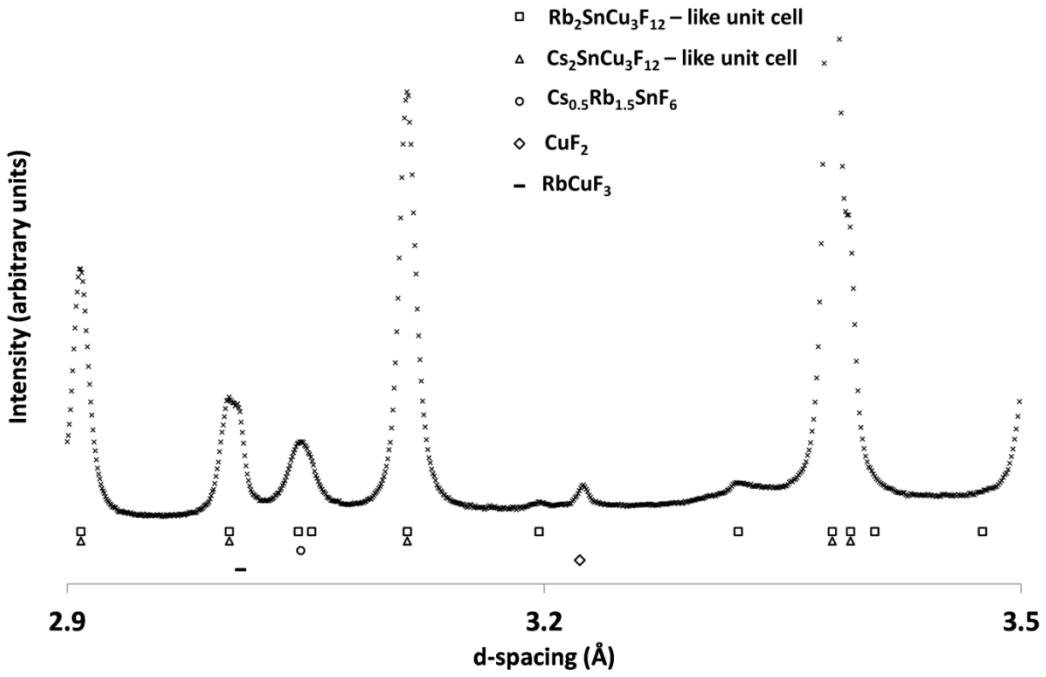

Figure 5.12: SXPD pattern for $Cs_{0.5}Rb_{1.5}SnCu_3F_{12}$ at ambient temperature. $Rb_2SnCu_3F_{12}$ like unit cell refers to a rhombohedral cell of ($a \approx 14.019$ Å, $c \approx 20.356$ Å), $Cs_2SnCu_3F_{12}$ like unit cell refers to a rhombohedral cell of ($a \approx 7.010$ Å, $c \approx 20.356$ Å)

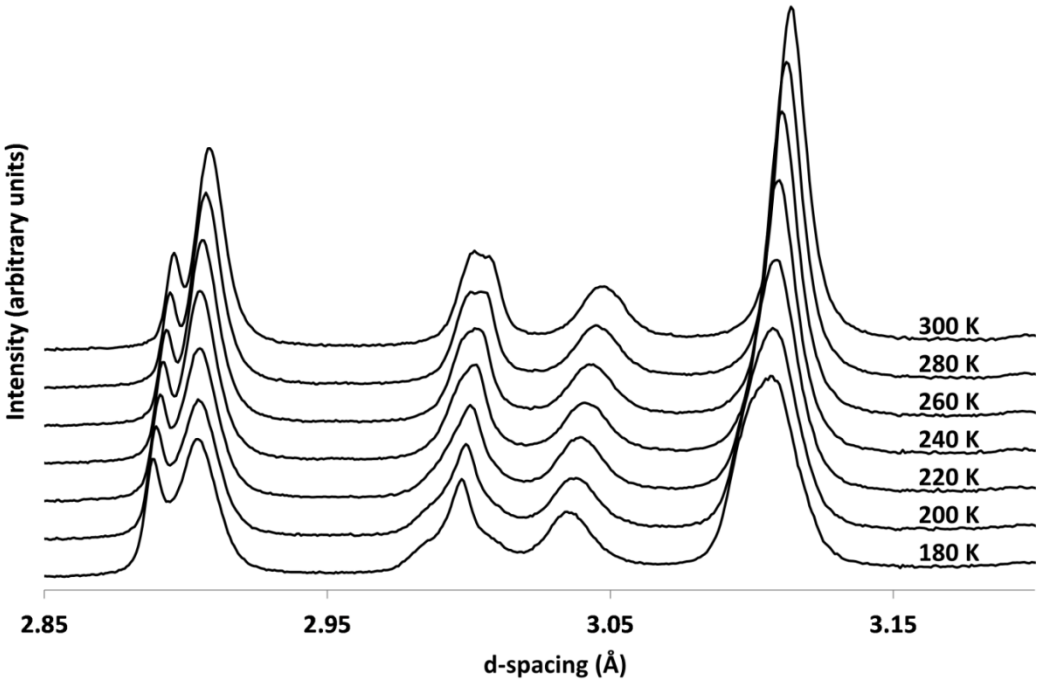

Figure 5.13: SXPD data for $Cs_{0.5}Rb_{1.5}SnCu_3F_{12}$ at a range of temperatures. Patterns off-set on y-axis for clarity.

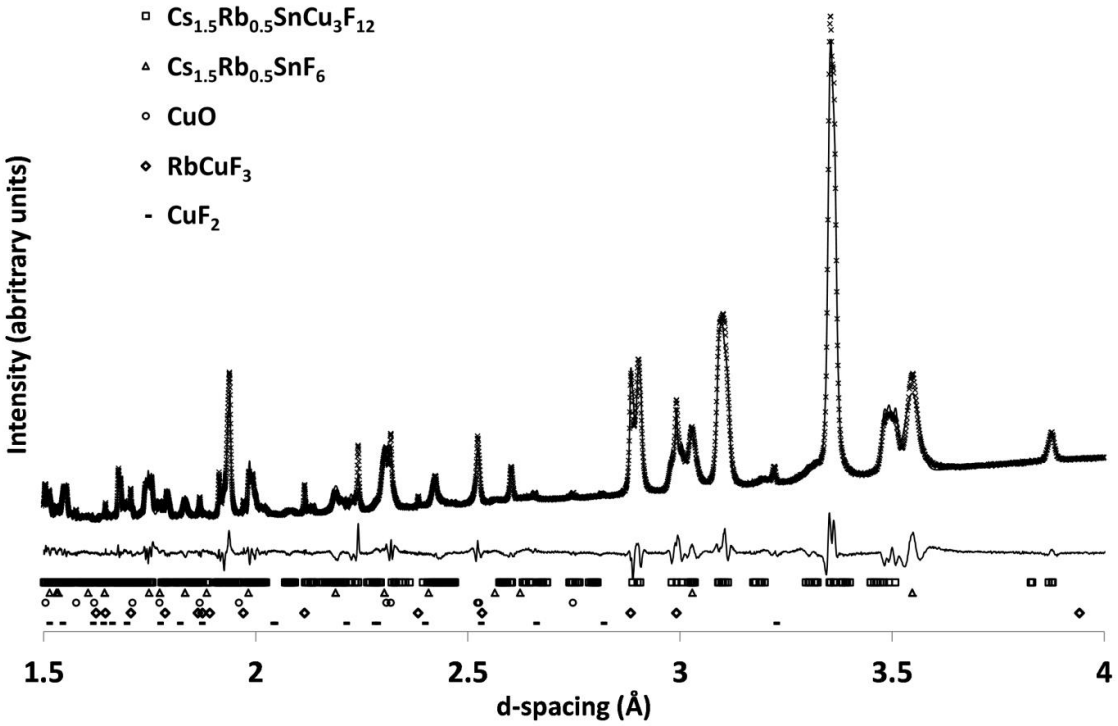

Figure 5.14: SXPD pattern for $Cs_{0.5}Rb_{1.5}SnCu_3F_{12}$ at 100 K and Rietveld refinement fit for both the main phase and impurities.

Unfortunately the low resolution makes further analysis challenging and particular difficulty is found when trying to determine the exact transition point. So, in order to determine the transition point the agreement factors from each fit were examined (as in section 5.3.1). This showed that a divergence from the rhombohedral and the triclinic fit began at 280 K – 30 K higher than that found for $Rb_2SnCu_3F_{12}$ (Figure 5.15). Like $Rb_2SnCu_3F_{12}$, there is a smooth change in unit cell volume (Figure 5.16), even when passing through phase transitions.[i]

[i] All refinements and a table of lattice parameters as a function of temperature available in appendix A.5.3.3.

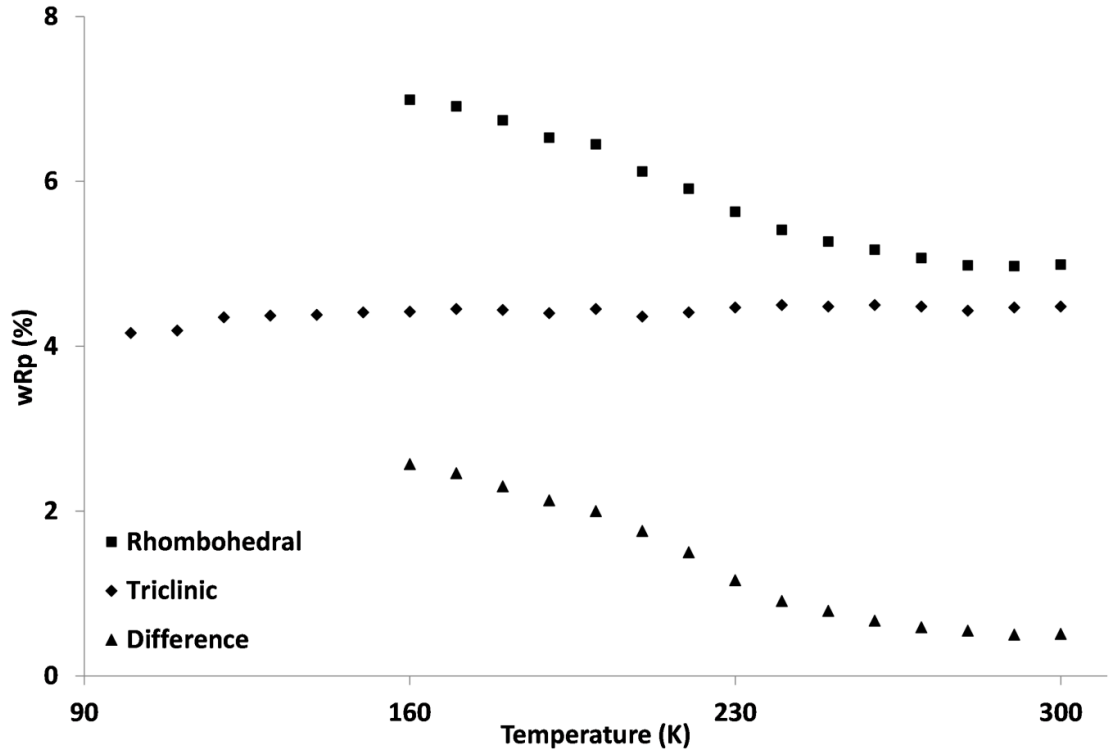

Figure 5.15: wRp (%) for rhombohedral ($R\bar{3}$) and triclinic ($P\bar{1}$) model Rietveld refinements for $Cs_{0.5}Rb_{1.5}SnCu_3F_{12}$ at various temperatures showing the improved fit of the triclinic model < 280 K.

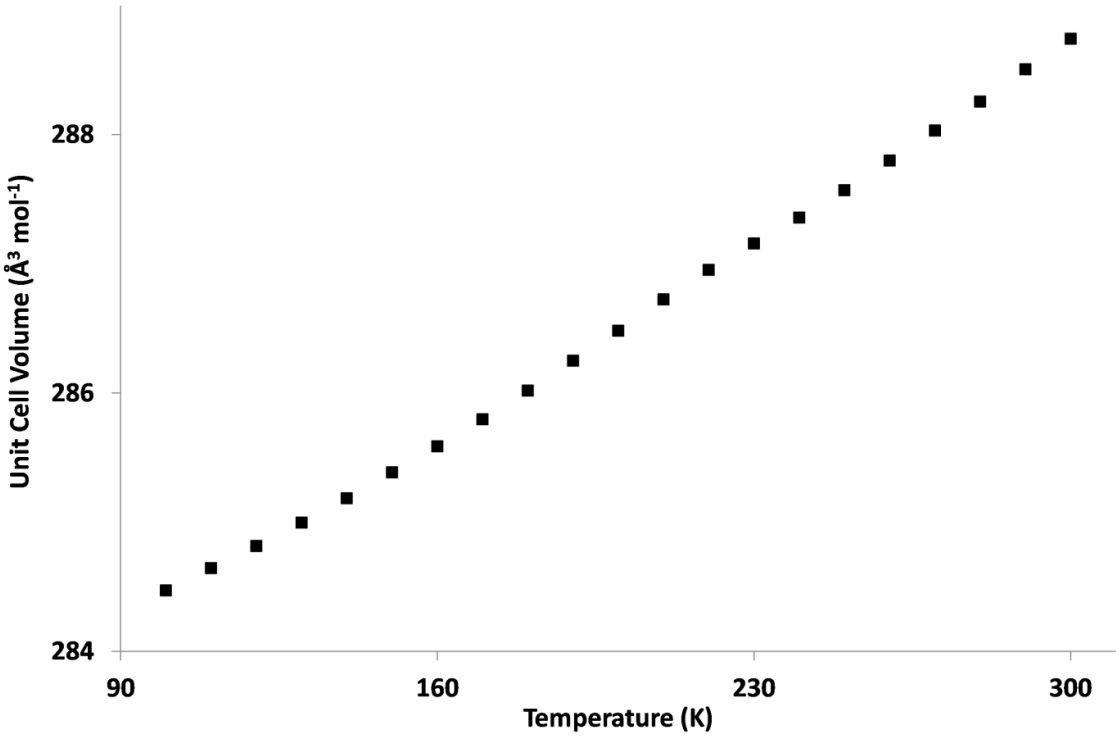

Figure 5.16: Molar volume as a function of temperature for $Cs_{0.5}Rb_{1.5}SnCu_3F_{12}$ as derived from SXPD data.

5.4 Structural trends in the $A_2SnCu_3F_{12}$ solid solution

From the data above we can draw some conclusions on the behaviour of the $A_2SnCu_3F_{12}$ solid solution where A = Rb^+, Cs^+. Observing the change in lattice volume at room temperature we find that it is, as expected, maximised at 100 % Cs^+ A-site occupancy and minimised at 100 % Rb^+ A-site occupancy (Figure 5.17). This is clearly related to the atomic radii of Cs^+ and Rb^+. In the intermediate occupancies we find that the change in volume is non-linear and it is suggested that at higher Cs^+ occupancies there is such little change in volume as the large size of Cs^+ dominates.

Further investigation of the unit cell parameters at room temperature suggests that the reduction in cell volume is closely related to changes in the *ab*-plane as opposed to the *c*-axis (Figure 5.18). In this case $CsRbSnCu_3F_{12}$ has been removed as it is present in the primitive monoclinic cell at room temperature – conversion of all the other studied members of the solid solution to the primitive monoclinic cell shows that it follows the trend, however.[j] This preferential change in the *ab*-plane compared to the *c*-axis is different from that found for changes in volume with reducing temperature; with reducing temperature it is found that the dominant parameter is the change in the *c*-axis (Figure 5.19). Thus, in order to accommodate different sized A^+ it seems that it is preferential for the kagome lattice to shrink or expand in the *ab*-plane but on cooling the majority of the shrinkage is found between the kagome layers instead.

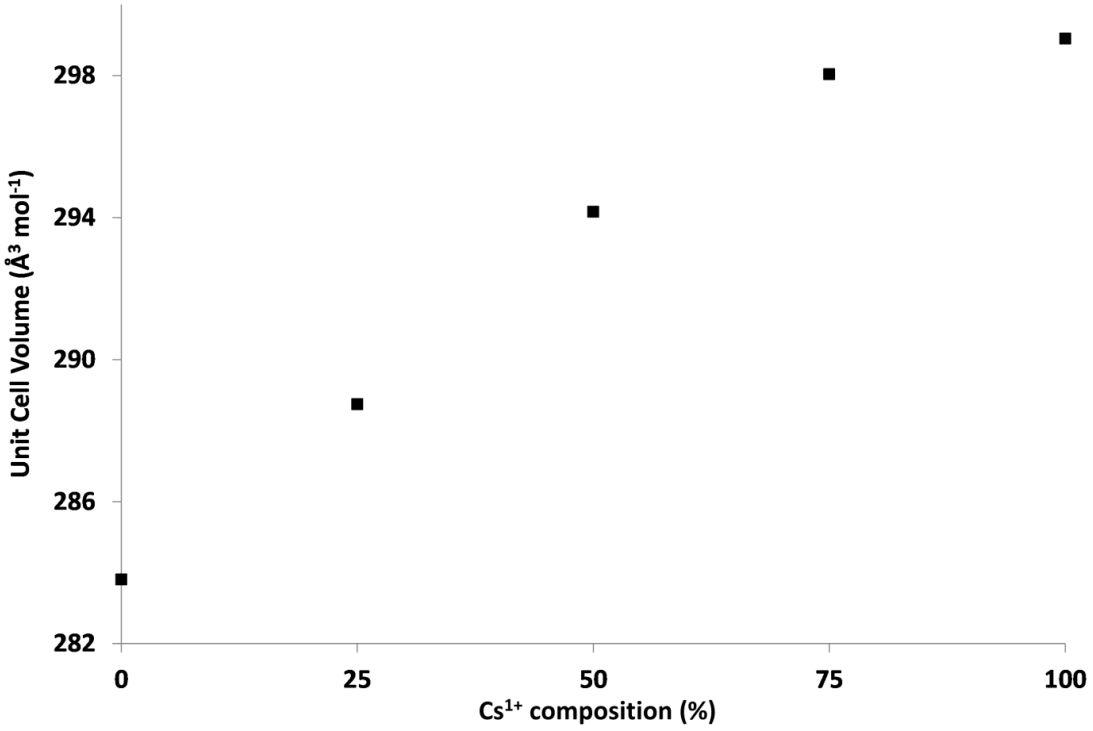

Figure 5.17: Molar volume of unit cell as a function of % occupation of A-site by Cs^+ (and inverse occupation for Rb^+). Values derived from SXPD data using the GSAS program.[4]

[j] Plots of primitive, monoclinic unit cell parameters for $CsRbSnCu_3F_{12}$ and other analysed members of the solid solution (converted from the rhombohedral parameters) are available in appendix A.5.4.

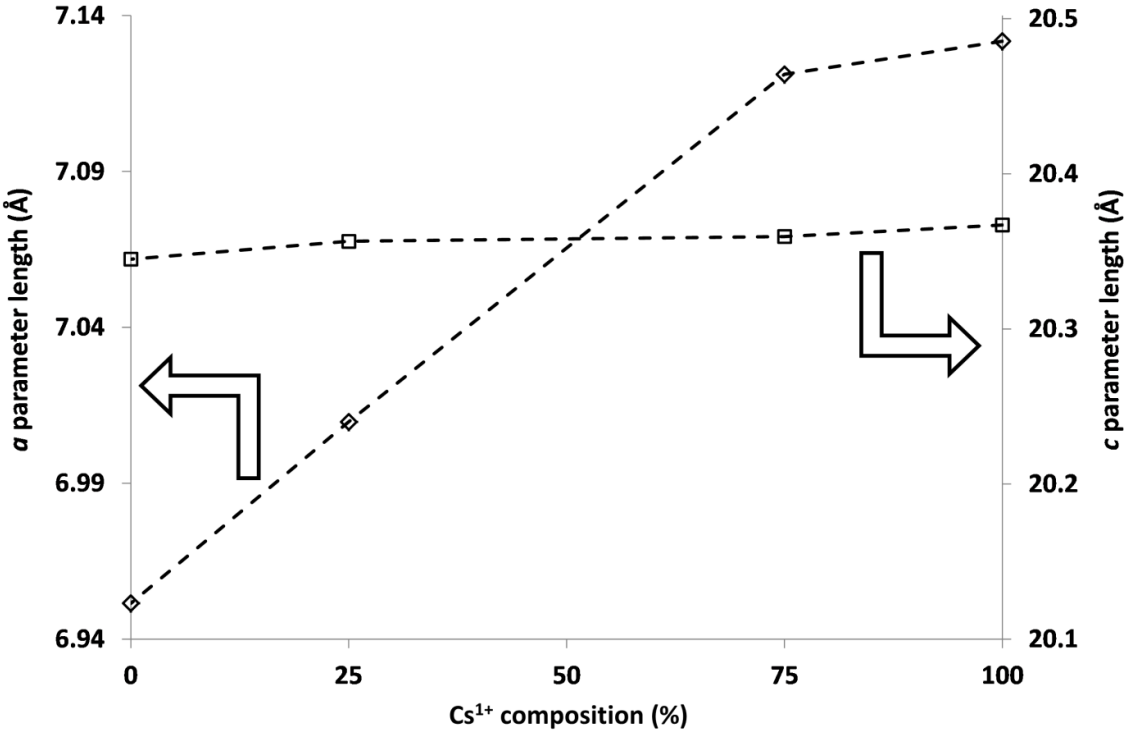

Figure 5.18: *a* and *c* unit cell parameters for $A_2SnCu_3F_{12}$ (A=Cs, Rb) solid solution. Dashed lines are only a guide to the eye. Axes are adjusted to represent the same percentage change in order to display lack of change in *c* parameter. Data derived from SXPD data.

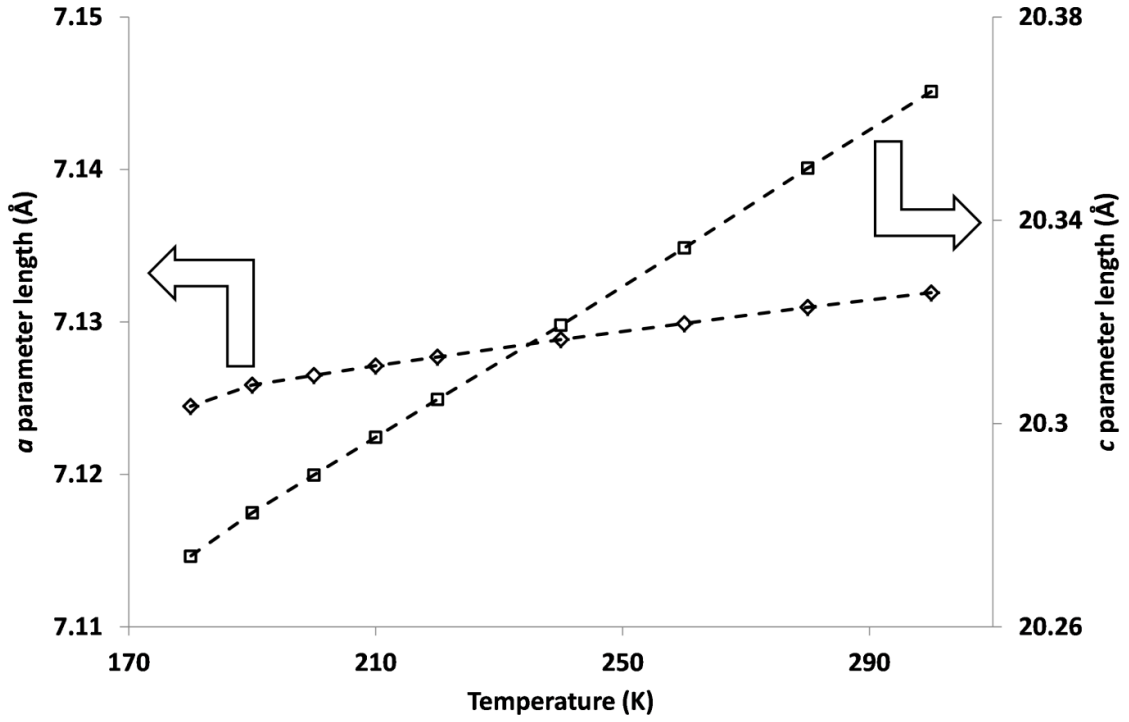

Figure 5.19: *a* and *c* unit cell parameters for $Cs_2SnCu_3F_{12}$. Dashed lines are only a guide to the eye. Axes are adjusted to represent the same percentage change in order to display lack of change in *a* parameter. Data derived from SXPD data.

Another point of interest is the temperatures of the phase transitions; these occur at different temperatures for different compositions (Table 5.7).

Table 5.7: Approximate phase transition temperatures for $A_2SnCu_3F_{12}$ solid solution (A = Rb, Cs) assuming $(CsRb)SnCu_3F_{12}$ shows a transition.

% Cs^+ on A-site	Transition temperature (K)
100	170
75	250
50	> 300
25	280
0	250

Assuming that $CsRbSnCu_3F_{12}$ does in fact show a phase transition above the surveyed temperature range then we can suggest that transition temperature shows a maximum at 50:50 Rb^+:Cs^+ A-site occupation. It is important to note, however, that opposite ends of the solid-solution do not show the same behaviours and the mid-point may show a third behaviour.

5.5 Magnetic properties of $Cs_2SnCu_3F_{12}$ powder

The magnetic properties of $Cs_2SnCu_3F_{12}$ single crystals have previously been studied but only briefly.[2] This suggested two anomalies in magnetism vs. temperature measurements; one broad peak with its maximum at ≈ 38K and a sharp peak at 20.2 K. The latter anomaly is suggested to be due to 3-dimensional magnetic ordering of a weak ferromagnetic type. As previous measurements sought to align the single crystal it is found that perpendicular to the kagome layer the inter-layer interactions cancel out. This ordering is thought to be due to the adoption of an orthorhombic distortion [2] which results in two different magnetic exchange interactions. This suggestion of two different exchanges is at odds with the structure found at 100 K; this monoclinic distortion leads to three unique Cu^{2+} – Cu^{2+} bond distances and therefore three different exchange interactions.

In order to probe the magnetic behaviour of the powder for comparison to single crystal measurements, magnetically pure samples were synthesised. Measurements were then performed at both medium field (2000 Oe) and low field (20 Oe).[k] At 2000 Oe the transition at 20.2 K is still visible but there is also a clear anomaly at ~ 53 K which signals the beginning of divergence between ZFC and FC data with lowering temperature (Figure 5.20). Unfortunately, at low temperatures (< 10 K) there is a small background due to paramagnetic impurity spins. The behaviour around the 20.2 K anomaly is qualitatively similar to that previously reported and it is suggested that the same weak ferromagnetism is occurring.

At 20 Oe there are also two transitions at the same temperatures found for 2000 Oe but in this case the behaviour is more unusual. At the first transition there is a divergence of ZFC/FC measurements but they then go onto create an approximate mirror image of each

[k] Under the direction of Prof. A. N. Vasiliev and Mr A. Golovanov, Faculty of Physics, Moscow State University.

other with the x-axis as the mirror plane. The second transition increases the absolute magnitude of the measured magnetism. Thus, the ZFC values are negative which, at first sight, might suggest diamagnetism (Figure 5.21).[I]

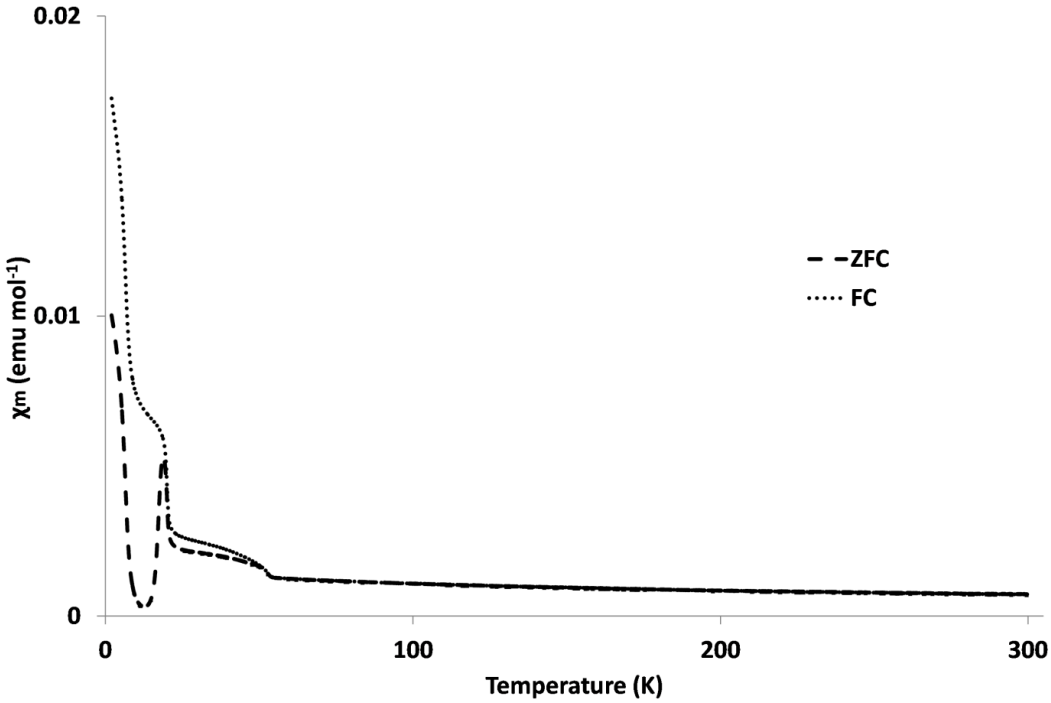

Figure 5.20: ZFC and FC measurements for $Cs_2SnCu_3F_{12}$ powder in a field of 2000 Oe. Note two transitions.

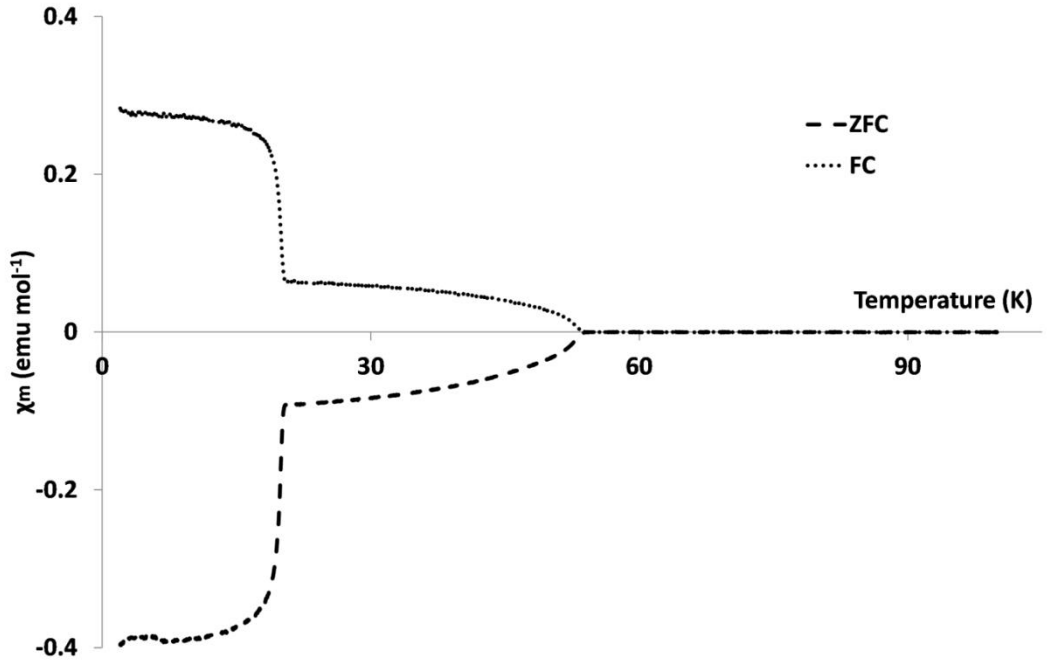

Figure 5.21: ZFC and FC measurements for $Cs_2SnCu_3F_{12}$ powder in a field of 20 Oe. Note two transitions and the negative values for ZFC data.

[I] All magnetic data available in .csv format in appendix A.5.5.

The two transitions suggest that there are possibly two structural transitions present or two phases which order magnetically at different temperatures.[m] In order to determine the correct reasoning for the two transitions the sample was reheated in a sealed copper tube with XeF_2 at 773 K for 3 days. This led to the disappearance of the higher temperature anomaly suggesting that two phases were originally present (Figure 5.22 and Figure 5.23). Note the second sample has been measured at 1000 Oe and 20 Oe. At 1000 Oe the sample appears to still give a negative value below the 20.2 K transition.

The change in magnetic measurements would appear to suggest that two phases were originally present with different ordering temperatures. SXPD data suggests that there is only one phase however – due to the high resolution it is usually possible to see subtle phase separations as shoulders on peaks or splittings. Laboratory-based XRPD was performed on both samples used for magnetic analysis although its low quality makes further analysis unreliable. There are subtle differences suggesting that a change may have taken place (Figure 5.24) but it is no way conclusive – further structural determination would be necessary or another technique such as NPD or ^{119}Sn Mössbauer to confirm the number of unique Sn^{4+} sites, for example.

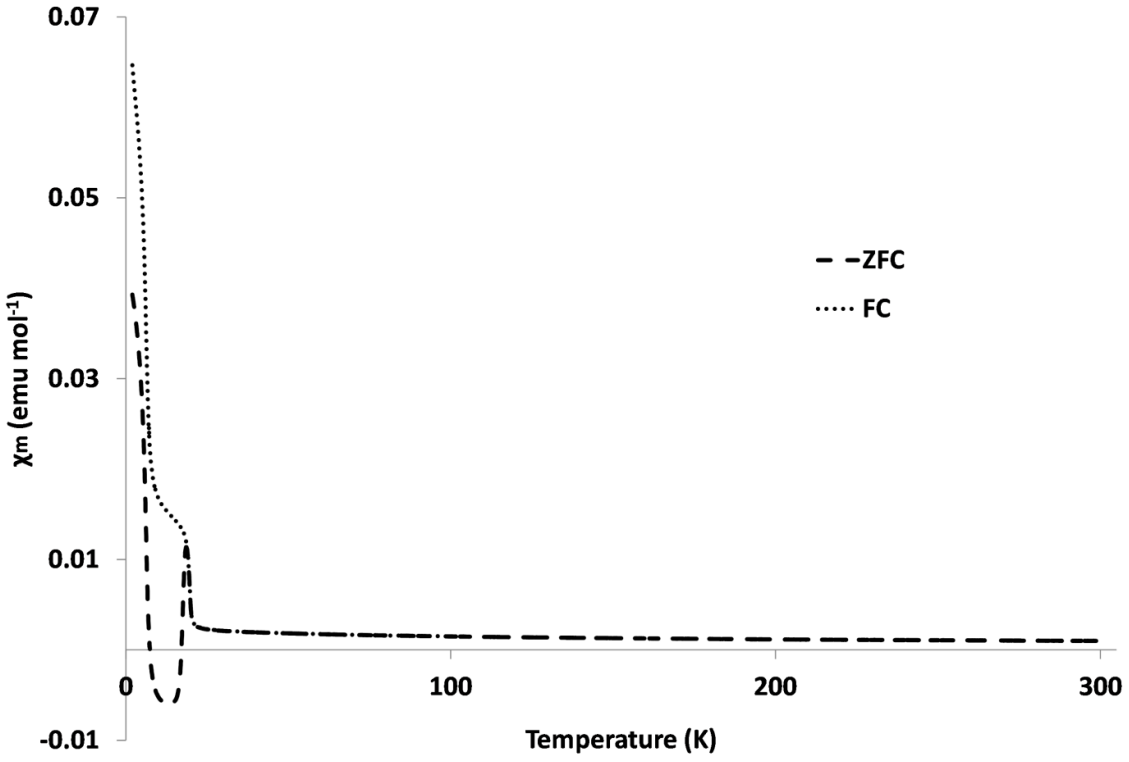

Figure 5.22: ZFC and FC measurements for $Cs_2SnCu_3F_{12}$ powder in a field of 1000 Oe. Note one transition.

[m] A different, less pure, sample has been measured which shows the same behaviour. This, magnetically impure sample was synthesised in the same manner as those samples for SXPD and NPD studies.

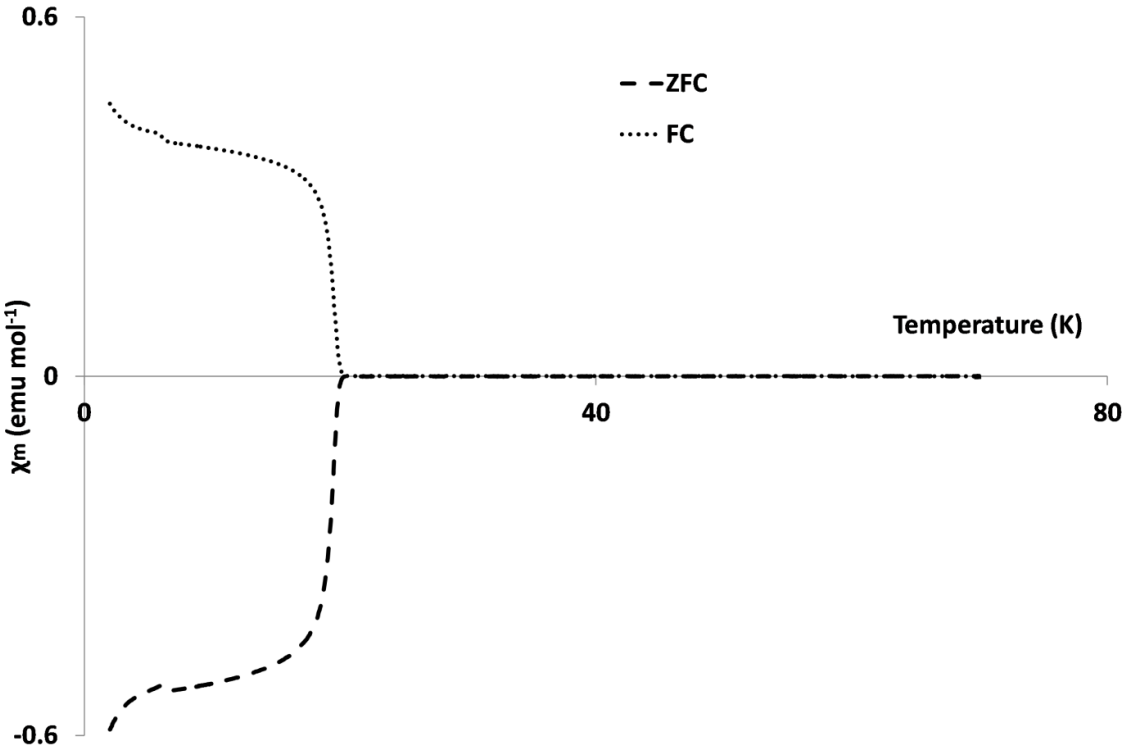

Figure 5.23: ZFC and FC measurements for $Cs_2SnCu_3F_{12}$ powder in a field of 20 Oe. Note one transition.

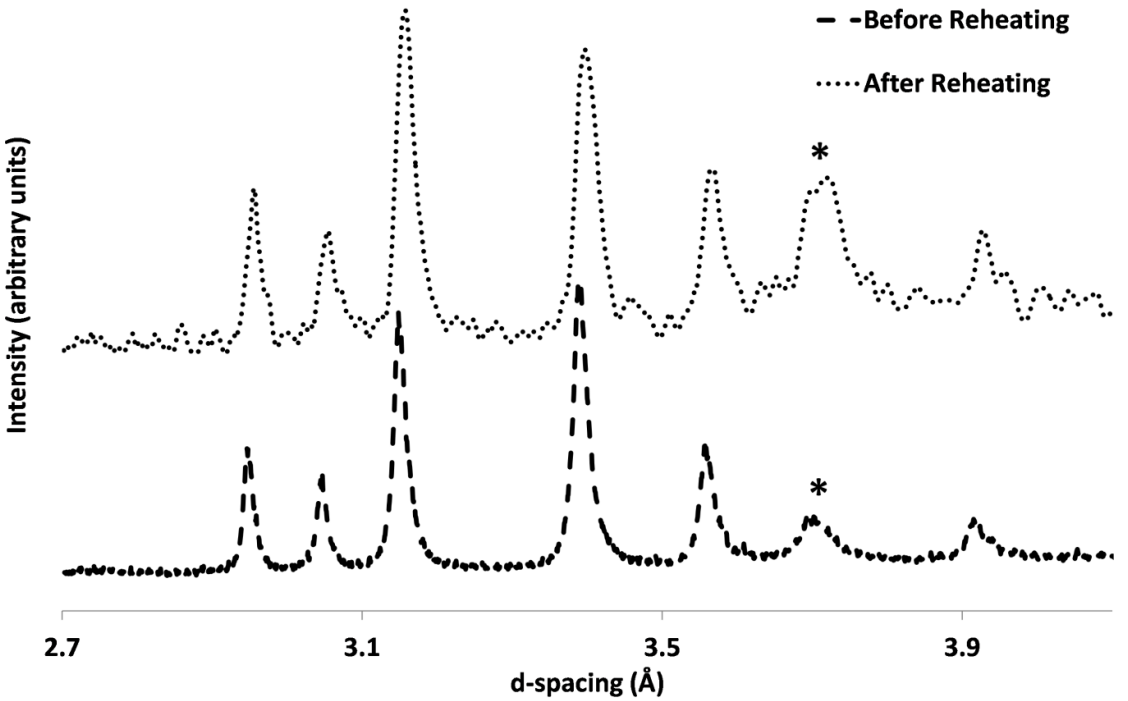

Figure 5.24: XRPD patterns for $Cs_2SnCu_3F_{12}$ before and after re-heating. * is a peak due to Cs_2SnF_6.

The nature of the negative magnetic moment or apparent diamagnetism is also not clear. A change from paramagnetism to diamagnetism is usually a sign of superconductivity but this is unlikely for this material – it is white in colour which indicates a large energy gap between the valence and conduction band. In general, superconductors are dark in colour. Most likely is an error in measurement. An opposing remnant magnetisation in the measurement equipment may freeze in a magnetic moment at low temperature and give the appearance of diamagnetism. In this case, the negative magnetic moment is very similar to the positive moment at low field which suggests that an error in sign is occurring. In this case the only way to correctly identify the cause of the apparent magnetic moment would be to exclude superconductivity by transport measurements and then low temperature NPD to identify the presence of magnetic ordering and possibly a magnetic unit cell.

5.6 Conclusions

$Cs_2SnCu_3F_{12}$ has been found to undergo an as yet unreported phase change from a rhombohedral to a primitive monoclinic unit cell much like that found for the sister phase, $Cs_2TiCu_3F_{12}$. It has also been found to show some unusual, but potentially explainable, magnetic behaviour. This magnetic behaviour also suggests the presence of a two-phase system unless annealed to completion although no evidence of this has been found in the high resolution SXPD data. Examination of the solid solution $Cs_{2-x}Rb_xSnCu_3F_{12}$ (x = 0.5, 1.0, 1.5) shows varying behaviour versus composition. $Cs_{1.5}Rb_{0.5}SnCu_3F_{12}$ appears to behave very similarly to $Cs_2SnCu_3F_{12}$ but with an elevated transition temperature. $Cs_{0.5}Rb_{1.5}SnCu_3F_{12}$ shows similar behaviour to $Rb_2SnCu_3F_{12}$ but with, again, an elevated transition temperature and in this case no second, re-entrant, phase transition. The middle-member, $CsRbSnCu_3F_{12}$, of the solid-solution appears to be closest to $Cs_2SnCu_3F_{12}$ as it is found to occur in a primitive, monoclinic unit cell at low temperature. This unit cell symmetry persists to the highest temperature surveyed (300 K), which does not allow the discrimination between $Cs_2SnCu_3F_{12}$ like behaviour or a third behaviour unrelated to either end-member.

1. K. Morita, M. Yano, T. Ono, H. Tanaka, K. Fujii, H. Uekusa, Y. Narumi and K. Kindo, *J. Phys. Soc. Jpn.*, 2008, **77**, 043707.
2. T. Ono, K. Morita, M. Yano, H. Tanaka, K. Fujii, H. Uekusa, Y. Narumi and K. Kindo, *Phys. Rev. B*, 2009, **79**, 174407.
3. S. P. Thompson, J. E. Parker, J. Potter, T. P. Hill, A. Birt, T. M. Cobb, F. Yuan and C. C. Tang, *Rev. Sci. Instrum.*, 2009, **80**, 075107.
4. A. C. Larson and R. L. Von Dreele, 2000.
5. B. H. Toby, *J. Appl. Cryst.*, 2001, **34**, 210-213.
6. B. J. Campbell, H. T. Stokes, D. E. Tanner and D. M. Hatch, *J. Appl. Crystallogr.*, 2006, **39**, 607-614.
7. A. S. Wills, Program available from www.ccp14.ac.uk, v.4.0.7

6 Structural, electrical and magnetic properties of the hexagonal ferrites, $MFeO_3$ (where M = Y, Yb or In)

In order to better understand the behaviour of a multiferroic it is sometimes helpful to substitute ions in order to observe the changes that occur and thus correlate the composition/structure with electrical and magnetic effects. In the case of $YMnO_3$ one obvious substitution is Mn^{3+} for Fe^{3+}. Both of these ions have the same Shannon radii (Fe^{3+}: 0.58 Å, Mn^{3+}: 0.58 Å both in the 5-coordinate case)[1] and are stable in the 3+ oxidation state. Synthesis techniques for $YFeO_3$, and those with A-site atoms related to Y^{3+}, have been previously reported. These have mostly used soft synthesis routes, for example solution precursor methods,[2-4] spray-ICP[5] or thin-film techniques[6] and as such have led to poorly crystalline samples. Further heating of samples has been reported to result in the irreversible formation of the orthorhombic, perovskite-like form of $YFeO_3$, indicating that the hexagonal phase is metastable;[2] this is the opposite case from $YMnO_3$.[7]

In the literature there are varying reports of the structural details; $YFeO_3$[3] and $InFeO_3$[8] have both been reported in the space group $P6_3/mmc$ – akin to the high temperature, paraelectric phase of $YMnO_3$ – whereas $YbFeO_3$ has been reported to be in the $P6_3cm$ space group, with a potentially ferrielectric structure.[9] It is of key interest to establish the details of the structures as there is significant interest in the high temperature ferrielectric → paraelectric transition in $YMnO_3$[10] and a related structure which shows the same or a related transition may be important. There are also important considerations in terms of the magnetic and electrical behaviour; $MMnO_3$ (where M = a rare earth, Y or In) have not been studied in great detail but studies in solid solutions of $YbMn_{1-x}Fe_xO_3$ have shown interesting results in terms of magnetism. Although synthesis of the hexagonal phase was only possible up to x = 0.3 it was found that the magnetic ordering temperature increases with x. This is thought to be due to increasing covalency in the Mn/Fe – O – Mn/Fe bonds. The magnetoelectric effect was also reported to be present.[11] $YMn_{1-x}Fe_xO_3$ has been synthesised up to x = 0.2 and magnetic analysis shows that T_N decreases with increasing x. This is thought to be due to competition between ferromagnetic Mn – O – Fe interactions and antiferromagnetic Mn – O – Mn interactions. This doesn't occur in the ytterbium analogue as the magnetic Yb^{3+} ions act to strengthen the manganese influence by allowing interaction along the *c*-axis.[12]

6.1 Experimental

The synthesis of hexagonal $YFeO_3$, $YbFeO_3$ and $InFeO_3$ has been reported before using many different techniques. In the case of $YFeO_3$ and $YbFeO_3$ it was found that the citrate-based sol-gel technique was the simplest procedure.[3] For $InFeO_3$ a hydroxide precipitate method was chosen.[13]

6.1.1 Synthesis of $YFeO_3$ and $YbFeO_3$

Stoichiometric amounts of $Fe(NO_3)_3 \cdot 9H_2O$ (99.99 %, Sigma Aldrich) and $Y(NO_3)_3 \cdot 6H_2O$ (99.9 %, Sigma Aldrich) or $Yb(NO_3)_3 \cdot 5H_2O$ (99.999 %, Sigma Aldrich) were dissolved in deionised water at ~ 330 K with stirring. Citric acid (99.5 %, Sigma Aldrich) was then added in a ratio of 2 moles citric acid to 1 mole metal nitrates. Aqueous ammonia was then added in order to neutralise the solution before evaporating to a gel at a temperature of 330 – 380 K. In order to decompose the gel it was heated on a hot plate to approximately 620 K which leads to a dark

brown/black powder. This powder was then placed in an alumina crucible and heating in air at 973 K for ten hours.

6.1.2 Synthesis of $InFeO_3$

Stoichiometric amounts of $InCl_3$ (99.999 %, Sigma Aldrich) and $Fe(NO_3)_3 \cdot 9H_2O$ (99.99 % Sigma Aldrich) were dissolved in deionised water at room temperature. Concentrated aqueous ammonia was then added which led to the precipitation of the metal hydroxides which could then be collected by filtration under suction. The resulting orange crystallites were then dried in air before calcination at 973 K for ten hours.

6.1.3 Analytical techniques

Laboratory based X-ray powder diffraction (XRPD) was performed using a Stoe Stadi-P diffractometer operating in transmission mode and utilising Fe $K_{\alpha 1}$ radiation.

Neutron powder diffraction (NPD) was performed at the GEM beamline, ISIS pulsed neutron and muon source, Oxfordshire.[14] Samples of both $YFeO_3$ and $YbFeO_3$ of ~ 2 g [a] each were loaded into cylindrical vanadium cans. For $YFeO_3$, patterns were collected at 10, 35, 60, 85, 110, 135, 160, 185, 210, 325, 260, 280 and 298 K. For $YbFeO_3$ patterns were collected at 10, 50, 90, 110, 130, 150, 160, 170, 180, 190, 210, 230, 260, 298, 373, 473, 573, 673, 723, 773, 823 and 873 K.

Synchrotron X-ray powder diffraction (SXPD) was carried out at beamline I11, Diamond Light Source Ltd., Oxfordshire.[15] For $InFeO_3$ the sample was loaded into a glass capillary and subject to study at room temperature. Low temperature data (30 K) was collected for $YFeO_3$ using a closed cycle PheniX cryostat (Oxford Cryosystems) which had been adapted to hold samples in a capillary geometry. The powder was attached to a copper wire using glycerol. In both cases multi-analyser crystal detectors were used.

Rietveld refinement was performed using GSAS [16] and the EXPGUI interface.[17] This analysis sought to fit lattice parameters, phase fractions, peak profile shape (both Gaussian and Lorentzian) and thermal parameters (grouped by atom type).

Magnetic measurements were performed on a Quantum Designs MPMS-XL SQUID. Powder samples were mounted in gelatine capsules before being secured in plastic straws. The straws were then mounted on the end of a standard rod. Data were recorded in a field of 10000 Oe while warming the sample from 2 K to 300 K in both cooling out of field (ZFC) and cooling in field (FC) cycles.

Dielectric measurements were performed on pressed powder compacts of $YFeO_3$ and $YbFeO_3$. $YFeO_3$ had platinum electrodes sputtered onto the circular faces of the pellet and $YbFeO_3$ was subject to the application of conductive silver paint followed by curing at 373 K. The dielectric constant and dielectric loss was determined for both samples between 50 and 300 K at frequencies between 100 Hz and 10 MHz using an Agilent 4294A AC impedance

[a] The samples had a particularly low density, possibly as a result of microstructure.

analyser. Polarisation/field measurements were conducted up to ~ 25 kV cm^{-1} and between 1 Hz and 2 kHz on an aixACCT TF2000 analyser.

^{57}Fe Mössbauer spectroscopy was conducted using a constant acceleration Wissel spectrometer in transmission mode.[b] This utilised a ^{57}Co/Rh γ-ray source and was calibrated relative to α-Fe. Lorentzian line fitting was performed using RECOIL software.

6.2 Results

The results and discussion will be presented separately as there are a number of techniques in use which combine to give an overall picture.

6.2.1 Crystallography and structure of $MFeO_3$

The structure of $YFeO_3$ has previously been reported as $P6_3/mmc$ (a ≈ 3.5099(3) Å, c ≈ 11.759(2) Å)[3] but NPD experiments show the presence of super-structure peaks which suggest a cell of $\sqrt{3}a$ parameter (a = 6.0805(5) Å, c = 11.7637(11) Å) and this is fitted well in the $P6_3cm$ space group previously reported for $YMnO_3$ (Figure 6.1). There is severe peak broadening due to the small crystallites produced by the soft synthesis techniques.[c]

Although a good fit is achieved for $YFeO_3$ at room temperature it is clear there is an area of poor fit between d ≈ 1.6 – 2.2 Å (Figure 6.2). The reasons for this are unknown but will be discussed further in Section 6.3.1. Due to this poorly fitted area and the large peak width the $P6_3cm$ model can only be described as approximate at this stage and so it would be unrealistic to extract much more data than lattice parameters. Observing the changes in lattice parameter from 10K to ambient temperature it is found that the evolution of the a parameter is steady whereas for the c parameter we find little change over the whole range (Figure 6.3).[d]

$YbFeO_3$ was also analysed by NPD and confirmed to be present in the $P6_3cm$ space group at room temperature with a = 5.9882(6) Å, c = 11.7440(14) Å (Figure 6.4). This reduction in unit cell size is commensurate with the smaller size of Yb^{3+} as compared to Y^{3+}. Once again there is an anomaly in the range d ≈ 1.6 – 2.2 Å and the same peaks are found to be responsible. This further suggests that there may be some unusual structural behaviour occurring. $YbFeO_3$ was observed above and below ambient temperature (Figure 6.5). In this case we find below ambient temperature the c parameter once again shows very little change whereas the a parameter appears to decrease at a normal rate. There is a curious anomaly between 110 and 210 K were the change in lattice parameter is no longer linear. Above room temperature we find that the lattice parameters increase uniformly until 873 K where there is a decrease in the c parameter. This decrease may be indicative of a further change in the sample although further measurements would be required in order to gain further information.

[b] Data collected and processed by Dr. S. D. Forder, Sheffield Hallam University, Sheffield, U.K.
[c] This crystallite size was found to be approximately 10 nm from transition electron microscopy.
[d] All refinements and tables of lattice parameters as a function of temperature are included in appendix A.6.2.1; this is for all M.

$InFeO_3$ was studied by SXPD and this suggested the high symmetry, non-polar space group previously reported;[8] $P6_3/mmc$. This can be assigned despite a significant broadening found for the sample (Figure 6.6). The unit cell parameters found are a = 3.32771(6) Å, c = 12.1887(4) Å which represents a decrease in a (when multiplied by $\sqrt{3}$ for comparison) but an increase in c. This is thought to be related to less interaction of the A^{3+}-site ion with the equatorial O^{2-} of the FeO_5 trigonal bipyramid. This occurs as the radius of In^{3+} is sufficiently small (Y^{3+}: 0.900 Å, Yb^{3+}: 0.868 Å, In^{3+}: 0.800 Å for 6-coordinate [1]) as to be unable to support the required coordination sphere of 7 O^{2-} for the $P6_3cm$ unit cell like that found for $YMnO_3$. This leads to the trigonal bipyramidal layer not corrugating in order to maintain the higher A-site coordination and therefore appearing as a flat layer of corner sharing FeO_5 trigonal bipyramids.

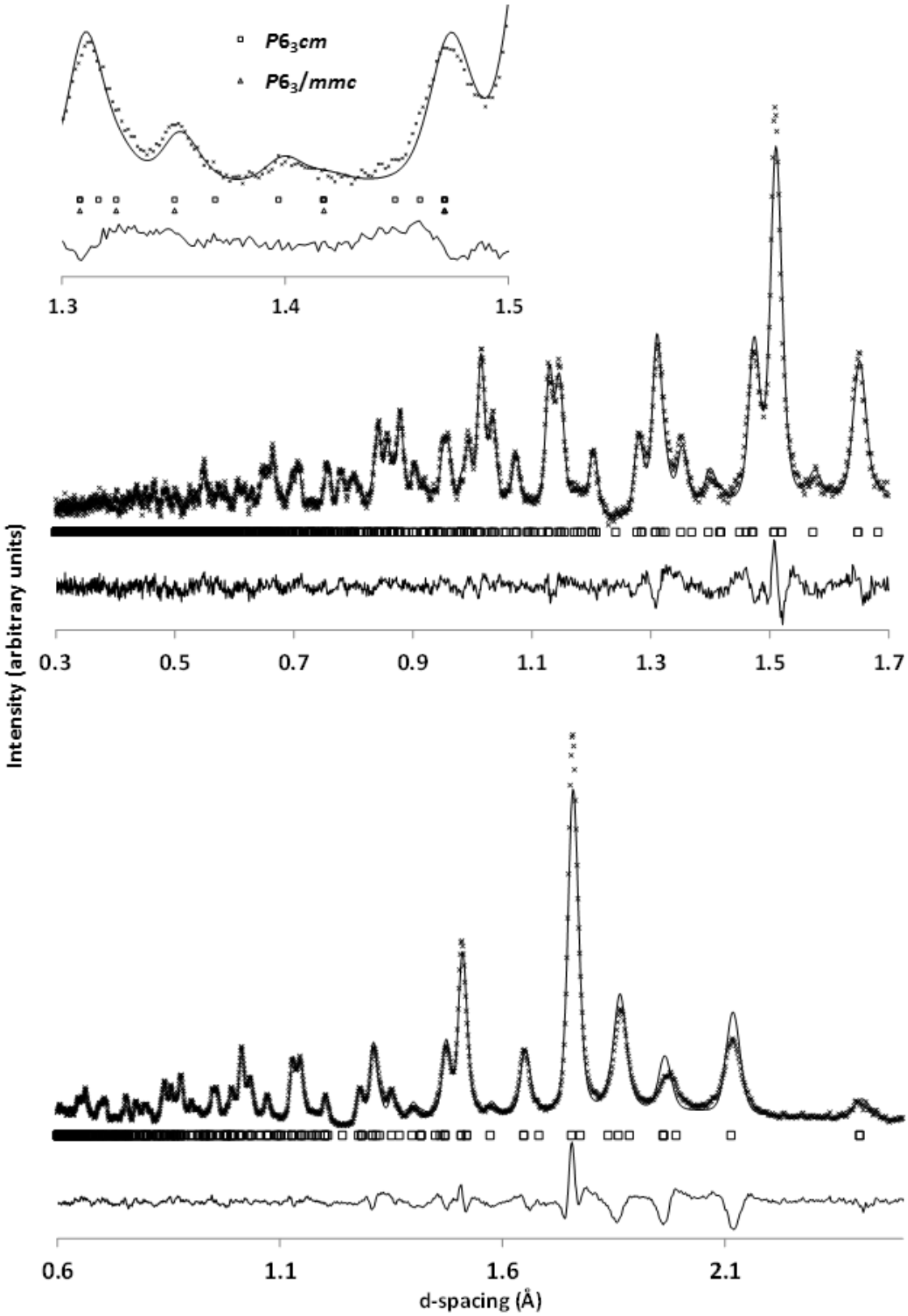

Figure 6.1: NPD patterns for $YFeO_3$ at ambient temperature. Top pattern is backscattering bank, bottom pattern is 91.3 ° bank, inset shows peak positions for *P*6$_3$*cm* and *P*6$_3$/*mmc* and in particular an unassigned super-structure peak for the latter symmetry.

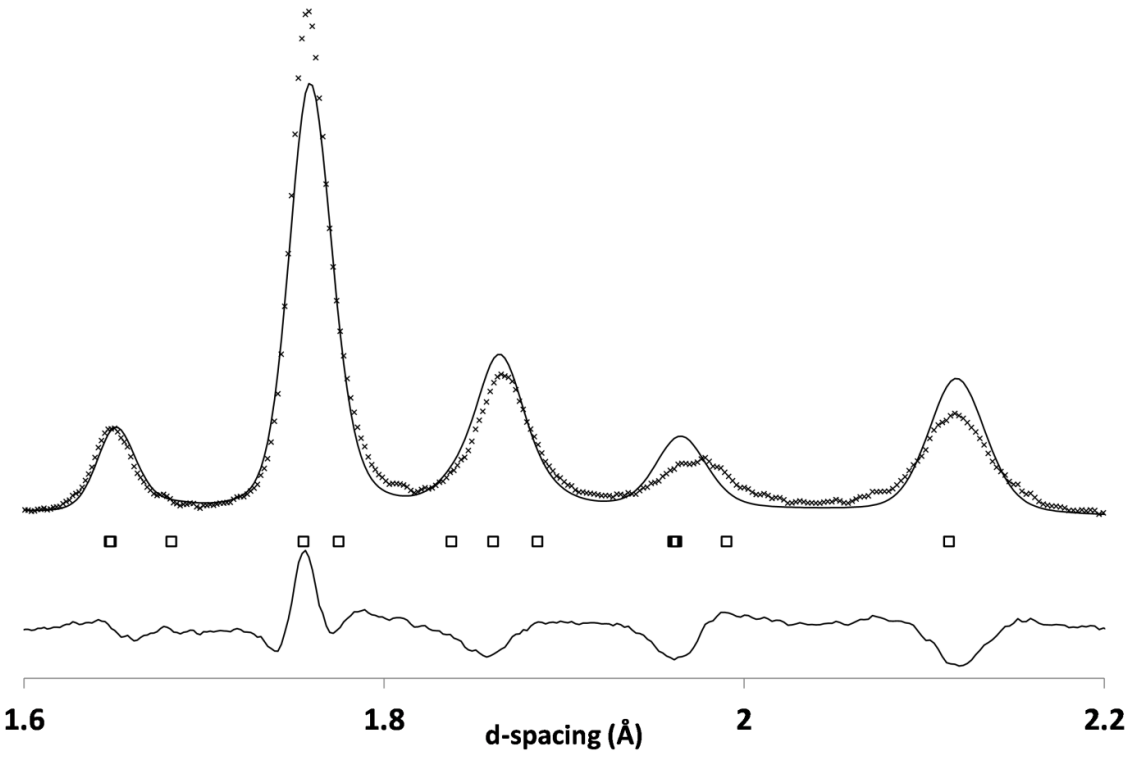

Figure 6.2: NPD pattern and Rietveld fit for $YFeO_3$ showing poorly fitted area between d = 1.6 and 2.2 Å.

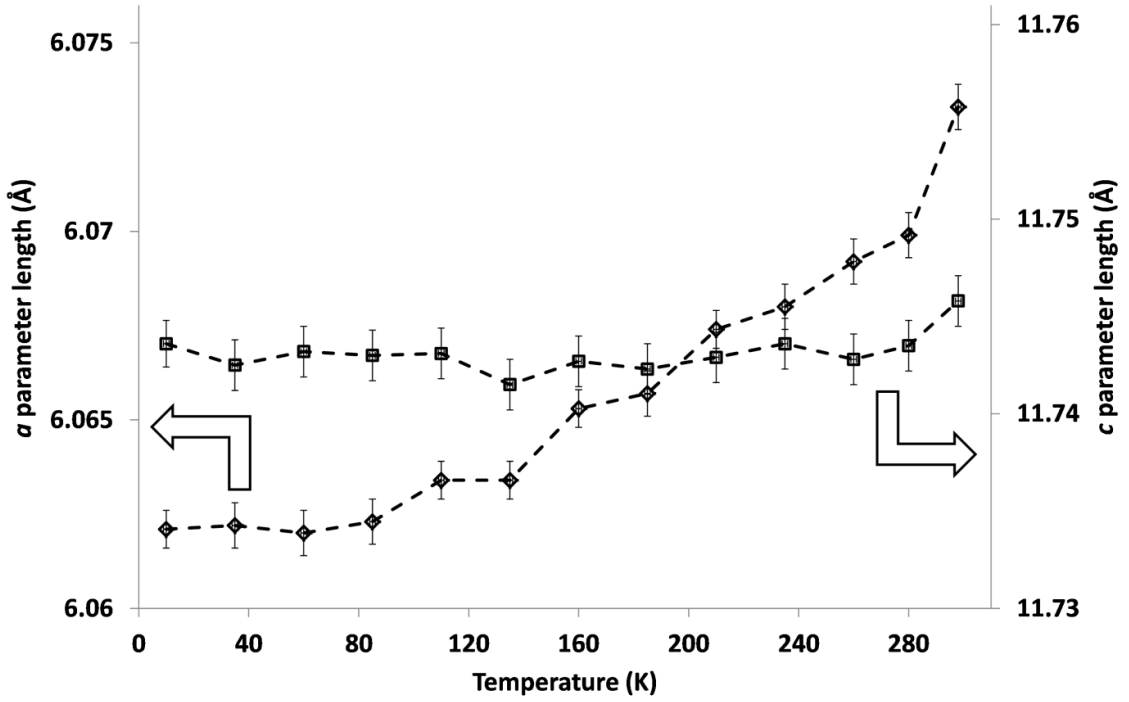

Figure 6.3: Change in lattice parameters for $YFeO_3$ with temperature as derived from NPD data. Dashed lines are only a guide to the eye. Axes set so as to show same percentage change.

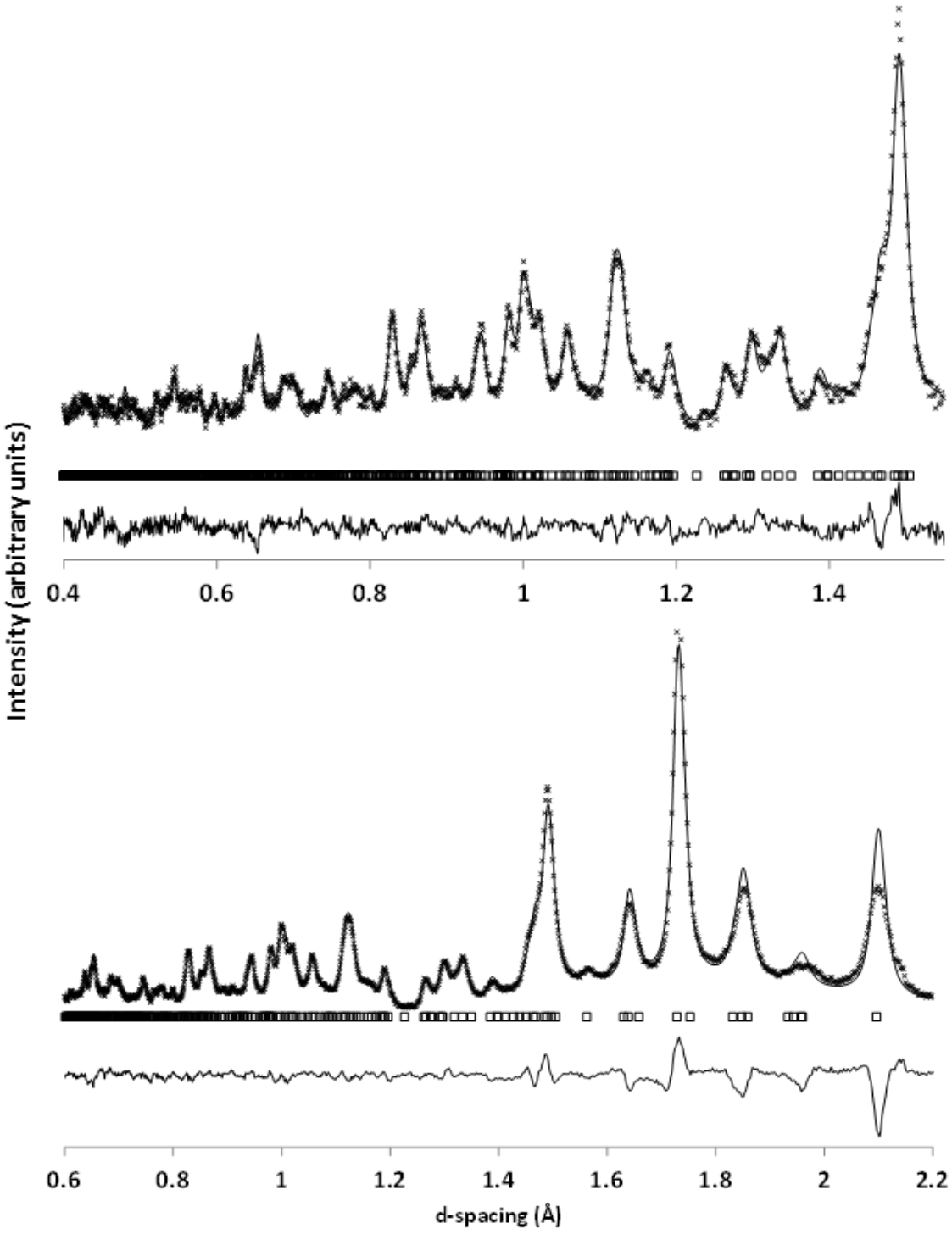

Figure 6.4: NPD patterns for $YbFeO_3$ and Rietveld fit for the *P*6_3*cm* space group. Top pattern is backscattering bank and bottom pattern is 91.3 °. Both patterns taken at ambient temperature.

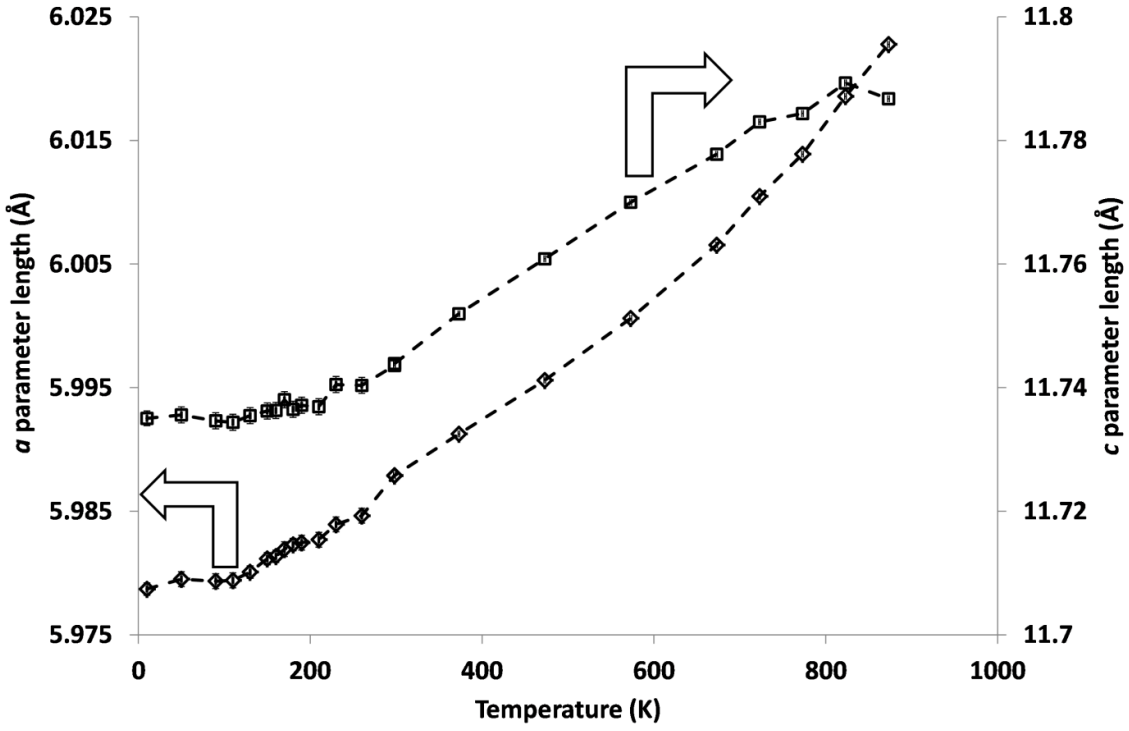

Figure 6.5: Lattice parameters for $YbFeO_3$ versus temperature as derived from NPD data in the $P6_3cm$ space group.

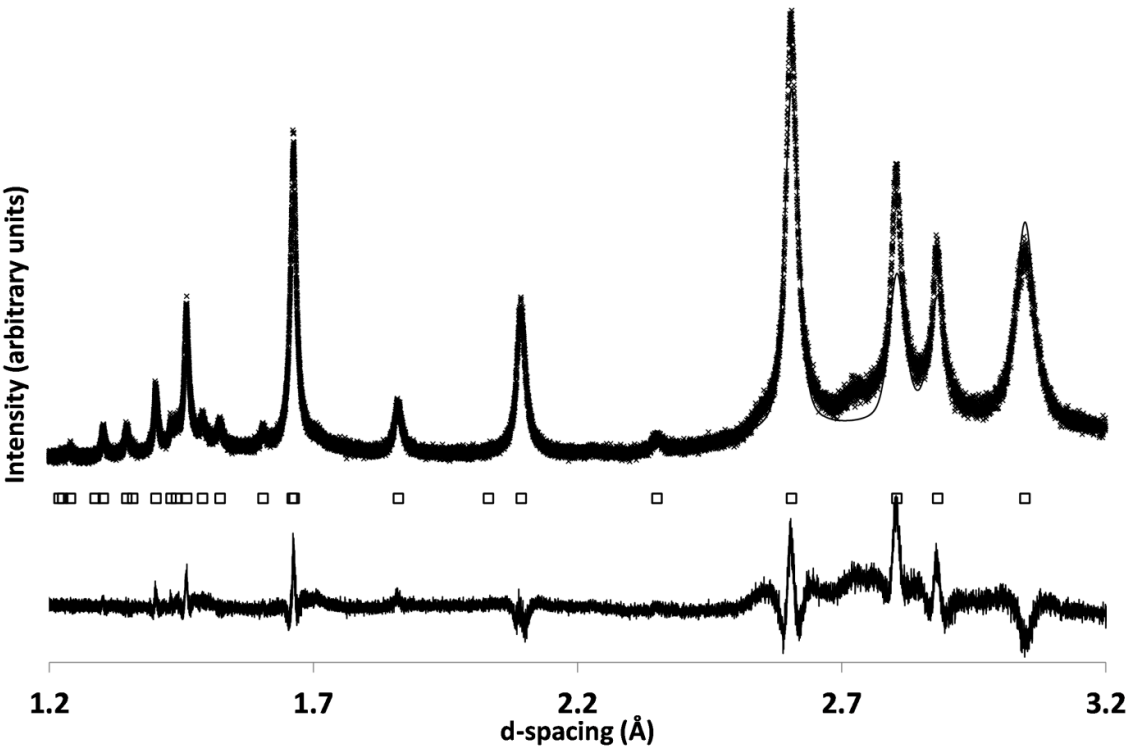

Figure 6.6: SXPD pattern of $InFeO_3$ at RT fitted with $P6_3/mmc$ space group.

6.2.2 Electrical studies of $MFeO_3$

Dielectric data for both $YFeO_3$ and $YbFeO_3$ show anomalies below room temperature which take the form of a maximum in the real part of permittivity (ε') along with a coincident maximum in the imaginary part (ε")[ef].

For $YFeO_3$ a maximum in (ε') is observed at ~ 130 K alongside a coincident, yet subtle, maximum in (ε"). The same effect is observed and more pronounced in $YbFeO_3$; the temperature at which this occurs is also increased to 150 K (Figure 6.7).

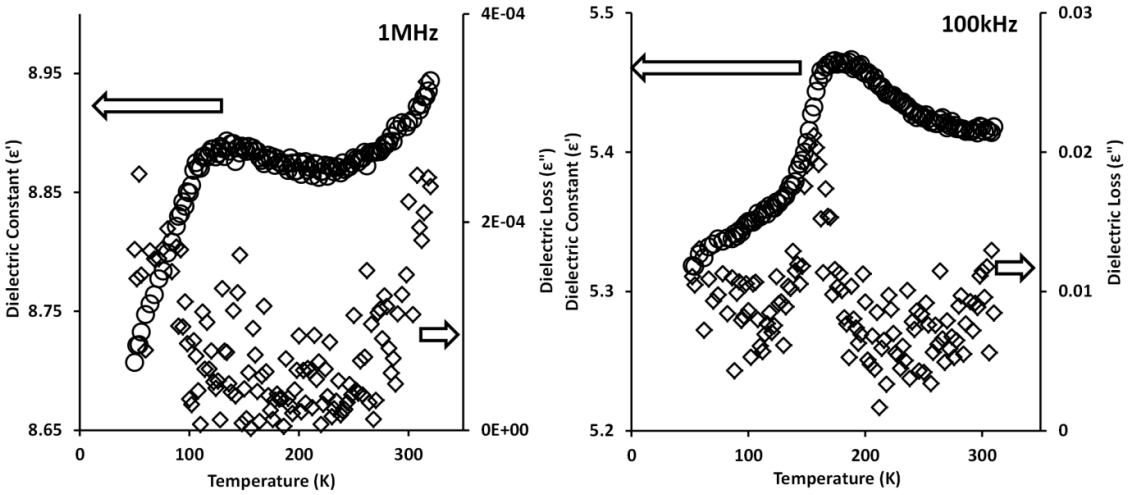

Figure 6.7: Dielectric constant (ε') and loss (ε") for $YFeO_3$ (left) and $YbFeO_3$ (right) below ambient temperature.

Such changes in dielectric constant are often indicative of structural transitions as there is a direct relationship between it and the arrangement of ions (and also bonds). Another possibility is an interaction between the magnetic and electronic properties of the system. This will be investigated further in Section 6.3.2.

Polarisation vs. field measurements were attempted on pellets of both $YFeO_3$ and $YbFeO_3$ but hysteresis loops characteristic of a ferro/ferrielectric were not acquired. This may be a result of the microstructure, rather than an intrinsic sample property, although it is difficult to alter the microstructure while retaining the hexagonal polymorph of $YFeO_3$, due to the requirements of synthesis.

6.2.3 Magnetic properties of $MFeO_3$

None of the $MFeO_3$ investigated appear to follow the Curie-Weiss law at the highest temperature measured, 300 K. This makes acquiring quantitative data challenging but there are some points which can be noted.

Both $YFeO_3$ and $InFeO_3$ appear to show approximately similar behaviour and so may have the same qualitative behaviour. $1/\chi$ vs. T for $YFeO_3$ does not show a linear region even up

[e] It is noted that the dielectric constant is particularly low for these materials and it is suggested that this may be as a result of the microstructure.
[f] All dielectric data can be found in appendix A.6.2.2 in .csv format

to ambient temperature which suggests that a truly paramagnetic state is never reached – at the very least the system does not follow the Curie-Weiss law. There is also a divergence of the zero field cooled (ZFC) and field cooled (FC) data which begins at ~ 21 K. The lack of adherence to the Curie-Weiss law is confirmed by the negative gradient of $\chi_m T$ vs. T; a reasonably simple paramagnetic system should show a plateau (Figure 6.8). $InFeO_3$ is similar except there is a more pronounced linear region between 200 and 300 K in a plot of $1/\chi$ vs. T. The divergence in this case appears at a higher temperature, ~ 36 K. Once again there is no plateau in $\chi_m T$ vs. T (Figure 6.9) indicating that despite the linear region in the $1/\chi$ vs. T data there is still the possibility that paramagnetism is not the dominant behaviour.[g]

There are two spin states available to Fe^{3+} (d^5) in a trigonal bipyramidal geometry; S = 3/2 giving $\chi_m T$ of 1.879 emu K mol^{-1} and S = 5/2 giving $\chi_m T$ = 4.385 emu K mol^{-1}. A plot of $\chi_m T$ vs. T should give the relevant value when at the point of magnetic saturation (i.e. a plateau) and for our system we find that $YFeO_3$ gives $\chi_m T$ = 1.24 emu K mol^{-1} and $InFeO_3$ gives $\chi_m T$ = 0.925 emu K mol^{-1} at 300 K. These numbers are far from the lowest value expected indicating that higher temperature measurements would be required. If the $1/\chi$ vs. T data is observed between 200 and 300 K, however it is possible to get some interesting results. Application of the Curie-Weiss law ($\chi = C/(T - T_{CW})$) reveals that a negative Curie-Weiss temperature (T_{CW}) is found for both $YFeO_3$ and $InFeO_3$ and it is also possible to extract Curie constants (C) (Table 6.1).

Table 6.1: Quantitative magnetic data for $YFeO_3$ and $InFeO_3$ derived from $1/\chi$ vs. T plots between 200 and 300 K in a field of 10000 Oe.

$YFeO_3$	
Curie constant, C, (emu K mol_{Cu}^{-1})	4.60
Effective moment, μ_{eff}, (μ_{BM})	6.07
Curie-Weiss temperature, T_{CW}, (K)	-810
$InFeO_3$	
Curie constant, C, (emu K mol_{Cu}^{-1})	2.38
Effective moment, μ_{eff}, (μ_{BM})	4.37
Curie-Weiss temperature, T_{CW}, (K)	-474

From Table 6.1 we can see that there is a large difference between the magnetic moments of the two samples. For a system with S = 3/2 we would expect μ_{eff} = 3.87 μ_{BM} and for S = 5/2, μ_{eff} = 5.92 μ_{BM}. We can see from that data that $YFeO_3$ would appear to be in the 5/2 spin state and $InFeO_3$ is closer to the 3/2 spin state. The Curie-Weiss temperatures are also of interest as the high negative magnitudes suggest strongly antiferromagnetically coupled systems. $InFeO_3$ appears to less strongly interacting than $YFeO_3$, however and this may be related to the larger inter-layer spacing found for $InFeO_3$. A system exhibiting high-spin and low-spin with the change of only one magnetically passive ion would be unusual so caution is advised in this interpretation – there is still no clear magnetic saturation at this temperature and high temperature measurements would be required to confirm these

[g] All magnetic data is present in appendix A.6.2.3 in .csv format for all M.

calculations. There is agreement of the data for $YFeO_3$ with that previously observed, however.[18]

The low temperature divergence is also of interest as it indicates a degree of spin freezing or possibly, superparamagnetism, the latter being common in materials with a particularly small particle size. With the large negative Curie-Weiss temperatures calculated, though, any ordering is unlikely to be ferromagnetic and more likely to be due to a weak net magnetic moment due to canting or only partially cancelled spins.

$YbFeO_3$ shows slightly different behaviour but there is still no strict following of the Curie-Weiss law approaching room temperature (Figure 6.10). There is also a more subtle divergence between ZFC and FC data beginning at ~ 18 K. Once again examination of a plot of $\chi_m T$ vs. T shows that magnetic saturation has not been reached and the maximum value of $\chi_m T$ reached is 3.35 emu K mol^{-1}. In $YbFeO_3$ there will also be a magnetic contribution from Yb^{3+} (f^{13}) and so the expected values for this system would be 4.45 emu K mol^{-1} for Fe^{3+} S = 3/2 and 6.95 emu K mol^{-1} for Fe^{3+} S = 5/2. It is possible to calculate some quantitative values from a plot of $1/\chi$ vs. T (between 200 and 300 K) (Table 6.2).

Table 6.2: Quantitative magnetic data for $YbFeO_3$ derived from $1/\chi$ vs. T plots between 200 and 300 K at a field of 10000 Oe.

	$YbFeO_3$
Curie constant, C, (emu K mol_{Cu}^{-1})	5.78
Effective moment, μ_{eff}, (μ_{BM})	6.80
Curie-Weiss temperature, T_{CW}, (K)	-217

The Curie constant yields an unexpected value for the effective moment in this case, 6.798 μ_{BM}. This is intermediate between the two expected values of 5.968 μ_{BM} for a system with Fe^{3+} in a 3/2 spin state and 7.46 μ_{BM} for a system with Fe^{3+} in a 5/2 spin state. It is difficult to draw conclusions in such a situation but it is possible that Curie-Weiss paramagnetism is not taking place in the area studied. The Curie-Weiss temperature is also suspiciously small given the known values for $InFeO_3$ and $YFeO_3$ although still indicates predominantly strong antiferromagnetic coupling.

The divergence of ZFC/FC is different from that found for $YFeO_3$ and $InFeO_3$ suggesting different behaviour. In this case it appears that superparamagnetism is not the case and there may be some ferromagnetic freezing. It is also suggested that Yb^{3+} also participates in the magnetic ordering at reduced temperature.

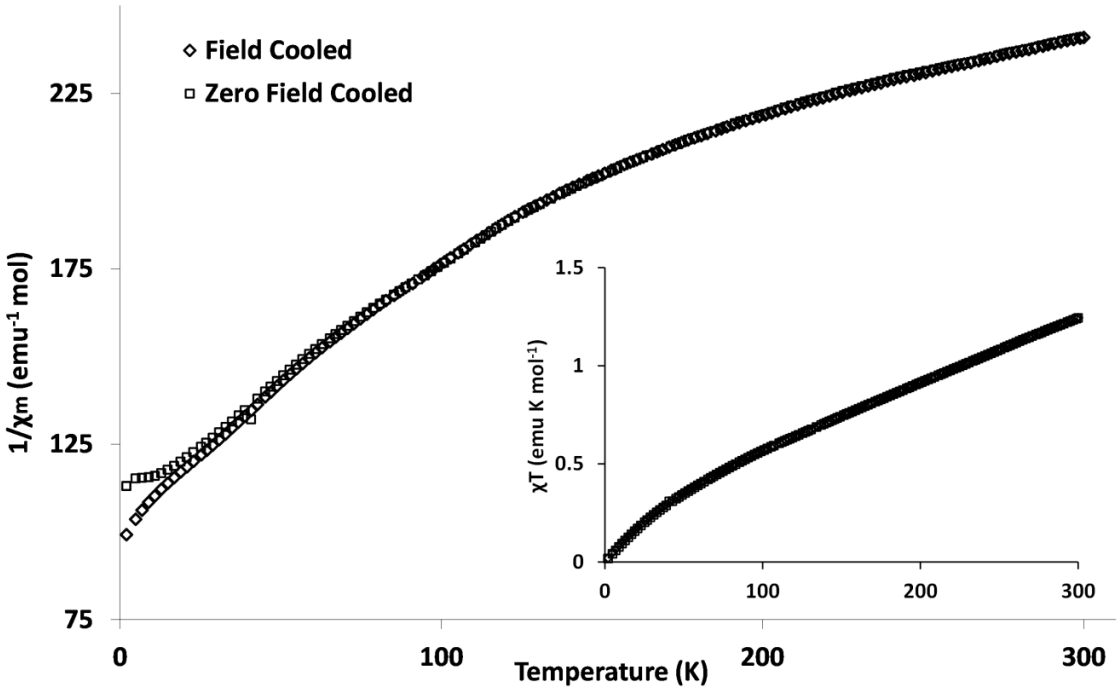

Figure 6.8: $1/\chi_m$ vs. T for $YFeO_3$ and $\chi_m T$ vs. T (inset). Data collected in a field of 10000 Oe.

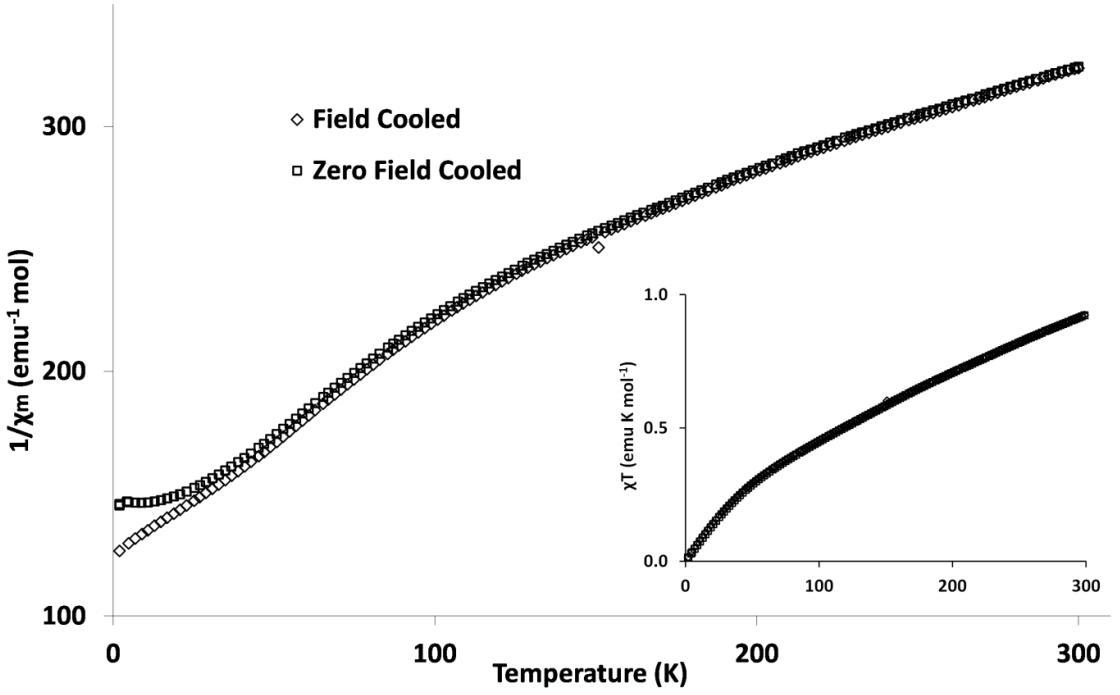

Figure 6.9: $1/\chi_m$ vs. T for $InFeO_3$ and $\chi_m T$ vs. T (inset). Data collected in a field of 10000 Oe.

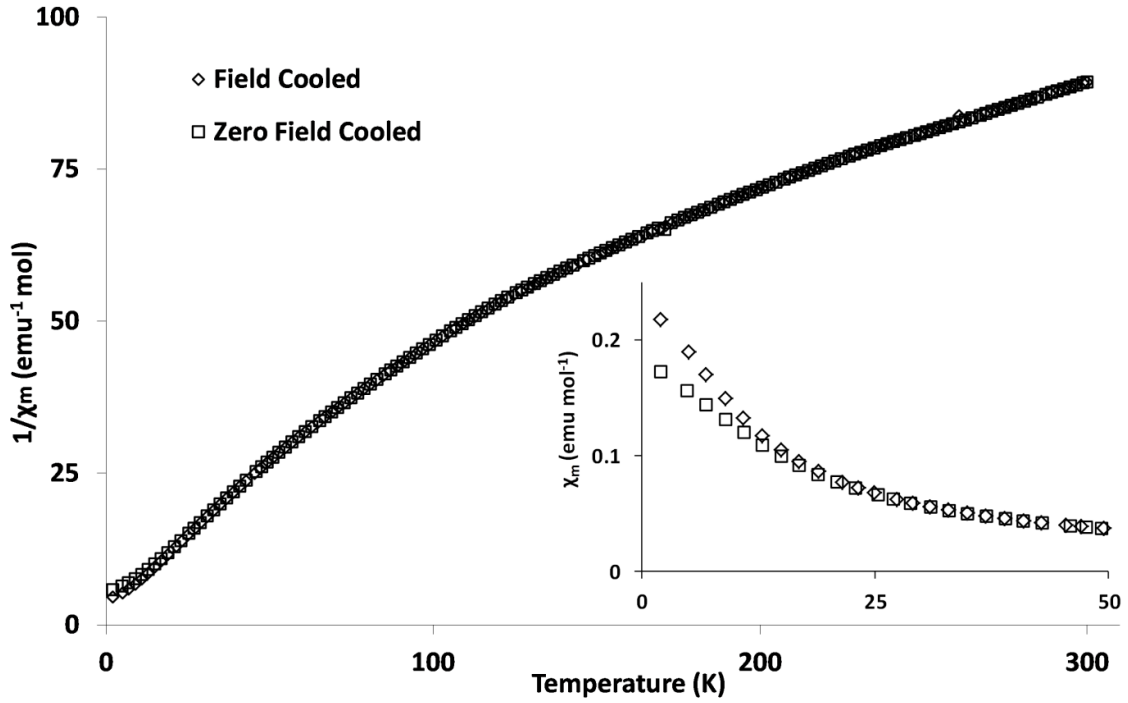

Figure 6.10: $1/\chi_m$ vs. T for $YbFeO_3$ and χ_m vs. T (inset) showing subtle divergence of ZFC and FC measurements. Data collected at 10000 Oe.

6.2.4 Mössbauer studies of $MFeO_3$

$MFeO_3$ was subject to ^{57}Fe Mössbauer spectroscopy in order to probe the number and nature of unique iron sites present within the structure. Both $YFeO_3$ and $YbFeO_3$ show two doublets with isomer shifts of expected values for Fe^{3+}. The data can be modelled by two doublets of approximately 1:1 ratio (Figure 6.11) which agrees with previous observations of $YbFeO_3$.[5] A small sextet is observed in the $YFeO_3$ spectrum which may be assigned as α-Fe_2O_3 or is possibly related to superparamagnetism. In order to conclusively assign the sextet, variable temperature Mössbauer spectroscopy would be required in order to observe any change in overall contribution. $InFeO_3$ is similar in appearance to $YFeO_3$ but in this case it is found that the spectrum is well fitted by a single doublet; there is also a sextet present (Figure 6.11). This indicates that where $YFeO_3$ and $YbFeO_3$ have two distinct Fe^{3+} sites, $InFeO_3$ has only one. This single doublet has previously been observed in $InFeO_3$.[13] A more recent study has found the same doublet for $YFeO_3$ but in this case the doublets are less evenly matched, 78:22 ratio, suggesting the Fe^{3+} sites are not equally represented.[18]

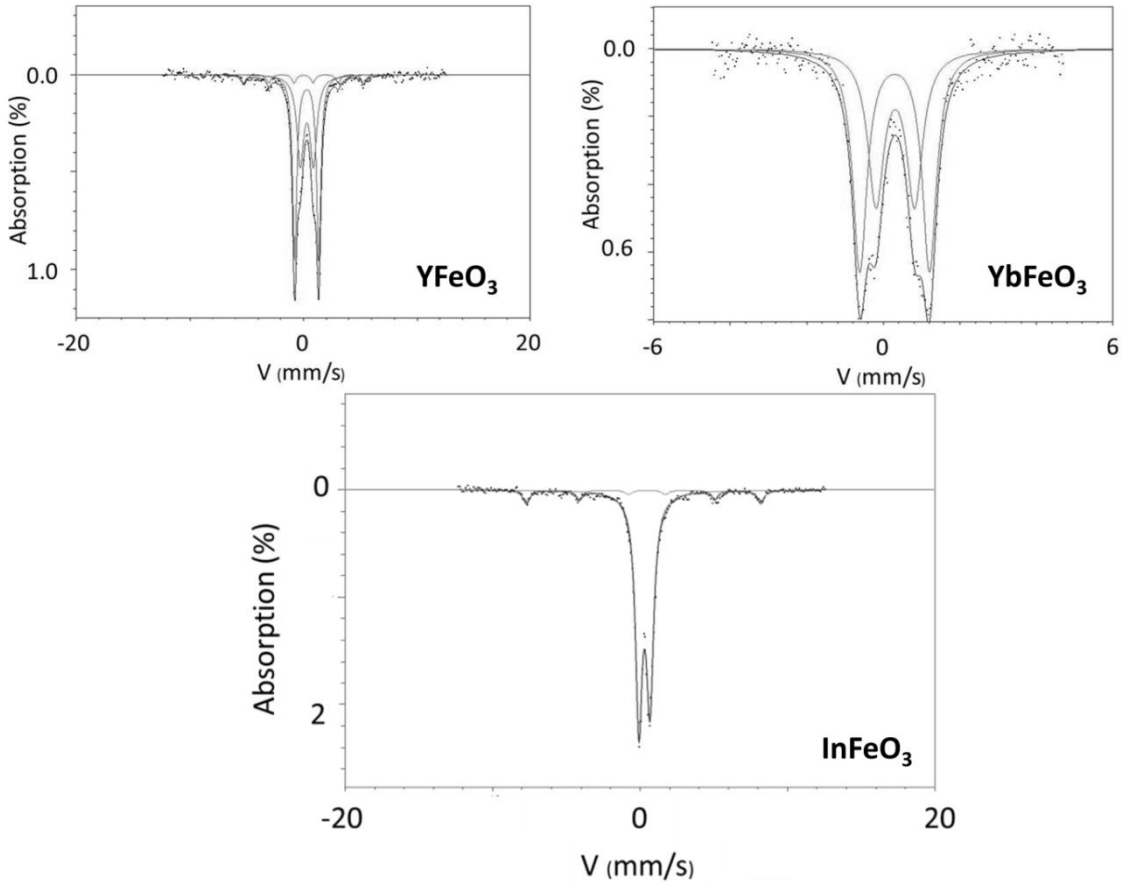

Figure 6.11: Fitted Mössbauer spectra for $MFeO_3$.

Table 6.3: Mössbauer parameters for $YFeO_3$, $YbFeO_3$ and $InFeO_3$ with α-Fe_2O_3 included for comparison.[h]

$YFeO_3$	CS (mm/s)	QS (mm/s)	w+ (mm/s)	w-/w+	Area (%)
Doublet 1	0.29	2.13	0.22	1	52.5
Doublet 2	0.30	1.18	0.37	1	39.7
	CS (mm/s)	QS (mm/s)	H (T)	w3 (mm/s)	Area (%)
Sextet	0.02	0.00	32.8	0.22	7.80
$YbFeO_3$	CS (mm/s)	QS (mm/s)	w+ (mm/s)	w-/w+	Area (%)
Doublet 1	0.29	1.82	0.23	1	56.5
Doublet 2	0.31	1.01	0.25	1	43.5
$InFeO_3$	CS (mm/s)	QS (mm/s)	w+ (mm/s)	w-/w+	Area (%)
Doublet 1	0.31	0.75	0.32	0.92	89.3
	CS (mm/s)	QS (mm/s)	H (T)	w3 (mm/s)	Area (%)
Sextet	0.37	-0.12	49.3	0.28	10.7
α-Fe_2O_3[19]	0.45	-0.17	50.7		

[h] CS = chemical shift relative to a predefined standard – in this case α-Fe_2O_3; QS = "quadrupole splitting" – the distance between the two peak maxima; w+ = line width of high velocity peak; w-/w+ is asymmetry in low and high velocity line widths; H = effective hyperfine fields; w3 = line width of the most intense sextet peak.

6.3 Discussion

It is of note that in the results there are a number of phenomena that may benefit from using more than one technique to understand them. The anomalies present in the NPD data for $YFeO_3$ and $YbFeO_3$ (6.3.1), coincident anomalies in magnetic, electrical and structural behaviour (6.3.2) and the low temperature magnetic behaviour (6.3.3) all require different perspectives in order to build an understanding of them.

6.3.1 A two-phase model

The presence of the anomalous, poorly fitted peak at d ≈ 1.6 – 2.2 Å in the NPD data suggests that the proposed $P6_3cm$ model derived from ambient temperature $YMnO_3$ is not completely correct. There does not appear to be an impurity which explains this anomaly nor does it appear to be the result of preferential orientation. The Mössbauer spectroscopy data is also of interest as (discounting the small sextet in $YFeO_3$) there is an indication that there are two distinct Fe^{3+} sites within the sample. In the $P6_3cm$ model there is only one Fe^{3+} site. This might indicate that the space group is wrong particularly as the approximate site occupancies are 50:50. Both $YFeO_3$ and $YbFeO_3$ give no indication of displaying a supercell from the present diffraction data, and there is no mention of this in previous reports. Thus it was decided to analyse the possible distortions available in the hexagonal cell of metrics described in Section 6.2.1. Using ISODISTORT,[20] this leads to 3 possible lower symmetry space groups: $P6_3$, $P31m$ and $P3c1$. Of these three new groups there is only one which has two Fe^{3+} sites and therefore satisfies the Mössbauer spectra; $P31m$. In $YFeO_3$ this does not yield a fit which fully accounts for the anomaly despite refinement of the atomic coordinates (Figure 6.12).[i]

Another possible explanation for the poor fit and the two Fe^{3+} site is a phase separation; this would entail the presence of two hexagonal $YFeO_3$ phases that have slightly different lattice parameters. Although it is difficult to probe the nature of this separation it does give a better fit of the anomalous region (Figure 6.13). In this case the $YFeO_3$ model phases were set to be identical although in practice it is accepted that there must be some difference in order to drive the phase separation. The overall composition in this case refines to a 60:40 ratio of phase A and phase B which is close to the 57:43 ratio of doublets indicated by the Mössbauer spectrum. For $YbFeO_3$ we find there is also an improvement in fit and each phase is refined to be present in a ratio of 53:47 (Figure 6.14) in close agreement with that found by Mössbauer spectroscopy. It is noted that it is not perfect, however.

[i] Refinement of this and the 2 phase models are included in appendix A.6.3.1.

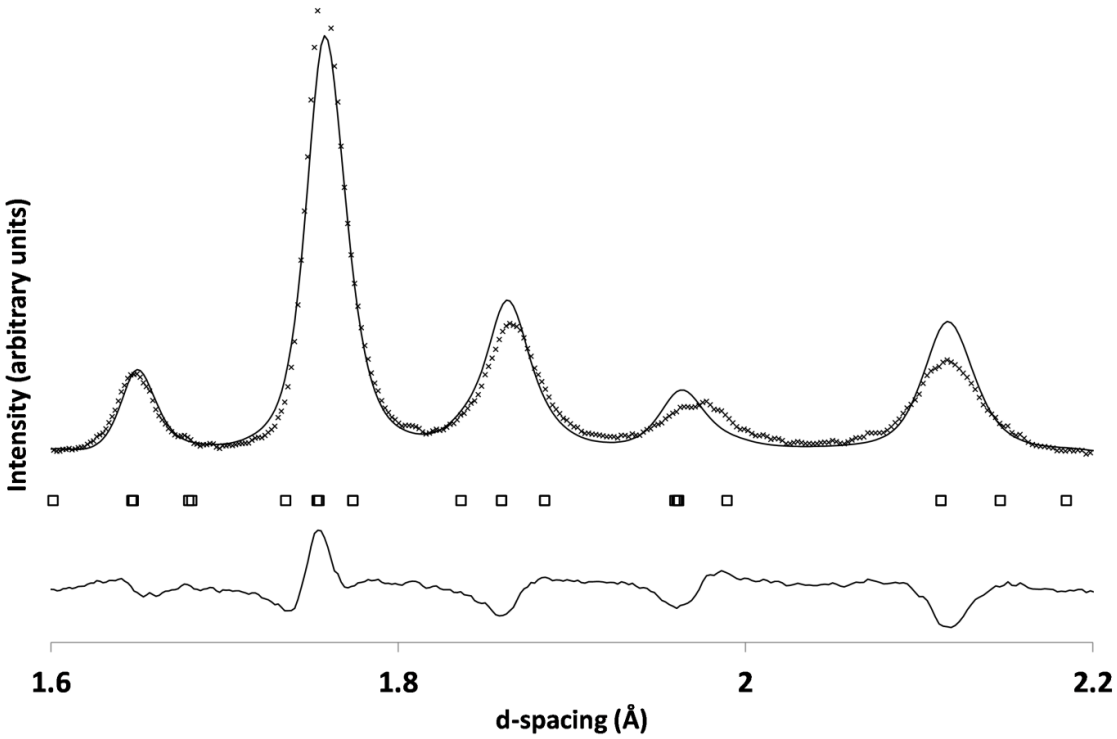

Figure 6.12: Rietveld refinement fit of *P*31*m* model for $YFeO_3$ NPD pattern at room temperature between d = 1.6 – 2.2 Å. Note fit is still not ideal and aesthetically shows little improvement over the *P*6_3*cm* model.

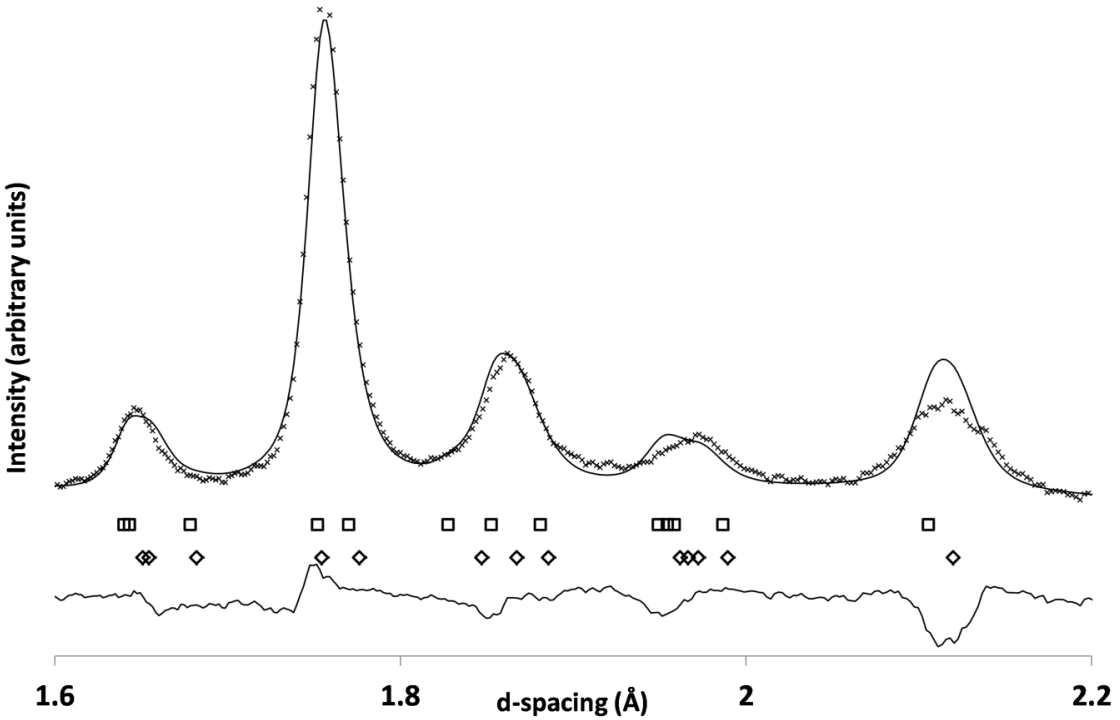

Figure 6.13: Rietveld refinement of two similar *P*6_3*cm* models against $YFeO_3$ NPD pattern at ambient temperature.

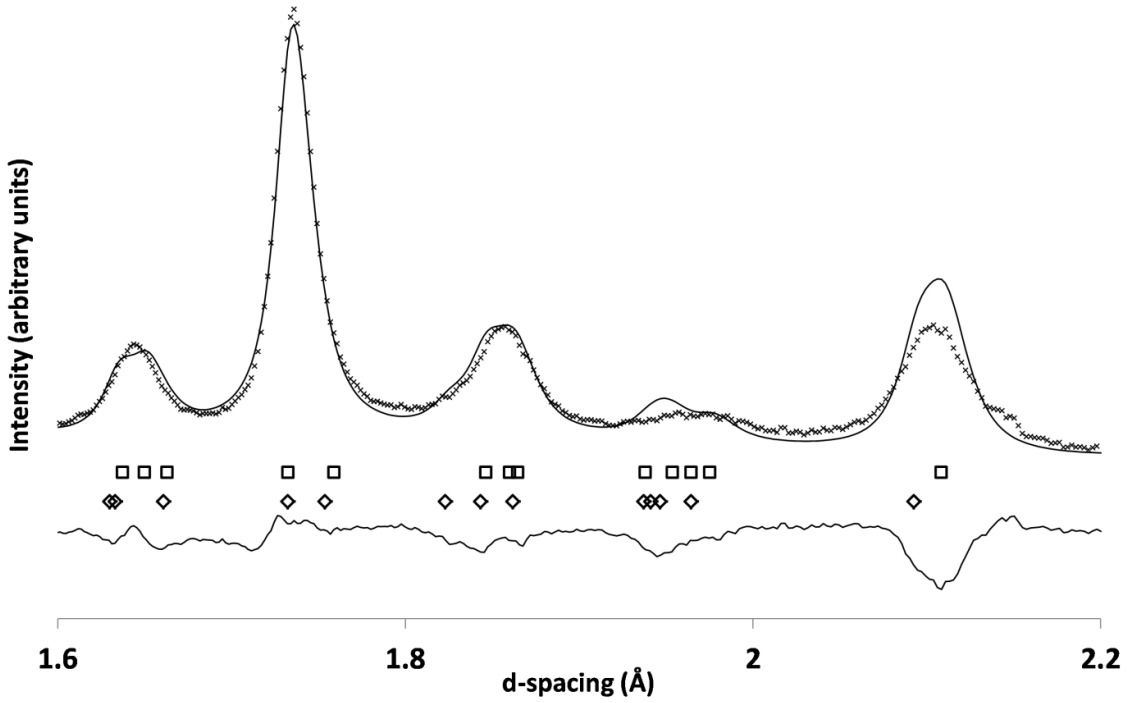

Figure 6.14: Rietveld refinement of two similar *P*6$_3$*cm* models against YbFeO$_3$ NPD pattern at ambient temperature.

Table 6.4: Unit cell parameters and weight percentages for YFeO$_3$ and YbFeO$_3$ two *P*6$_3$*cm* model refinements as derived from Rietveld refinements.

YFeO$_3$	*a* (Å)	*c* (Å)	Weight %
Phase 1	6.0690(17)	11.695(3)	60.1
Phase 2	6.0776(25)	11.834(5)	39.9
YbFeO$_3$			
Phase 1	6.0013(20)	11.850(4)	52.7
Phase 2	6.0009(22)	11.679(5)	47.3

The presence of two phases simultaneously has been suggested before [18] but in the context of a phase transition at a reduced temperature due to size – thus in the case of YFeO$_3$ there would be both the *P*6$_3$*cm* phase and the *P*6$_3$/*mmc* phase present simultaneously. This does not seem to be the case however as the poorly fitted area (d ≈ 1.6 – 2.2 Å) is still present at 10 K. Another, more likely, explanation, is a strain or size effect which causes the adoption of a different structure below a critical particle size or a "core-shell" model which is dependent on the volume of the surface compared to the volume of the bulk. Both these circumstances would support the Mössbauer data which gives a ~ 50:50 site occupancy in our data and a 78:22 occupancy in a previously reported paper – this would suggest the amount of each phase is related to the details of the synthesis and potentially particle size average and distribution.

6.3.2 Magnetic-electrical-structural link

It has been noted in the results that there are anomalies in the structural, magnetic and electrical data with reducing temperature. In $YFeO_3$ there is an electrical anomaly (in dielectric constant and loss) at 130 K. There is a subtle change in magnetic behaviour at this temperature as well which is best visualised in the derivative of $1/\chi$ vs. T (Figure 6.15). This suggests a possible, small magnetoelectric effect but the same is not seen in $YbFeO_3$.

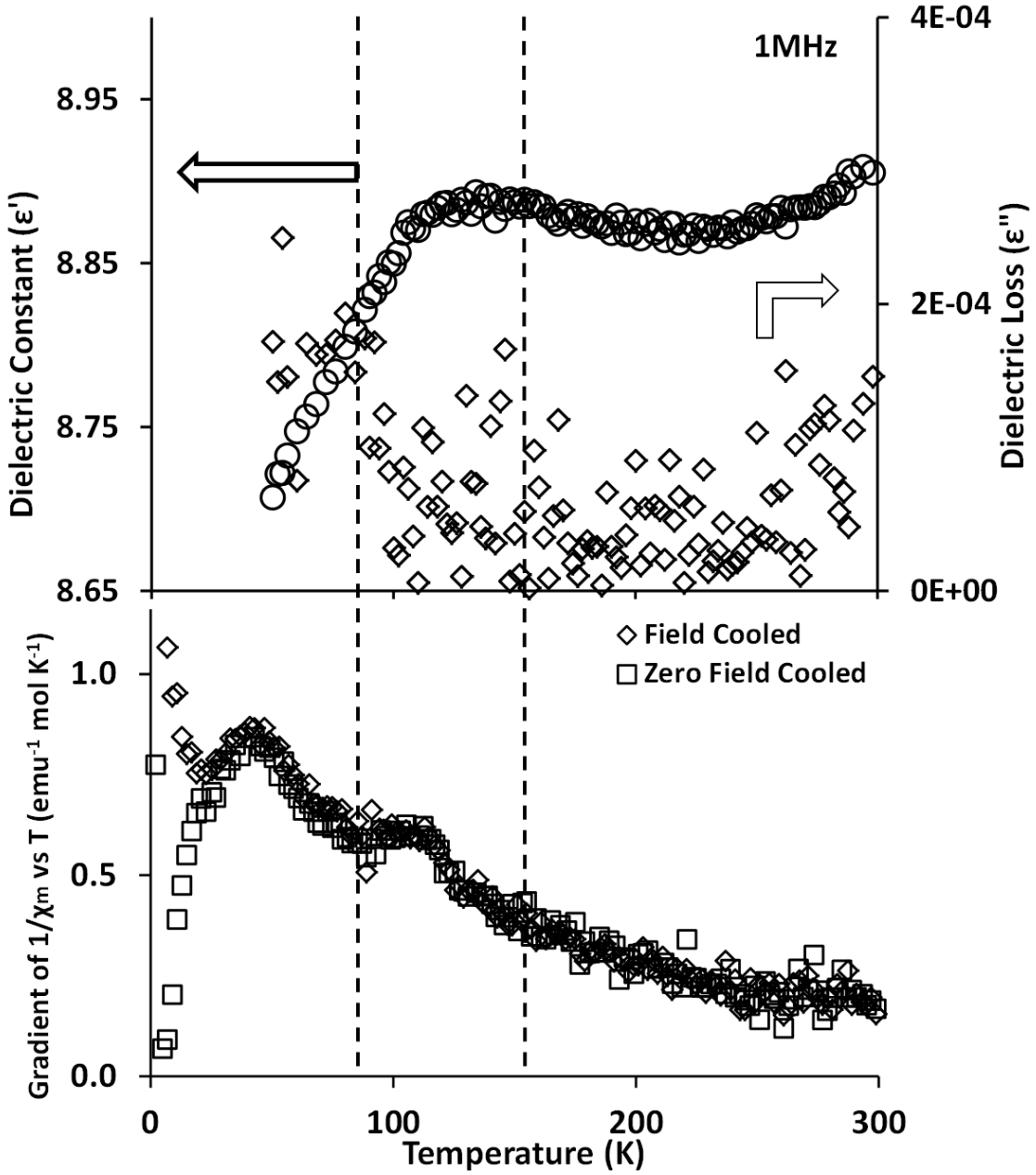

Figure 6.15: Derivative of $1/\chi$ vs. T and dielectric measurements for $YFeO_3$ at coincident temperatures. Dashed lines indicate position of coincident anomalies.

In $YbFeO_3$ there is no equivalent anomaly in the magnetic data but there is an anomaly in the lattice parameters which is also coincident with the electrical anomaly (Figure 6.16).

This suggests that the change in the lattice parameter (and assumedly concurrent change in structure) may be directly responsible. The motivation for this structural anomaly is unknown and hard to propose given the uncertainty about the phase details.

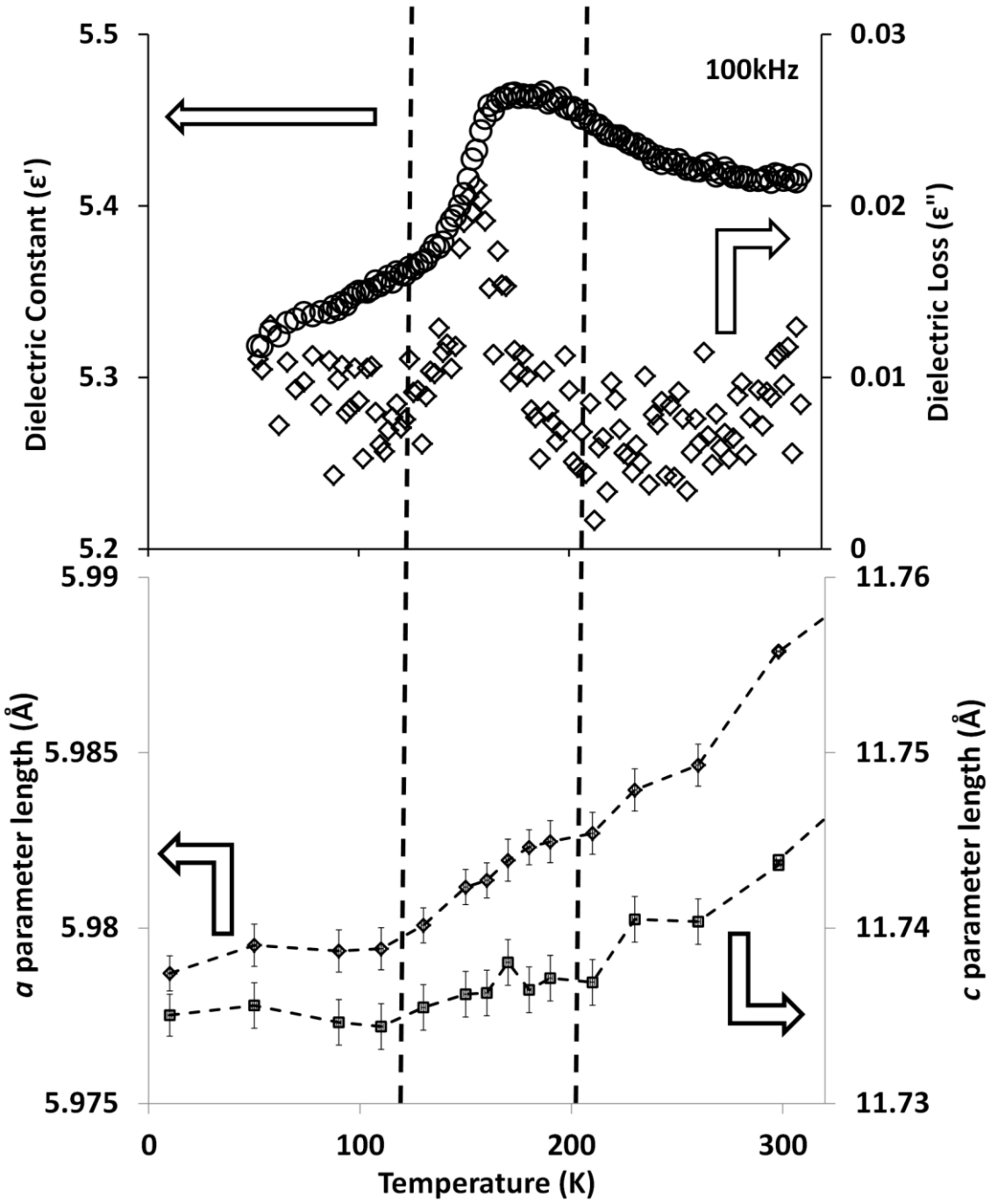

Figure 6.16: Lattice parameters vs. temperature (axes represent same % change) and dielectric measurements vs. temperature for $YbFeO_3$. Dashed lines indicate area of coincident anomalies.

Another feature of note is an increase in background at high d-spacing (3.5 – 5.5 Å) which begins to occur at the same point as the anomalies. This increase in background is the beginning of the growth of reflections possibly due to magnetic order (Figure 6.17 and Figure

6.18) suggesting that some short range behaviour may be occurring either structurally or magnetically. The magnetic structure is discussed more fully in Section 6.3.3.

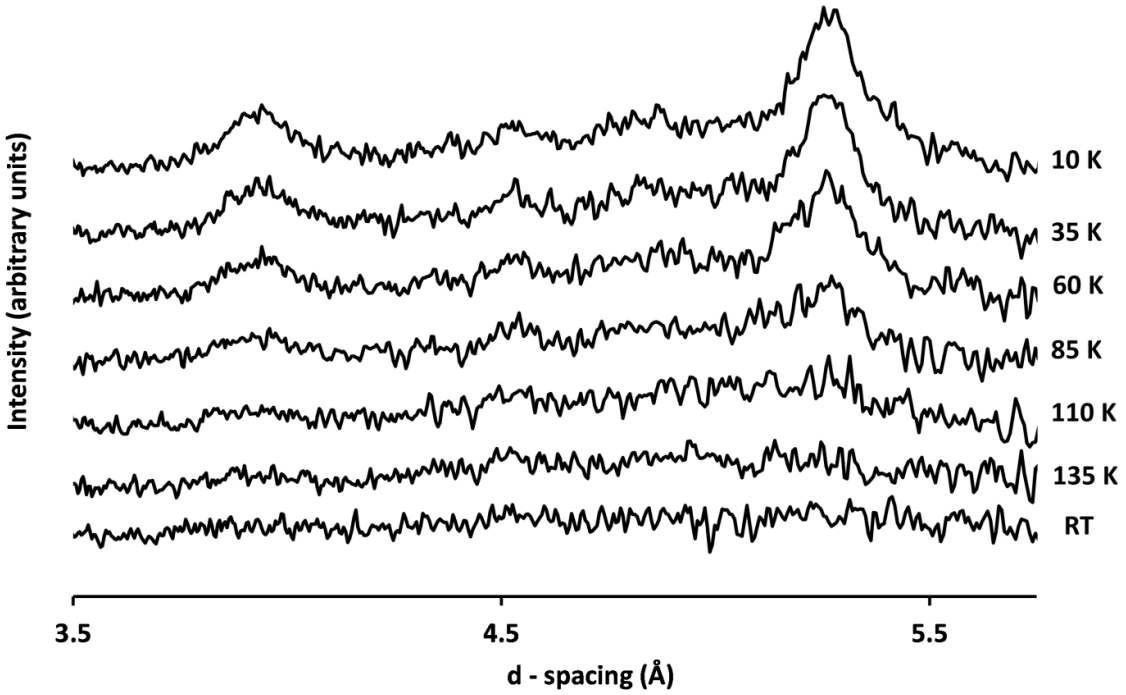

Figure 6.17: High d-spacing region for $YFeO_3$ NPD data showing gradual appearance of peaks with lowering temperature.

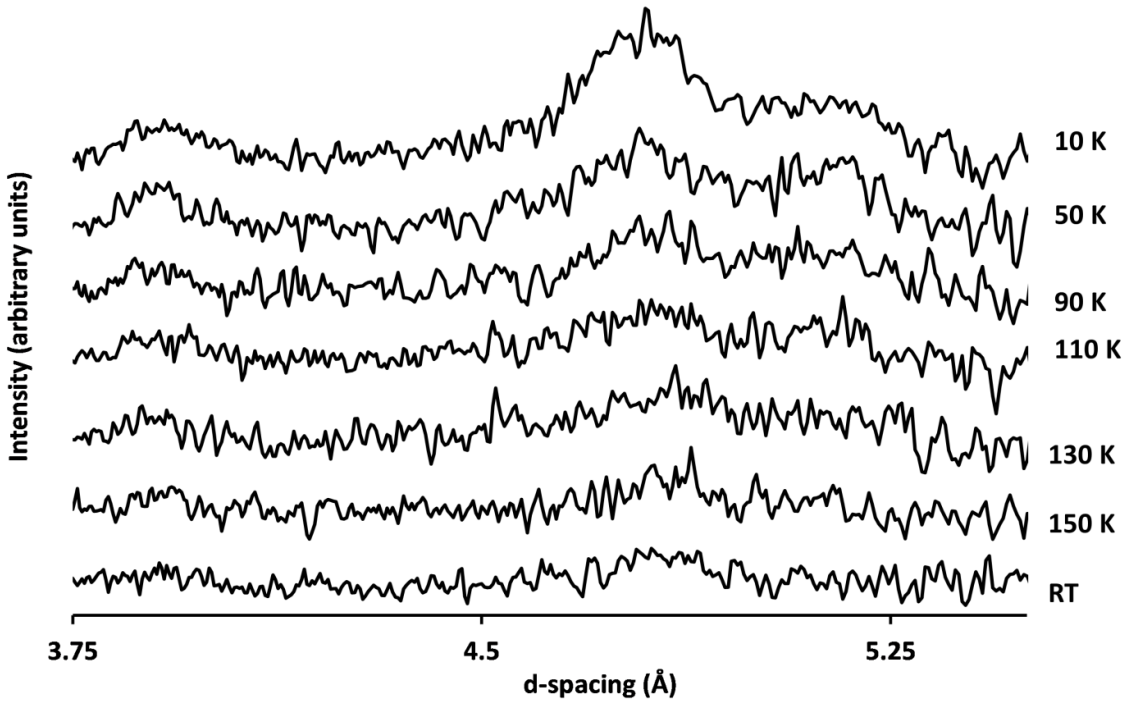

Figure 6.18: High d-spacing region for $YbFeO_3$ NPD data showing gradual appearance of peaks with lowering temperature.

6.3.3 Low temperature magnetic structure

As shown in Figure 6.17 and Figure 6.18 there is the appearance of peaks at high d-spacing with lowering temperature. In order to probe their origin, i.e. to decide between structural or magnetic reflections, low temperature synchrotron diffraction was employed on $YFeO_3$ (Figure 6.19). Synchrotron X-ray diffraction does not interact with magnetic moments and therefore peaks present in NPD data but not SXPD are likely magnetic in origin.

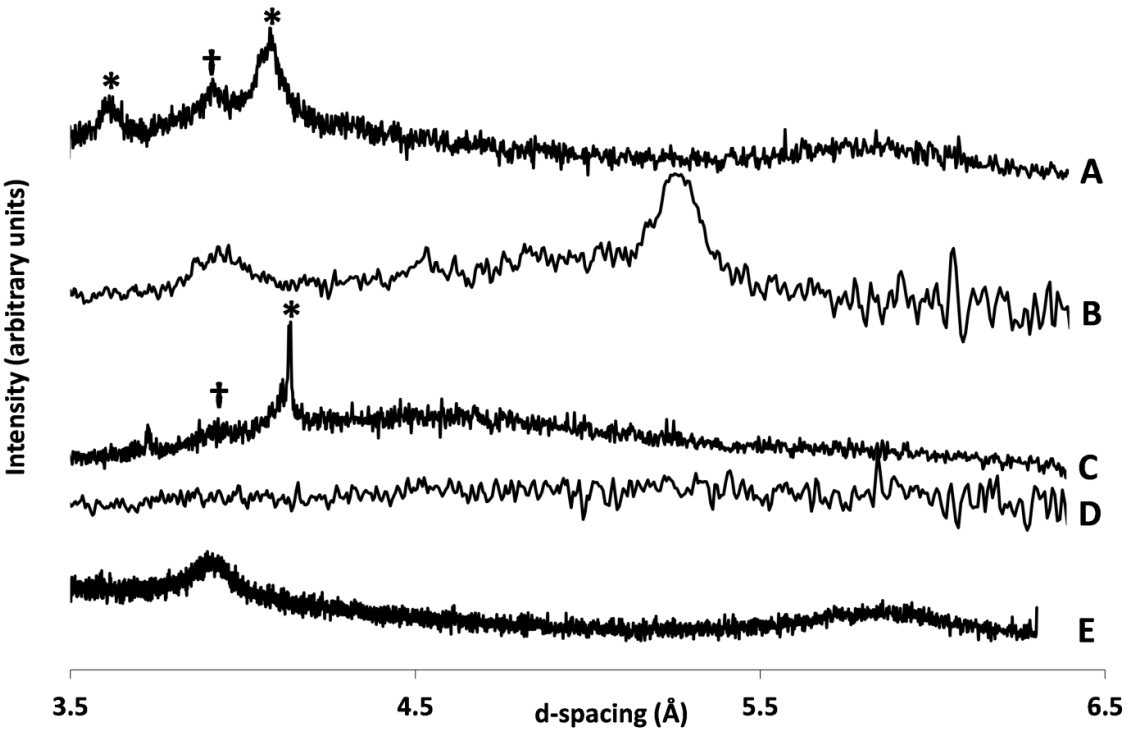

Figure 6.19: Comparisons of SXPD and NPD data. A = SXPD at 30 K, B = NPD at 35 K, C = SXPD at RT (copper wire set up for PheniX cryostat), D = NPD at RT, E = SXPD at RT (glass capillary set up). Peaks marked * are due to sample environment, † are allowed structural reflections.

The lack of a strong peak at d ≈ 5.2 Å in the SXPD data but its presence in the NPD data suggests that the peaks seen at high d-spacing and low temperatures are magnetic in nature and indicate long-range magnetic ordering. It is noted that there is no anomaly visible in the susceptibility data that indicates the adoption of this magnetic ordering but such has been reported previously for $YbMnO_3$.[21]

It is possible to fit peaks due to magnetic order using Shubnikov groups and previous commensurate models have been suggested for $YMnO_3$; $P6_3cm$, $P6_3'c'm$, $P6_3'cm'$, $P6_3c'm'$, $P6_3$ and $P6_3'$.[22] Attempts at Rietveld refinement using these space groups led to poor refinements with both $P6_3$ and $P6_3'$ and being too unstable to converge (Table 6.5).[j] All refinements also fail to account for a weak peak at d ≈ 4.5 Å which can only be indexed by expanding the unit

[j] Refinements are present in appendix A.6.3.3 along with selected plots of refinements for both $YFeO_3$ and $YbFeO_3$.

cell (potentially by tripling the *c*-axis) but the quality of data is insufficient to unambiguously assign the correct magnetic unit cell or the space group in particular. It has also been shown that it is impossible to discriminate between the suggested structures without the aid of polarised neutron experiments on single crystals [22] or secondary harmonic generation measurements.[23]

Table 6.5: Quality of fit for Rietveld refinements for $YFeO_3$ structural (*P*6_3*cm*) and magnetic unit cell for NPD data at 10 K.

	wRp (%)	Rp (%)	χ^2
P6_3*cm*	3.24	2.70	5.10
P6_3'*c*'*m*	3.26	2.77	5.15
P6_3'*cm*'	3.23	2.62	5.05
P6_3*c*'*m*'	3.27	2.78	5.18
P6_3	unstable		
P6_3'	unstable		

The same Rietveld refinements were attempted for $YbFeO_3$ but in this case there were no un-indexed peaks suggesting a commensurate unit cell. Once again the models are poor, however, and the Yb^{3+} moments were not included (Table 6.6).

Table 6.6: Quality of fit for Rietveld refinements for $YbFeO_3$ structural (*P*6_3*cm*) and magnetic unit cell for NPD data at 10 K.

	wRp (%)	Rp (%)	χ^2
P6_3*cm*	2.76	2.29	5.23
P6_3'*c*'*m*	2.76	2.28	5.23
P6_3'*cm*'	2.77	2.29	5.24
P6_3*c*'*m*'	2.76	2.27	5.21
P6_3	unstable		
P6_3'	unstable		

Once again it is clear that no distinction can be made between the possible magnetic space groups. As discussed previously, however, synchrotron experiments were only performed on $YFeO_3$ and so the origin of the extra peaks in $YbFeO_3$ is possibly structural. Recent studies on thin films of this material have suggested the presence of magnetic ordering below 50 K, however,[24, 25] suggesting that the reflections are likely magnetic in origin.

Analysing the peak integrals as a function of temperature we can also observe some interesting behaviour; taking the most intense "magnetic" peak in $YFeO_3$ and $YbFeO_3$. In $YFeO_3$ this is found to increase with decreasing temperature before saturating (Figure 6.20). This is expected behaviour for a magnetic peak as with reducing temperature the magnetic moment reaches a maximum. In $YbFeO_3$ there is an increasing rise to the lowest temperature recorded. This suggests that the peaks are structural or, more likely, the magnetism is not saturated at

the lowest temperature measured, 10 K (Figure 6.21).[k] One possibility is the ordering of the Yb^{3+} moments occurs at a lower temperature or is "triggered" by the ordering of the Fe^{3+} moments. The latter phenomena has been reported before in $HoMn_2O_5$.[26]

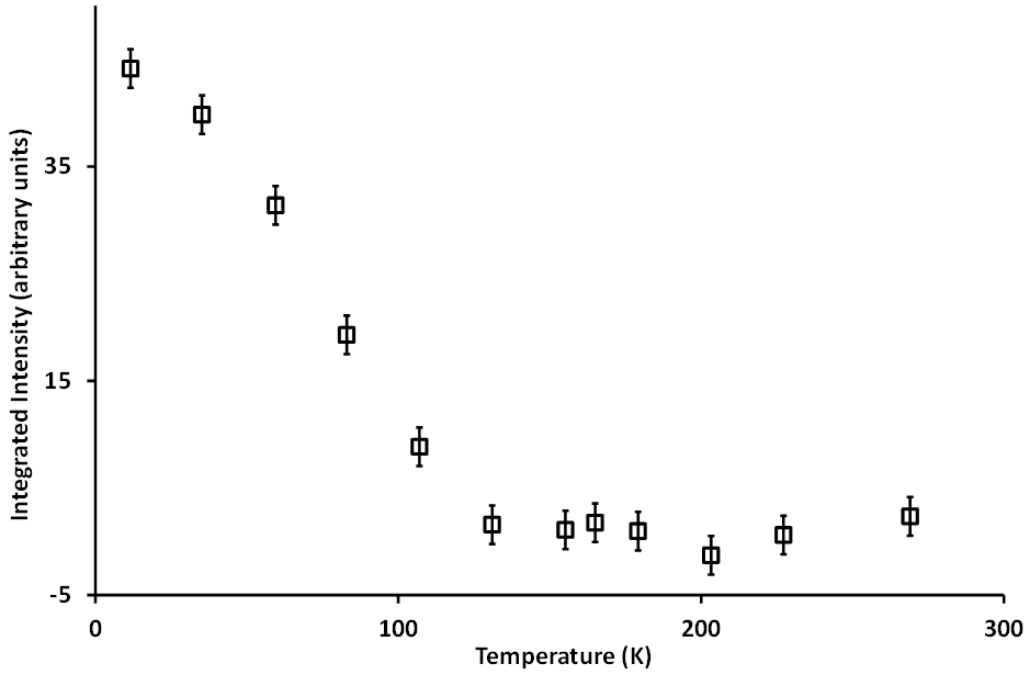

Figure 6.20: Integrated intensity of the (1 0 0) magnetic peak as a function of temperature for $YFeO_3$ showing saturation, as derived from NPD data.

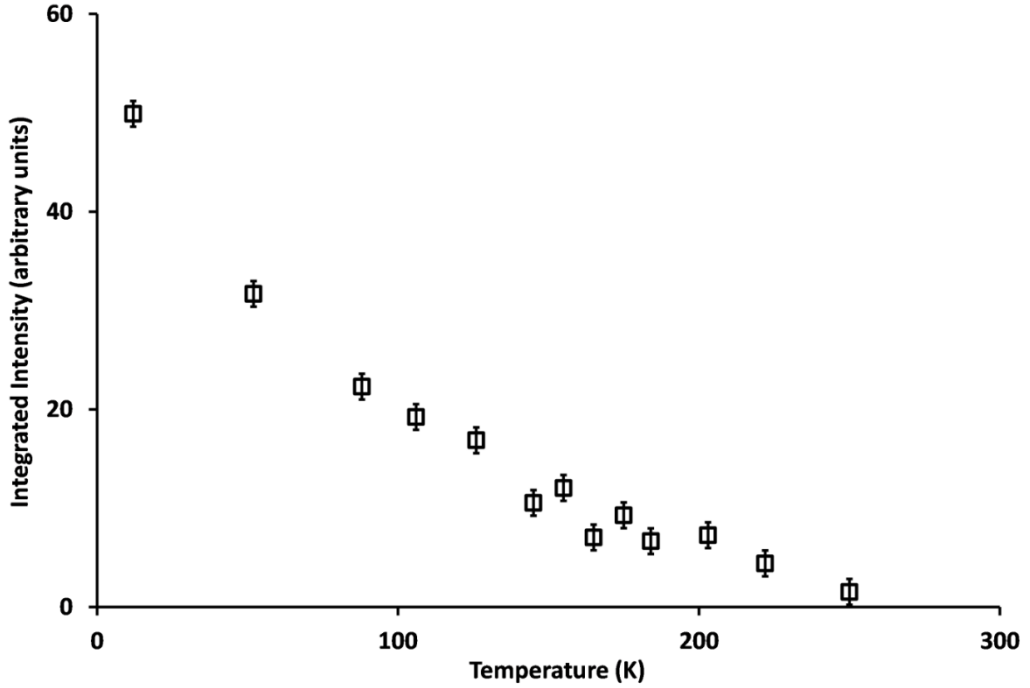

Figure 6.21: Integrated intensity of the (1 0 0) magnetic peak as a function of temperature for $YbFeO_3$ showing no saturation, as derived from NPD data.

[k] Measurements performed by Dr. W. Kockelmann, ISIS neutron and muon source, Oxfordshire, U.K.

6.4 Conclusion

$YFeO_3$ and $YbFeO_3$ have been found to crystallise in the space group $P6_3cm$ like the ambient temperature phase of $YMnO_3$, whereas $InFeO_3$ was found to adopt the space group $P6_3/mmc$ like the high temperature, paraelectric phase of $YMnO_3$. Further experiments on $YFeO_3$ and $YbFeO_3$ found that there were low temperature anomalies in the dielectric constant and dielectric loss which suggests a possible structural change leading to a change in electrical response. Magnetic measurements suggest that there is low temperature magnetic ordering for all M but at higher temperatures there is no paramagnetic behaviour even at the highest temperature measured (300 K). The Mössbauer spectra of all M suggest that the assignment of $YFeO_3$ and $YbFeO_3$ in the $P6_3cm$ space group may be correct but due to the suggestion of two iron sites there may be two similar phases present simultaneously. Due to the broadening of the diffraction data due to small crystallite size, however, ascertaining the details of both phases is not possible. $InFeO_3$ is found to have a single iron site supporting the conclusion that it occurs in the space group $P6_3/mmc$. The electrical anomaly in $YFeO_3$ is found to be coincident with a small change in the gradient of $1/\chi_m$ vs. T in suggesting a possible connection between the electrical and magnetic behaviour. In $YbFeO_3$ the electrical anomaly is not coincident with a magnetic anomaly but does occur at approximately the same temperature as an irregularity in lattice parameters; in this case it is suggested that the electrical anomaly is related to a change in structure which, due to data quality, cannot be measured to a satisfactory level of accuracy. Low temperature magnetic readings and low temperature NPD suggest that there is magnetic ordering in both $YFeO_3$ and $YbFeO_3$ with a small ferromagnetic component. It is also suggested that the ordering of Fe^{3+} precedes and may even trigger the ordering of Yb^{3+} in $YbFeO_3$.

1. R. D. Shannon, *Acta Crystallogr., Sect. A: Found Crystallogr.*, 1976, **32**, 751-767.
2. O. Yamaguchi, H. Takemura, M. Yamashita and A. Hayashida, *J. Electrochem. Soc.*, 1991, **138**, 1492-1494.
3. J. Li, U. G. Singh, T. D. Schladt, J. K. Stalick, S. L. Scott and R. Seshadri, *Chem. Mater.*, 2008, **20**, 6567-6576.
4. L. Wu, J. C. Yu, L. Z. Zhang, X. C. Wang and S. K. Li, *J. Solid State Chem.*, 2004, **177**, 3666-3674.
5. Y. Mizoguchi, H. Onodera, H. Yamaguchi, M. Kagawa, Y. Syono and Y. Hirai, *Mater. Sci. Eng., A*, 1996, **A217**, 164-166.
6. A. A. Bossak, I. E. Graboy, O. Y. Gorbenko, A. R. Kaul, M. S. Kartavtseva, V. L. Svetchnikov and H. W. Zandbergen, *Chem. Mater.*, 2004, **16**, 1751-1755.
7. H. W. Brinks, H. Fjellvag and A. Kjekshus, *J. Solid State Chem.*, 1997, **129**, 334-340.
8. D. M. Giaquinta, W. M. Davis and H. C. Zurloye, *Acta Crystallogr. Sect. C: Cryst. Struct. Commun.*, 1994, **50**, 5-7.
9. M. Inoue, T. Nishikawa, T. Nakamura and T. Inui, *J. Am. Ceram. Soc.*, 1997, **80**, 2157-2160.
10. A. S. Gibbs, K. S. Knight and P. Lightfoot, *Phys. Rev. B*, 2011, **83**, 094111.
11. S. L. Samal, T. Magdaleno, K. V. Ramanujachary, S. E. Lofland and A. K. Ganguli, *J. Solid State Chem.*, 2010, **183**, 643-648.

12. M. Zaghrioui, J. M. Greneche, C. Autret-Lambert and M. Gervais, *J. Magn. Magn. Mater.*, 2011, **323**, 509-514.
13. I. Nodari, A. Alebouyeh, J. F. Brice, R. Gerardin and O. Evrard, *Mater. Res. Bull.*, 1988, **23**, 1039-1044.
14. W. G. Williams, R. M. Ibberson, P. Day and J. E. Enderby, *Physica B*, 1997, **241**, 234-236.
15. S. P. Thompson, J. E. Parker, J. Potter, T. P. Hill, A. Birt, T. M. Cobb, F. Yuan and C. C. Tang, *Rev. Sci. Instrum.*, 2009, **80**, 075107.
16. A. C. Larson and R. L. Von Dreele, 2000.
17. B. H. Toby, *J. Appl. Cryst.*, 2001, **34**, 210-213.
18. P. Jiang, J. Li, A. W. Sleight and M. A. Subramanian, *Inorg. Chem.*, 2011, **50**, 5858-5860.
19. L. Machala, R. Zboril and A. Gedanken, *J. Phys. Chem. B*, 2007, **111**, 4003-4018.
20. B. J. Campbell, H. T. Stokes, D. E. Tanner and D. M. Hatch, *J. Appl. Crystallogr.*, 2006, **39**, 607-614.
21. X. Fabreges, I. Mirebeau, P. Bonville, S. Petit, G. Lebras-Jasmin, A. Forget, G. Andre and S. Pailhes, *Phys. Rev. B*, 2008, **78**, 214422.
22. P. J. Brown and T. Chatterji, *J. Phys. Condens. Matter*, 2006, **18**, 10085-10096.
23. M. Fiebig, D. Frohlich, K. Kohn, S. Leute, T. Lottermoser, V. V. Pavlov and R. V. Pisarev, *Phys. Rev. Lett.*, 2000, **84**, 5620-5623.
24. Y. K. Jeong, J. H. Lee, S. J. Ahn, S. W. Song, H. M. Jang, H. Choi and J. F. Scott, *J. Am. Chem. Soc.*, 2012, **134**, 1450-1453.
25. H. Iida, T. Koizumi, Y. Uesu, K. Kohn, N. Ikeda, S. Mori, R. Haumont, P. E. Janolin, J. M. Kiat, M. Fukunaga and Y. Noda, *J. Phys. Soc. Jpn.*, 2012, **81**, 024719.
26. G. Beutier, A. Bombardi, C. Vecchini, P. G. Radaelli, S. Park, S. W. Cheong and L. C. Chapon, *Phys. Rev. B*, 2008, **77**, 172408.

7 Studies of $MInO_3$ (where M = Dy, Tb)

The ferroelectricity in hexagonal $YMnO_3$ is directly related to the crystal structure as it is a geometric ferroelectric. Indeed the replacement of Mn^{3+} by Ga^{3+} is found to have little effect on the structure and therefore it has been proposed that the polarisation along the *c*-axis would be similar in both cases.[1] The replacement of Mn^{3+} with a larger cation would therefore be assumed to perturb the structure in some way and so lead to a change in polarisation and the ferroelectricity of the material. In the past a number of $YMnO_3$ like structures have been synthesised with In^{3+} in the place of Mn^{3+}.[2] This leads to an oversized ion present on the B-site[a] and so an extra stress in the *c*-plane which has been shown to increase the corrugation of the BO_5 layer.[3] This further corrugation acts as a barrier to the transition to the paraelectric $P6_3/mmc$ phase pushing it to higher temperatures (~ 1500 K for $DyInO_3$ vs. 1253 K for $YMnO_3$) and increasing the polarisation (10 μCcm^{-2} for $ErInO_3$ vs. ~ 6 μCcm^{-2} for $YMnO_3$).[3] Another point of note in these materials is the lack of transition metals on the B-site; this will cause the only magnetic ordering to be directly from the A-site, if a suitable cation is present.

Both $DyInO_3$ and $TbInO_3$ have been previously synthesised and the former has been studied using high temperature X-ray powder diffraction. The transition between the ferroelectric $P6_3cm$ phase and the paraelectric $P6_3/mmc$ phases was found to be ~ 1500 K and commensurate with some decomposition to the binary phases.[3] $TbInO_3$ is found to require sealing in Pt or Au capsules to prevent the oxidation of Tb or the reduction of In.[2] This suggests that the compound is metastable in nature. A brief report has also displayed some specific heat and magnetisation measurements on both $TbInO_3$ and $DyInO_3$ which suggests that there is no magnetic ordering transition down to 0.05 K in either material.[4]

7.1 Experimental

7.1.1 Synthesis of $DyInO_3$ and $TbInO_3$

Synthesis techniques were based on that previously described for $DyInO_3$ with the exception of ball milling.[3] Stoichiometric amounts of Dy_2O_3 (99.99+ %, Sigma Aldrich) and In_2O_3 (99.99 %, Sigma Aldrich) were ground under acetone and pelletised using a uniaxial press. The resulting pellet was then heated to 1623 K for 6 hours with heating/cooling at 20 K min^{-1}. The pellet was then reground under acetone before re-pelletising and heating to 1673 K for 48 hours (with the previous heating/cooling rate).

Stoichiometric amounts of Tb_4O_7 (99.9 %, Sigma Aldrich) and In_2O_3 (99.99 %, Sigma Aldrich) (w.r.t. metals) were ground under acetone and pelletised using a uniaxial press. The resultant (dark brown) pellet was heated at 1673 K for 6 hours (heating/cooling at 20 K min^{-1}). This yields a mustard yellow pellet. Further heating is found to cause a loss of crystallinity and a return to the dark brown colour of the starting materials particularly on the surfaces exposed to air. It is suggested that $TbInO_3$ is a metastable phase.

7.1.2 Analytical techniques

Laboratory based X-ray powder diffraction (XRPD) was performed using a Stoe Stadi-P

[a] Shannon radii: Mn^{3+} 0.645 Å (high spin), Ga^{3+} 0.620 Å, In^{3+} 0.800 Å. All these radii are for 6-coordinate systems for comparison.

diffractometer operating in transmission mode and utilising Cu $K_{\alpha 1}$ radiation in order to confirm the presence of the desired phases.

Neutron powder diffraction (NPD) was performed at beamline GEM, ISIS pulsed neutron and muon source, Oxfordshire.[5] A sample of $TbInO_3$ of ~ 4 g was loaded into a cylindrical vanadium can. NPD data were collected at room temperature, (in a furnace) 333, 373, 473, 573, 593, 613, 633, 653, 673, 693, 713, 733, 753, 773, 823, 873, 923, 973, 1073 and 1173 K on heating. Equilibration times of approximately 10 minutes per temperature were applied.

Synchrotron X-ray powder diffraction (SXPD) was carried out at beamline I11, Diamond Light Source Ltd., Oxfordshire.[6] A sample of $DyInO_3$ was loaded into a glass capillary and diffraction data collected at room temperature, 423, 573, 723, 873, 1023, 1173 K on heating and 873 and 573 K on cooling.

Rietveld refinement was performed using GSAS[7] and the EXPGUI interface.[8] This analysis sought to fit lattice parameters, phase fractions, peak profile shape (both Gaussian and Lorentzian), atomic coordinates and thermal parameters.

Magnetic measurements were performed on a Quantum Designs MPMS-XL SQUID. Powder samples were mounted in gelatine capsules before being secured in plastic straws. The straws were then mounted on the end of a standard rod. Data were recorded in a field of 10000 Oe while warming the sample from 2 K to 300 K in both cooling out of field (ZFC) and cooling in field (FC) cycles.

Polarisation/field measurements were conducted between 1 Hz and 2 kHz on an aixACCT TF2000 analyser.

7.2 Structural studies of $MInO_3$

$DyInO_3$ was subject to SXPD and it was found to be well fitted in the $P6_3cm$ space group at room temperature, with a = 6.29385 (6) Å and c = 12.28902(14) Å which is in agreement with previous studies.[2, 3] Unfortunately, dysprosium and indium have particularly high X-ray absorption parameters thus it is not possible to reliably refine the atomic coordinates in order to gain further information. The lattice parameters are not affected by this problem, however.

On heating[b] it is found that there is an approximately linear increase in both the a and c unit cell parameters which is reversed on cooling (Figure 7.1). There is no hysteresis visible in the lattice parameters on heating and cooling. As expected, the unit cell volume also shows a linear increase with temperature (Figure 7.2).

The linear increase in lattice parameters and lack of hysteresis suggests that there are no phase transitions occurring in the investigated area. Examination of the SXPD patterns at various temperatures shows the presence of peaks which are due to the larger $P6_3cm$ supercell

[b] All refinements are available in appendix A.7.2 along with tables of lattice parameters for both $DyInO_3$ and $TbInO_3$.

and not present in the high symmetry $P6_3/mmc$ phase (Figure 7.3) (the latter having an *a* parameter of $a / \sqrt{3}$ of the former).

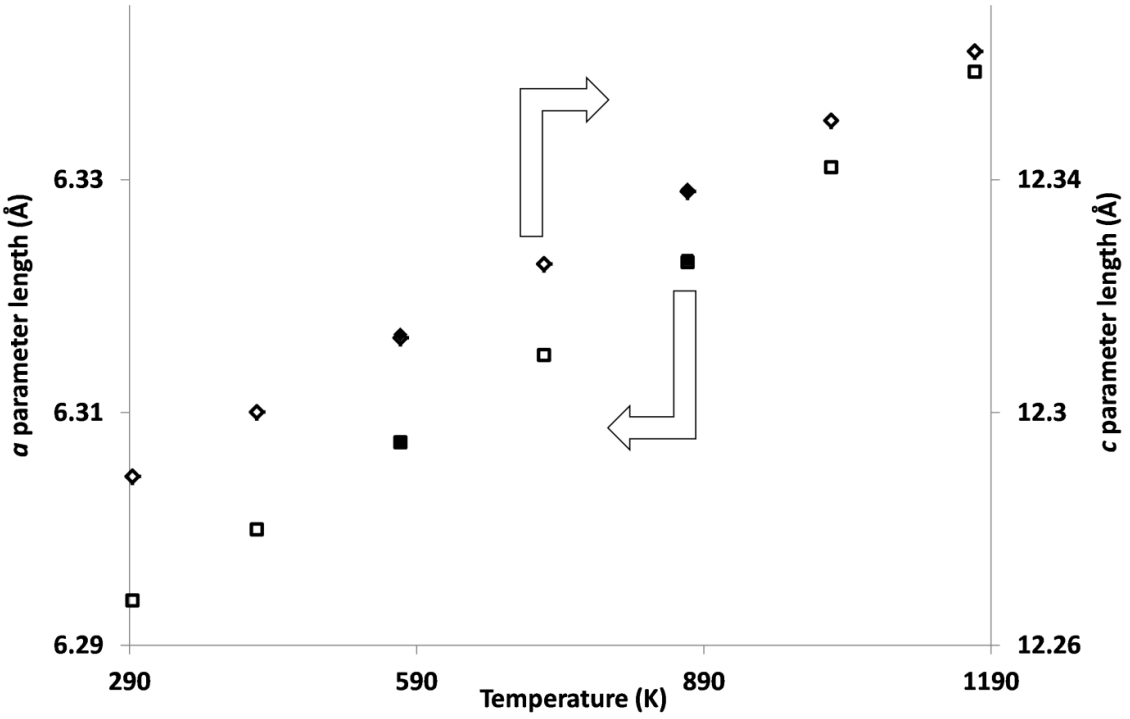

Figure 7.1: *a* and *c* unit cell parameter for $DyInO_3$ vs. temperature as derived from SXPD data. Open shapes refer to heating cycle, filled shapes to cooling. Note the overlap of heating and cooling measurements at 593 and 873 K. Error bars are smaller than data point size.

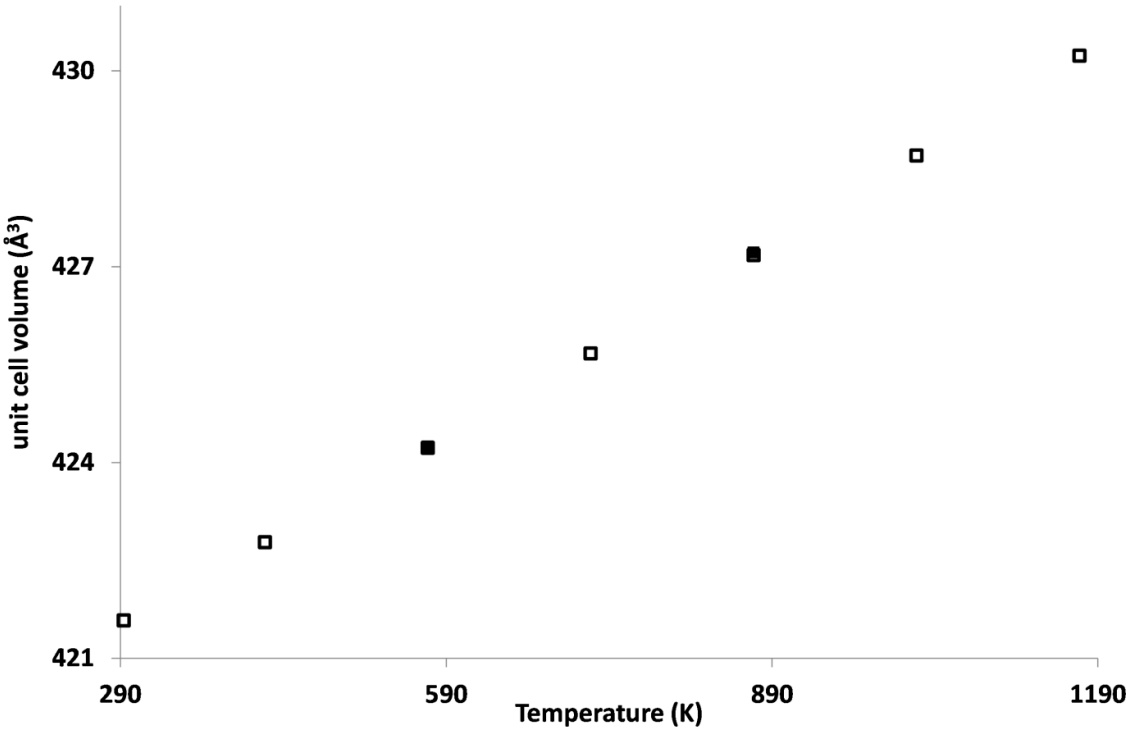

Figure 7.2: Unit cell volume for $DyInO_3$ vs. temperature as derived from SXPD data. Open shapes refer to heating cycle, filled shapes to cooling. Note overlap of heating and cooling measurements at 593 and 873 K. Error bars are smaller than data point size.

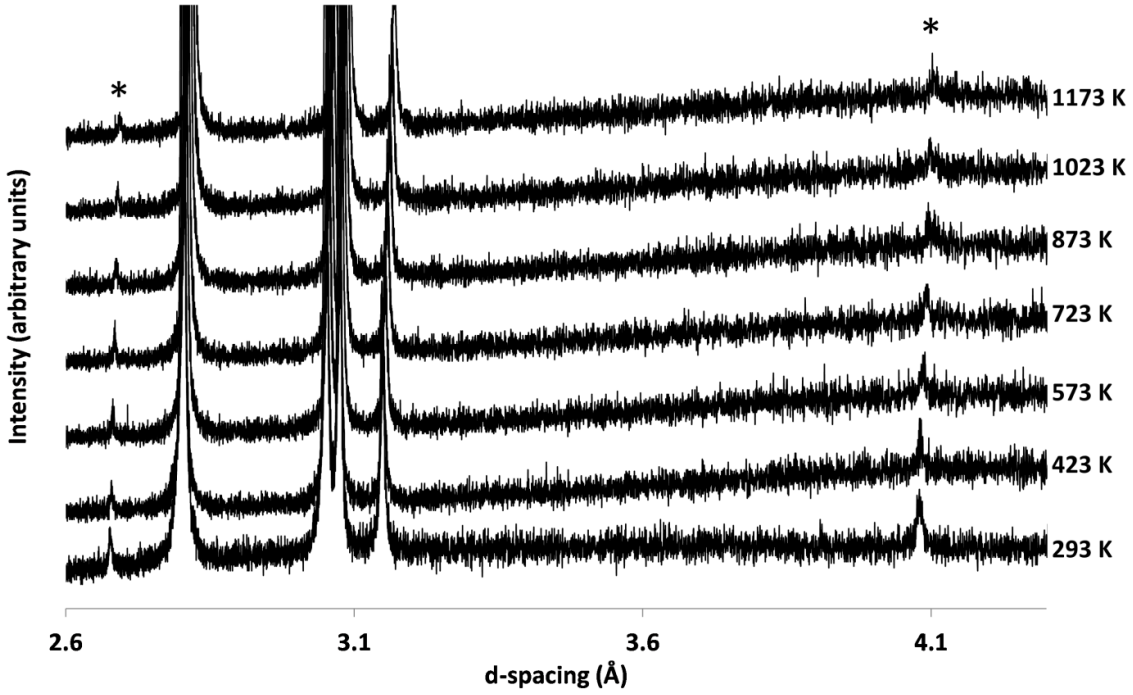

Figure 7.3: SXPD patterns for $DyInO_3$ at various temperatures. * indicates peaks allowed in $P6_3cm$ supercell but not $P6_3/mmc$ parent unit cell; in particular (1 0 4) at d ≈ 2.7 Å and (1 0 2) at d ≈ 4.1 Å. Patterns off-set on y-axis for clarity.

$TbInO_3$ was investigated by NPD and so absorption was less of a problem affecting data quality. Should $DyInO_3$ have been investigated by NPD there may have still been absorption problems due to the particularly high absorption cross-section of Dy (994 barns) compared to In (193.8 barns) and Tb (23.4 barns).[c, 9] The structure of $TbInO_3$ can therefore be modelled dependably in order to give reliable and precise atomic coordinates. The lattice parameters at room temperature are found to be a = 6.31309(6) Å, c = 12.29542(16) Å when modelled in the $P6_3cm$ unit cell which compares favourably with previous reports [2] (a = 6.319(4) Å, c = 12.295(8) Å). The atomic coordinates are also found to be similar to the archetypal $YMnO_3$ at room temperature (Table 7.1) thus leading to similar inter-atomic distances (Table 7.2).

Table 7.1: Atomic coordinates and thermal parameters for $TbInO_3$ at room temperature derived from NPD and a comparison to previous studies on $YMnO_3$.[10]

Atom	x	y	z	U_{ISO} (Å^2) x 100
Tb1	0	0	0.2674(4)	0.28(4)
Tb2	1/3	2/3	0.2354(4)	0.53(3)
In1	0.3313(9)	0	0	0.183(15)
O1	0.30895(25)	0	0.1696(3)	0.59(3)
O2	0.64068(27)	0	0.3302(3)	0.60(3)
O3	0	0	0.4693(4)	0.48(6)
O4	1/3	2/3	0.0220(3)	0.62(4)
Y1	0	0	0.2728(5)	1.16(7)
Y2	1/3	2/3	0.2325(4)	1.30(5)
Mn1	0.3177(9)	0	0	0.80(5)
O1	0.3074(4)	0	0.1626(4)	1.55(7)
O2	0.6427(3)	0	0.3355(4)	1.05(6)
O3	0	0	0.4744(6)	1.25(10)
O4	1/3	2/3	0.0169(5)	1.42(7)

Table 7.2: Inter-atomic distances for $TbInO_3$ at room temperature derived from NPD and a comparison to previous studies on $YMnO_3$.[10]

Atoms	$TbInO_3$ distances (Å)	$YMnO_3$ distances (Å)
Tb1 (Y1) – O1 (x3)	2.2911(25)	2.261
Tb1 (Y1) – O2 (x3)	2.3960(22)	2.309
Tb1 (Y1) – O3	2.482(3)	2.289
Tb2 (Y2) – O1 (x3)	2.3299(13)	2.271
Tb2 (Y2) – O2 (x3)	2.3381(16)	2.304
In1 (Mn1) – O1	2.090(4)	1.856
In1 (Mn1) – O2	2.096(4)	1.893
In1 (Mn1) – O3	2.126(6)	1.975
In1 (Mn1) – O4 (x2)	2.1277(29)	2.105

[c] Absorptions taken for neutrons with a speed of 2200 m s^{-1}.

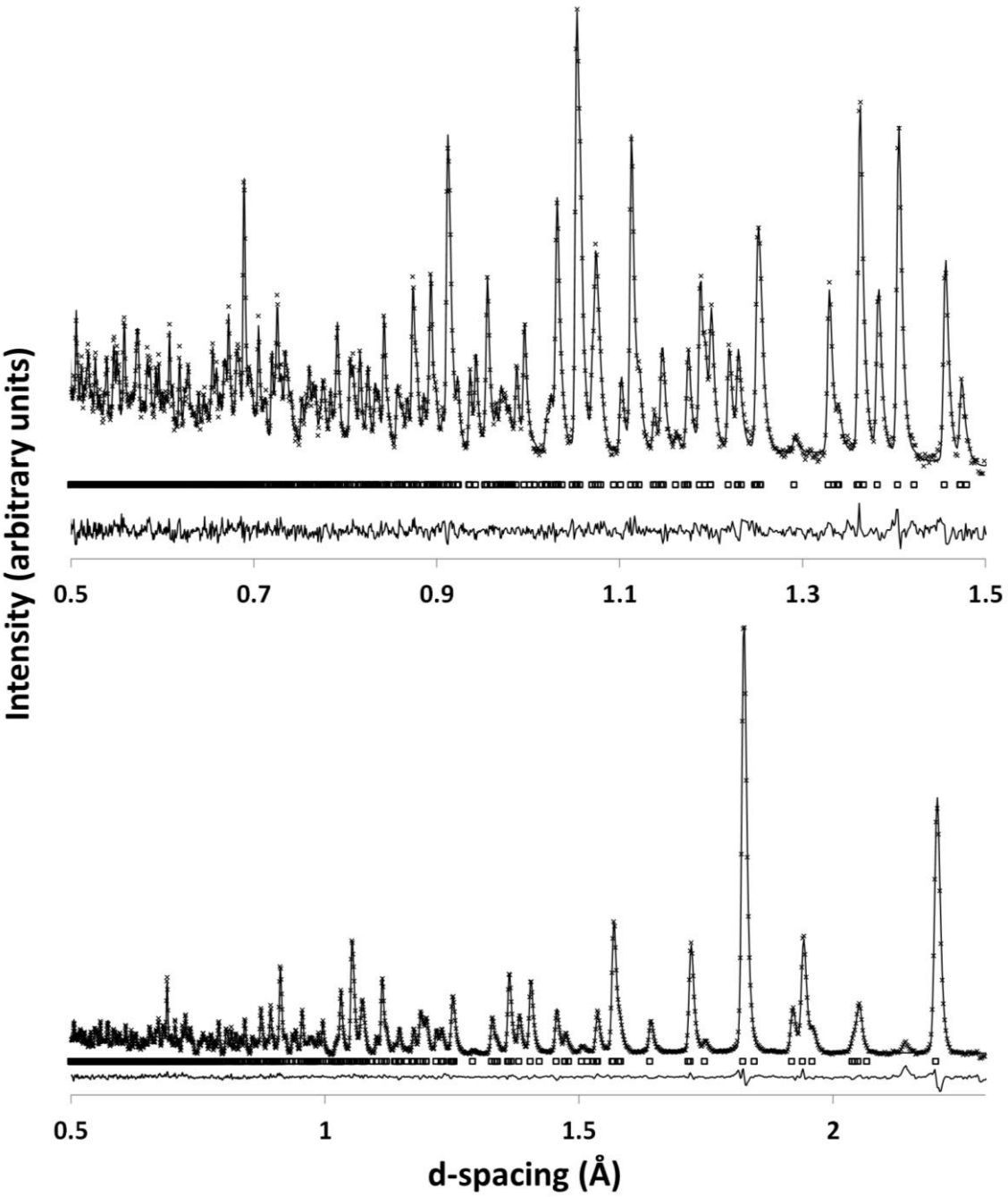

Figure 7.4: NPD Rietveld refinements for $TbInO_3$ at room temperature. Top is backscattering detector bank (6) and below is 79 ° - 104 ° detector bank (5) on the GEM diffractometer, ISIS. There is a small peak at *d* ≈ 2.15 Å attributable to the vanadium sample holder.

On heating there is an approximately linear increase in the *c* parameter but the *a* parameter shows a subtle curvature, with gradient increasing with temperature (Figure 7.5). It is also noted that there appears to be a small anomaly for the room temperature data point which has been assumed to be at 293 K – it is possible that there is an error in temperature as the measurement was taken at ambient temperature and outside of the furnace. Unit cell volume also shows the subtle increase in gradient with temperature found for the *a* parameter. At 1273 K the system is found to decompose irreversibly to Tb_2O_3 and In_2O_3.

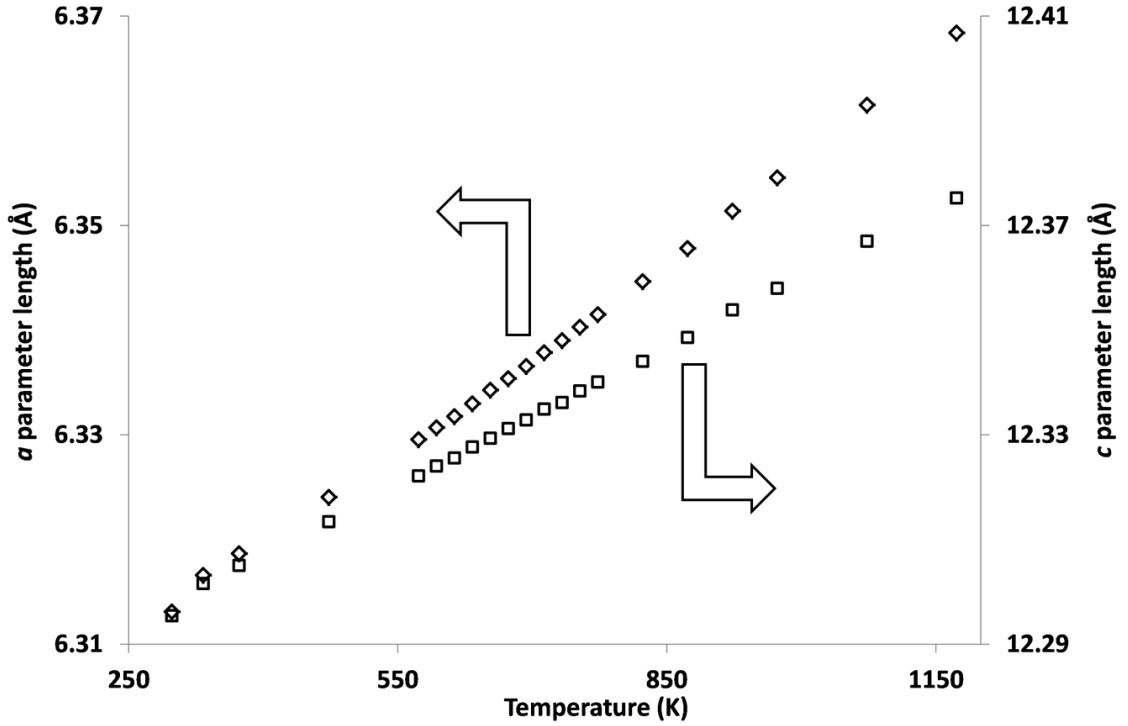

Figure 7.5: *a* and *c* unit cell parameters as a function of temperature for $TbInO_3$ as derived from NPD data.

With increasing temperature there is evidence, in the form of superstructure peaks, for the system remaining in the $P6_3cm$ space group; their continued presence suggests that the $P6_3cm \rightarrow P6_3/mmc$ phase transition is outside of the temperature range studied and the stability range of the compound.

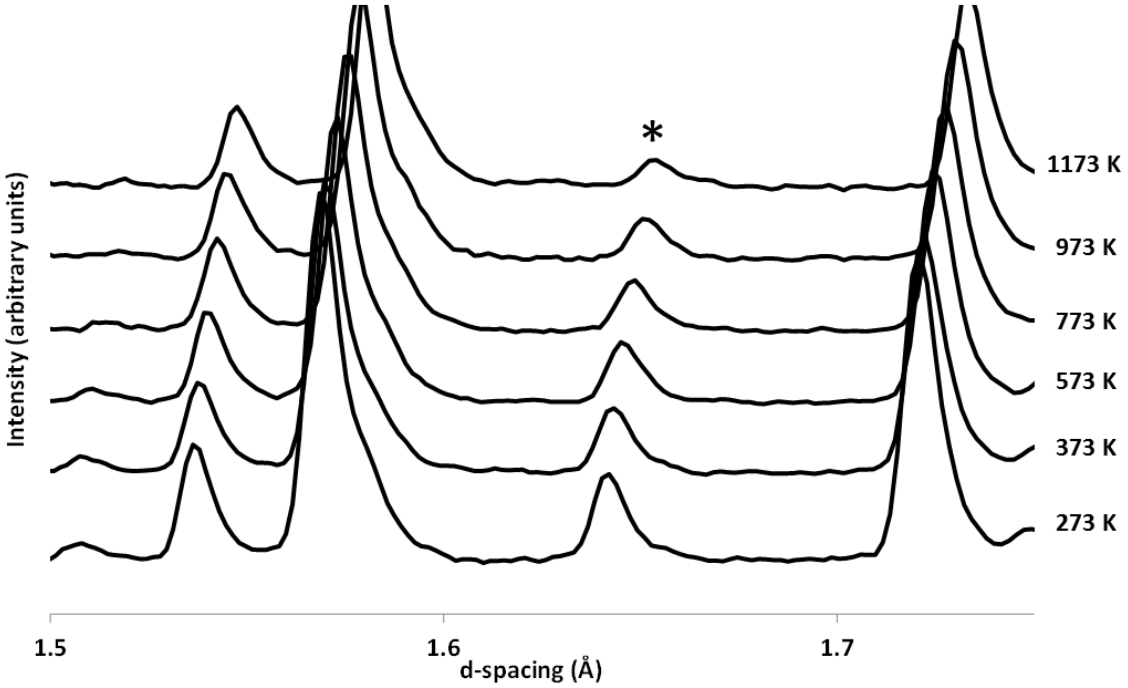

Figure 7.6: NPD patterns for $TbInO_3$ at various temperatures. * indicates (2 0 6) superstructure peak d ≈ 1.64 Å indicating the presence of the larger $P6_3cm$ supercell. Patterns off-set on y-axis for clarity.

As the atomic coordinates can be reliably refined further analysis of changes in the structure can be performed. Observing the gap between the Tb1 and Tb2 planes as a function of temperature it is found that the gap begins to close faster at ~ 800 K possibly indicating a change in behaviour (Figure 7.7). It would be expected that the system is tending towards ΔTb = 0, which is the case in the $P6_3/mmc$ phase.

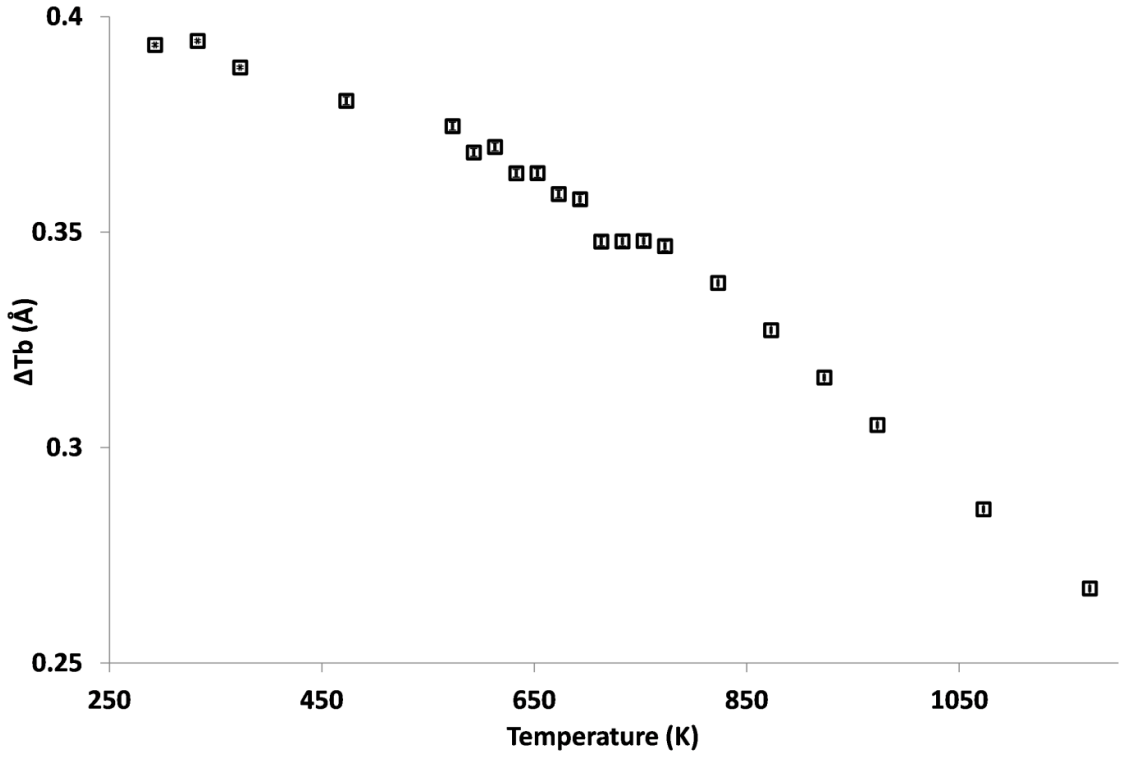

Figure 7.7: Difference between Tb^{3+} layers on *c*-axis (ΔTb) as a function of temperature for $TbInO_3$. Note change of gradient at ~ 800 K.

The equatorial tilt of the InO_5 trigonal bipyramids – measured by the angle of the equatorial oxygen plane (O3 and O4) against the unit cell – is found to decrease more steeply above ~ 800 K (Figure 7.8) with the overall trend being towards 0 °. Both these indicators suggest that $TbInO_3$ is tending towards the high symmetry $P6_3/mmc$ unit cell found for high temperature $YMnO_3$ with increasing temperature. Along with this it would be expected that the O3 and O4 equatorial oxygens of the InO_5 trigonal bipyramids are tending towards their ideal positions (in order to adopt the high symmetry $P6_3/mmc$ unit cell). This is found not to be the case, however; O4 tends towards the ideal position but O3 appears to diverge from it – once again this behaviour appears exaggerated above ~ 800 K (Figure 7.9). There also appears to be some unusual behaviour at room temperature but more measurements would be required in order to probe this area further.

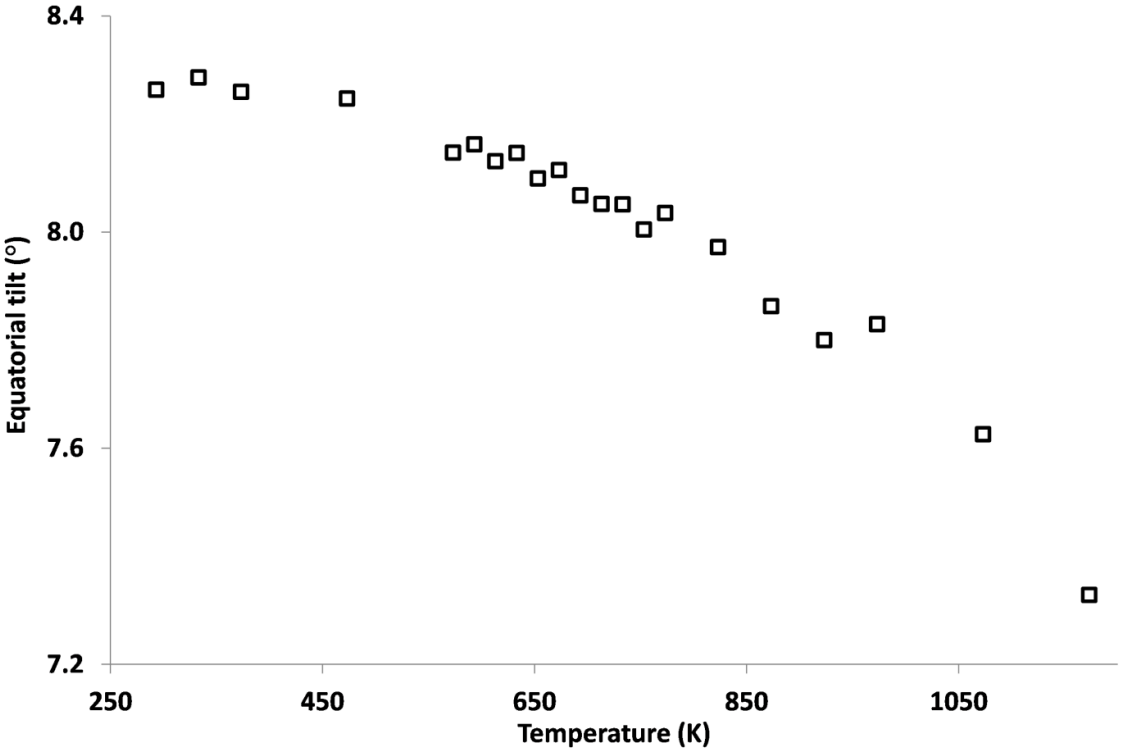

Figure 7.8: Equatorial tilt of InO_5 trigonal bipyramids in terms of equatorial oxygens (O3 and O4) in $TbInO_3$. Values derived from Rietveld refinements of NPD data.

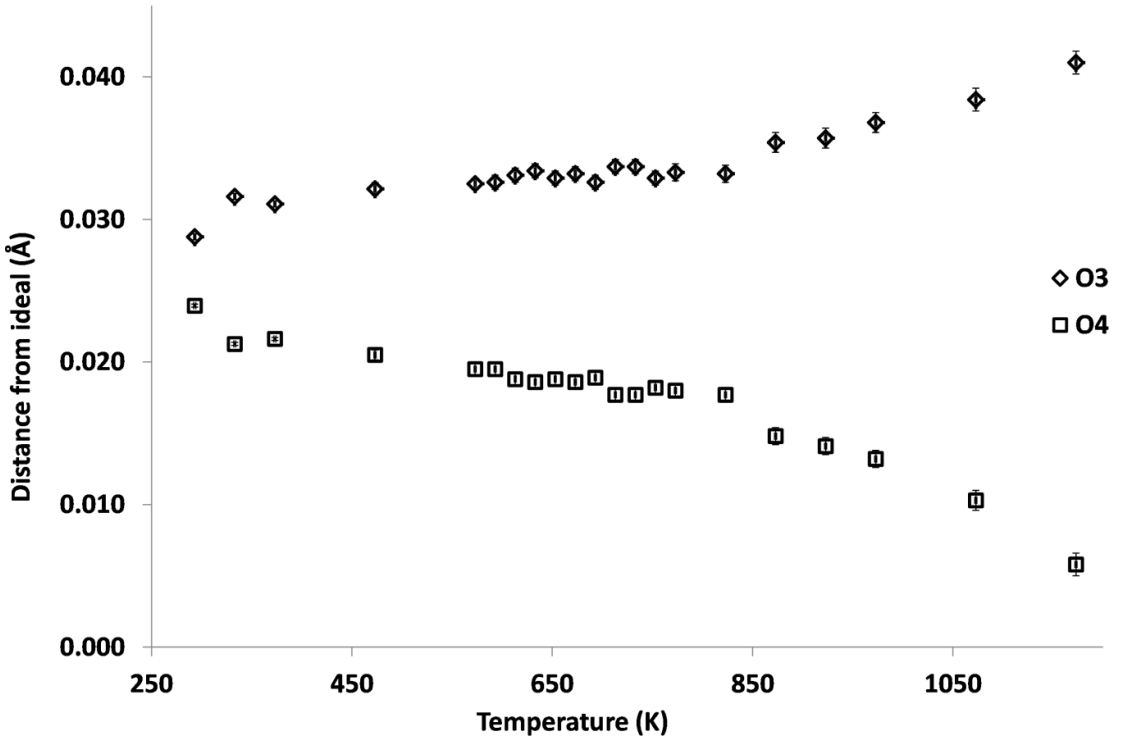

Figure 7.9: Distance from ideal (i.e. the position for the high symmetry $P6_3/mmc$ unit cell) for O3 and O4 along the *c*-axis as derived from NPD data.

Similar behaviour has been reported in the past and suggested to be an isosymmetric phase transition ($P6_3cm \rightarrow P6_3cm$) in a similar NPD study on $YMnO_3$.[10] In this case it was suggested that there would be a corresponding decrease in polarisation with rising temperature due to the decrease in tilt of the trigonal bipyramids and the reducing distance between the Tb^{3+} ions. However, plotting an approximation of the polarisation [d] along the *c*-axis shows that there is very little change except for a small area with marginally increased polarisation at low temperature (Figure 7.10). The almost linear nature shows the system is behaving quite differently from the $YMnO_3$ case.

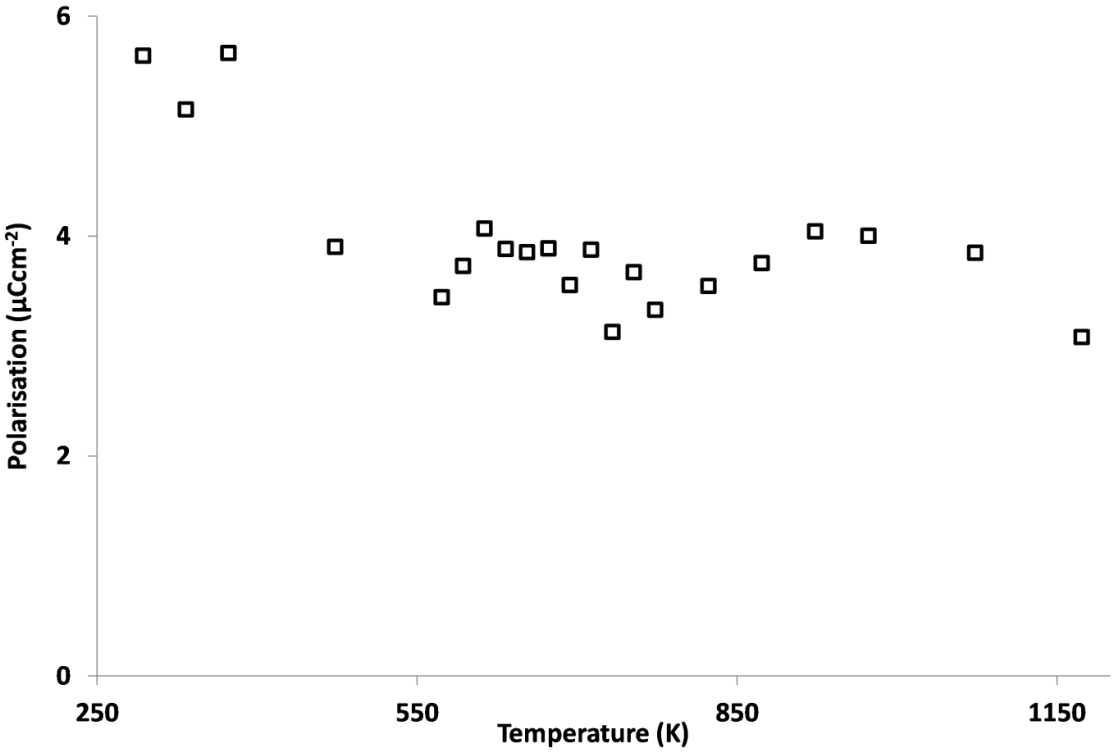

Figure 7.10: Polarisation of $TbInO_3$ along the *c*-axis as a function of temperature, based on atomic coordinates derived from NPD data.

Another key difference is the Tb1 – O(1/2/3) bond lengths (coordination shown in Figure 7.11); for $YMnO_3$ these have been reported to show an anomaly at the isosymmetric transition temperature. This consists of a large increase Y1 – O3 distance with increasing temperature indicating a loss of bonding and the adoption of a 6 – coordinate Y – O coordination sphere. For $TbInO_3$ the Tb1 – O(1/2/3) distances remain approximately constant throughout the temperature range studied (Figure 7.12). There is once again a small anomaly at ~ 800 K which appears to show the beginning of a slightly different trend.

[d] This formula used is $P = \sum_i \frac{\Delta c_i Q_i e m_i}{V}$ where Δc_i is the difference along the *c*-axis from the centrosymmetric case, Q_i is the ionic charge, *e* is the charge of an electron, m_i is the site multiplicity and *V* is the unit cell volume.

In order to probe if there was a phase change to $P6_3/mcm$ – another possible unit cell with the same metrics – the unit cell was refined at selected temperatures in order to compare the quality of fit. It was found that the $P6_3cm$ unit cell is superior in fit at all temperatures surveyed (Table 7.3).

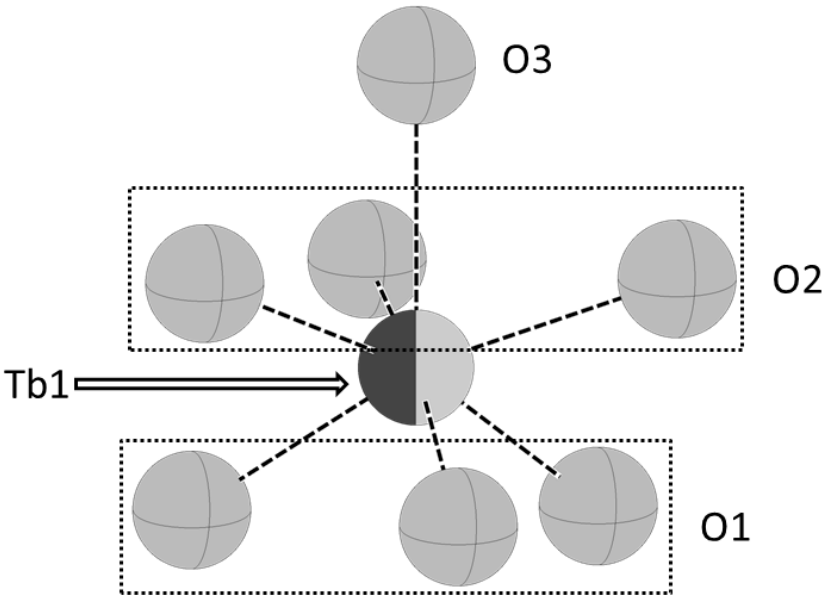

Figure 7.11: Coordination of Tb1 to surrounding O^{2-}.

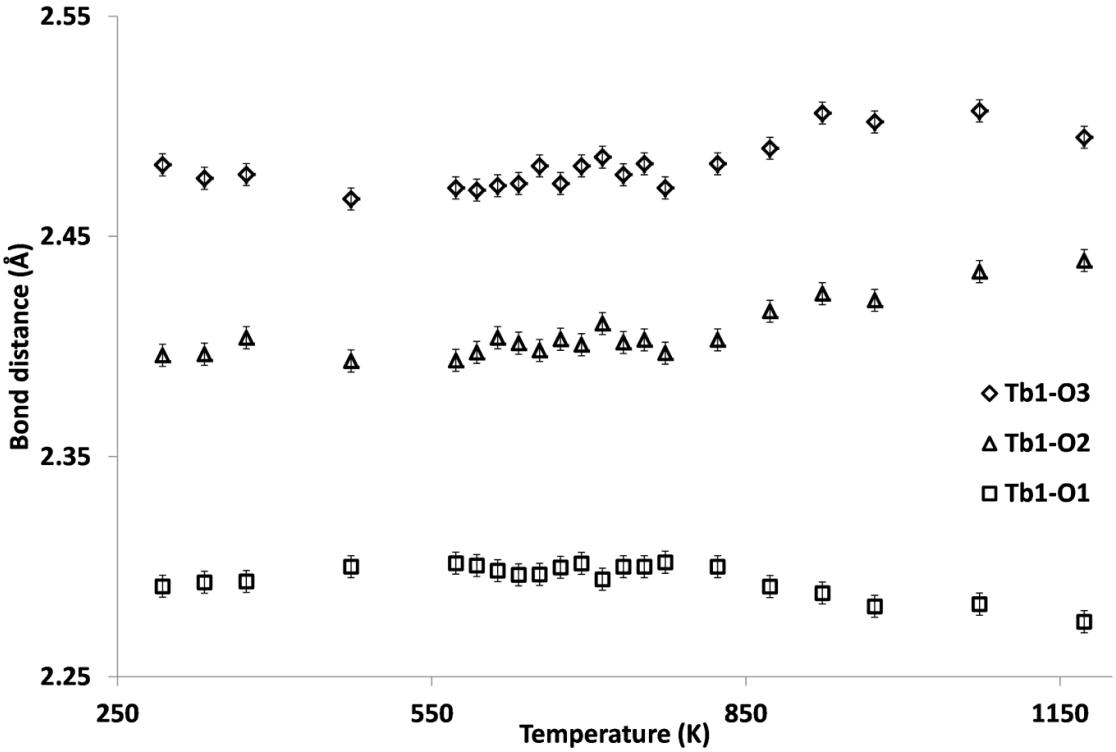

Figure 7.12: Tb1 – O(1/2/3) bond distances as a function of temperature for $TbInO_3$ as derived from NPD data.

Table 7.3: Fit quality for $P6_3cm$ and $P6_3/mcm$ models (with same unit cell metrics) for $TbInO_3$ at various temperatures; atomic coordinates are refined.

	$P6_3cm$			$P6_3/mcm$		
Temp. (K)	χ^2	wRp (%)	Rp (%)	χ^2	wRp (%)	Rp (%)
RT	1.269	2.12	1.93	23.55	9.12	5.73
373	1.052	2.45	2.38	18.16	10.18	6.48
473	1.073	2.47	2.34	15.83	9.50	6.07
573	1.247	2.38	2.23	17.39	8.90	5.66
673	1.283	2.41	2.26	14.87	8.20	5.32
773	1.395	2.50	2.31	12.92	7.63	5.01
873	1.298	2.69	2.50	8.991	7.09	4.84
973	1.292	2.68	2.54	7.765	6.58	4.58
1073	1.326	2.72	2.51	6.575	6.05	4.23
1173	1.566	2.95	2.64	5.671	5.62	4.06

It would appear that in this case if there is indeed an isosymmetric phase transition it is much more subtle than that found for $YMnO_3$. In order to probe the symmetric distortion modes from $P6_3/mmc$ for the $P6_3cm$ models calculated, the ISODISTORT program was employed.[11] This shows broadly similar behaviour to that found for $YMnO_3$ (Figure 7.13) except in this case the K_1 mode is stable and only the Γ_2^- mode changes with temperature (specifically at ~ 800 K). The latter mode is related to the movement of the axial InO_5 O^{2-} in order to make the environment around In^{3+} more anisotropic. It is also related to the movement of Tb^{3+} along the *c*-axis. This leads to its environment changing as well with the Tb1 – O1 distance decreasing and the Tb1 – O2 distance increasing. It is these two movements which retain the polarisation while the gap between the Tb1 and Tb2 layers is decreasing – the traditional main source of polarisation.

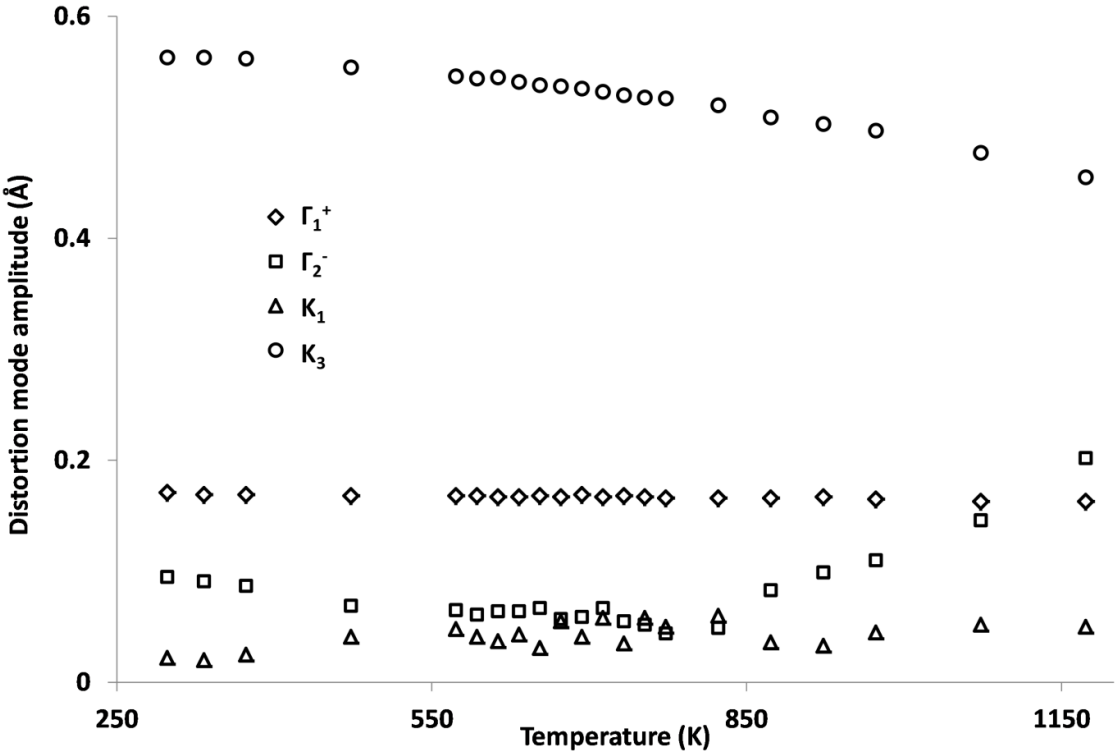

Figure 7.13: Distortion mode amplitudes (parent cell normalised) for $TbInO_3$ calculated at a range of temperatures using the ISODISTORT program.[11]

7.3 Magnetic and electrical behaviour of $MInO_3$

Both $TbInO_3$ and $DyInO_3$ were subject to magnetic measurements [e,f] in order to survey for magnetic ordering – one of the ordering parameters found in $YMnO_3$. $TbInO_3$ shows no divergence between zero field cooled (ZFC) and field cooled (FC) measurements which suggests that there is no ferromagnetic ordering or spin-glass like behaviour (Figure 7.14). A plot of $1/\chi_m$ vs. T shows a straight line for the full temperature range measured (2 – 300 K). There is no indication of any magnetic ordering occurring throughout this range. Some quantitative values can be extracted from this data (Table 7.4). We find that the effective moment, μ_{eff}, is in close agreement with the calculated value for an f^8 lanthanide; 9.72 μ_{BM}. This confirms that the large majority of the terbium ions are in the 3+ state, if not all. The Curie-Weiss temperature, T_{CW}, is -16.7 K which indicates that the interactions within $TbInO_3$ are predominantly antiferromagnetic. Based on this lack of ordering, and previous reports of no ordering down to 0.05 K [4] it is possible to estimate the frustration index ($f = |T_{CW}| / T_N$) is at least 334 indicating that the magnetic structure is very frustrated. A plot of $\chi_m T$ vs. T can be used to observe if the system is magnetically saturated at the highest temperature measured. The expected value is 12.41 emu K mol^{-1} and it is found that, at 300 K, $\chi_m T$ is ~ 11.9 emu K mol^{-1} suggesting that saturation has almost been achieved (Figure 7.15).

[e] Magnetic data is present in appendix A.7.3 in .csv format.

[f] Magnetic measurements were performed with the assistance of Dr. A. Kusmartseva, University of Edinburgh.

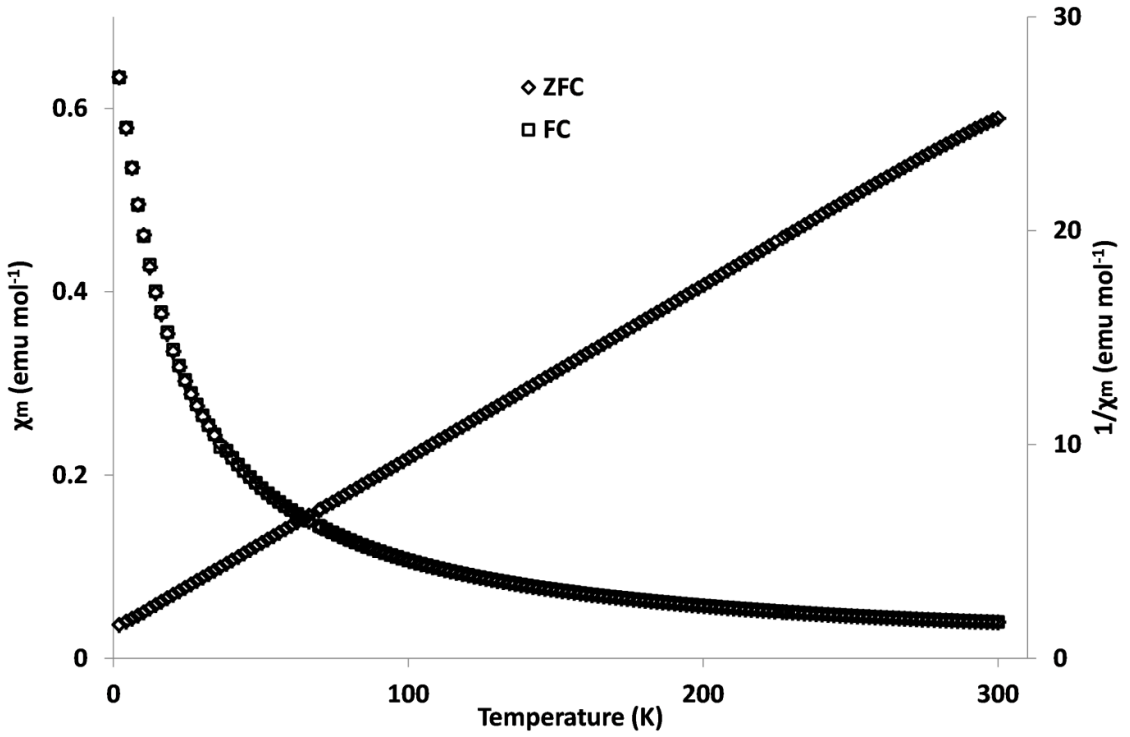

Figure 7.14: χ_m vs. T (ZFC and FC) and $1/\chi_m$ vs. T (ZFC) for $TbInO_3$ measured in a field of 10000 Oe.

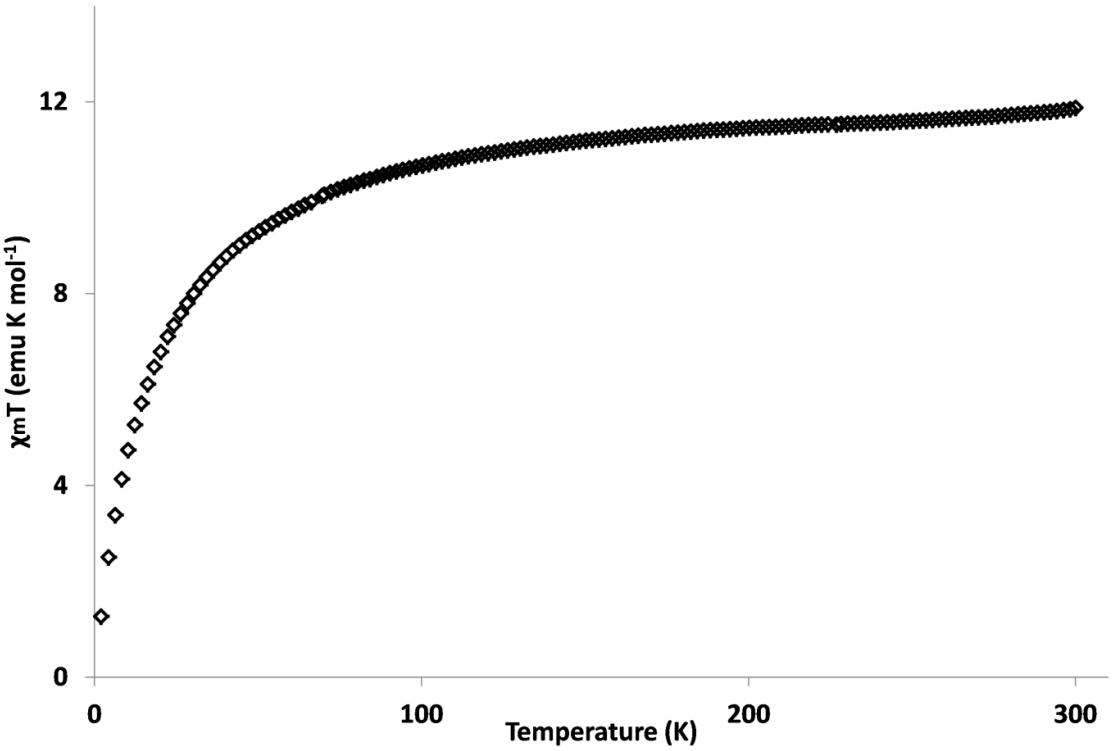

Figure 7.15: $\chi_m T$ vs. T for $TbInO_3$ as measured in a field of 10000 Oe.

Table 7.4: Quantitative magnetic data for $TbInO_3$ extracted from a plot of $1/\chi_m$ vs. T between 2 and 300 K in a field of 10000 Oe.

Curie constant, C, (emu K mol_{Cu}^{-1})	12.41
Effective moment, μ_{eff}, (μ_{BM})	9.96
Curie-Weiss temperature, T_{CW}, (K)	-16.7

Similar magnetic behaviour is found for $DyInO_3$. Once again there is no divergence between the ZFC and FC data which again indicates the absence of ferromagnetic ordering or spin glass behaviour. A plot of $1/\chi_m$ vs. T shows that the data is linear with the exception of a small increase in gradient at 30 K (on cooling) (Figure 7.16). Above this temperature it is once again possible to extract some quantitative data (Table 7.5). μ_{eff} in this case is found to be close to that expected for Dy^{3+} (10.8 μ_{BM}) which reinforces that the dominant oxidation state for dysprosium is 3+. The Curie Weiss temperature is negative but slightly less than that found for $TbInO_3$ (-12.7 K for $DyInO_3$ vs. -16.7 K for $TbInO_3$). This indicates that interactions are antiferromagnetic and again, from previous reports of no magnetic ordering as low as 0.05 K, the frustration index remains particularly high; 255. A plot of $\chi_m T$ vs. T for $DyInO_3$ suggests the system is close to magnetically saturated at 300 K (Figure 7.17). For the saturated system it would be expected that $\chi_m T$ = 14.59 emu K mol^{-1} whereas at 300 K $\chi_m T$ is found to be ~ 13.35 emu K mol^{-1}.

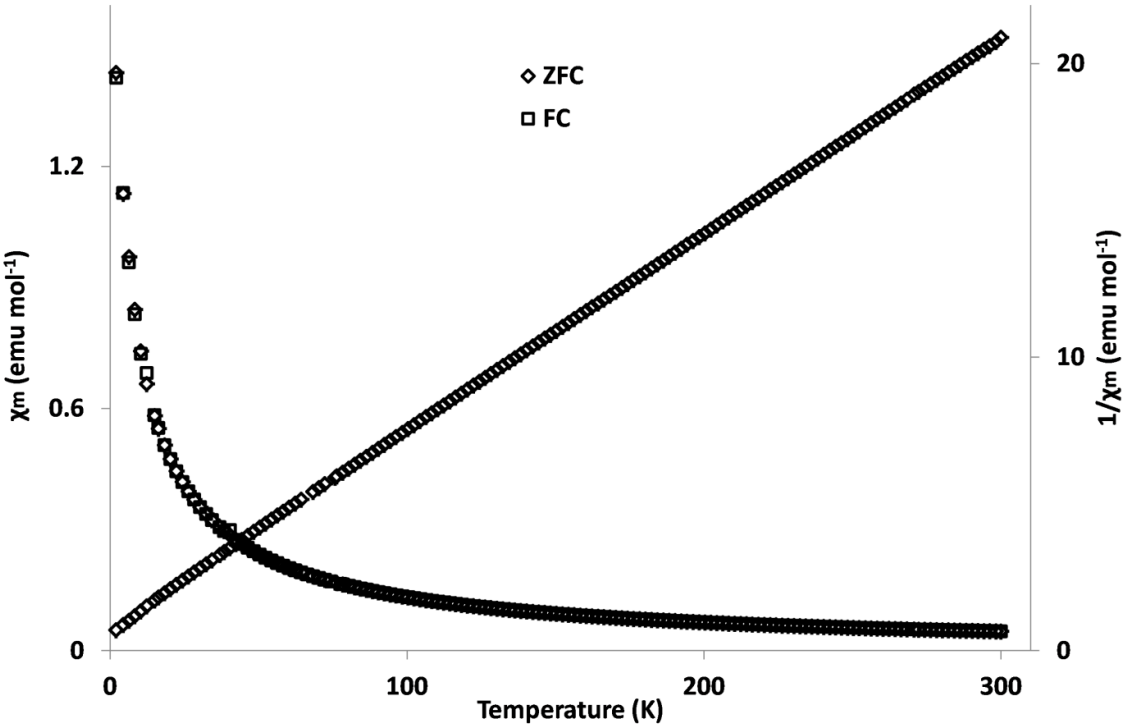

Figure 7.16: χ_m vs. T (ZFC and FC) and $1/\chi_m$ vs. T (ZFC) for $DyInO_3$ measured in a field of 10000 Oe.

Table 7.5: Quantitative magnetic data for $DyInO_3$ extracted from a plot of $1/\chi_m$ vs. T between 40 and 300 K in a field of 10000 Oe.

Curie constant, C, (emu K mol_{Cu}^{-1})	14.95
Effective moment, μ_{eff}, (μ_{BM})	10.94
Curie-Weiss temperature, T_{CW}, (K)	-12.7

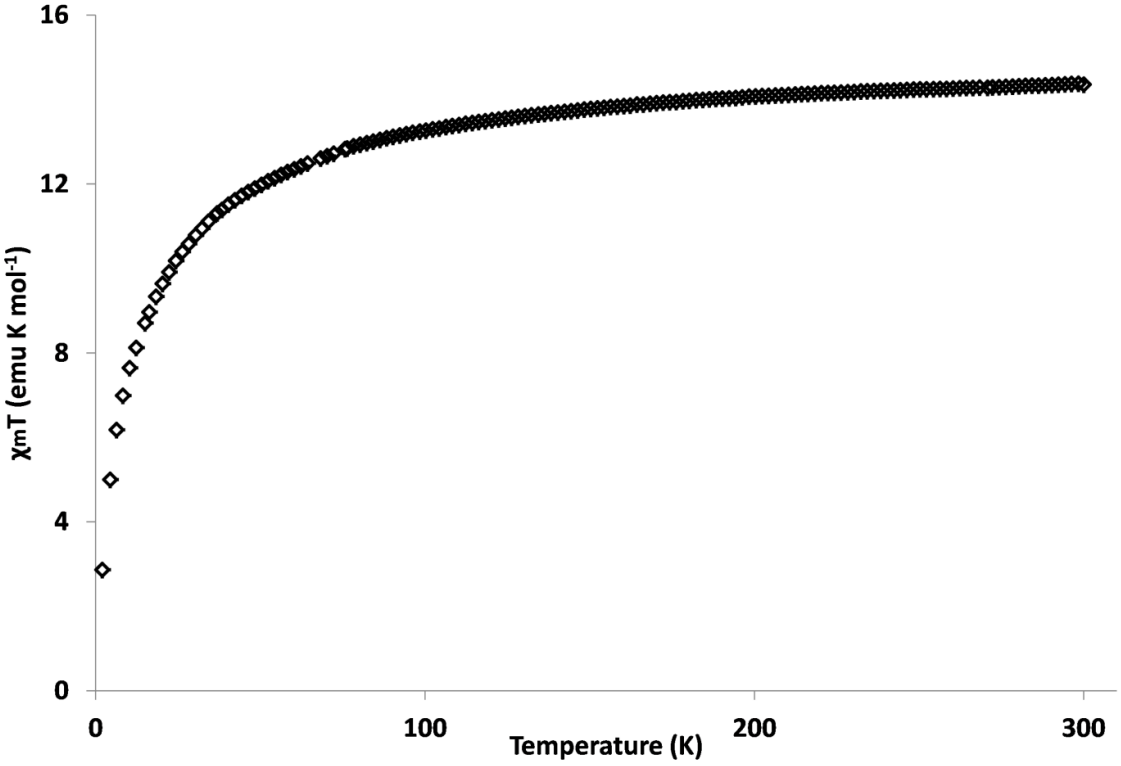

Figure 7.17: $\chi_m T$ vs. T for $DyInO_3$asd measured in a field of 10000 Oe.

Polarisation vs. field measurements were attempted at RT on both $TbInO_3$ and $DyInO_3$ but in both cases failed to give a reliable indication of ferroelectricity – only large cigar-shaped loops were achieved at high voltages and low frequency. This is indicative of a lossy dielectric. This does not preclude the presence of pyro- or piezo-electricity or the presence of ferroelectricity at other temperatures.

7.4 Conclusions

$DyInO_3$ and $TbInO_3$ have been studied using SXPD and NPD, respectively. Due to absorption effects it was challenging to acquire much more than lattice parameters for $DyInO_3$ and to observe the continued existence of the non-centrosymmetric unit cell up to the highest temperature measured. $TbInO_3$ was found not to suffer from such absorption issues and is atomic movements were analysed at a number of different temperatures. For $TbInO_3$ it was found that below ~ 800 K the system is tending towards the more symmetric $P6_3/mmc$ but above ~ 800 K a second distortion begins to take place which leads to a retention of the unit cell polarisation in $TbInO_3$. This second behaviour is suggested to be a particularly subtle

isosymmetric phase transition ($P6_3cm$) similar to that previously reported for $YMnO_3$.[10] Magnetic investigations agree with previously reported work suggesting that no long-range magnetic order is present [4] with the exception that our data only goes down to 2 K (compared to 0.05 K previously reported). It is found that if no ordering occurs above 0.05 K then the frustration parameter of the system is particularly high, at least 330 and 250 for $TbInO_3$ and $DyInO_3$, respectively. Polarisation vs. field measurements were found not to show any evidence for either system being ferroelectric. It is noted that in this case $MInO_3$ where M = Dy, Tb appears to not be a multiferroic under the conditions measured showing the importance of structure activity relationships in functional materials.

1. U. Adem, A. A. Nugroho, A. Meetsma and T. T. M. Palstra, *Phys. Rev. B*, 2007, **75**, 014108.
2. C. Pistorius and G. J. Kruger, *J. Inorg. Nucl Chem.*, 1976, **38**, 1471-1475.
3. T. Tohei, H. Moriwake, H. Murata, A. Kuwabara, R. Hashimoto, T. Yamamoto and I. Tanaka, *Phys. Rev. B*, 2009, **79**, 144125.
4. E. Mun, V. Zapf, C. Batista and S. W. Cheong, *Specific heat and magnetization measurements in RInO3 (R = Ty and Dy)*, National High Magnetic Field Laboratory, Pulsed Field Facility at LANL, 2011.
5. W. G. Williams, R. M. Ibberson, P. Day and J. E. Enderby, *Physica B*, 1997, **241**, 234-236.
6. S. P. Thompson, J. E. Parker, J. Potter, T. P. Hill, A. Birt, T. M. Cobb, F. Yuan and C. C. Tang, *Rev. Sci. Instrum.*, 2009, **80**, 075107.
7. A. C. Larson and R. L. Von Dreele, 2000.
8. B. H. Toby, *J. Appl. Cryst.*, 2001, **34**, 210-213.
9. V. F. Sears, *Neutron News*, 1992, **3**, 29-37.
10. A. S. Gibbs, K. S. Knight and P. Lightfoot, *Phys. Rev. B*, 2011, **83**, 094111.
11. B. J. Campbell, H. T. Stokes, D. E. Tanner and D. M. Hatch, *J. Appl. Crystallogr.*, 2006, **39**, 607-614.

8 Conclusions and future work

A number of points are worth noting from this work which highlight the effects that chemical substitution can have on the frustrated triangular lattices studied.

8.1 Analogues of $YMnO_3$

Substitution of Mn^{3+} in the archetypal geometric multiferroic $YMnO_3$ with Fe^{3+} leads to a number of changes to the material. One key and quickly noticeable change is the metastability of the material which leads to challenges in its synthesis and also characterisation – the soft chemistry techniques used only produce a material with a particularly small crystallite size. Despite this there are a number of measurements that can be performed in order to survey its properties. It is also possible to substitute simultaneously the A-site cation, and this was performed with Yb^{3+} and In^{3+}. At room temperature it is found that there is an element of size control which leads to the material with the smallest A-site occupant, $InFeO_3$, adopting the high symmetry $P6_3/mmc$ form found for high temperature $YMnO_3$. For $YbFeO_3$ and $YFeO_3$ further studies using NPD indicate that the structure is similar to $YMnO_3$. Further data gained from Mössbauer spectroscopy suggests that $YFeO_3$ and $YbFeO_3$ are not as simple as $YMnO_3$ and small anomalies within the NPD data add weight to the possibility that there are two very similar phases simultaneously present. A.C. impedance spectroscopy on $YFeO_3$ and $YbFeO_3$ shows low temperature anomalies which are coincident with anomalies in the magnetic moment and unit cell parameters, respectively. In both cases the electrical anomaly appears to be coincident with an increasing background in the NPD data at high d-spacing. This higher background is suggested to be related to short-range ordering and long-range ordering is indicated in both the NPD and magnetic data, with the latter showing the presence of magnetic reflections (assumed in the case of $YbFeO_3$) at 85 K for $YFeO_3$ and 90 K for $YbFeO_3$. Ferroelectric properties were not observed in either $YFeO_3$ or $YbFeO_3$.

Further substitution of the B-site for In^{3+} and the A-site for Dy^{3+} and Tb^{3+} appears to partially alleviate the metastability. $TbInO_3$ requires precise synthesis conditions to acquire a single phase sample – further heating leads to decomposition. Both samples are found to be structurally similar to $YMnO_3$ and certainly of the same symmetry. $TbInO_3$ was also studied in depth using NPD between RT and 1173 K; the data from this suggests the possibility of a subtle isosymmetric phase transition at ~ 800 K. From the structural data acquired it would appear that $TbInO_3$ maintains a consistent polarisation over the entire range surveyed. Interestingly, neither $DyInO_3$ nor $TbInO_3$ showed any magnetic ordering between 2 and 300 K. This is in line with previous reports and is consistent with the magnetic B-site ion being removed and only the A-site being able to order. Ferroelectric behaviour was not observed in either material at room temperature. Thus, $TbInO_3$ and $DyInO_3$ do not show multiferroic properties over the temperature range studied.

It is found that substitution of ions can have a large effect on the properties of $YMnO_3$ analogues from the stability of the material to the magnetic and electrical properties. The study of these analogues helps the understanding of geometric multiferroic materials and it would be interesting to study the materials reported above further. This could take the form of further structural analysis of $MFeO_3$ by techniques such as pair distribution function or transmission electron microscopy for example. Low temperature studies of $InFeO_3$ could also

be interesting in order to establish if the non-centrosymmetric $P6_3cm$ structure is adopted. The synthesis of further examples of A and B-site substituted analogues and the measurement of their properties would also be of interest.

8.2 Materials from the family $A_2MCu_3F_{12}$

Two new members of this family were synthesised: $Cs_2TiCu_3F_{12}$ and $Rb_2TiCu_3F_{12}$. As with most of this family, difficulty was found in trying to synthesise single phase samples due to the reactivity of the fluoride starting materials. $Cs_2TiCu_3F_{12}$ appears as structurally and symmetrically similar, at ambient temperature, to the previously synthesised sister materials $Cs_2ZrCu_3F_{12}$ and $Cs_2SnCu_3F_{12}$ ($R\bar{3}m$). On cooling the powder a transition to ($P2_1/n$) symmetry is found at approximately 250 K. The single crystal behaves differently however – on cooling there is a transition to an $R\bar{3}$ cell which is similar to that found for $Rb_2SnCu_3F_{12}$. This leads to the suggestion that there is some crystallite size dependence when it comes to the phase transition pathway. Magnetically this sample shows strong antiferromagnetic interactions and the powder is found to undergo some ordering even at ~ 21 K. Magnetic measurements on single crystals, however, proved more challenging and it is difficult to compare the behaviours of the differing morphologies. $Rb_2TiCu_3F_{12}$ powder crystallises in a triclinic unit cell at room temperature and with reducing temperature the cell becomes further distorted – it is suggested that the cell may have a higher symmetry above 320 K. Magnetically there appears to be an anomaly at 50 K, rather higher than that found for $Cs_2TiCu_3F_{12}$.

Synthesis of the previously reported phase $Rb_2SnCu_3F_{12}$ also provides some interesting insights. The crystal structure at room temperature is found to adopt a unit cell with *a* and *b* parameters doubled when compared to $Cs_2SnCu_3F_{12}$ (symmetry $R\bar{3}$) and the powder structure reported in this thesis confirms this. On cooling, a transition is found leading to a triclinic cell like that found for $Rb_2TiCu_3F_{12}$ at ~ 250 K and, on further cooling, the symmetry reverts to $R\bar{3}$ at ~ 190 K. This is suggested to be a rare example of a re-entrant structural transition. Further information was sought by single crystal analysis, but it was found that the same behaviour did not occur in the single crystal – this suggests that once again crystallite size may be dominant in controlling which transitions can occur.

In order to further observe the Sn^{4+} containing members of this family the solid solution $Cs_{2-x}Rb_xSnCu_3F_{12}$ (x = 0, 0.5, 1.0, 1.5) was synthesised. $Cs_2SnCu_3F_{12}$ powder was found to behave much like $Cs_2TiCu_3F_{12}$ powder with the rhombohedral → monoclinic transition occurring at ~ 170 K. With increasing Rb^{1+} content a range of behaviours is found;

- x = 0.25 shows very similar behaviour to the Cs^{1+} rich end-member but with a higher transition temperature,
- x= 0.5 appears as primitive at room temperature and below and
- x = 0.75 shows behaviour similar to $Rb_2SnCu_3F_{12}$ but without the re-entrant transition and once again the transition temperature is increased.

Magnetically, $Cs_2SnCu_3F_{12}$ is found to show some interesting behaviour which suggests the presence of two phases – on first measurement there appeared to be two transitions and

further calcination leads to one of these transitions disappearing suggesting only one phase is left.

In all these cases it is found that the $A_2MCu_3F_{12}$ family is deficient in its ability to maintain a perfect kagome lattice down to low temperature and thus provide promise of quantum spin liquid behaviour. It is found, however, that the family provides a rich range of structural transitions and at the lower temperature there appears to be some interesting magnetic behaviour which would benefit from further investigation. Further work could take the form of improving the purity of samples in order to conduct more precise measurements and possibly investigating the materials at even lower temperatures.

8.3 Future work

In both studies there is opportunity for further work which could help to clarify and expand on the results contained in this thesis. For the systems analogous to $YMnO_3$ there are a number of possible avenues for further study. In the case of $MFeO_3$ one of the main barriers to structural understanding lies in the nano-structural nature of the material; one way to better model the structure may be through the use of the Pairing Distribution Function (PDF) method. PDF uses distances between pairs of atoms to propose a model and is particularly useful in the understanding of nano-materials as there is no associated peak broadening. Thus, PDF could help with the understanding of the precise structural features at room temperature and below. In the case of materials based on $MInO_3$ one possible avenue is the measurement of the polarisation as a function of temperature – particularly for $TbInO_3$ – in order to confirm the isosymmetric phase transition. NPD at lower temperatures would also be of interest in order to check for magnetic reflections and probe the unusual magnetic behaviour. Synthesis of further analogues is also very welcome in order to compare and contrast structural, electrical and magnetic behaviours.

For the systems based upon $A_2MCu_3F_{12}$ the main issues encountered are related to the purity of the samples. Further improvements in synthetic techniques would assist in the precise determination of magnetic properties. For the $A_2TiCu_3F_{12}$ systems it would be of interest to observe the low temperature NPD pattern in order to attempt to model the magnetic reflections. A further understanding of the $Rb_2SnCu_3F_{12}$ system would be particularly advantageous due to its unusual structurally re-entrant transition behaviour. This would primarily require the synthesis of a pure powder and preferably include an element of crystallite/grain size control. This would allow the structural details of the material to be analysed and, in the case of the latter, allow the effect of size to be quantified. More broadly, within this system there are a number of behaviours apparent – studies of various solid-solutions would most likely prove fruitful.

A.3.2.1

Lattice parameters vs. temperature for $Cs_2TiCu_3F_{12}$

Unit cell parameters for $Cs_2TiCu_3F_{12}$ as a function of temperature

Temperature (K)	a (Å)	b (Å)	c (Å)	α °	β °	γ °	V (Å^3)
300	7.090323(18)	= a	19.91020(9)	90	90	120	866.839(6)
300 (monoclinic equivalent)	7.79768	7.09032	10.53928	90	97.36237	90	577.892
280	7.08882(2)	= a	19.89705(10)	90	90	120	865.899(7)
280 (monoclinic equivalent)	7.79349	7.08882	10.53517	90	97.33828	90	577.266
260	7.08613(2)	= a	19.87823(11)	90	90	120	864.422(8)
260 (monoclinic equivalent)	7.78734	7.08613	10.52881	90	97.30789	90	576.282
240	7.78574(7)	7.07736(6)	10.51028(14)	90	97.2250(4)	90	574.544(7)
220	7.78215(4)	7.07119(4)	10.49608(7)	90	97.1697(4)	90	573.073(3)
200	7.77779(5)	7.06549(5)	10.48363(7)	90	97.1156(4)	90	571.679(8)
180	7.77302(5)	7.05964(5)	10.47140(7)	90	97.0590(4)	90	571.260(8)
160	7.76895(5)	7.05496(5)	10.46105(7)	90	97.0087(4)	90	569.082(9)
140	7.76513(6)	7.05081(5)	10.45189(9)	90	96.9628(4)	90	568.025(9)
120	7.76151(6)	7.04702(5)	10.44330(8)	90	96.9176(4)	90	567.043(9)
100	7.75776(5)	7.04320(4)	10.43444(6)	90	96.8692(4)	90	566.039(8)

Quality of fit for $Cs_2TiCu_3F_{12}$ as a function of temperature

		Fitted		- Background	
Temperature (K)	χ^2	wR_p (%)	R_p (%)	wR_p (%)	R_p (%)
300	6.06	8.45	6.48	6.45	5.54
280	3.81	9.72	7.49	7.20	6.32
260	4.00	9.90	7.68	7.73	6.72
240	3.67	9.53	7.33	6.71	6.00
220	3.40	9.52	7.34	6.79	6.08
200	3.42	9.54	7.37	6.84	6.13
180	3.40	9.44	7.31	6.90	6.13
160	3.45	9.45	7.33	6.98	6.19
140	3.47	9.51	7.40	7.24	6.36
120	3.40	9.44	7.38	7.32	6.40
100	5.15	8.03	6.24	6.54	5.54

A.3.3
Comparison of SCXRD and NPD parameters for $Rb_2TiCu_3F_{12}$

Table 1: Lattice parameters for main phase and impurities in $Rb_2TiCu_3F_{12}$ NPD data.

Phase	a (Å)	b (Å)	c (Å)	α (°)	β (°)	γ (°)
$Rb_2TiCu_3F_{12}$	10.3710(12)	10.3541(14)	10.3374(11)	83.729(13)	83.641(10)	83.936(6)
Rb_2TiF_6	5.9215(5)	= a	4.8105(8)	90	90	120
CuO	4.715(5)	3.423(3)	5.235(5)	90	100.78(5)	90

Table 2: Lattice parameters for main phase and impurities in $Rb_2TiCu_3F_{12}$ SXPD data from a high quality sample.

Phase	a (Å)	b (Å)	c (Å)	α (°)	β (°)	γ (°)
$Rb_2TiCu_3F_{12}$	10.3529(7)	10.3506(8)	10.3440(3)	83.838(7)	83.832(7)	83.9111(14)
Rb_2TiF_6	5.9325(4)	= a	4.8082(6)	90	90	120
CuO	4.6857(2)	3.42384(12)	5.1309(2)	90	99.529(3)	90

Table 3: Lattice parameters for main phase and impurities in $Rb_2TiCu_3F_{12}$ SXPD data from a lower quality sample.

Phase	a (Å)	b (Å)	c (Å)	α (°)	β (°)	γ (°)
$Rb_2TiCu_3F_{12}$	10.3520(9)	10.3481(10)	10.3405(4)	83.865(8)	83.865(8)	83.954(2)
Rb_2TiF_6	5.9378(14)	= a	4.7878(15)	90	90	120
CuO	4.6850(2)	3.42423(13)	5.1308(2)	90	99.525(3)	90

Table 4: Lattice parameters for main phase and impurities in $Rb_2TiCu_3F_{12}$ SXPD data from a lower quality sample after cooling to 85 K and then reheating.

Phase	a (Å)	b (Å)	c (Å)	α (°)	β (°)	γ (°)
$Rb_2TiCu_3F_{12}$	10.3537(7)	10.3486(8)	10.3398(4)	83.849(6)	83.849(6)	83.956(2)
Rb_2TiF_6	5.9377(14)	= a	4.7933(16)	90	90	120
CuO	4.6850(22)	3.42406(14)	5.1307(2)	90	99.522(3)	90

By comparing tables 3 and 4 it is clear that at 300 K the data is self-consistent for the same sample. By including table 2 in our comparison we can see that other data from SXPD is also similar to what we would expect. Any differences could be accounted for by variations in the accuracy of the temperature equipment. When the NPD data (Table 1) is included, however, we see differences not only in the main phase but also in the impurities. The data for CuO can be disregarded in the NPD case as it makes up < 1 % of the overall composition by weight. The phase of interest, $Rb_2TiCu_3F_{12}$, gives some key information; the large (relative) divergence between the cell lengths and cell angles would suggest that it is at a lower temperature than the SXPD data. As discussed in the main text there may also be some other factor which also contributes to the difference as the values from the NPD data do not match directly with lower temperatures from the SXPD data.

Lattice parameters vs. temperature for $Rb_2TiCu_3F_{12}$

Unit cell parameters for $Rb_2TiCu_3F_{12}$ as a function of temperature on cooling

Temperature (K)	a (Å)	b (Å)	c (Å)	α °	β °	γ °	V (Å^3)
300	10.3520(9)	10.3481(10)	10.3405(4)	83.865(8)	83.865(8)	83.954(2)	1090.11(15)
280	10.3486(7)	10.3426(7)	10.3310(4)	83.870(6)	83.869(6)	84.005(2)	1088.29(11)
260	10.3363(5)	10.3488(4)	10.3182(4)	83.834(4)	83.872(4)	84.100(2)	1086.40(8)
240	10.3316(4)	10.3473(4)	10.3074(4)	83.799(3)	83.890(3)	84.177(2)	1084.71(7)
220	10.3260(4)	10.3446(4)	10.2987(4)	83.784(3)	83.905(3)	84.240(2)	1083.04(7)
200	10.3209(4)	10.3410(4)	10.2908(4)	83.785(3)	83.927(3)	84.295(2)	1081.44(7)
180	10.3151(4)	10.3373(4)	10.2843(4)	83.791(3)	83.949(3)	84.343(2)	1079.88(7)
160	10.3102(4)	10.3335(4)	10.2783(4)	83.797(3)	83.974(3)	84.381(2)	1078.47(7)
140	10.3054(4)	10.3298(4)	10.2730(4)	83.809(2)	84.002(3)	84.415(2)	1077.16(7)
120	10.3003(4)	10.3256(4)	10.2683(4)	83.826(3)	84.027(3)	84.441(2)	1075.81(7)
100	10.2956(4)	10.3220(4)	10.2642(4)	83.845(3)	84.057(3)	84.459(2)	1074.64(7)
85	10.2924(4)	10.3190(4)	10.2614(4)	83.861(3)	84.080(3)	84.468(2)	1073.79(7)

Quality of fit for $Rb_2TiCu_3F_{12}$ as a function of temperature on cooling

		Fitted		- Background	
Temperature (K)	χ^2	wR_p (%)	R_p (%)	wR_p (%)	R_p (%)
300	7.79	16.38	11.30	22.44	15.21
280	8.15	16.74	11.60	22.97	15.50
260	8.16	16.81	11.55	23.14	15.32
240	7.77	16.49	11.35	22.60	14.89
220	7.59	16.36	11.27	22.24	14.63
200	7.46	16.25	11.25	22.03	14.54
180	7.15	15.94	11.05	21.46	14.14
160	7.16	15.91	11.00	21.48	14.12
140	6.95	15.69	10.89	21.18	13.97
120	6.34	14.85	10.34	20.52	13.46
100	6.36	14.81	10.36	20.57	13.60
85	10.65	13.58	9.42	19.37	12.48

Unit cell parameters for $Rb_2TiCu_3F_{12}$ as a function of temperature on heating

Temperature (K)	a (Å)	b (Å)	c (Å)	α °	β °	γ °	V (Å^3)
300	10.3537(7)	10.3486(8)	10.3398(4)	83.849(6)	83.849(6)	83.956(2)	1090.22(12)
280	10.3416(4)	10.3532(4)	10.3275(3)	83.830(4)	83.849(4)	84.0437(18)	1088.26(7)
260	10.3365(4)	10.3519(4)	10.3157(3)	83.792(3)	83.863(3)	84.1321(19)	1086.44(7)
240	10.3313(4)	10.3498(4)	10.3059(3)	83.776(3)	83.878(3)	84.1986(19)	1084.76(7)
220	10.3253(3)	10.3457(3)	10.2976(3)	83.773(2)	83.901(3)	84.255(2)	1082.96(5)
200	10.3204(4)	10.3425(4)	10.2904(4)	83.772(2)	83.924(3)	84.306(2)	1081.48(7)
180	10.3149(4)	10.3385(4)	10.2841(4)	83.779(2)	83.948(3)	84.349(2)	1079.95(7)
160	10.3097(4)	10.3339(4)	10.2787(4)	83.793(2)	83.977(3)	84.380(2)	1078.49(7)
140	10.3053(4)	10.3298(4)	10.2732(4)	83.804(2)	84.003(3)	84.415(2)	1077.15(7)
120	10.3000(4)	10.3259(4)	10.2690(4)	83.823(3)	84.030(3)	84.438(2)	1075.88(7)
100	10.2956(4)	10.3219(4)	10.2644(4)	83.845(3)	84.059(3)	84.460(2)	1074.64(7)

Quality of fit for $Rb_2TiCu_3F_{12}$ as a function of temperature on heating

		Fitted		- Background	
Temperature (K)	χ^2	wR_p (%)	R_p (%)	wR_p (%)	R_p (%)
300	6.43	15.35	10.74	21.71	14.75
280	6.52	15.46	10.82	21.77	14.83
260	6.67	15.58	10.88	21.82	14.65
240	6.52	15.40	10.77	21.53	14.37
220	6.14	14.99	10.45	21.06	13.95
200	5.86	14.69	10.26	20.85	13.72
180	5.68	14.45	10.10	20.35	13.33
160	5.30	14.00	9.86	19.97	13.02
140	5.49	14.11	9.95	20.04	13.14
120	5.57	14.14	9.98	20.07	13.18
100	5.57	14.03	9.85	20.13	13.08

A.3.4
Kapton data subtraction

0.0077 g of Kapton was loaded into a straw which was mounted in the standard way. The straw was the cooled in field (in this case 2000 Oe to match the single crystal measurements) from ~ 300 to 54 K while measuring the magnetic moment. This yielded the data found in the file "Kapton raw data.csv" also in this appendix. From this χ was calculated:

$$\chi = {}^{Magnetic\ moment}/_{Field}$$

χ per unit mass, χ_g, was then calculated by:

$$\chi_g = {}^{\chi}/_{0.0077g}$$

This allows an average χ_g to be calculated which in this case is 8.23×10^{-7} emu Oe^{-1} g^{-1}. The readings show no temperature dependence. χ_g (multiplied by the amount of Kapton used in the sample measurements) can then be subtracted from the χ of the samples. This leaves a de-convoluted value of χ for the single crystal samples from which quantitative values can be calculated.

A.4.2

Lattice parameters vs. temperature for $Rb_2SnCu_3F_{12}$ – synchrotron

Unit cell parameters for $Rb_2SnCu_3F_{12}$ as a function of temperature on heating ("run 1")

Temperature (K)	Phase (**% wt. if mix**)	a (Å)	b (Å)	c (Å)	α °	β °	γ °	V (Å^3)
500	Rhombohedral	13.94812(6)	= a	20.53959(12)	90	90	120	3460.62(3)
	(Triclinic equivalent)	10.57000	= a	= a	82.56883	= α	= α	1121.672
490	Rhombohedral	13.94604(6)	= a	20.52881(13)	90	90	120	3457.77(3)
	(Triclinic equivalent)	10.56676	= a	= a	82.58469	= α	= α	1120.892
460	Rhombohedral	13.93994(6)	= a	20.49862(12)	90	90	120	3449.67(3)
	(Triclinic equivalent)	10.55756	= a	= a	82.62833	= α	= α	1118.653
430	Rhombohedral	13.93159(6)	= a	20.47108(13)	90	90	120	3440.91(3)
	(Triclinic equivalent)	10.54795	= a	= a	82.65977	= α	= α	1116.092
400	Rhombohedral	13.92390(6)	= a	20.44376(14)	90	90	120	3432.52(3)
	(Triclinic equivalent)	10.53867	= a	= a	82.69280	= α	= α	1113.66
370	Rhombohedral	13.91713(6)	= a	20.41938(13)	90	90	120	3425.10(3)
	(Triclinic equivalent)	10.53044	= a	= a	82.72260	= α	= α	1111.512
340	Rhombohedral	13.91014(6)	= a	20.38799(12)	90	90	120	3416.39(3)
	(Triclinic equivalent)	10.52059	= a	= a	82.76626	= α	= α	1109.063
310	Rhombohedral	13.90384(5)	= a	20.35509(12)	90	90	120	3407.79(3)
	(Triclinic equivalent)	10.51074	= a	= a	82.81521	= α	= α	1106.693
300	Rhombohedral	13.90210(4)	= a	20.34514(10)	90	90	120	3405.28(17)
	(Triclinic equivalent)	10.50783	= a	= a	82.83052	= α	= α	1106.003
280	Rhombohedral **(39.2)**	13.89777(7)	= a	20.32400(18)	90	90	120	3399.62(4)
	(Triclinic equivalent)	10.50137	= a	= a	82.86117	= α	= α	1104.424

	Triclinic **(60.8)**	10.5026(3)	10.51362(28)	10.48876(22)	82.808(2)	82.744(2)	83.020(1)	1133.27(3)
250	Triclinic	10.49567(13)	10.47100(10)	10.50961(12)	82.789(1)	83.158(1)	82.777(1)	1130.495(17)
220	Rhombohedral **(22.3)**	13.8786(7)	= a	20.2781(18)	90	90	120	3382.6(4)
	(Triclinic equivalent)	10.48304	= a	= a	82.89823	= α	= α	1099.201
	Triclinic **(77.7)**	10.48925(12)	10.45785(10)	10.50314(12)	82.752(1)	83.272(1)	82.813(1)	1127.924(17)
190	Rhombohedral **(91.3)**	13.87539(7)	= a	20.24422(17)	90	90	120	3375.37(4)
	(Triclinic equivalent)	10.47435	= a	= a	82.95884	= α	= α	1097.36
	Triclinic **(8.7)**	10.4838(6)	10.4535(6)	10.4973(6)	82.677(4)	83.375(4)	82.806(5)	1126.27(8)
160	Rhombohedral	13.86966(5)	= a	20.21848(12)	90	90	120	3368.300(21)
	(Triclinic equivalent)	10.46629	= a	= a	82.99496	= α	= α	1095.355
130	Rhombohedral	13.86474(5)	= a	20.19561(12)	90	90	120	3362.105(22)
	(Triclinic equivalent)	10.45921	= a	= a	83.02762	= α	= α	1093.607
100	Rhombohedral	13.86106(7)	= a	20.17396(16)	90	90	120	3356.72(4)
	(Triclinic equivalent)	10.45294	= a	= a	83.06152	= α	= α	1092.128

Quality of fit for $Rb_2SnCu_3F_{12}$ as a function of temperature on heating ("run 1")

		Fitted		- Background	
Temperature (K)	χ^2	wR_p (%)	R_p (%)	wR_p (%)	R_p (%)
500	10.83	13.36	9.05	16.05	10.40
490	6.428	14.49	10.26	16.39	11.18
460	6.526	14.54	10.28	16.32	11.13
430	7.658	15.55	10.85	17.30	11.79
400	8.173	15.80	10.97	17.46	11.85
370	8.190	15.88	11.07	17.48	11.99
340	7.941	15.83	11.21	17.27	12.08
310	7.528	15.65	11.33	17.10	12.22
300	13.05	14.16	10.01	15.98	11.15
280	10.05	16.56	12.55	16.66	12.84
250	11.75	17.55	13.33	18.60	14.06
220	11.51	16.67	12.68	17.27	13.03
190	9.358	14.56	10.80	13.67	10.45
160	8.113	15.13	10.99	15.06	11.00
130	8.270	15.17	11.07	14.88	10.98
100	10.07	14.97	11.13	13.87	10.63

Unit cell parameters for $Rb_2SnCu_3F_{12}$ as a function of temperature on heating ("run 2")

Temperature (K)	Phase (**% wt. if mix**)	a (Å)	b (Å)	c (Å)	α °	β °	γ °	V (Å^3)
300	Rhombohedral	13.90136(3)	= a	20.34751(8)	90	90	120	3405.308(17)
	(Triclinic equivalent)	10.50801	= a	= a	82.82338	= α	= α	1105.953
270	Rhombohedral **(43.6)**	13.89434(8)	= a	20.31782(24)	90	90	120	3369.91(5)
	(Triclinic equivalent)	10.49853	= a	= a	82.86359	= α	= α	1103.564
	Triclinic **(56.4)**	10.50190(18)	10.48263(11)	10.51051(15)	82.780(1)	83.051(1)	82.776(2)	1132.267(19)
255	Triclinic	10.50300(13)	10.47915(8)	10.512712(13)	82.778(1)	83.121(1)	82.779(1)	1132.400(13)
240	Triclinic	10.49444(10)	10.46618(7)	10.50598(10)	82.764(1)	83.193(1)	82.796(1)	1129.512(13)
225	Rhombohedral **(7.7)**	13.89663(29)	= a	20.2693(11)	90	90	120	3389.92(17)
	(Triclinic equivalent)	10.48911	= a	= a	82.97109	= α	= α	1102.186

	Triclinic **(92.3)**	10.50331(10)	10.45844(8)	10.49071(11)	82.811(1)	83.258(1)	82.759(1)	1128.146(14)
210	Rhombohedral **(63.1)**	13.87922(8)	= a	20.25544(24)	90	90	120	3379.11(5)
	(Triclinic equivalent)	10.47845	= a	= a	82.94714	= α	= α	1098.487
	Triclinic **(36.9)**	10.49949(19)	10.45566(17)	10.48611(22)	82.817(2)	83.293(1)	82.751(2)	1127.010(29)
195	Rhombohedral	13.87647(5)	= a	20.24278(10)	90	90	120	3375.661(25)
	(Triclinic equivalent)	10.47452	= a	= a	82.96510	= α	= α	1097.505
180	Rhombohedral	13.87379(4)	= a	20.22854(10)	90	90	120	3371.983(24)
	(Triclinic equivalent)	10.47028	= a	= a	82.98657	= α	= α	1096.486

Quality of fit for $Rb_2SnCu_3F_{12}$ as a function of temperature on heating ("run 2")

		Fitted		- Background	
Temperature (K)	χ^2	wR_p (%)	R_p (%)	wR_p (%)	R_p (%)
300	2.692	10.17	7.70	11.05	8.14
270	2.626	10.03	7.66	11.00	8.18
255	4.199	12.72	9.54	15.79	11.23
240	5.970	10.74	7.87	13.23	9.11
225	3.116	10.92	8.33	12.05	8.82
210	3.077	10.85	8.36	11.75	8.75
195	2.836	10.44	8.12	11.42	8.73
180	2.818	10.40	8.02	11.16	8.46

Unit cell parameters for $Rb_2SnCu_3F_{12}$ as a function of temperature on cooling ("run 2")

Temperature (K)	Phase (**% wt. if mix**)	a (Å)	b (Å)	c (Å)	α °	β °	γ °	V (Å^3)
300	Rhombohedral	13.90182(3)	= a	20.34270(7)	90	90	120	3404.729(16)
	(Triclinic equivalent)	10.50718	= a	= a	82.83472	= α	= α	1105.861
285	Rhombohedral	13.89791(4)	= a	20.33113(8)	90	90	120	3400.877(20)
	(Triclinic	10.50297	= a	= a	82.84683	= α	= α	1104.714

	equivalent)							
270	Rhombohedral **(63.5)**	13.89442(4)	= a	20.31730(12)	90	90	120	3396.857(25)
	(Triclinic equivalent)	10.49845	= a	= a	82.86490	= α	= α	1103.559
	Triclinic **(36.5)**	10.51043(34)	10.5030(4)	10.48293(20)	82.769(3)	82.775(3)	83.040(1)	1132.36(3)
255	Rhombohedral **(38.6)**	13.89169(12)	= a	20.3053(4)	90	90	120	3393.51(7)
	(Triclinic equivalent)	10.49467	= a	= a	82.88150	= α	= α	1102.614
	Triclinic **(61.4)**	10.49833(15)	10.47358(10)	10.50884(13)	82.774(1)	83.129(1)	82.777(1)	1130.881(18)
240	Triclinic	10.49470(17)	10.46909(10)	10.50395(17)	82.788(2)	83.163(1)	82.878(2)	1129.604(16)
225	Triclinic	10.49122(14)	10.46121(9)	10.50165(13)	82.765(1)	83.230(1)	82.810(1)	1128.276(14)
210	Rhombohedral **(12.5)**	13.87923(26)	= a	20.2587(8)	90	90	120	3379.66(14)
	(Triclinic equivalent)	10.47915	= a	= a	82.94041	= α	= α	1098.599
	Triclinic **(87.5)**	10.49899(13)	10.45381(10)	10.48701(14)	82.825(1)	83.298(1)	82.759(1)	1126.898(17)
195	Rhombohedral **(80.1)**	13.87636(6)	= a	20.24244(16)	90	90	120	3375.55(3)
	(Triclinic equivalent)	10.47439	= a	= a	82.96548	= α	= α	1097.470
	Triclinic **(19.9)**	10.4957(3)	10.4533(3)	10.4826(4)	82.826(3)	83.317(2)	82.737(2)	1126.01(5)
180	Rhombohedral	13.87359(5)	= a	20.22969(10)	90	90	120	3372.076(24)
	(Triclinic equivalent)	10.47043	= a	= a	82.98357	= α	= α	1096.490
165	Rhombohedral	13.87119(4)	= a	20.21524(9)	90	90	120	3368.501(22)
	(Triclinic equivalent)	10.46627	= a	= a	83.00633	= α	= α	1095.514

Quality of fit for $Rb_2SnCu_3F_{12}$ as a function of temperature on cooling ("run 2")

		Fitted		- Background	
Temperature (K)	χ^2	wR_p (%)	R_p (%)	wR_p (%)	R_p (%)
300	4.463	9.51	7.13	10.81	7.87
285	2.732	10.77	8.22	11.70	8.72
270	2.327	9.88	7.45	10.30	7.60

255	2.759	10.68	8.18	11.76	8.76
240	3.962	12.58	9.43	15.06	10.74
225	6.478	11.48	8.39	14.33	9.82
210	3.505	11.60	8.90	13.09	9.61
195	2.721	10.22	7.86	11.08	8.26
180	2.736	10.28	7.97	10.87	8.34
165	4.718	9.56	7.25	10.53	7.74

Lattice parameters vs. temperature for $Rb_2SnCu_3F_{12}$ – neutron

Unit cell parameters for $Rb_2SnCu_3F_{12}$ as a function of temperature

Temperature (K)	Phase (**% wt. if mix**)	a (Å)	b (Å)	c (Å)	α °	β °	γ °	V (Å^3)
300	Rhombohedral	13.9010(3)	= a	20.3413(9)	90	90	120	3404.09(15)
	(Triclinic equivalent)	10.50652	= a	= a	82.83514	= α	= α	1105.659
220	Triclinic	10.4857(10)	10.4512(6)	10.5030(10)	82.744(7)	83.317(4)	82.827(7)	1126.92(7)
150	Rhombohedral	13.8664(3)	= a	20.1927(8)	90	90	120	3362.40(17)
	(Triclinic equivalent)	10.45932	= a	= a	83.03870	= α	= α	1093.801
25	Rhombohedral	13.8514(3)	= a	20.1098(8)	90	90	120	3341.38(17)
	(Triclinic equivalent)	10.43492	= a	= a	83.16599	= α	= α	1087.969

Quality of fit for $Rb_2SnCu_3F_{12}$ as a function of temperature

		Fitted		- Background	
Temperature (K)	χ^2	wR_p (%)	R_p (%)	wR_p (%)	R_p (%)
300	7.941	4.16	4.58	6.15	5.56
220	6.651	3.45	3.48	4.01	3.85
150	8.740	4.61	4.25	5.25	4.69
25	8.485	4.54	4.33	5.09	4.72

A.5.2

Lattice parameters vs. temperature for $Cs_2SnCu_3F_{12}$ – neutron

Unit cell parameters for $Cs_2SnCu_3F_{12}$ as a function of temperature

Temperature (K)	a (Å)	b (Å)	c (Å)	α °	β °	γ °	V (Å^3)
300	7.13155(6)		20.3610(3)				896.801(18)
300 (monoclinic equivalent)	7.93829	7.13155	10.67124		98.25131		597.867
165	7.8951(3)	7.1196(4)	10.6398(5)		98.0747(29)		592.13(5)
150	7.90569(17)	7.10976(18)	10.61490(29)		97.9377(16)		590.921(26)
100	7.89656(16)	7.09752(15)	10.58758(25)		97.8209(16)		587.871(22)

Quality of fit for $Cs_2SnCu_3F_{12}$ as a function of temperature

		Fitted		- Background	
Temperature (K)	χ^2	wR_p (%)	R_p (%)	wR_p (%)	R_p (%)
300	3.808	4.55	3.65	5.26	4.14
165	4.512	4.96	4.18	5.89	5.09
150	3.417	4.28	3.45	4.71	3.48
100	3.453	4.33	3.49	4.68	3.43

Lattice parameters vs. temperature for $Cs_2SnCu_3F_{12}$ – synchrotron (Run 1)

Unit cell parameters for $Cs_2SnCu_3F_{12}$ as a function of temperature

Temperature (K)	a (Å)	b (Å)	c (Å)	α °	β °	γ °	V (Å^3)
300	7.131913(11)		20.36532(5)				897.0858(28)
300 (monoclinic equivalent)	7.93962	7.13191	10.67248		98.25995		598.0572
280	7.130960(12)		20.35025(5)				896.184(3)
280 (monoclinic equivalent)	7.93504	7.13096	10.66844		98.22747		597.456
260	7.129898(12)		20.33456(5)				895.225(3)
260 (monoclinic equivalent)	7.93026	7.12990	10.66416		98.19415		596.817
240	7.128841(12)		20.31934(5)				894.289(3)
240 (monoclinic equivalent)	7.92560	7.12884	10.66000		98.16200		596.193
220 (heating)	7.127702(13)		20.30475(5)				893.362(3)
220 (heating) (monoclinic equivalent)	7.92111	7.12770	10.65589		98.13210		595.575
220 (cooling)	7.127737(13)		20.30493(6)				893.379(3)
220 (cooling) (monoclinic equivalent)	7.92117	7.12774	10.65596		98.13231		595.586
210 (heating)	7.127123(13)		20.29730(6)				892.889(3)
210 (heating) (monoclinic equivalent)	7.91881	7.12712	10.65380		98.11680		595.259
210 (cooling)	7.12720(13)		20.29742(6)				892.913(3)
210 (cooling) (monoclinic equivalent)	7.91887	7.12720	10.65389		98.11654		595.275
200 (heating)	7.126498(13)		20.28987(6)				892.406(3)
200 (heating) (monoclinic equivalent)	7.91651	7.12650	10.65167		98.10189		594.937
200 (cooling)	7.126651(13)		20.28978(6)				892.440(3)
200 (cooling) (monoclinic equivalent)	7.91653	7.12665	10.65179		98.10050		594.960
190 (heating)	7.125861(14)		20.28245(6)				891.920(4)
190 (heating) (monoclinic equivalent)	7.91420	7.12586	10.64953		98.08709		594.613
190 (cooling)	7.126027(13)		20.28235(6)				891.329(3)
190 (cooling) (monoclinic equivalent)	7.91422	7.12603	10.64966		98.08558		594.219
180 (heating)	7.124463(15)		20.27389(6)				891.193(4)
180 (heating) (monoclinic equivalent)	7.91135	7.12446	10.64647		98.07499		594.129

180 (cooling)	7.124969(14)		20.27409(6)				891.329(4)
180 (cooling) (monoclinic equivalent)	7.91155	7.12497	10.64697		98.07172		594.219
170 (heating)	7.91261(8)	7.11983(8)	10.63580(12)		98.0341(6)		593.302(11)
170 (cooling)	7.91228(8)	7.12088(8)	10.63694(12)		98.0345(6)		593.428(11)
160 (cooling)	7.91058(8)	7.11723(7)	10.62982(11)		98.0103(5)		592.635(11)
140	7.90781(8)	7.10996(7)	10.61670(11)		97.9630(5)		591.160(10)
120	7.90443(8)	7.10505(7)	10.60627(11)		97.9189(5)		589.983(11)
100	7.90102(4)	7.10058(4)	10.59669(6)		97.8770(3)		588.885(6)

Quality of fit for $Cs_2SnCu_3F_{12}$ as a function of temperature

		Fitted		- Background	
Temperature (K)	χ^2	wR_p (%)	R_p (%)	wR_p (%)	R_p (%)
300	7.045	12.53	8.92	14.01	9.94
280	4.759	14.07	10.33	14.88	10.99
260	4.871	14.14	10.41	14.83	10.99
240	4.924	14.17	10.43	14.71	10.92
220 (heating)	5.131	14.36	10.56	14.76	10.95
220 (cooling)	5.047	14.35	10.54	14.73	10.94
210 (heating)	5.245	14.47	10.66	14.91	11.08
210 (cooling)	5.085	14.43	10.61	14.74	10.97
200 (heating)	5.241	14.42	10.57	14.68	10.89
200 (cooling)	5.064	14.38	10.56	14.59	10.86
190 (heating)	5.247	14.46	10.62	14.59	10.86
190 (cooling)	5.089	14.42	10.67	14.56	10.93
180 (heating)	5.225	14.55	10.64	14.53	10.80
180 (cooling)	5.152	14.46	10.65	14.48	10.80
170 (heating) *	12.19	20.58	14.32	20.21	13.99
170 (cooling) *	12.14	20.54	14.23	20.30	13.99
160 (heating) *	12.32	20.60	14.33	20.26	14.06
160 (cooling) *	12.59	20.69	14.39	20.50	14.20
140 *	13.07	20.92	14.70	20.61	14.50
120 *	13.54	21.07	14.96	20.80	14.83
100	11.64	14.74	10.86	14.66	10.93

*CuO removed from refinement hence poorer fit.

Lattice parameters vs. temperature for $Cs_2SnCu_3F_{12}$ – synchrotron (Run 2)

Unit cell parameters for $Cs_2SnCu_3F_{12}$ as a function of temperature

Temperature (K)	a (Å)	b (Å)	c (Å)	α °	β °	γ °	V (Å^3)
300	7.131728(14)		20.36700(6)				897.113(4)
300 (monoclinic equivalent)	7.94005	7.13173	10.67267		98.26574		598.075
200	7.126750(16)		20.29022(7)				892.484(4)
200 (monoclinic equivalent)	7.91668	7.12675	10.65197		98.10092		594.989
190	7.126132(16)		20.28167(7)				891.953(4)
190 (monoclinic equivalent)	7.91406	7.12613	10.64961		98.08299		594.635
180	7.124720(16)		20.27249(7)				891.196(4)
180 (monoclinic equivalent)	7.91102	7.12472	10.64641		98.06936		594.131
170	7.91245(4)	7.12068(4)	10.63520(7)		98.0288(3)		593.335(6)
165	7.91165(4)	7.11871(4)	10.63149(6)		98.0129(3)		592.927(6)
160	7.91081(4)	7.11689(4)	10.62815(6)		98.0008(3)		592.544(6)
150	7.90892(4)	7.11365(4)	10.62188(6)		97.9775(3)		591.817(6)
140	7.90691(4)	7.11072(4)	10.61611(6)		97.9541(3)		591.136(5)

Quality of fit for $Cs_2SnCu_3F_{12}$ as a function of temperature

		Fitted		- Background	
Temperature (K)	χ^2	wR_p (%)	R_p (%)	wR_p (%)	R_p (%)
300	9.283	9.65	7.37	11.52	8.62
200	10.11	10.37	7.96	11.96	9.06
190	9.832	10.32	7.95	11.85	9.02
180	10.04	10.45	8.02	11.81	8.98
170	7.946	10.11	7.91	10.76	8.20
165	7.949	10.07	7.89	10.71	8.16
160	7.928	10.10	7.93	10.67	8.18
150	7.942	10.14	7.96	10.69	8.18
140	8.175	10.26	8.06	10.77	8.26

A.5.3.1

Lattice parameters vs. temperature for $Cs_{1.5}Rb_{0.5}SnCu_3F_{12}$

Unit cell parameters for $Cs_{1.5}Rb_{0.5}SnCu_3F_{12}$ as a function of temperature

Temperature (K)	a (Å)	b (Å)	c (Å)	α °	β °	γ °	V (Å^3)
300	7.12113(2)		20.35953(10)				894.120(6)
300 (monoclinic equivalent)	7.93475	7.12113	10.66165		98.3255		596.080
290	7.12030(2)		20.35171(9)				893.569(6)
290 (monoclinic equivalent)	7.93227	7.12030	10.65925		98.3115		595.713
280	7.11915(2)		20.34356(10)				892.924(6)
280 (monoclinic equivalent)	7.92960	7.11915	10.65650		98.2986		595.283
270	7.11738(3)		20.33477(11)				892.092(7)
270 (monoclinic equivalent)	7.92657	7.11738	10.65305		98.2888		594.728
260	7.11636(3)		20.33190(13)				891.711(9)
260 (monoclinic equivalent)	7.92544	7.11636	10.65154		98.2887		594.474
250	7.92512(7)	7.10748(6)	10.64518(11)		98.2227(5)		593.453(9)
240	7.92649(6)	7.10836(6)	10.63926(10)		98.2094(5)		593.319(9)
230	7.92065(5)	7.10332(5)	10.62659(8)		98.1951(5)		591.778(7)
220	7.91831(5)	7.10094(5)	10.61998(7)		98.1779(4)		591.062(7)
210	7.91596(5)	7.09596(4)	10.61376(7)		98.1582(4)		590.363(6)
200	7.91366(4)	7.09596(4)	10.60799(7)		98.1364(4)		589.696(6)
190	7.91148(4)	7.09358(4)	10.60274(6)		98.1151(4)		589.075(6)
180	7.90935(4)	7.09126(4)	10.59762(6)		98.0823(5)		588.472(6)
170	7.90729(4)	7.08902(4)	10.59274(6)		98.0705(4)		587.895(6)
160	7.90525(4)	7.08694(4)	10.58807(6)		98.0487(4)		587.343(6)
150	7.90335(4)	7.08493(4)	10.58370(6)		98.0272(4)		586.824(6)
140	7.90139(4)	7.08305(4)	10.57952(6)		98.0060(4)		586.316(6)
130	7.89947(4)	7.08120(4)	10.57533(6)		97.9852(4)		585.824(6)
120	7.89764(4)	7.07951(4)	10.57135(6)		97.9650(4)		585.358(6)
110	7.89575(4)	7.07788(4)	10.56755(6)		97.9447(4)		584.901(6)
100	7.89388(4)	7.07631(4)	10.56384(6)		97.9246(4)		584.456(6)

Quality of fit for $Cs_{1.5}Rb_{0.5}SnCu_3F_{12}$ as a function of temperature

		Fitted		- Background	
Temperature (K)	χ^2	wR_p (%)	R_p (%)	wR_p (%)	R_p (%)
300	12.01	3.53	2.43	5.35	3.91
290	12.58	3.63	2.51	5.54	4.06
280	13.62	3.77	2.62	5.90	4.30
270	15.24	3.98	2.76	6.44	4.63
260	16.30	4.13	2.87	6.61	4.74
250	9.888	3.22	2.25	4.39	3.22
240	9.606	3.18	2.21	4.36	3.18
230	9.275	3.13	2.19	4.30	3.15
220	8.913	3.07	2.15	4.21	3.09
210	8.737	3.03	2.12	4.09	2.99
200	8.531	3.01	2.11	4.02	2.95
190	8.627	3.02	2.12	4.03	2.97
180	8.718	3.03	2.14	4.07	3.01
170	8.762	3.05	2.15	4.08	3.02
160	8.893	3.06	2.17	4.13	3.05
150	8.947	3.07	2.18	4.15	3.06
140	8.934	3.07	2.18	4.15	3.04
130	8.818	3.04	2.18	4.15	3.05
120	9.067	3.08	2.19	4.18	3.05
110	9.388	3.13	2.23	4.28	3.13
100	9.436	3.14	2.24	4.32	3.14

A.5.3.2

Lattice parameters vs. temperature for $CsRbSnCu_3F_{12}$

Unit cell parameters for $(CsRb)SnCu_3F_{12}$ as a function of temperature

Temperature (K)	a (Å)	b (Å)	c (Å)	α °	β °	γ °	V (Å^3)
300	7.92369(9)	7.08376(7)	10.60375(12)		98.7057(8)		588.326(11)
290	7.92193(9)	7.08134(8)	10.59904(12)		98.6826(9)		587.769(11)
280	7.92011(9)	7.07871(8)	10.59437(12)		98.6567(9)		587.198(12)
270	7.91923(9)	7.07505(9)	10.59036(12)		98.6184(9)		586.666(12)
260	7.91779(8)	7.07177(8)	10.58685(12)		98.585(9)		586.145(11)
250	7.91536(8)	7.06978(8)	10.58305(12)		98.5642(9)		585.622(11)
240	7.91285(8)	7.06796(8)	10.57919(12)		98.4557(9)		585.102(11)
230	7.91030(8)	7.06634(8)	10.57542(12)		98.5268(9)		584.599(11)
220	7.90756(8)	7.06498(8)	10.57144(12)		98.5113(9)		584.088(11)
210	7.90484(8)	7.06356(8)	10.56758(12)		98.4945(9)		583.582(12)
200	7.90202(9)	7.06241(9)	10.56365(13)		98.4791(9)		583.085(12)
190	7.89935(9)	7.06121(9)	10.56007(13)		98.4641(10)		582.614(13)
180	7.89665(10)	7.06003(10)	10.55656(14)		98.4484(10)		582.148(13)
170	7.89392(10)	7.05902(10)	10.55307(14)		98.4352(11)		581.691(14)
160	7.89124(11)	7.05815(11)	10.54971(15)		98.4227(11)		581.256(15)
150	7.88868(11)	7.05724(11)	10.54652(16)		98.4090(12)		580.837(15)
140	7.88611(12)	7.05639(12)	10.54343(17)		98.3967(13)		580.426(16)
130	7.88363(12)	7.05546(13)	10.54053(17)		98.3830(13)		580.028(17)
120	7.88108(13)	7.05486(13)	10.53760(18)		98.3715(14)		579.647(17)
110	7.87887(13)	7.05384(13)	10.53484(18)		98.3573(14)		579.270(18)
100	7.87649(14)	7.05304(14)	10.53210(19)		98.3443(14)		578.898(18)

Quality of fit for $(CsRb)SnCu_3F_{12}$ as a function of temperature

		Fitted		- Background	
Temperature (K)	χ^2	wR_p (%)	R_p (%)	wR_p (%)	R_p (%)
300	14.93	3.85	2.51	7.96	4.68
290	15.73	3.96	2.56	8.20	4.79
280	16.65	4.07	2.61	8.53	4.94
270	17.07	4.10	2.64	8.60	5.02
260	17.17	4.12	2.67	8.49	5.02
250	17.27	4.13	2.68	8.37	4.99
240	17.72	4.17	2.71	8.32	5.00
230	18.01	4.22	2.74	8.31	5.01
220	18.53	4.27	2.79	8.29	5.04
210	19.45	4.37	2.83	8.47	5.14
200	20.07	4.46	2.88	8.62	5.23
190	21.19	4.57	2.96	8.85	5.39
180	21.95	4.65	2.99	9.01	5.45
170	22.91	4.77	3.06	9.25	5.59
160	23.76	4.85	3.11	9.40	5.68
150	24.75	4.94	3.14	9.61	5.76
140	25.43	5.03	3.19	9.76	5.85
130	26.30	5.10	3.24	9.92	5.93
120	28.31	5.27	3.33	10.27	6.09
110	34.54	5.69	3.58	10.85	6.45
100*	17.16	4.01	2.80	5.60	3.88

* Atomic parameters and preferential orientation also refined.

A.5.3.3

Lattice parameters vs. temperature for $Cs_{0.5}Rb_{1.5}SnCu_3F_{12}$

Unit cell parameters for $Cs_{0.5}Rb_{1.5}SnCu_3F_{12}$ as a function of temperature

Temperature (K)	a (Å)	b (Å)	c (Å)	α °	β °	γ °	V (Å^3)
300	14.01939(12)		20.35651(26)				3464.91(6)
300 (triclinic equivalent)	10.56280	10.56280	10.56280	83.16018	83.16018	83.16018	1154.97
290	14.01676(12)		20.34747(26)				3462.07(6)
290 (triclinic equivalent)	10.55898	10.55898	10.55898	83.17094	83.17094	83.17094	1154.02
280	14.01399(12)		20.33782(27)				3459.07(6)
280 (triclinic equivalent)	10.55569	10.55569	10.55569	83.18255	83.18255	83.18255	1153.02
270	10.54210(23)	10.56569(19)	10.55035(29)	83.2983(12)	83.1014(11)	83.1905(15)	1152.13(5)
260	10.53850(23)	10.56347(18)	10.54686(28)	83.3136(12)	83.1112(11)	83.2014(15)	1151.20(4)
250	10.53449(22)	10.56179(17)	10.54338(27)	83.3331(12)	83.1196(11)	83.2126(15)	1150.28(4)
240	10.53035(22)	10.56098(18)	10.53974(26)	83.3565(12)	83.1256(11)	83.2250(14)	1149.43(4)
230	10.52545(21)	10.56131(16)	10.53611(24)	83.3865(12)	83.1277(11)	83.2375(14)	1148.63(4)
220	10.52050(20)	10.56163(15)	10.53238(23)	83.4237(12)	83.1252(11)	83.2487(13)	1147.81(4)
210	10.51582(20)	10.56093(15)	10.52853(22)	83.4591(12)	83.1228(12)	83.2593(13)	1146.90(4)
200	10.51138(19)	10.55954(15)	10.52476(21)	83.4920(12)	83.1201(12)	83.2652(13)	1145.93(4)
190	10.50734(19)	10.55796(15)	10.52121(21)	83.5193(12)	83.1206(12)	83.2716(12)	1145.00(4)
180	10.50338(19)	10.55607(15)	10.51787(20)	83.5455(12)	83.1227(12)	83.2776(12)	1144.07(4)
170	10.49971(18)	10.55405(15)	10.51474(20)	83.5687(12)	83.1266(12)	83.2845(12)	1143.18(3)
160	10.49620(18)	10.55204(15)	10.51195(20)	83.5882(12)	83.1333(12)	83.2921(12)	1142.35(3)
150	10.49307(18)	10.54984(15)	10.50924(20)	83.6069(12)	83.1392(12)	83.2987(13)	1141.45(3)
140	10.48993(18)	10.54764(15)	10.50657(20)	83.6236(12)	83.1479(12)	83.3061(13)	1140.74(3)
130	10.48699(18)	10.54547(15)	10.50415(20)	83.6387(12)	83.1566(12)	83.3137(13)	1139.99(3)
120	10.48430(18)	10.54328(15)	10.50172(20)	83.6526(12)	83.1663(12)	83.3213(13)	1139.26(3)
110	10.48171(18)	10.54113(15)	10.49960(19)	83.6637(12)	83.1761(12)	83.3282(13)	1138.58(3)
100	10.47920(18)	10.53895(15)	10.49737(19)	83.6769(12)	83.1853(12)	83.3358(13)	1137.89(3)

Quality of fit for $Cs_{0.5}Rb_{1.5}SnCu_3F_{12}$ as a function of temperature

		Fitted		- Background	
Temperature (K)	χ^2	wR_p (%)	R_p (%)	wR_p (%)	R_p (%)
300	27.61	4.99	2.96	11.70	6.02
290	27.15	4.97	2.95	11.65	5.99
280	27.39	4.98	2.96	11.76	6.02
270	22.22	4.48	2.93	8.31	5.30
260	22.32	4.50	2.94	8.48	5.37
250	22.18	4.48	2.94	8.48	5.37
240	22.46	4.50	2.95	8.43	5.37
230	22.09	4.47	2.94	8.19	5.25
220	21.59	4.41	2.90	7.97	5.12
210	21.05	4.36	2.85	7.85	5.02
200	21.97	4.45	2.91	7.85	5.06
190	21.54	4.40	2.89	7.61	4.95
180	22.08	4.44	2.91	7.56	4.95
170	22.10	4.45	2.92	7.51	4.92
160	21.97	4.42	2.91	7.45	4.90
150	21.90	4.41	2.91	7.38	4.87
140	21.52	4.38	2.89	7.32	4.84
130	21.42	4.37	2.89	7.23	4.81
120	21.31	4.35	2.89	7.17	4.79
110	19.44	4.19	2.80	6.85	4.61
100	19.07	4.16	2.80	6.73	4.58

A.5.4

Lattice parameters of the series $Cs_{2-x}Rb_xSnCu_3F_{12}$ in monoclinic setting

Adjusting the rhombohedral unit cells at room temperature to their monoclinic setting we can easily compare with the primitive, monoclinic unit cell of $(CsRb)SnCu_3F_{12}$. Axes have been adjusted to represent the same % change for easy comparison.

a parameter vs A-site occupation of Cs^{1+}:

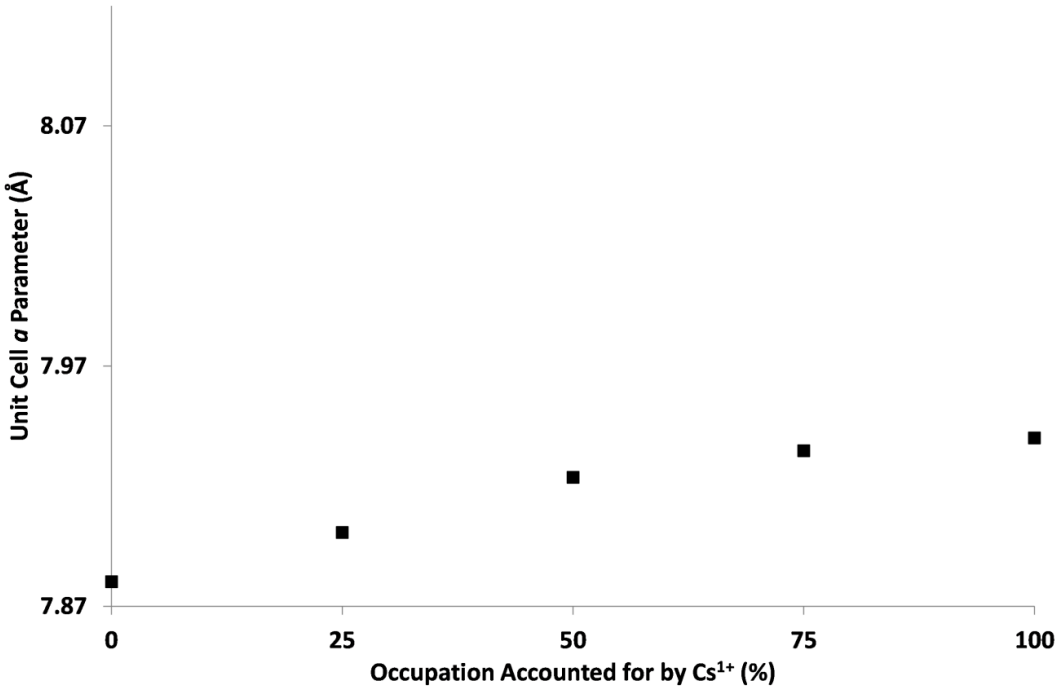

b parameter vs A-site occupation of Cs^{1+}:

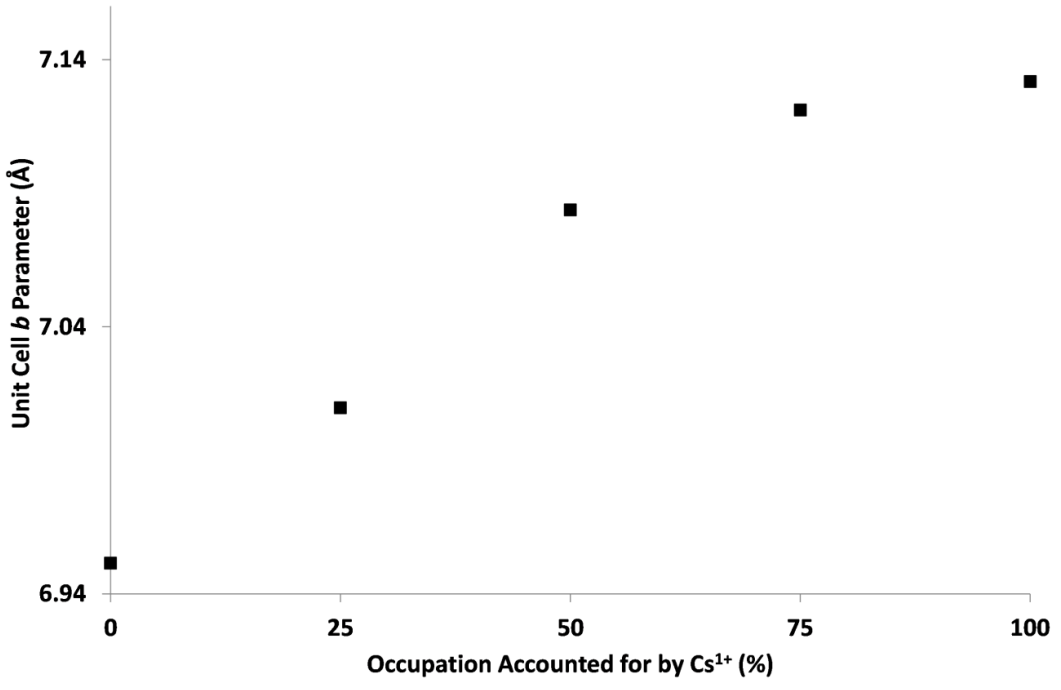

c parameter vs A-site occupation of Cs^{1+}:

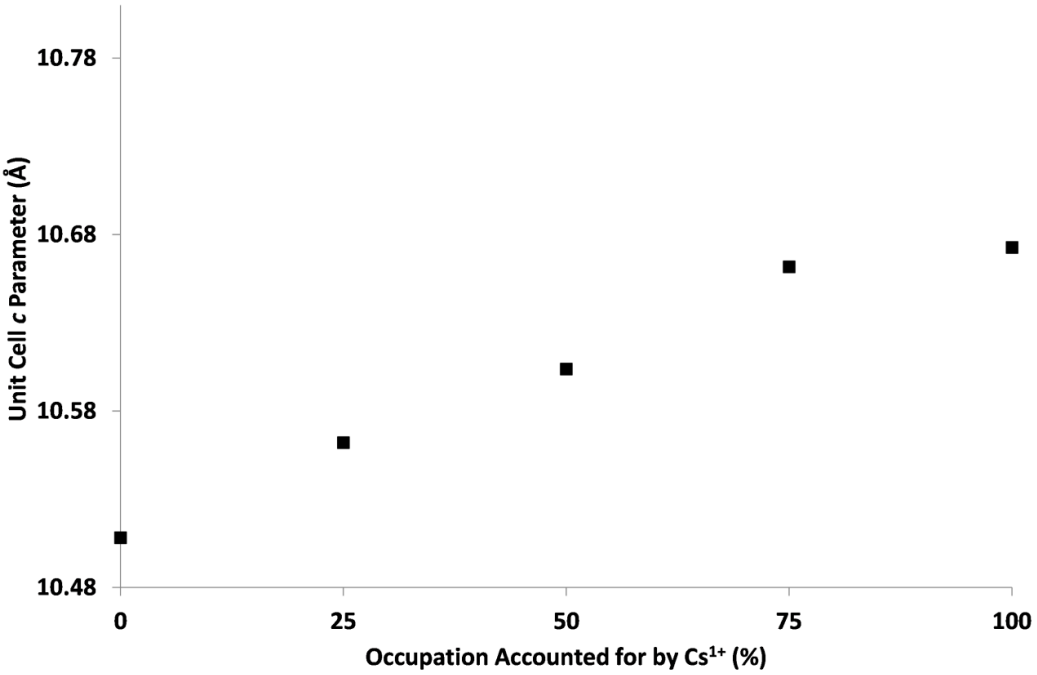

β parameter vs A-site occupation of Cs^{1+}:

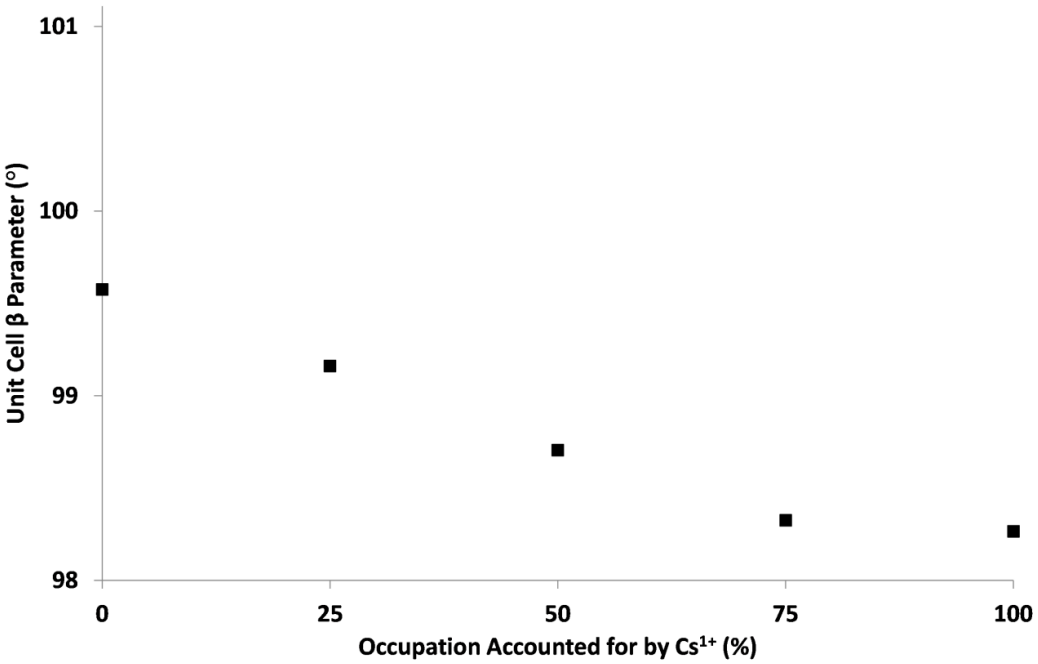

A.6.2.1

Lattice parameters vs. temperature for $YFeO_3$

Unit cell parameters for $YFeO_3$ as a function of temperature

Temperature (K)	a (Å)	b (Å)	c (Å)	α °	β °	γ °	V (Å^3)
RT	6.0733(6)	= b	11.7458(13)	90	90	120	375.20(9)
280	6.0699(6)		11.7435(13)				374.70(9)
260	6.0692(6)		11.7428(13)				374.60(9)
235	6.0680(6)		11.7436(13)				374.48(9)
210	6.0674(5)		11.7429(13)				374.37(9)
185	6.0657(6)		11.7423(13)				374.16(9)
160	6.0653(6)		11.7427(13)				374.11(9)
135	6.0634(6)		11.7415(13)				373.84(9)
110	6.0634(5)		11.7431(12)				373.88(9)
85	6.0623(6)		11.7430(13)				373.75(9)
60	6.0620(6)		11.7431(13)				373.72(9)
35	6.0622(6)		11.7425(13)				373.73(9)
10	6.0621(5)		11.7437(12)				373.75(8)

Quality of fit for $YFeO_3$ as a function of temperature (over 4 banks)

		Fitted		- Background	
Temperature (K)	χ^2	wR_p (%)	R_p (%)	wR_p (%)	R_p (%)
RT	3.549	3.20	2.60	4.24	3.04
280	3.146	3.25	2.70	4.24	3.07
260	3.198	3.27	2.71	4.27	3.14
235	3.198	3.26	2.69	4.22	3.11
210	3.208	3.28	2.71	4.31	3.15
185	3.163	3.24	2.69	4.23	3.13
160	3.311	3.31	2.71	4.33	3.19
135	3.369	3.32	2.70	4.35	3.20
110	3.352	3.31	2.70	4.36	3.18
85	3.380	3.32	2.69	4.36	3.17
60	3.487	3.36	2.84	4.36	3.23
35	3.517	3.35	2.90	4.34	3.34
10	5.186	3.27	2.78	4.32	3.18

Lattice parameters vs. temperature for $YbFeO_3$

Unit cell parameters for $YbFeO_3$ as a function of temperature

Temperature (K)	a (Å)	b (Å)	c (Å)	α °	β °	γ °	V (Å^3)
873	6.0237(8)	= b	11.7822(17)	90	90	120	370.24(12)
823	6.0186(8)		11.7893(18)				369.83(13)
773	6.0140(8)		11.7843(19)				369.12(14)
723	6.0105(8)		11.7830(18)				368.64(13)
673	6.0066(7)		11.7778(17)				368.00(12)
573	6.0006(8)		11.7701(18)				367.03(12)
473	5.9956(7)		11.7573(17)				366.02(12)
373	5.9913(7)		11.7520(18)				365.32(12)
RT (furnace)	5.9814(6)		11.7312(14)				363.48(9)
RT (cryo)	5.9927(5)		11.7531(13)				365.54(8)
260	5.9888(5)		11.7485(13)				364.91(8)
230	5.9873(5)		11.7471(13)				364.69(8)
210	5.9866(5)		11.7446(13)				364.53(8)
190	5.9871(5)		11.7462(13)				364.64(8)
180	5.9856(5)		11.7431(13)				364.37(8)
170	5.9853(5)		11.7447(13)				364.37(8)
160	5.9846(5)		11.7427(13)				364.23(8)
150	5.9812(6)		11.7363(14)				363.61(10)
130	5.9842(5)		11.7436(13)				364.21(8)
110	5.9794(6)		11.7344(14)				363.34(10)
90	5.9835(5)		11.7427(13)				364.09(8)
50	5.9833(5)		11.7430(13)				364.08(8)
10	5.9826(5)		11.7427(13)				363.98(8)

Quality of fit for $YbFeO_3$ as a function of temperature (over 4 banks)

		Fitted		- Background	
Temperature (K)	χ^2	wR_p (%)	R_p (%)	wR_p (%)	R_p (%)
873	1.779	4.25	3.87	5.38	4.43
823	1.793	3.91	3.48	5.32	4.05
773	1.811	3.95	3.49	5.30	4.06
723	1.721	3.85	3.37	5.21	3.92
673	1.737	3.86	3.35	5.18	3.89
573	1.736	3.82	3.48	5.05	4.01
473	1.543	3.54	3.15	4.17	3.37
373	1.594	3.49	3.11	4.61	3.49
RT (furnace)	3.066	3.01	2.52	4.28	3.07
RT (cryo)	5.455	2.79	2.19	4.10	2.82
260	3.375	2.91	2.34	4.15	2.90
230	3.483	2.95	2.40	4.18	2.97
210	3.483	2.94	2.38	4.20	2.97
190	3.561	2.97	2.41	4.22	3.01
180	3.542	2.95	2.38	4.16	2.94
170	3.524	2.93	2.38	4.11	2.91
160	3.528	2.93	2.37	4.16	2.97
150	3.629	2.96	2.38	4.17	2.97
130	3.642	2.96	2.38	4.13	2.95
110	3.735	2.99	2.42	4.21	3.00
90	3.582	2.92	2.33	4.10	2.92
50	3.752	2.98	2.38	4.14	2.95
10	5.777	2.90	2.34	4.07	2.87

A.6.3.3
Magnetic fits for $YFeO_3$

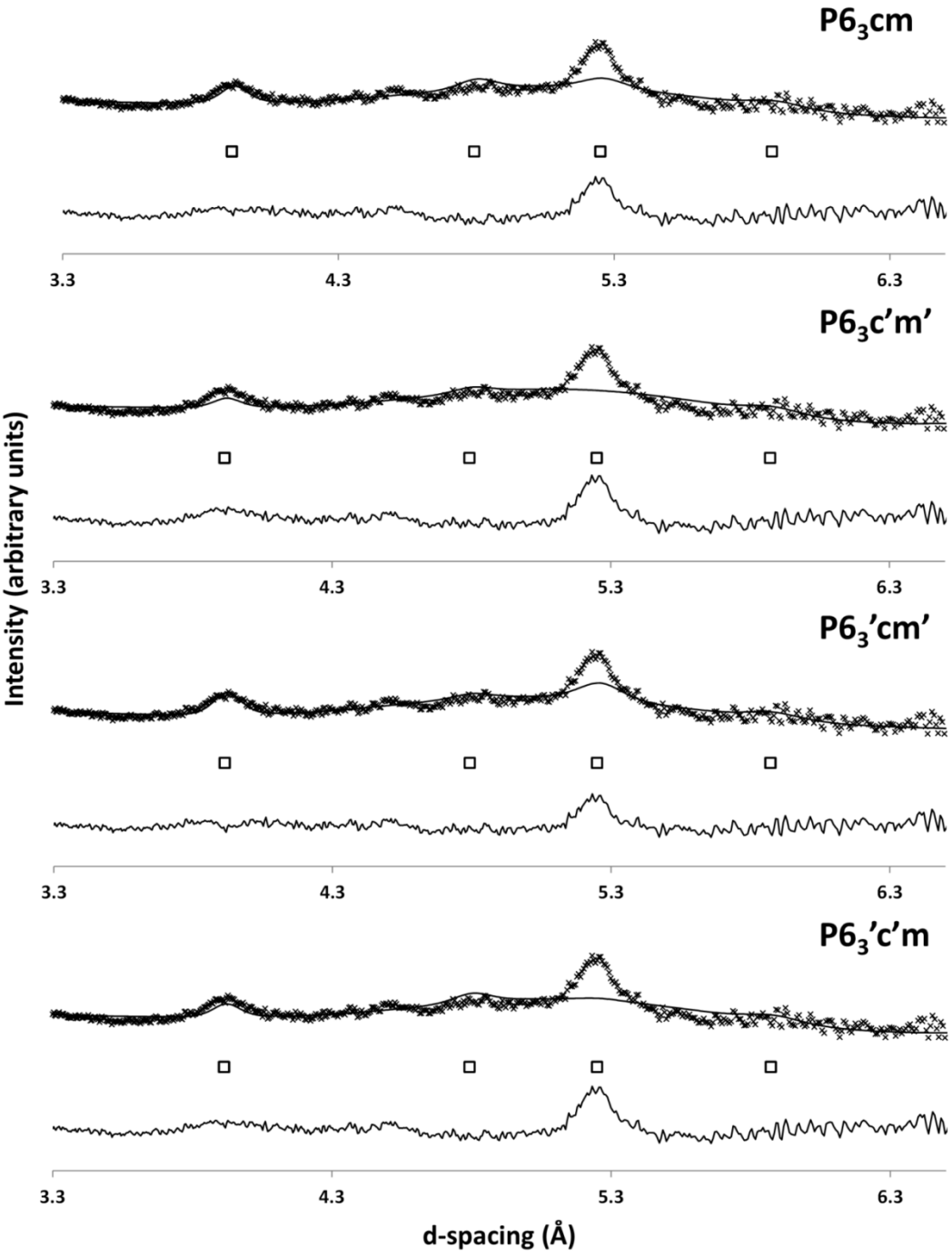

Magnetic fits for $YbFeO_3$

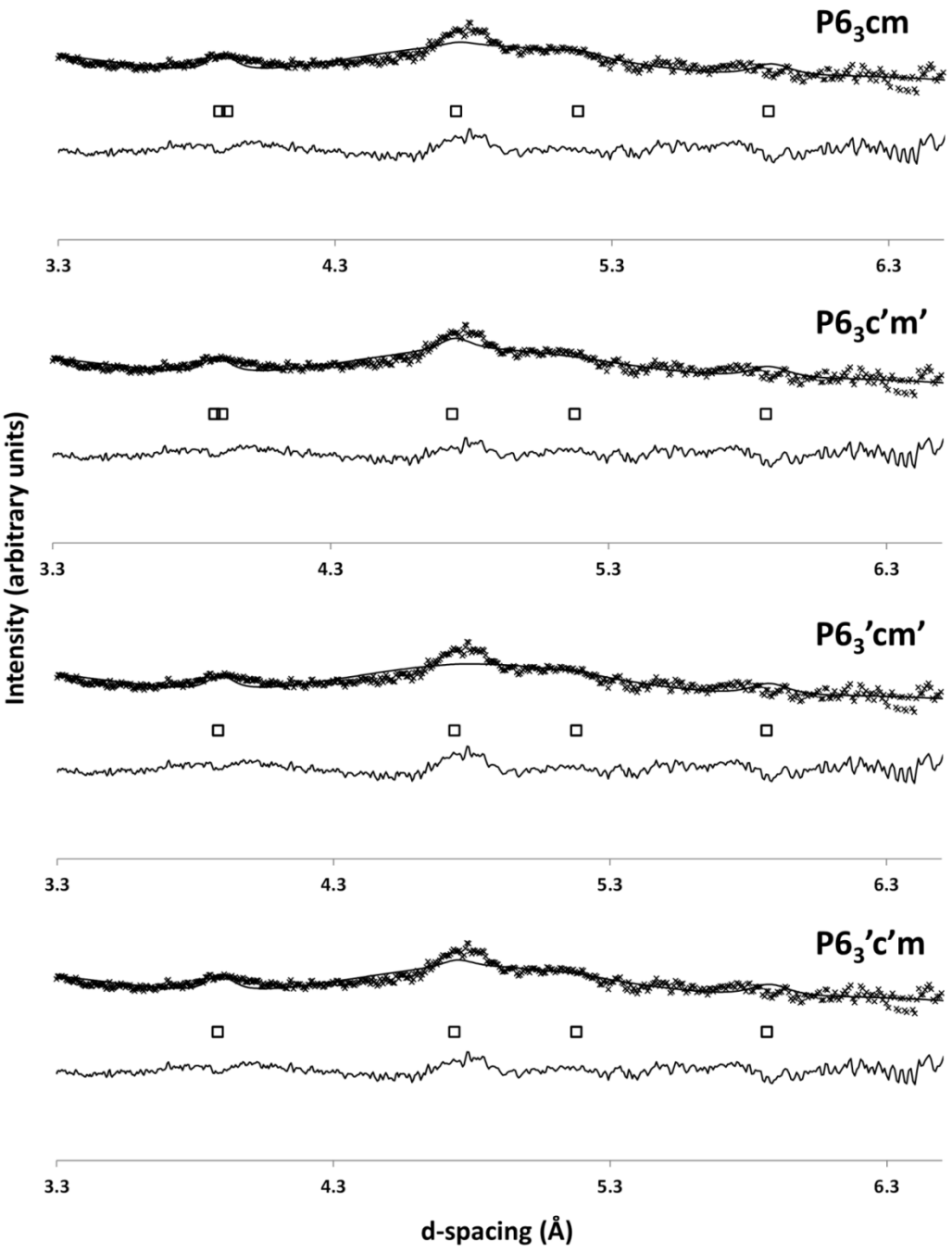

A.7.2

Lattice parameters vs. temperature for $DyInO_3$

Unit cell parameters for $DyInO_3$ as a function of temperature

Temperature (K)	a (Å)	b (Å)	c (Å)	α °	β °	γ °	V (Å^3)
RT	6.29458(5)	= b	12.29054(10)	90	90	120	421.730(8)
423	6.29996(5)		12.30009(12)				422.780(7)
573	6.30745(5)		12.31285(12)				424.225(8)
573 (cooling)	6.30745(4)		12.31342(11)				424.245(7)
723	6.31494(5)		12.32553(12)				425.672(8)
873	6.32292(5)		12.33799(12)				427.180(8)
873 (cooling)	6.32312(5)		12.33834(13)				427.219(8)
1023	6.33108(5)		12.35018(13)				428.706(9)
1173	6.33929(5)		12.36208(14)				430.233(9)

Quality of fit for $DyInO_3$ as a function of temperature

		Fitted		- Background	
Temperature (K)	χ^2	wR_p (%)	R_p (%)	wR_p (%)	R_p (%)
RT	0.8257	17.61	13.77	18.78	15.40
423	0.9944	22.38	17.47	25.40	19.91
573	0.9901	22.34	17.48	25.03	19.78
573 (cooling)	1.000	22.20	17.33	24.60	19.51
723	0.9532	21.82	17.08	24.86	19.55
873	0.9450	21.78	17.05	24.49	19.30
873 (cooling)	0.9810	22.21	17.38	25.43	19.80
1023	0.9584	22.01	17.25	25.82	20.00
1173	0.9609	22.09	17.28	25.90	20.10

Lattice parameters vs. temperature for $TbInO_3$

Unit cell parameters for $TbInO_3$ as a function of temperature (in $P6_3cm$ symmetry)

Temperature (K)	a (Å)	b (Å)	c (Å)	α °	β °	γ °	V (Å^3)
RT	6.31309(6)	= b	12.29542(16)	90	90	120	424.383(10)
333	6.31660(7)		12.30158(17)				425.068(11)
373	6.31866(7)		12.30504(18)				425.465(11)
473	6.32405(7)		12.31342(18)				426.481(12)
573	6.32955(7)		12.32214(19)				427.526(12)
593	6.33070(7)		12.32403(19)				427.747(12)
613	6.33176(8)		12.32558(19)				427.944(13)
633	6.33298(8)		12.32769(19)				428.182(13)
653	6.33428(8)		12.32935(20)				428.416(13)
673	6.33538(8)		12.33121(20)				428.629(13)
693	6.33656(8)		12.33286(20)				428.846(13)
713	6.33786(8)		12.33493(20)				429.094(14)
733	6.33902(8)		12.33618(21)				429.294(14)
753	6.34030(8)		12.33837(21)				429.544(14)
773	6.34151(9)		12.34011(21)				429.769(15)
823	6.34465(9)		12.34405(23)				430.332(16)
873	6.34782(10)		12.34862(24)				430.922(16)
923	6.35139(10)		12.35389(24)				431.591(16)
973	6.35457(10)		12.35801(25)				432.167(17)
1073	6.36151(11)		12.36702(26)				433.427(18)
1173	6.36841(13)		12.3751(3)				434.654(22)

Quality of fit for $TbInO_3$ as a function of temperature (in $P6_3cm$ symmetry and over 4 detector banks)

		Fitted		- Background	
Temperature (K)	χ^2	wR_p (%)	R_p (%)	wR_p (%)	R_p (%)
RT	1.268	2.12	1.93	2.04	1.94
333	1.046	2.44	2.39	2.44	2.41
373	1.052	2.45	2.38	2.48	2.37
473	1.073	2.47	2.34	2.45	2.35
573	1.247	2.38	2.23	2.42	2.31
593	1.268	2.40	2.23	2.47	2.28
613	1.265	2.39	2.23	2.46	2.33
633	1.268	2.39	2.25	2.43	2.33
653	1.325	2.45	2.30	2.51	2.41
673	1.283	2.41	2.26	2.45	2.34
693	1.327	2.45	2.34	2.50	2.43
713	1.309	2.43	2.25	2.47	2.38
733	1.358	2.47	2.32	2.60	2.53
753	1.369	2.48	2.29	2.51	2.43
773	1.395	2.50	2.31	2.57	2.45
823	1.254	2.65	2.48	2.66	2.62
873	1.298	2.69	2.51	2.65	2.60
923	1.290	2.68	2.54	2.70	2.70
973	1.292	2.68	2.54	2.66	2.69
1073	1.326	2.72	2.51	2.64	2.65
1173	1.566	2.95	2.64	2.75	2.74